Durham E-Theses

The bulk from the boundary; holography and AdS/CFT

Hammersley, John

How to cite:

Hammersley, John (2008) *The bulk from the boundary; holography and AdS/CFT*, Durham theses, Durham University. Available at Durham E-Theses Online: http://etheses.dur.ac.uk/2906/

The bulk from the boundary; holography and AdS/CFT

John Hammersley

A Thesis presented for the degree of
Doctor of Philosophy

Centre for Particle Theory
Department of Mathematical Sciences
Durham University
England

March 2008

Dedicated to

John and Valerie Hammersley

The bulk from the boundary; holography and AdS/CFT

John Hammersley

Submitted for the degree of Doctor of Philosophy

March 2008

Abstract

In this thesis we consider various methods by which one can extract (in detail) the metric structure of asymptotically anti-de Sitter spacetime, using only information from the boundary. This is motivated by the AdS/CFT correspondence, in particular the relation between geometrical properties of the bulk and certain field theory quantities such as "bulk-cone singularities" of two-point functions and entanglement entropy. These CFT quantities are directly related to endpoints of null bulk geodesics and regularised proper area of certain bulk minimal surfaces, respectively. Focussing initially on static, spherically symmetric spacetimes, we demonstrate how the endpoints of null geodesics, and the endpoints (along with the proper length) of zero-energy spacelike geodesics allow us to reconstruct the bulk spacetime metric, and detail explicit iterative algorithms by which the metric functions can be extracted numerically using this data, to an arbitrarily high degree of accuracy. The stability of the methods is demonstrated both via examples, and by an analytic consideration of the errors. Refinements of the algorithms are presented, and we consider the differences in how the two types of geodesic probe the bulk. We focus on a realistic application of our methods, namely extracting the physical properties of a "star" in AdS, which leads to an analysis of how their total mass varies with their core density in higher dimensions. We find the existence of a critical dimension (d_c) separating two distinct regimes of behaviour; monotonic for $d > d_c$, and oscillatory for $d < d_c$. Finally, we consider how our iterative algorithms can be generalised to metrics with less symmetry, and discuss possible directions for future research.

Declaration

The work in this thesis is based on research carried out at the Centre for Particle Theory, the Department of Mathematical Sciences, Durham University, England. No part of this thesis has been submitted elsewhere for any other degree or qualification and it is all my own work unless referenced to the contrary in the text.

Specifically, chapter 2 contains a review of pertinent background material; chapters 3 and 4 contain my own work from (and further extensions to) [1,2]; chapter 5 contains my own work from both [2] and [3], with the dynamical systems analysis (section 5.5) suggested by Vladislav Vaganov following his work in [4]; chapter 6 is original work yet to be published, and finally chapter 7 contains the discussion.

Acknowledgements

This thesis is dedicated to my parents, and they deserve a great deal of credit for getting me to a position in which I am able to write one. Without their support and encouragement throughout my life, I think it's fair to say this PhD wouldn't have happened, and so I thank them both for everything they have done.

This extends out to the rest of my family and friends whom I have grown up with and met along the way. Greg, you have provided a constant source of laughter, song and close friendship, which has helped immeasurably over the years, and I thank you for that. Even the pigeon jokes.

Since I have been at Durham, I've met so many fantastic people it's hard to know where to start! My housemates and fellow marksmen James, Kemal, Martyn and Simon have contributed to both "insightful" discussion and late nights on the town, both of which are essential for a successful PhD. The darts team from all the years, including Wendy who taught me my first words of Chinese, and especially Rob for his unsuppressible happiness; the "Mary's girls" whom we met via darts and who joined us on many of the nights out; my fellow post-grads who I've shared many a confused moment and cup of tea with; Sharry and the footballers; my supervisor Veronika for the frankly amazing job she's done at answering my random questions and providing help and direction with my work; the rest of the staff and secretaries for some memorable Christmas parties; the members of the uni dancesport team (especially Rose - "have *you* got a medal?!"), which I finally got round to joining just in time, and which led to a meeting with a certain girl named Liz, on a very cold coach to Manchester!

She's the most amazing person I've ever met; beautiful, funny, intelligent, the list goes on...Liz, I love you, you've made me the happiest man in the world :-)

Contents

List of Figures

List of Tables

Chapter 1

Introduction

A great deal of current research is directed towards an ultimate theory, one which will unify all four fundamental forces of nature and from which our universe will appear as a natural solution to the relevant equations, be they in whatever form they may be. Of the four fundamental forces there has already been great progress towards unification: firstly came the unification of electromagnetism (itself an intertwining of electricity and magnetism) with the weak force, developed by Glashow, Salam and Weinberg (among others) in the late 1960s [5–9]. This was followed by the development of the Standard Model, discussed further in later paragraphs, which emerged in the early 1970s as a unification of this electro-weak force with quantum chromodynamics, the theory of the strong nuclear force [10, 11]. All that remained was to include gravity and the dream of theoretical physicists would be realised.

Indeed, it has often been said that physics is on the verge of being wrapped up completely; Professor Stephen Hawking remarked in the late 1980s that physicists would soon "know the mind of God" [12]! Life (and physics), however, is rarely so simple, as the last 20 years or so has proven; despite a great deal of effort and countless promising ideas, including the well publicised string theory [13–16] alongside others such as loop quantum gravity (see [17, 18] and references therein), modifications to general relativity ("modified gravity" theories) [19], and Braneworld scenarios [20], we are still searching for the "missing link" to full unification. In a large number of these proposed theories, hidden extra dimensions play an important role in making them both consistent with experiment and allowing for the presence

of gravity, and it is to extra dimensions that we now turn our attention.

In 1921, the German mathematician Theodor Kaluza published a paper entitled "Zum Unitätsproblem der Physik" [21], containing an intriguing proposal detailing how Maxwell's equations of electromagnetism could emerge from general relativity if one increased the number of spacetime dimensions from four to five. This is one of the first cases of extra dimensions being used as a tool for unification, however, his work was ignored for many subsequent years (despite support from various other scientists, such as Einstein) as attention was focused on quantum electrodynamics and more phenomenological approaches, which gave highly accurate predictions for particle interactions.

This led to a remarkable forty year period of combining experimental observations and theoretical explanation. The progress made in continually developing quantum field theory to account for every physical phenomena, such as the introduction of quarks to describe the strong interactions, which was mathematically described by the non-Abelian gauge theories of Yang and Mills [22], culminated in the development of the highly successful $SU(3) \times SU(2) \times U(1)$ gauge model of particle physics we have today, known as the Standard Model (SM) [23]. It explained all of the experimental results then available, and has been verified to a high degree of precision in numerous tests since.

Even with the huge successes of the SM in explaining the interaction and composition of the constituents of the universe, it is still an incomplete theory, most famously evident in the irreconcilability of the quantum mechanics upon which it is based with Einstein's general relativity; thus far there has been no success in incorporating gravity into the framework of the Standard Model.

There are numerous other issues, such as the fact that a significant number of the constants (e.g. particle masses) do not emerge naturally from the theory, but need to be put in by hand; the inability of the theory to explain the observed (non-zero) value of the cosmological constant; and the hierarchy problem (among others - see [24] for a recent discussion of physics beyond the SM), all of which suggest the Standard Model is perhaps only an approximation to some deeper, underlying theory of nature yet to be discovered. The resolution of these various problems have

taken many forms, with the most promising early candidate (especially with respect to quantizing gravity) involving a radical new description of physics at small length scales, replacing the idea of particles as being pointlike (i.e. zero dimensional) with a theory of one-dimensional extended objects: string theory.

Such ideas (including, but not restricted to string theory) led to a revival in the Kaluza-Klein theory of hidden dimensions, and it was soon realised that one extra dimension was not enough for the theory to be suitable for describing the real world. By dropping the restriction that we work in four dimensions, one is able to make anomaly-free formulations of string theory; in the late 1960's the appropriate number of dimensions was found to be twenty six (as a consistency requirement for quantising the relativistic open (bosonic) string). It is worth emphasising that whereas Kaluza postulated an additional dimension and specifically chose to work through the calculations in such a setting, here we have no such choice; it is the theory itself which fixes the dimensionality of spacetime.

Bosonic string theory was the first mathematically formulated string theory description of quantum gravity and provides a good introduction to how particle physics can be viewed as the interactions of higher dimensional strings, however, it was not without significant problems. As indicated by its name, it is a theory containing only bosons, the force-carriers; it has no fermions and hence no (fermionic) matter content. This gives an obvious incompatibility with the world in which we live, which is compounded by the additional presence of a particle with imaginary mass in the theory: the tachyon.

These issues were all resolved remarkably simply in the mid 1980's however, with the advent of a second revolutionary idea, namely supersymmetry, which appears naturally when one attempts to incorporate fermions into the theory.[1] In practical terms, supersymmetry is the idea that every particle has a superpartner, with the requirement that the spins of the two partners differ by one half; hence every boson should have a fermionic partner, and vice versa. There are further complications,

---

[1]Although the idea of superstrings was first considered in 1971, the advent of QCD led to it being neglected until the intense period of development from 1984-85, known as the "first superstring revolution", when the five distinct string theories were formulated (see page 5).

however, as none of the standard model particles can be partnered to one another, and so one requires (at the least) a doubling of the number of particles, which must be sufficiently heavy so as to have remained out of reach of the current crop of particle colliders (the characteristic energy scale for supersymmetry breaking is thought to be in the range 100 GeV - 1 TeV). In the near future, data from the Large Hadron Collider at CERN (which will probe upto the 14 TeV range) may well reveal the existence of these super-partners; this would be the first direct evidence for supersymmetry and represent a major breakthrough in the search for unification.

Returning to our original thoughts, how does the inclusion of fermions affect the dimensionality of spacetime required for a consistent theory? The same calculation (the cancelling of the conformal anomaly) which yielded a value of $d = 26$ for the bosonic string can similarly be applied to these supersymmetric string theories, and again gives a specific value: we no longer need twenty six, but instead require $d = 10$. In other words, six additional dimensions alongside the four we see in the everyday world.

How does one argue for a theory of extra dimensions despite a complete lack of any evidence for their existence? The most fundamental length scale one can construct from the three constants of nature is known as the Planck length (l_p) and is of order 10^{-33} cm, which is far below the lengths currently accessible to experiment; hence it is quite possible for these extra dimensions to be compactified such that they are too small to be seen. Indeed, for string theory to be used for unification, one would naturally expect the string length scale (and hence the size of the extra dimensions) to be comparable to l_p.

Although this compactification of the six extra spatial dimensions cannot be arbitrary, there is a rich field of possibilities to choose from, of which a large class are what are known as Calabi-Yau spaces [25,26]. This leads to a vast landscape of solutions, of which some have been shown to lead to physics similar to that given by the Standard Model (see [27] for a recent review and further references), and it is hoped by many that (at least) one setup will result in a theory which describes our universe completely. Unfortunately, there are so many possible choices of Calabi-Yau manifold (and subsequent values of magnetic fluxes), that there are approximately 10^{500}

possible vacua [28, 29], each one giving different resultant physics! Thus without some way of structuring the possible solutions (see [30] for an interesting proposal by Candelas *et al.*) the problem of finding one which gives a sufficiently small value for the cosmological constant is virtually impossible (NP complete).[2]

Before this landscape of possible solutions was discovered, there was another rather unwanted aspect to string theory, in that there were five distinct versions! Rather than having discovered a unique theory of nature, introducing strings had led to five different possibilities, with no obvious reason why one should be favoured over the others. This was a result of the extra degrees of freedom the one-dimensional strings have over the pointlike particles they replaced; one can have both open and closed strings, and furthermore, these strings can be either oriented or unoriented. Whilst one must always include closed strings (as they can always be formed by joining the ends of an open string together), one can choose them to be either oriented or not, and also include either variety of open string. By the end of 1985, the five different string theories were all known, and were called Type I, Type IIA, Type IIB, $SO(32)$ heterotic and $E_8 \times E_8$ heterotic.

This was the case until 1995, when the "second superstring revolution" took place, which revealed that rather than having five distinct theories, they are all related to one another via certain dualities; thus in the fundamental sense, they are equivalent, and can be viewed as being being perturbative expansions of some underlying theory about different points.[3] This gave renewed enthusiasm to string theorists, as did the subsequent discovery by Witten that the underlying theory had an eleven dimensional solution, which he named M-theory in his talk given at that year's "Future Perspectives in String Theory" conference (STRINGS '95) [34].

The two dualities are known as S-duality and T-duality, and they relate theories

---

[2]This huge landscape of solutions (among other issues concerning a lack of predictive power) has led to significant criticism of string theory [31, 32], and especially the anthropic principle used by some to justify the selection of the vacua [33].

[3]Note that even though the underlying theory might be unique, as we mentioned earlier there may still be many consistent solutions (i.e. quantum vacua) - it is a particular solution which will describe our universe, and one of the biggest challenges to string theory is how this selection of the correct vacua is made.

at strong and weak coupling, and large and small distances respectively. In other words, two string theories are S-dual if one evaluated at strong coupling is equivalent to the other evaluated at weak coupling; this particular duality relates the Type I and $SO(32)$ theories, and so $f_{\text{Type I}}(g_s) = f'_{SO(32)}(1/g_s)$ for some physical quantity f, where g_s is the coupling constant. This link between the two theories is a rather surprising one at first, as at face value the two theories seem very different; Type I is a theory of open and closed unoriented strings, in contrast to the oriented closed strings of $SO(32)$ heterotic. At strong coupling, however, $SO(32)$ does have open string excitations; these are not seen in the weak coupling limit as they are unstable. Type IIB string theory is S-dual to itself, and is hence invariant under the replacement $g_s \to 1/g_s$. This conveniently allows one to gain an understanding of the strong coupling regime, via the considerably easier to work with weak coupling limit.

T-duality is an equivalence between string theories with different compactifications, and can be understood by observing the possible excitations of a string in the presence of a circular[4] dimension of radius R; one can have both Kaluza-Klein excitations, which contribute an $(n/R)^2$ term to the overall mass-squared, and winding-mode excitations of closed strings, which contribute an $(mR/l_s^2)^2$ term. With these dependencies on R, the mass-squared is then invariant under the exchange $m \leftrightarrow n$ and $R \leftrightarrow l_s^2/R$; the closed string spectrum for a compactification of radius R is identical to that for a compactification of radius l_s^2/R, and what was interpreted as a Kaluza-Klein excitation in the first description now appears as a winding-mode excitation in the second. Thus two theories A and B with circular dimensions of radius R_A and R_B respectively are said to be T-dual if these two radii are related by the equality $R_A = (l_s)^2/R_B$, where l_s is the fundamental string length scale. This implies that when one circle becomes large, the other must become small, and hence we have the remarkable property that a string theory on a compactified dimension of tiny scale is indistinguishable from one whose compactified dimension is huge! The two type II theories are related by a T-duality, as are the two heterotic

---

[4]The T in T-duality stands for "Toroidal", and with this terminology, a circle is the definition of a one-dimensional torus.

theories.

Even with these new theoretical insights, string theory still suffered from a lack of any testable predictions and a seemingly endless landscape from which to pick and choose parameters on which to base predictions; this appeared to be (and still does to some extent) a significant hurdle to progress. A new method for studying string theory and relating it to the field theory descriptions that had proven so accurate as models of the real world was needed, and help arrived, as is often the case in physics, from a slightly unexpected direction: holography.

Just over a decade ago now, a bold new correspondence was proposed by Juan Maldacena, relating superstring theory on particular ten-dimensional backgrounds with supersymmetric Yang-Mills (SYM) theories in four dimensions: the AdS/CFT correspondence [35–37]. The original form of the conjecture postulated that Type IIB string theory with $AdS_5 \times S^5$ boundary conditions is equivalent to $N = 4$ super Yang-Mills theory, and opened up a whole new set of possibilities for exploring string theory. For a comprehensive (if slightly dated) review, see [38]; further references are given in chapter 2.

This correspondence owed its conception to another important realisation about string theory that occurred in the mid 1990s, that strings are not the only extended objects one can consistently construct within its framework. Before the discovery of the dualities mentioned earlier, it had only been possible to formulate string theory perturbatively, i.e. in powers of g_s. As, however, there is no reason why the string coupling constant g_s should be small, this would not necessarily give a sensible analysis, and indeed had masked some important features of the theories.

Specifically, the existence of higher dimensional extended objects known as p-branes (with p labelling the number of spatial dimensions), which have a tension which diverges in the weak coupling limit (and hence are invisible to perturbation theory), was realised, and these extended objects became the subject of much discussion. This resulted in the crucial discovery of Polchinski [39] that extremal p-branes are the dynamical walls on which open strings can begin or end, named Dirichlet p-branes, or D-branes for short (see section 2.2). By considering a stack of parallel D-branes, and comparing the physics in the limits of strong and weak gravitational

coupling, Maldacena was able to postulate the above duality, which is discussed in greater detail in the following chapter. We also give a more precise formulation of the conjecture, and the important properties pertinent to the work in this thesis; here we describe some of the research it has led onto.

The holographic principle itself has inspired many ways of exploring different spacetime configurations. The basic idea of holography, that physics in a region of space can be described by the fundamental degrees of freedom on its boundary, was originally applied to the area of quantum gravity by 't Hooft [40] and Susskind [41], but it was Maldacena's development which put these thoughts into a more concrete setting. Revitalising the ideas of holography and extra dimensions, and developing them into something more tangible, his conjecture has led to many interesting new insights into (for example) the black hole information paradox [42], probing behind horizons [43–52, among others], and the description of gravitational objects from a field theory viewpoint (see e.g. [53–58]), to give but a few of the more geometrical ones.

Since its original postulation, there has been considerable work on both attempting to prove the correspondence mathematically to as high a level as possible, and in extending the ideas to other possible gauge/gravity dualities. The mathematical work has led to unexpected developments in such fields as integrability (see e.g. [59]), and there has been good progress in discovering links between bulk and boundary quantities, and in the matching of parameters on the two sides; despite this, a full proof still seems quite a way off.

The work on developing alternatives to AdS/CFT which might be more applicable physically originally inspired hopes of a "dS/CFT" correspondence [60, 61], driven by evidence suggesting that our universe has an asymptotically de Sitter future [62–64], however, instability problems and difficulties in producing physically realistic models have hampered progress in this direction [65], and it is unclear as to how much further this could be taken. What seems apparent is that a great deal of numerical analysis of possible models will be needed alongside the theoretical proposals and the data provided by the observational studies.

Consequently there has instead been strong interest in generalising the correspon-

dence by developing dualities between asymptotically anti-de Sitter backgrounds and more realistic gauge theories than simply $N = 4$ SYM, in particular quantum chromodynamics (the theory of the strong nuclear force) mentioned earlier, which has significant supporting experimental data. This work, often referred to as AdS/QCD, is important for a number of reasons discussed below, and there are several recent reviews of current progress, see e.g. [66, 67]. Although not directly related to our work, this extension of the original gauge/gravity proposal of Maldacena provides further motivation for studying the dualities between field theories and (asymptotically) anti-de Sitter backgrounds, such as the procedures for the holographic reconstruction of the bulk we develop in this thesis.

Conceptually, AdS/QCD allows one to use a critical string theory description of nature to yield results compatible with a four dimensional gauge theory such as QCD, with the benefit that there is greater scope for phenomenological work and a natural link with experiment, unlike the original AdS/CFT proposal (where the super conformal field theory could only be used to model physical behaviour in a narrow range of situations, such as the one dimensional quantum many body systems described in section 2.2.2). The recent discovery of a quark-gluon plasma state at the Relativistic Heavy Ion Collider (RHIC) [68] has provided strong motivation for the further development of AdS/QCD; the data can be used to test the predictions of the theories, which in turn provide a mechanism for performing otherwise difficult strong coupling calculations. This direct link with quarks in one sense brings us full circle, as in the 1970s one of the original motivations for studying strings was to explain the then new observations of quark confinement in QCD.

Quarks are currently the smallest objects observed in nature, although this has only been possible indirectly, as they are not to be found outside the hadrons. This is due to the confining nature of the strong force which holds them together, and the fact that unlike other forces it does not decrease with distance; as a quark-antiquark pair is pulled apart, the energy between them grows, until eventually it is more energetically favourable to produce a new particle (a pion, say). It is here that one of the first notions of a "string" type structure appears in particle physics, in the flux tubes responsible for the confinement of the quarks: they can be modelled

as strings. Experimentally, by measuring the Regge trajectories of the mesons one observes an (almost) linear relation between the angular momentum J and the mass squared of the tube, $J = \alpha + \alpha' M^2$, and these results are sensibly explained by a string model of the mesons where they are viewed as massive quarks connected by relativistic strings (see e.g. [69]).

The work on both AdS/CFT and AdS/QCD is ongoing, and whilst the difficulty in performing equivalent calculations in both the field theory and the string theory dual has left much still to be done, there has been significant progress on both sides of the correspondence(s). This difficulty in calculating equivalent results has its benefits, as we often have that objects which are mathematically complex on one side have a simpler description in the dual theory: this has led to a "dictionary" of relationships being built up between the two dual theories. One then uses this dictionary to further understand their equivalence, which facilitates further research to continually expand and develop more subtle relationships, until we will hopefully arrive at both a proof of the AdS/CFT correspondence (whether at the highest level or only in either the 't Hooft or large λ limit, see the following chapter for more details) and a more complete string theory picture of QCD.

Thus endeavoring to build up this dictionary will serve to both deepen our understanding and reveal new insights into the holographic relation between string and field theories, and it is with this in mind that we present the work in this thesis. In our research we focus on how known quantities in the field theory can be used to determine the geometric structure of the dual spacetime: we investigate how the bulk can be holographically reconstructed from information contained on the boundary.

How is the structure of the bulk manifested in the boundary data? The different states of the CFT correspond to different geometries in the bulk; the vacuum state is dual to the pure anti-de Sitter background, and thermal states correspond to black holes in AdS, where the Hawking temperature of the horizon can be interpreted as the temperature of the CFT. In general, one can view asymptotically AdS geometries as deformations of pure AdS by normalisable modes, which correspond to excited states in the CFT obtained by acting on the vacuum state with the relevant operator, as is discussed further in the following chapter (see section 2.2.1). Whilst these

general features of the bulk appear readily available from the field theory, what we aim to explore here is how a more systematic consideration of certain boundary information can lead to a detailed picture of the bulk interior. Rather than simply being able to distinguish between large and small deformations in the bulk, we propose numerical methods by which one can extract the pertinent information about the deep interior of the bulk to an arbitrarily high degree of accuracy (given an accurate knowledge of the requisite boundary information).

A natural method for exploring the geometry of the bulk is via geodesic probes, as they are the trajectories of unaccelerated test particles. Due to the negative curvature of an (asymptotically) AdS spacetime, the boundary can be compactified (see appendix A) such that both null and spacelike geodesics can travel out to the boundary in finite coordinate time; indeed, one can consider such geodesics which both begin and end on the boundary, with their body lying in the bulk. One can imagine characterising such geodesics by their endpoints on the boundary, and grouping all the geodesics with one endpoint coincident, thus forming "sets" of geodesic probes. Then, rather than using the spacetime to specify the geodesics, can one use the geodesics to specify the spacetime? In other words, given just this distribution of endpoints, can the properties of the bulk in which the corresponding geodesics propagated be accurately determined?

Whilst the probing of the spacetime geometry via geodesics would be interesting simply from a general relativity point of view, it takes on added significance when one also has that the endpoints of the geodesics are related to certain quantities in the CFT living on the boundary. This is true for both the null and spacelike boundary-to-boundary geodesics, and we shall consider both in turn. In the case of null geodesics, in section 2.2.1 we observe how their endpoints are related to singularities in the (two-point) correlation functions of operators inserted on the boundary; in other words, that the correlation function between any two points on the boundary which can be connected by a null geodesic path diverges. This implies that given the two-point correlation function data, one could then in principle recover the corresponding distribution of null geodesic endpoints.

For a static, spherically symmetric spacetime, this distribution is equivalent to

the set of null geodesics which originate from the same point of the boundary. Using the visualisation of anti-de Sitter spacetime as a cylinder (given in Appendix A), for a geodesic with a fixed starting point $\phi_{start} = t_{start} = 0$ on the boundary, one then has two endpoint coordinates to consider, (ϕ_{end}, t_{end}), labelling the final values of ϕ and t as the probe returns to the boundary after traversing the bulk; figures 3.1 and 3.2 show some examples of how the distributions vary in different asymptotically AdS spacetimes. It is worth noting that in these symmetric cases, the null geodesic probes can at most determine one function's worth of information about the metric (due to their zero proper length resulting in no sensitivity to the overall conformal factor of the metric), and this is precisely the same amount of information contained in the set of endpoints, which can be thought of as a function $t_{end}(\phi_{end})$.[5]

The process by which one can extract this information is helped significantly by the fact that the normalised angular momentum of each null geodesic probe is available directly from the gradient of the endpoints, as we show explicitly in section 3.1.1. This remarkable fact emphasises the holographic nature of the bulk, and whilst here we demonstrate how such a relation provides the basis for a numerical reconstruction of the metric, it also gives hope that with further development one could produce an explicit (analytical) map between the endpoint data and the spacetime geometry.

Interestingly, we find a somewhat analogous method involving spacelike geodesics, albeit through a somewhat different route from the field theory. Returning to the ideas of holography and black holes, one of the original (and most striking) applications of the holographic principle was in relating the entropy of a black hole to the area of its horizon [40, 41]. In order to prevent a violation of the second law of thermodynamics, black holes must carry entropy; Bekenstein conjectured that this entropy was proportional to the horizon area [70]. After further research by Hawking showing that black holes emit radiation [71], which corresponds to a certain temperature, the entropy relation was then stated as an equality: $S_{BH} = A/4G$, where

---

[5]The idea that the endpoint information of boundary-to-boundary geodesics could be used (in principle) to recover the corresponding bulk metric was discussed in a study of black hole singularities in AdS/CFT by Festuccia and Liu, [51].

A is the horizon area and G is Newton's constant (in units with $\hbar = c = k = 1$). This thermodynamic argument was then strengthened in 1996, when Strominger and Vafa gave a microscopic description of the Bekenstein-Hawking entropy, S_{BH}, for BPS black holes [72].

The idea of entropy being linked with an area rather than a volume (as one naturally expects from thermodynamics) is not, however, restricted to the case of black holes. In quantum mechanical systems, there is a different type of entropy known as entanglement entropy, which is derived from the von-Neumann entropy by reducing the amount of information available in its computation. For a system divided into two subsystems A and B, the entanglement entropy for A is given by:

$$S_A = -\mathrm{tr}\rho_A \log(\rho_A) \tag{1.0.1}$$

where $\rho_A = \mathrm{tr}_B |\Phi\rangle\langle\Phi|$ is the reduced density matrix (for subsystem A), which is obtained by taking the partial trace of the total density matrix $\rho = |\Phi\rangle\langle\Phi|$ over B (at zero temperature; for finite temperature systems, this is replaced by $\rho = \exp^{-\beta H}$, see section 2.2.2 for further details).

One can physically think of S_A as the entropy for an observer of subsystem A alone, cutoff from any information contained in B; such ideas about entanglement have been at the heart of quantum mechanics since Einstein, Podolsky and Rosen first asked questions about the nature of measurement and how the very act of "taking a measurement" might affect the system. This led to the formulation of the EPR paradox [73], which highlighted problems with our intuition when dealing with the quantum world; a mathematical solution was presented by Bell in 1964 [74], and Bell's theorem and inequalities have been the focus of much work on entanglement in recent years, especially with the goal of developing a functional quantum computer (see e.g. [75] for an overview).

Entanglement entropy is also being used to investigate quantum criticality in low-dimensional many body systems (see e.g. [76, 77]), and with the development of Density Matrix Renormalisation Group (DMRG) techniques [78], the ability to numerically generate entanglement entropy data for various different systems with increasingly complicated coupling between particles is increasing rapidly. Originally designed for static, one-dimensional systems, further extensions of the DMRG tech-

niques have led to progress in dynamical systems and in higher dimensions [79]. With this numerical data, many interesting ideas about quantum systems have emerged (see section 2.2.2), and work often focuses on taking either the thermodynamic limit or some other simplification to obtain an analytic form for S_A in this limit, however, one wonders if there isn't more to be gleaned directly from the actual data.

How does this tie in with our work on geodesic probes? Until recently, there had been no detailed interpretation of the entanglement entropy from the gravitational point of view, despite the focus on such relations due to the aforementioned AdS/CFT correspondence. In early 2006, however, an intriguing proposal was put forward by Ryu and Takayanagi [80, 81] relating the entanglement entropy of a subsystem in a CFT to the area of a *minimal surface* in the bulk. In (2+1) dimensions, the area of the minimal surface in question corresponds to the proper length, $\mathcal{L}$, of a *zero-energy spacelike geodesic* (i.e. one at fixed time) connecting the two endpoints of region A through the bulk, as illustrated in figure 2.6. A geodesic with longer proper length will then naturally probe deeper into the bulk; by varying the angular momentum of the geodesic, one can effectively choose the depth to which the geodesic penetrates, as we shall see explicitly in the following chapters. Once again considering static, spherically symmetric spacetimes, by choosing a set of boundary-to-boundary geodesics with starting point fixed and varying endpoint, one can systematically probe the interior of the bulk and reconstruct the metric function, albeit in the restricted case of (2+1) dimensions.

In both cases (using null and spacelike geodesics to extract bulk information), we demonstrate that the boundary data can be used to extract at most one function's worth of information about the interior. This is to be expected by noting that the null geodesics are not sensitive to the overall conformal factor of the metric, and the static spacelike geodesics cannot probe the timelike part. Crucially, however, this means the two different types of geodesic can access different features of the bulk metric, and whilst one cannot use either individually to determine the full metric in the most general static, spherically symmetric cases:

$$ds^2 = -k(r)dt^2 + h(r)dr^2 + r^2d\Omega^2 \tag{1.0.2}$$

one can use them in conjunction in order to do so (although in order to justify using

the spacelike geodesic probes, we must restrict ourselves to three bulk dimensions).

As has often been found in the past (and not just in physics!), being able to do something in principle and actually doing it in practice are two very different things, and without further insight, one might suspect the same would be true here. Given this boundary data for the geodesics, how does one use it to extract the information about the bulk? Interestingly, the procedure is remarkably similar in both methods, and the significant idea (especially in producing a numerically feasible algorithm) is that the gradient of the boundary data immediately reveals further information about the connecting geodesic. For example, in the spacelike case, after plotting the proper length against the angular separation of the endpoints, see figure 4.1, taking the gradient $d\mathcal{L}/d\phi$ at any point immediately yields the angular momentum of the corresponding static spacelike geodesic.

The essence of both methods then is that one can focus on specific radii by systematically using geodesics which penetrate to different depths in the bulk. For null geodesics, there is only one effective parameter which determines the minimum radius obtained by the geodesic in a given spacetime, namely the ratio of the angular momentum to the energy. When this ratio is close to one, the geodesic probe travels around the edge of the spacetime; as it is reduced, the probe travels deeper into the spacetime before returning out to the boundary. For static spacelike geodesics, the effective parameter is the angular momentum itself (as the energy is zero by definition); the smaller the angular momentum, the closer to the centre the geodesic descends. The simple relation between the gradient of the boundary data and the geodesic's effective parameter then allows the minimum radius of the geodesic to be determined, and by working iteratively from large r, one can reconstruct the metric function of the bulk.

Are there any metrics which we cannot fully probe with geodesics? A natural answer is those containing a singularity, as the incoming geodesics will not return back out to the (same) boundary if they have passed behind the horizon; the null geodesics will terminate at the singularity, and those spacelike geodesics which don't will reach a different boundary to the one they originated from (see e.g. [47]). Thus for our iterative methods, we might then expect that one could probe down to the

horizon radius, r_h, and no further; whilst this is true for the spacelike geodesics, the cutoff point for the null probes is at a larger radius, $r_c > r_h$, and indeed there are also non-singular metrics which cannot be fully probed by the null geodesics, as we see in section 3.4.

There are further extensions one might consider, such as removing one of the symmetry constraints, allowing the metric an angular or temporal variation, as well as radial. These possibilities are investigated in chapter 6, where we see how the iterative methods must be adapted to work in these more complicated scenarios. Similarly, one could ask what the minimal surfaces of Ryu and Takayanagi's relation to the entanglement entropy are in higher dimensions, and whether these can be used to extract the metric in such cases, see [82].

Finally, one should also note that there have been numerous other approaches to probing the bulk structure, for example the use of one-point functions to distinguish between star and black hole geometries in AdS [56], however, these primarily focus on how the presence of singularities and other specific objects in the bulk manifest themselves in the field theory data. Indeed, most proposals take some specific calculation one can perform in either the field theory or the bulk, and then explicitly show how it matches to a corresponding calculation on the other side of the duality in some limit, thus often giving only qualitative relations for the overall dualities. Although these calculations can be fruitful in both providing evidence for the AdS/CFT correspondence, and leading to further conjectures on other gauge/gravity dualities, there is still not the facility for taking a set of generic field theory data and asking what the gravity dual to the theory might look like.

In a similar fashion, numerical work often concludes by taking some (e.g. thermodynamic) limit, in order to obtain an analytic result; here we instead use the full spread of numerical data on the field theory side to obtain a full (numerical) reconstruction of the metric. This provides a simple procedure for testing hypothesised dualities, assuming of course one can obtain the required data from the field theory; entanglement entropy calculations for example are notoriously hard to perform in systems with complicated interactions, and this difficulty becomes a near impossibility in higher dimensions. This is one of the reasons why one wanted to

be able to compute them holographically! However, given the recent developments in DMRG techniques mentioned above, there is increasing numerical data for the entanglement entropy of complex systems. The very nature of this data, where its functional form is impossible to write down analytically, provides the ideal input for the methods presented here. Not only can these iterative methods be used in practice, their derivation highlights possible intriguing links between null and (static) spacelike geodesics, due to the way the gradient function of the boundary data yields the effective parameter for the corresponding geodesic in both cases.

Before we continue with the rest of the thesis, here is an outline of what is to come: In the next chapter we give some background information on the topics mentioned above. Specifically, we introduce the ideas of a gauge/gravity duality in more rigorous terms, describing the formalism of the AdS/CFT correspondence in greater detail, including the links between two-point correlators and null geodesics, and entanglement entropy and zero-energy spacelike ones. We conclude the section by reviewing the relevant geodesic equations, and their behaviour in pure AdS.

Chapter 3 then develops in detail the proposal for probing the bulk with null geodesics, reproducing and extending the original work presented in [1], and gives examples of extracting the bulk metric numerically for various deformations to pure AdS. Using the derived relation between the gradient of the endpoints and the normalised angular momentum mentioned earlier, together with the endpoint data, we devise a simple iterative method for extracting the bulk metric, beginning close to the boundary where the spacetime can be taken to be approximately pure AdS. Although the proposed method is both stable and reasonably efficient, after analysing the accuracy of the various approximations used in the method, we develop an alternative formalism which greatly improves the overall efficiency by removing the least accurate approximation.

The chapter continues by performing a stability analysis of the iterative process, demonstrating that any errors which occur are quickly suppressed at subsequent steps, and analytically explaining the robustness of the numerical procedure. Finally, the chapter concludes by examining those spacetimes whose metrics cannot be fully recovered from the endpoint data, due to the presence of a sufficiently

large deformation such that the effective potential for the null geodesics becomes non-monotonic at some critical radius, r_c.

In chapter 4, we perform a similar analysis for spacelike geodesic with zero energy, seeing strong parallels in the way one can consider a "spread of endpoints" (although in this case, one of these "endpoints" is in fact the proper length), whose gradient yields the angular momentum of the corresponding geodesic (work originally presented in [2]). Following broadly the same format as for the null geodesics, we develop an iterative method for extracting the metric function, give numerical examples of this algorithm in action, and then consider the affect of any errors on its accuracy and stability, detailing why a linear approximation to part of an integral (which worked when used in the algorithm involving the null geodesics) can now no longer be used if one wants to avoid instabilities ruining the extraction.

A discussion on why the method reformulation performed in chapter 3 is also not applicable here is then presented, along with a brief comment on the validity of the estimates generated by these numerical methods. The chapter concludes with a section detailing an intriguing relation between null and spacelike geodesics this analysis of their endpoints has revealed; the boundary information of the null geodesics can be equivalently viewed as the boundary information of the spacelike geodesics in an alternative bulk!

Chapter 5 then details how one can extract both unknown functions $k(r)$ and $h(r)$ in (1.0.2) by a sequential application of the two iterative algorithms, as shown in [2], firstly using the spacelike geodesics to determine $h(r)$, then the null geodesics to determine $k(r)$. After testing the accuracy of using both methods in sequence, we then go on to consider how one can use the numerical reconstruction of the bulk in order to extract the pertinent information from a toy model of a perfect fluid gas of radiation. Restricting ourselves to three bulk dimensions (in order that the use of spacelike geodesics be well motivated) does limit the physical realism of the model, however, due to the non-dynamical nature of gravity in such a scenario.

This leads onto the second half of the chapter, based on the work in [3], where we perform an investigation into the stability of such radiating perfect fluid "stars" in arbitrary dimension d, motivated by the observation in [83] that the total mass

of such stars does not increase monotonically with the central density ρ_0 in the five dimensional case. We find that this oscillatory behaviour continues for d up to a certain critical dimension, which we determine numerically to be $d_c = 11.0$, above which the total mass *does* increase monotonically with ρ_0 (see figure 5.5). Further numerical modelling of the self-similar behaviour of the oscillations is then followed by a dynamical systems analysis, which gives a clear analytical derivation of the critical dimension by comparing the asymptotic behaviour at large ρ_0 to that of the system in the zero cosmological constant limit.[6] A consideration of the fixed points gives both a value for the critical dimension of $d_c = 10.964\ldots$, consistent with the numerical result, and also provides explicit values for certain parameters of the model of the self similar behaviour of the oscillations at large ρ_0.

In chapter 6 we attempt to generalise the methods for extracting the bulk information presented in earlier chapters to less symmetric cases. We find that each removal of a symmetry increases the dimension of the corresponding boundary information for the geodesics, for example in a non-static but still spherically symmetric bulk the endpoint plot for the null geodesics is now a two-dimensional surface, see figure 6.1. Our algorithms for extracting the bulk information are then affected in two main ways: firstly, the geodesic equation can no longer be written in integral form, meaning our methods must now be generalised to the differential case, and secondly, we no longer necessarily have the conserved quantities of energy and angular momentum along the geodesic.

This second point immediately asks the question of what our "endpoint gradients" $dt_{end}/d\phi_{end}$ and $d\mathcal{L}/d\phi_{end}$ now correspond to in terms of the geodesic parameters, and our numerical study finds a slightly surprising result; they now yield the *final* value of the (normalised) angular momentum as the geodesic reaches the boundary. With this new relation, we demonstrate (for the specific case of a three-dimensional metric with both angular and radial dependence) how one can again

---

[6]This analysis was suggested after correspondence with V. Vaganov, who also considered the behaviour of self-gravitating radiation in AdS_d in [4]. Work simultaneously conducted by P. H. Chavanis also found the critical dimension described here, via an alternative route, in his comprehensive study of relativistic stars with a linear equation of state, [84]. See section 5.2 for further comments.

construct iterative methods to extract the bulk via both types of geodesic, albeit with a slightly simplified choice of metric. These methods involving the differential form of the geodesic equation are important not simply for this extension to less symmetric cases, but also for higher dimensional work, where one no longer has the relevant minimal surface being a static spacelike geodesic (and indeed in the development of a fully covariant method).

The thesis then concludes in chapter 7 with a discussion of our results and possible future directions for the research.

Chapter 2

Background

Since its inception ten years ago, work on the AdS/CFT correspondence has led to many beautiful and previously unconsidered relations between geometry and quantum theory, and there is a great deal of literature on the subject, including numerous review papers and discussions (see [38, 85–89] and references therein). Here we outline the formulation of the duality, giving its original D-brane description, and observe the matching of symmetries between the two theories as a basic consistency check. We go on to detail the relationships between field theory quantities and boundary-to-boundary propagators pertinent to our work in the following chapters; specifically the singularities in two-point correlation functions of operators inserted on the boundary, which correspond to points connected by null geodesics in the bulk, and the entanglement entropy of quantum subsystems which relates to certain minimal surface areas in the bulk. The final section of this chapter contains a review of geodesic equations and the general properties of geodesics in Anti-de Sitter type backgrounds; further details appear in appendix A.

As was mentioned in the introduction, string theory was originally studied as a way to better understand quark confinement in QCD, however, the picture there was of an approximate, qualitative description of the flux tubes; in contrast, the AdS/CFT correspondence (and the other related gauge/gravity dualities developed subsequently, such as AdS/QCD) is conjectured to be an *exact* duality, with a precise matching of results on both sides. When performing calculations, however, it is often necessary to work in certain limits, where the strings are weakly coupled for example,
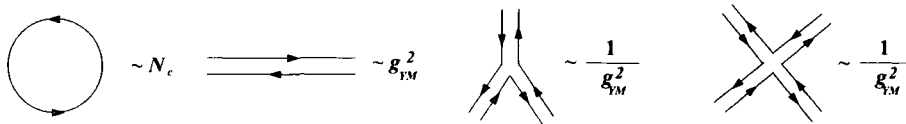
Figure 2.1: The Feynman rules for the gluon interactions in double line notation; every closed loop contributes a power of N_c, and the powers of g_{YM} arise from the propagators and vertices.

or one can use perturbation theory. An important quantity in describing these limits is known as the 't Hooft coupling, λ, and we begin by briefly describing its role in gauge/gravity dualities.

2.1 Gauge theories and strings; introducing the 't Hooft coupling

We begin by describing how a simple modification to QCD, proposed by 't Hooft [90] in 1974, can lead to a natural description of a field theory in terms of strings. In the original classification of the hadrons, one particle (Δ^{++}) consisted of three up quarks with parallel spins, a configuration forbidden by Pauli's exclusion principle. To explain this observation, quarks were proposed to have an additional SU(3) gauge degree of freedom, called colour charge. In his generalisation of QCD, 't Hooft considered instead the gauge group SU(N_c), and took the large N_c limit. In doing this, one finds an intriguing organisation of the perturbation series, as we shall now see.

In the large N_c limit, the dynamics of the system are dominated by the gluons, as the number of gluon degrees of freedom, $N_c^2 - 1$ is much greater than that of the quarks, $N_c N_f$, so we concentrate on gluon only interactions. In double line notation, the Feynman rules for the SU(N_c) gauge theory are given in figure 2.1, and we can see that the one loop gluon self-energy scales as $g_{YM}^2 N_c$, where g_{YM} is the coupling constant.

The quantity $\lambda \equiv g_{YM}^2 N_c$ is known as the 't Hooft coupling, and will appear again in our construction of the AdS/CFT correspondence in the next section: here we

$\sim \lambda N_c^2$ $\qquad\sim \lambda^2 N_c^2$ $\qquad\sim \lambda^3 N_c^2$ $\qquad\sim \lambda^2$
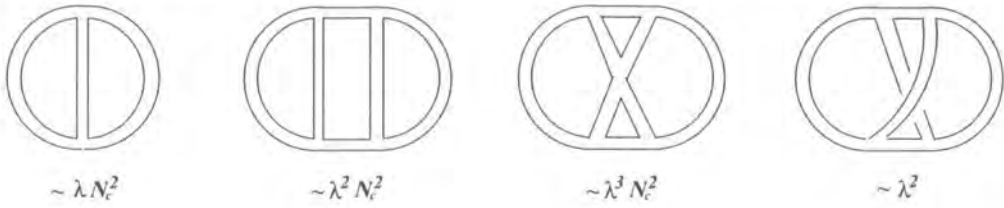
Figure 2.2: Various vacuum diagrams for the gluon interactions, where the coupling constant g_{YM} has been combined with the number of colours N_c such that the diagrams can be expressed in powers of λ and N_c. In this form, one observes that the non-planarity of the diagram is determined by the power of N_c^{-2}; hence in the large N_c limit, the non-planar diagrams such as the one on the right are suppressed.

Figure 2.3: The diagrams which are planar on the page can naturally be visualised as also being planar on the surface of a sphere (left). This two-dimensional representation can then be extended to those diagrams which are non-planar when drawn on the page, as they can be drawn as planar diagrams on two-dimensional surfaces of higher genus (right).

will keep it fixed while sending $N_c \to \infty$. By constructing further diagrams, which are shown in figure 2.2, we observe that they are naturally organised by topology: the non-planarity of a graph is determined by the power of N_c^{-2}, with the non-planar diagrams suppressed for N_c large.

How is this related to strings? We can firstly observe that there is a connection between these Feynman diagrams and higher (two) dimensional surfaces. Whilst the final diagram of figure 2.2 is non-planar when drawn on the page, it can be drawn as a planar diagram on the surface of a torus (all the planar diagrams can be visualised on the surface of a sphere), as shown in figure 2.3. This is true in general: the higher the degree of non-planarity, the higher the genus of the corresponding two-dimensional surface.

This can be translated to a string picture by labelling one direction on the surface the string direction, and one the evolution in time. The surfaces then represent (Euclidean) closed string world sheets, although a detailed relationship is not very well understood, and is difficult to formulate - one does not have a world sheet action description for example. Nonetheless, this unexpected appearance of strings in gauge theory phenomena demonstrates how extra dimensions can be used to provide an alternative description of the same physics; it is this duality which arises again in the AdS/CFT correspondence, but in a much more powerful and mathematically rigorous fashion.

2.2   Maldacena's Conjecture

Whilst the above appearance of strings in a gauge theory was rather imprecise and difficult to work with, it introduced two important concepts. Firstly, the idea that certain gauge theory objects can be viewed as projections from a higher dimensional background, and secondly, the 't Hooft coupling $\lambda \equiv g_{YM}^2 N_c$, which appeared in the classification of the Feynman diagrams above. Maldacena's conjecture, also known as the AdS/CFT correspondence, takes these ideas much further and proposes a specific map between the two sides of the duality.

The conjecture postulates that Type IIB superstring theory with $AdS_5 \times S^5$ boundary conditions is equivalent to $N = 4$ super Yang-Mills (SYM) theory with gauge group $SU(N_c)$, with the parameters of both theories related as follows:

$$g_{YM}^2 = 4\pi g_s \quad \text{and} \quad R^4 = 4\pi g_s N_c\, l_s^4 = \lambda\, l_s^4 \tag{2.2.1}$$

where g_s and g_{YM} are the string and Yang-Mills coupling respectively, and R is the AdS radius. From the above we can see how the correspondence has given an explicit relation between the string theory parameters R and l_s, and the 't Hooft coupling λ. The string length, l_s, is also often recast as the Regge trajectory $\alpha' = l_s^2$.

This is what is often referred to as the *strong form* of the AdS/CFT correspondence, and the equivalence of the two theories requires a precise map between the local, gauge invariant operators of the Yang-Mills side, and the states and fields of

the superstring theory. However, requiring a full quantum treatment of the superstring prevents more than a handful of calculations being performed on the string side, and so one instead works with weaker versions, obtained by taking appropriate limits. The first limit one could consider is the 't Hooft limit we used before: keep $\lambda \equiv g_{YM}^2 N_c \propto g_s N_c$ fixed, and let $N_c \to \infty$. As we saw in the previous section, on the SYM theory side this corresponds to a topological expansion of the Feynman diagrams; on the string theory side, after noting that we have $g_s \propto \lambda/N_c$, we can see that since λ is being kept fixed as $N_c \to \infty$, this limit corresponds to weak coupling string perturbation theory.

This limit is still rather difficult to work with however, and we have to go even further in order to obtain a tractable setting. Once the above limit has been taken, we are left with only one available parameter, namely λ; we can therefore examine the behaviour at the two ends of the spectrum, with λ either very small or very large. These limits arise naturally out of the D-brane picture which was first used to motivate the correspondence, and so we now present the duality from this perspective.

A consequence of exploring geometries with ten (say) dimensions is that strings are not the only extended objects one can describe; one can also define higher dimensional membranes, or "branes" for short, as we mentioned in the introduction. Dirichlet p-branes (Dp-branes) are massive $p + 1$ dimensional objects on which open strings can begin or end; the endpoints obey Neumann boundary conditions in the longitudinal directions, along the brane, and Dirichlet boundary conditions in the transverse directions, hence the name. They can also be viewed as topological defects, as when a closed string and a brane meet, the string can "split" at the point of contact to form an open string whose ends move along the brane.

Consider a stack of N_c parallel D3-branes: the lightest open string with both endpoints attached to a single brane is massless, as it can have arbitrarily short length. There is, however, a (non-zero) minimum mass for open strings connecting different (non-coincident) branes, due to a lower bound on the length of such strings given by the branes' separation distance. This separation is governed by the expectation values of scalar fields in the corresponding gauge theory, and we wish to consider
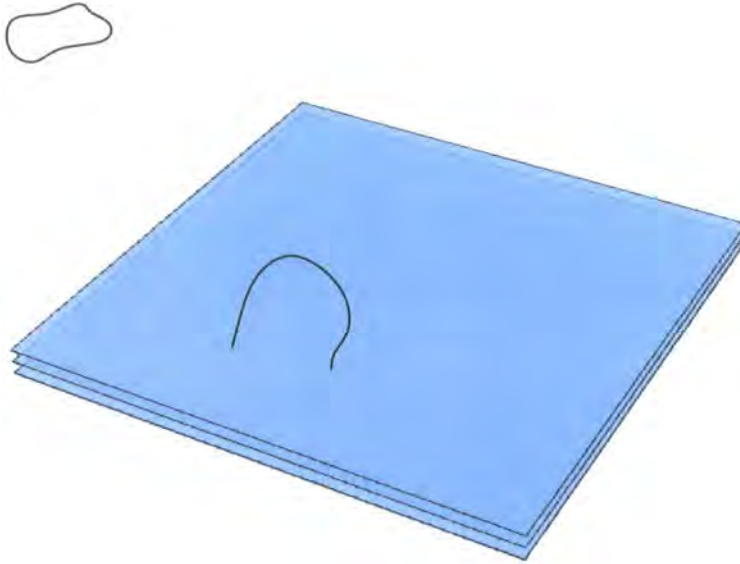
Figure 2.4: For $g_s N_c \ll 1$, the gravitational distortion of the branes is very small, and the stack of D3-branes can be viewed simply as boundary conditions for the open strings. The closed strings, however, propagate in the full ten-dimensional spacetime.

the setup where these expectation values vanish and the branes are coincident.

For a system of N_c branes, each of which couples to the gravitational degrees of freedom with strength g_s, the gravitational radius must scale as $g_s N_c$ (in string units), c.f. (2.2.1) above. Varying $\lambda \propto g_s N_c$ is then equivalent to varying the strength of the gravitational distortion caused by the branes.[1]

For the regime, $g_s N_c \ll 1$, this gravitational distortion is very small, and the spacetime is approximately flat. In this scenario, the D3-branes can be thought of as simply a boundary condition for open strings; their fluctuations are described by the open strings whose excitation modes all propagate in the worldvolume of

---

[1]One might initially imagine that the large λ-limit would be rather complicated, due to the effects of the strong gravitational coupling. As we shall see in the following analysis, however, close to the branes, their mass curves the spacetime into a throat geometry of the form $AdS_5 \times S^5$, and from (2.2.1) we see that in the large λ-limit, the size of the AdS radius R also becomes large, which greatly simplifies the effective geometry for the closed strings (only the massless string states survive).

Far from the throat, spacetime appears flat

Throat region has geometry
AdS$_5$ × S^5
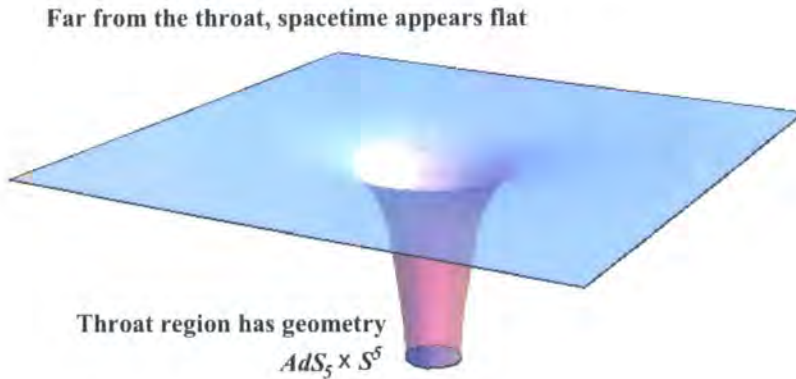
Figure 2.5: In the limit $g_s N_c \gg 1$, the large gravitational distortion affects the curvature of the spacetime in the region near the branes, forming a throat structure which has the geometry of $AdS_5 \times S^5$. In the asymptotic region away from the branes, however, the geometry is simply that of a flat ten-dimensional spacetime.

the branes (3+1 flat dimensions), see figure 2.4. Although closed strings are also present, they propagate in the full (flat) ten-dimensional spacetime and decouple from the open strings due to the weak string coupling (furthermore, for low energy excitations, they describe a decoupled linearised gravity theory, i.e. there are no interactions between the closed strings).

There are N_c^2 species of open strings in such a scenario, and so the gauge theory description is the maximally supersymmetric $U(N_c)$, however, in the low energy limit one can also decouple the $U(1)$ factor to leave $SU(N_c)$. The open string interactions are dependent on g_{YM}, the SYM coupling constant, and so at low energies we have that our description of the system is an interacting $N = 4$ SYM theory in four dimensions, alongside ten-dimensional gravity.

In the alternative limit, $g_s N_c \gg 1$, the backreaction of the branes on the background cannot be ignored, as the gravitational distortion is large, and the spacetime becomes curved, see figure 2.5. One therefore has to use the effective action for closed strings to describe the curvature, in other words, the supergravity theory in the full spacetime.

Low energy excitations are those which have arbitrarily low energy with respect to an observer at infinity, and there are two possible origins for such modes; those propagating in the (flat) asymptotic region, and those in the throat. The modes in

the asymptotic region again are non-interacting between themselves at low energies, and also decouple from those in the throat as their wavelength is too large for them to effectively probe the near-horizon region. The modes in the throat, very close to the horizon, are strongly red-shifted however, as they must climb the gravitational potential to reach the observer at infinity, and can therefore have arbitrarily high proper energy. As these excitations cannot easily escape to the asymptotic region, we again have two decoupled theories; interacting closed strings in the near-horizon region, alongside ten-dimensional gravity.

Given that in both the small and large λ-limits, we have decoupled gravity in the asymptotic region, our conjecture now becomes that the two different descriptions of the regions close to the branes are both describing the same physics, and hence are "dual" to one another. In the first limit, we had the gauge theory description of the open strings on the D3-brane; we are thus left with examining the geometry of the near-horizon region of the brane in figure 2.5.

The metric for an extremal D3-brane is given by:

$$ds^2 = \left(1 + \frac{R^4}{u^4}\right)^{-1/2}(-dt^2 + dx_1^2 + dx_2^2 + dx_3^2) + \left(1 + \frac{R^4}{u^4}\right)^{1/2}(du^2 + u^2 d\Omega_5^2) \quad (2.2.2)$$

which has a horizon at $u = 0$, and to obtain the metric for the background on which the interacting closed strings propagate, we then take the near horizon limit, which reduces (2.2.2) to:

$$ds^2 = \frac{u^2}{R^2}(-dt^2 + dx_1^2 + dx_2^2 + dx_3^2) + \frac{R^2}{u^2}du^2 + R^2 d\Omega_5^2 \quad (2.2.3)$$

or equivalently:

$$ds^2 = \frac{R^2}{z^2}(-dt^2 + dx_1^2 + dx_2^2 + dx_3^2 + dz^2) + R^2 d\Omega_5^2 \quad (2.2.4)$$

where $z = 1/u$ and we have rescaled the t and x_i coordinates accordingly. This metric is that for $AdS_5 \times S^5$ where both the 5-dimensional AdS part and the 5-dimensional sphere have the same radii of curvature, R.

Technically speaking, the metric given above with $0 < z < \infty$ does not cover the entire spacetime, only a Poincaré patch, and it is more common to consider the global anti-de Sitter cover (see appendix A for further details) with boundary

$\mathbb{R} \times S^3$ on which the gauge theory lives. The radial coordinate u (or z) is related to the effective energy scale of the gauge theory, and a UV regulator is therefore represented by a cutoff $u = u_{cutoff}$ at some finite u (or equivalently $z = z_{cutoff} > 0$). In other words, strongly coupled infrared behaviour (in the field theory) is related to physics in the deep interior of the supergravity bulk.

Since Maldacena's paper originally appeared, there have been many successful tests of this duality, see for example [91] and references therein. The simplest checks one can perform to show this correspondence between field and string theory is to observe the matching of symmetries. $N = 4$ SYM has an $SO(2,4)$ symmetry from conformal invariance (this is the conformal group in $(3 + 1)$ dimensions), and this matches with the isometry group of AdS_5. The isometry group of the 5-sphere, S^5 is $SU(4) \sim SO(6)$, which agrees with the rotational symmetry of the scalars (R-symmetry) of the gauge theory. Finally, note that both sides also contain 32 supersymmetries; on the string side these appear as Killing spinors due to $AdS_5 \times S^5$ being a maximally supersymmetric solution of Type IIB string theory, in the gauge theory description they include the 16 ordinary (Poincaré) supersymmetries, and 16 special supersymmetries required by the superconformal algebra.

Thus far we have argued the case for the duality without giving a precise formalism for the mapping between the two alternative descriptions; we now explore in more detail the field/operator correspondence (originally discussed in [36,37]), and in particular the gravity description of the two-point correlation functions of scalar operators.

In $N = 4$ SYM, deformation by a marginal operator changes the value of g_{YM} (the coupling constant); this then results in a change of the string coupling constant g_s (due to (2.2.1)). As g_s is given by the boundary value of the dilaton, this corresponds to changing this boundary value. Thus if one considers adding an interaction term $S_{int} = \int d^4x \phi_0(\vec{x}) \mathcal{O}(\vec{x})$ to the gauge theory action, where $\mathcal{O}$ is the corresponding operator, one expects that dual to each such operator there corresponds a string field such that its value at the boundary acts as a source for the operator. More precisely, one claims that:

$$\left\langle \exp\left(\int d^4x \phi_0(\vec{x}) \mathcal{O}(\vec{x}) \right) \right\rangle_{CFT} = \mathcal{Z}_{string} \left[\phi(\vec{x}, z)|_{z=0} = \phi_0(\vec{x}) \right] \qquad (2.2.5)$$

where the LHS represents the generating functional of connected correlation functions in the gauge theory. In other words, to calculate the correlation functions of $\mathcal{O}$ we take functional derivatives with respect to the (arbitrary) function ϕ_0, and then set $\phi_0 = 0$. The right hand side is the full partition function of the string theory, with the given boundary condition; in the large N_c, large λ limit this simplifies to $\mathcal{Z}_{string} \sim \exp(-S_{sugra})$, where S_{sugra} is the supergravity action evaluation on $AdS_5 \times S^5$.

We can use the above to compute gauge theory correlation functions by differentiating[2] (2.2.5) with respect to ϕ_0; differentiating twice gives the two-point function, three times the three-point function, and so on, and we now discuss further the properties of the particular case of two-point functions of scalar operators.

2.2.1 Two-point correlation functions

For a scalar field in AdS_5 of mass m, the action has the form (to linearised order, i.e. quadratic in the field perturbation):

$$S = \frac{1}{2} \int \mathrm{d}^5 x \sqrt{g} \left[g^{\mu\nu} \partial_\mu \phi \partial_\nu \phi + m^2 \phi^2 \right] = \frac{1}{2} \int \mathrm{d}^4 \vec{x} \frac{\mathrm{d}z}{z^3} \left[(\partial_z \phi)^2 + (\partial_i \phi)^2 + \frac{m^2}{z^2} \phi^2 \right] \tag{2.2.6}$$

where we are working in a Euclidean version of the Poincaré coordinates with $R = 1$. Note that to avoid any possible divergences at the boundary, we introduce a cutoff $z \geq \epsilon$, see footnote 3. The bulk to boundary propagator is a solution of $(\square - m^2)\phi = 0$ with asymptotic behaviour:

$$\phi(\vec{x}, z) \rightarrow z^{4-\Delta}(\phi_0(\vec{x}) + O(z^2)) + z^\Delta(A(\vec{x}) + O(z^2)) \tag{2.2.7}$$

where Δ is a root of $\Delta(\Delta - 4) = m^2$ and the two terms z^Δ and $z^{4-\Delta}$ represent the normalisable and non-normalisable modes respectively ($\phi_0(\vec{x})$ represents an external source function, and $A(\vec{x})$ a physical fluctuation). In other words, in the supergravity description, one can view asymptotically anti-de Sitter spacetimes as deformations of pure AdS by normalisable modes; this corresponds to an excited state obtained by

---

[2]From a string point of view, each differentiation sends a ϕ particle (a closed string state) into the AdS bulk.

acting (with the appropriate operator) on the field theory vacuum.[3]. The complete solution to the wave equation can then be found in terms of the bulk-to boundary propagator, $K_\Delta(z, \vec{x}, \vec{x})$:

$$\phi(\vec{x}, z) = \int \mathrm{d}^4\vec{y}\, K_\Delta(z, \vec{x}, \vec{y})\phi_0(\vec{y}) \tag{2.2.8}$$

with

$$K_\Delta(z, \vec{x}, \vec{y}) = \frac{\Gamma(\Delta)}{\pi^2\Gamma(\Delta - 2)} \left(\frac{z}{z^2 + |\vec{x} - \vec{y}|^2}\right)^\Delta \tag{2.2.9}$$

which gives

$$S[\phi_0] = -\frac{(\Delta - 2)}{\pi^2}\frac{\Gamma(\Delta)}{\Gamma(\Delta - 2)}\int \mathrm{d}^4\vec{x}\int \mathrm{d}^4\vec{y}\,\frac{\phi_0(\vec{x})\phi_0(\vec{y})}{|\vec{x} - \vec{y}|^{2\Delta}} \tag{2.2.10}$$

The two point function is then obtained by varying twice with respect to ϕ_0:

$$\langle\mathcal{O}(\vec{x})\mathcal{O}(\vec{y})\rangle = \frac{(2\Delta - 2)}{\pi^2}\frac{\Gamma(\Delta)}{\Gamma(\Delta - 2)}\frac{1}{|\vec{x} - \vec{y}|^{2\Delta}} \tag{2.2.11}$$

where we note the dependence on the inverse of the distance between the insertion points of the operators.[4] Thus for insertion points where $|\vec{x} - \vec{y}|$ is zero, the corresponding two point correlation function will be singular.

How is this related to null geodesics? In the context of AdS/CFT, one describes the field theory as living on the boundary of the bulk spacetime, thus the insertion points of operators are points on this boundary. As null geodesic paths by definition have zero proper length, one can then argue (see [83]) that the endpoints of such geodesics (on the boundary) should be manifest in the field theory as the insertion points of singular two point correlation functions.[5] This relationship can be applied in two directions; for a given spacetime, one could use the spectrum of null geodesic

---

[3]Note that this immediately implies that to get consistent behaviour for a massive field, one should change the boundary condition on the RHS of (2.2.5) to $\phi(\vec{x}, \epsilon) = \epsilon^{4-\Delta}\phi_0(\vec{x})$ and take the limit $\epsilon \to 0$. This then implies that ϕ_0 has dimension $[length]^{\Delta-4}$, since ϕ is dimensionless, from which one can deduce that the operator $\mathcal{O}$ must have dimension Δ.

[4]In fact one could have deduced the form of (2.2.11) from a consideration of symmetries; translational invariance implies it can only be a function of $\vec{x} - \vec{y}$, adding rotational invariance then further requires this be the modulus $|\vec{x} - \vec{y}|$, and finally invariance under scale transformations fixes the power to be -2Δ.

[5]This argument and possible loopholes is discussed further in [83].

endpoints to determine the locations of singular two-point correlators, or alternatively, given the insertion points of the singular functions, one could ascertain the endpoints of the null geodesics. In chapter 3 we investigate how if one takes such endpoint information as known, one can then use the geodesic equations to numerically determine the bulk structure, i.e. how one can recreate the bulk from the field theory.

Two-point functions are of course by no means the only field theory objects one can consider. For our specific goal of reconstructing the bulk from the boundary, another quantity which has a useful dual description in the gravity side is the entanglement entropy.

The observation that the insertion points of singular two-point functions on the boundary correspond to the endpoints of *null geodesics* passing through the bulk motivates an obvious question if one is considering boundary-to-boundary probes: do the endpoints of *spacelike geodesics* have any similar correspondence to a field theory quantity?

The properties of spacelike geodesics in pure AdS space are given in appendix A.3, and we observe that there are a number of interesting features of the endpoints (ϕ_{end}, t_{end}) for certain choices of angular momentum and energy. This also highlights the important point that the spacelike paths are determined by the independent values of both the angular momentum (J) and the energy (E), whereas null geodesics depend only on their ratio, $y \equiv J/E$ (see chapter 3). To restrict this extra freedom, one can instead consider a variety of subsets of the geodesics: keeping y fixed and sending $E \to \infty$ for example gives us the null geodesic limit.

Another simple choice is to fix $E = 0$, the set of zero-energy spacelike geodesics, and it is a property of these (namely their proper length) which will turn out to be related to the aforementioned quantity in the CFT: the entanglement entropy.

2.2.2 Entanglement entropy

The definition of the entanglement entropy for a subsystem of a quantum mechanical object such as a spin chain was given in the introduction, and stated that for a system

divided into two subsystems A and B, the entanglement entropy for A is given by:

$$S_A = -\mathrm{tr}\rho_A \log(\rho_A) \qquad (2.2.12)$$

where $\rho_A = \mathrm{tr}_B |\Phi\rangle\langle\Phi|$ is the reduced density matrix for subsystem A.[6]

How does one get from a description such as this to an expression which can be compared to a geometrical quantity such as a geodesic proper length? By observing that certain one-dimensional quantum systems at criticality can be effectively described by a two-dimensional CFT [76,92], one can use properties of the CFT to give an analytic form of the above entanglement entropy; it is this form which then matches with the geometrical calculation on the gravity side in the AdS_3 bulk.

Consider a quantum model with Hamiltonian $H(g)$ (with g a tunable experimental parameter), for example the transverse magnetic field strength in the Ising model. At a (quantum) critical point g_c, this model undergoes a continuous phase transition, and close to g_c the correlation length behaves as $\xi \sim |g - g_c|^{-\nu}$. At the critical point the correlation length diverges, and at g_c the system is said to be scale invariant; under renormalisation group (RG) transformations, different Hamiltonians with the same universal characteristics will flow to the same fixed point, fully determining the long-distance behaviour. This is because close to the phase transition, the universal properties of the model depend only on global features, not the microscopic details of the system.

This fixed point Hamiltonian for a one (space) dimensional system can then often be described using (1+1) continuum (quantum) field theory, as it is invariant under general rotations, scalings and translations; at the critical point, these symmetries form part of the larger conformal group (which preserves the angles between two intersecting curves). Thus at the critical point, where $\xi \to \infty$, the system is described by a conformal field theory in two dimensions.

We can then compute the entanglement entropy via path integral methods as

---

[6]Here we consider only static systems, so that ρ and ρ_A remain time independent. For a discussion of the time-evolution of the entanglement entropy see e.g [76]. Note also that $\rho = |\Phi\rangle\langle\Phi|$ is defined at zero temperature; for systems with a finite temperature $T = \beta^{-1}$, we have $\rho = \exp(-\beta H)$.

follows: consider a lattice quantum theory with coordinates $(\tau, x) \in \mathbb{R}^2$, where the (discrete) variable x labels the lattice sites, and τ is the Euclidean time, which is taken to be continuous.[7] For a commuting set of local observables (e.g. spin components) with set of eigenvalues denoted $\{\phi(x)\}$, the density matrix in a thermal state with temperature β^{-1} is given by:

$$\rho(\{\phi(x'')''\}|\{\phi(x')'\}) = Z(\beta)^{-1}\langle\{\phi(x'')''\}|\exp{(-\beta\hat{H})}|\{\phi(x')'\}\rangle \qquad (2.2.13)$$

where $\hat{H}$ is the operator describing the dynamics of the system, and the partition function Z is given by $Z(\beta) = \mathrm{tr}\exp{(-\beta\hat{H})} \equiv Z_1$. By considering the Euclidean path integral description, (2.2.13) can be expressed as:

$$\rho = (Z_1)^{-1}\int D\phi\exp{(-S_E(\phi))}\prod_x\delta(\phi(0,x) - \phi(x')')\prod_x\delta(\phi(\beta,x) - \phi(x'')'')$$
$$(2.2.14)$$

where $\phi(\tau, x)$ is the field defining the two dimensional CFT, and $S_E(\phi)$ is the Euclidean action. By setting $\phi(x)' = \phi(x)''$ and integrating over these variables, one finds that the normalisation requirement that $\mathrm{tr}\,\rho = 1$ is given by identifying $\tau = 0$ with $\tau = \beta$; the reduced density matrix for a subsystem A of the lattice (which we take to be a single interval with $x \in [u, v]$ for simplicity, with complement B) is then given by setting $\phi(x)' = \phi(x)''$ only for the points $x \in B$:

$$\rho_A = (Z_1)^{-1}\int D\phi\exp{(-S_E(\phi))}\prod_{x\in A}\delta(\phi(0,x) - \phi(x')')\prod_{x\in A}\delta(\phi(\beta,x) - \phi(x'')'')$$
$$(2.2.15)$$

By considering n copies of (2.2.15), each labelled by integer k, with $1 \leq k \leq n$, and with a cyclic identification $\phi(x)_k' = \phi(x)_{k+1}''$ (with $\phi(x)_n' = \phi(x)_1''$) for all x in A we can compute $\mathrm{tr}\,\rho_A^n$, which is given by the path-integral on an n-sheeted surface $\mathcal{R}_n$:

$$\mathrm{tr}\rho_A^n = (Z_1)^{-n}\int_{(\tau,x)\in\mathcal{R}_n}D\phi\exp{(-S_E(\phi))} \equiv \frac{Z_n}{(Z_1)^n} \qquad (2.2.16)$$

This then yields the desired entanglement entropy by use of the replica trick, which gives:

$$S_A = \lim_{n\to 1}\frac{\mathrm{tr}\rho_A^n - 1}{1 - n} = -\lim_{n\to 1}\frac{\partial}{\partial n}\mathrm{tr}\rho_A^n = -\lim_{n\to 1}\frac{\partial}{\partial n}\frac{Z_n}{(Z_1)^n} \qquad (2.2.17)$$

---

[7]The lattice spacing is denoted a, we will see in section 2.3 how this is related to the infrared cutoff in the bulk.

Thus for a given quantum system, by calculating the ratio $Z_n(A)/(Z_1)^n$, differentiating with respect to n and taking the $n \to 1$ limit, one can calculate the entanglement entropy. For the case of a $(1 + 1)$-dimensional CFT describing an infinitely long quantum system (at $T = 0$) with the subsystem A defined as a single interval of length $l \equiv v - u$, the ratio $Z_n(A)/(Z_1)^n$ is simply the vacuum expectation value, $\langle 0|0\rangle_{\mathcal{R}_n}$. As shown in [76], from an analysis of the holomorphic stress tensor, this gives:

$$\operatorname{tr} \rho_A^n = c_n \left(\frac{v - u}{a}\right)^{-(c/6)(n-1/n)} \tag{2.2.18}$$

where a is the lattice spacing (or equivalently the UV cutoff), and c is the central charge of the CFT. Hence we obtain:

$$S_A = \frac{c}{3} \log \frac{l}{a} + \text{constant} \tag{2.2.19}$$

One can perform similar calculations to obtain $\operatorname{tr}\rho_A^n$ and hence the entanglement entropy in systems at finite temperature, those with a finite boundary, and those where A is composed of multiple disjoint subsystems, among others. The case pertinent to our work, however, is that of a finite system with periodic boundary conditions, i.e. a spin chain on a circle. Denoting the total length by L, and with A as before (i.e. of length l), we have that

$$S_A = \frac{c}{3} \log \left(\frac{L}{\pi a} \sin \left(\frac{\pi l}{L}\right)\right) + \text{constant} \tag{2.2.20}$$

where we observe that due to the presence of the sin term, S_A is maximal when $l = L/2$, and is symmetric under the replacement $l \to L - l$.

It is this form of the entanglement entropy which was obtained holographically by Ryu and Takayanagi in [80,81]. They proposed that S_A (in a CFT_{d+1}) of subsystem A with $(d - 1)$-dimensional boundary ∂A is given by the area law:

$$S_A = \frac{\text{Area of } \gamma_A}{4\, G_N^{(d+2)}} \tag{2.2.21}$$

where γ_A is the static minimal surface whose boundary is given by ∂A, and $G_N^{(d+2)}$ is the Newton constant in $(d + 2)$ dimensions. For the $d = 1$ case of our example, this minimal surface corresponds to the proper length of a static, spacelike geodesic which connects the boundary of A through the AdS_3 bulk (defining two regions A
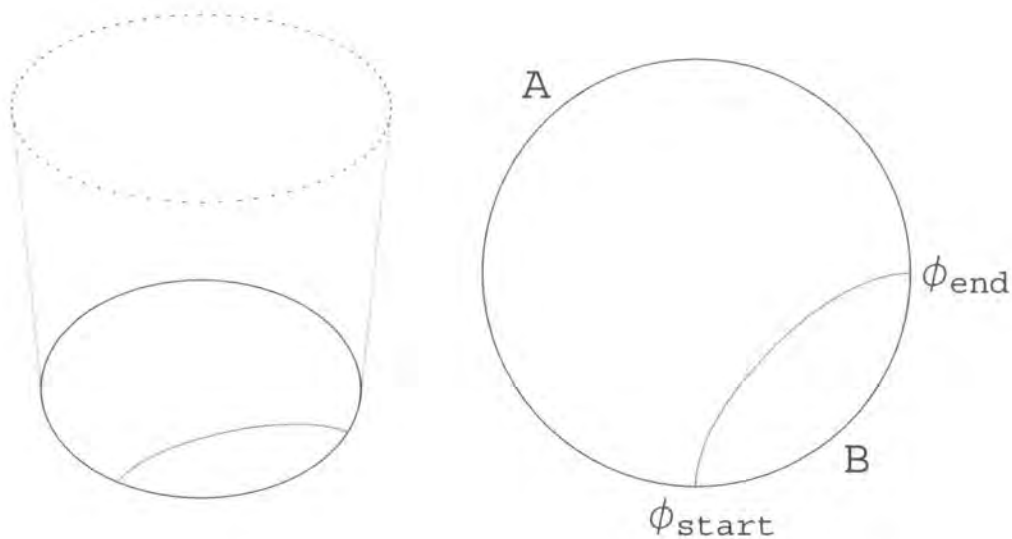
Figure 2.6: A zero-energy spacelike geodesic in AdS_3 (left plot), with the regions A and B highlighted (right plot). The entanglement entropy of subsection A is proportional to the proper length of this geodesic; thus one can holographically compute the entanglement entropy from the bulk information. One can also apply this relation in the opposite direction, however; by considering the geodesics as probes of an unknown bulk with a known field theory on the boundary, one can numerically determine the corresponding metric (see chapter 4 for details).

and B on the boundary as in figure 2.6); we explicitly show how calculating this proper length gives (2.2.20) in the section on geodesic probes below.

Since their original proposal, further evidence for the above "area law" has been given in a number of subsequent papers. In [93], the strong sub-additivity condition on the entanglement entropy was proven in this holographic setting, and indeed the geometrical picture provided by the geodesics (or in general, the minimal surfaces) is a useful setting in which to demonstrate such properties; other similar checks appeared in [94, 95], and a general proof of the area formula (2.2.21) was given in [96].

This idea was also applied to brane-world black hole scenarios, [97,98]. A detailed covariant proposal was also put forward [82], which identified the correct minimal surfaces to consider when calculating the entanglement entropy in the higher dimensional cases. Other recent developments include an generalisation of the replica

trick approach to compute the entanglement entropy in $SU(N)$ gauge theories in arbitrary dimension [99], a more detailed look at the four dimensional CFT case [100], and an asymptotic expansion for the entropy for the case of a free scalar field in an arbitrary background geometry [101]. Finally, we note that there has been much general work focusing on the numerical calculation of the entanglement entropy in various quantum systems, see [102–104] and references therein.

With such ideas in mind, in chapter 4 we investigate how to tackle the inverse problem to that solved by Ryu and Takayanagi, namely how to use the entanglement entropy for a given quantum system to reconstruct the geometry of the corresponding bulk. Restricting ourselves to three bulk dimensions, such a reconstruction is performed via the use of geodesic probes; we now provide a brief overview of their general properties, showing how symmetries in the metric simplify the geodesic equations, and visually demonstrating their behaviour in pure AdS. The analytic results for both null and spacelike geodesics are presented in appendix A, however, we include here the calculation of the proper length for static spacelike geodesics to explicitly show its relation to the entanglement entropy (2.2.20).

2.3   Boundary-to-boundary probes

Although there are an infinite number of paths one could consider when traversing a region of spacetime, geodesics are those followed by unaccelerated test particles, and are a natural tool to use in determining the background metric.

In our case, we wish to consider the behaviour of boundary-to-boundary geodesics in asymptotically anti-de Sitter bulks. Beginning in the most general static, spherically symmetric case, the geodesic equations for a d-dimensional metric[8] of the form:

$$ds^2 = -k(r)dt^2 + h(r)dr^2 + r^2 d\Omega_{d-2}^2 \qquad (2.3.1)$$

---

[8]Note that we now use d to represent the overall dimension of the bulk, as the majority of our work takes place one the gravity side of the AdS/CFT duality, and this will continue to be our definition for the rest of the thesis. Pure AdS is recovered in (2.3.1) by setting $k(r) = h(r)^{-1} = 1 + r^2/R^2$.

can easily be deduced given the obvious symmetries; both $k(r)$ and $h(r)$ depend only on the radial direction r. By firstly exploiting the rotational symmetry of the metric, we can suppress $(d-3)$ of the angular coordinates by setting the geodesics to lie in their equatorial plane; this replaces the $d\Omega_{d-2}^2$ with $d\phi^2$, where ϕ is the remaining angular coordinate.

The general geodesic equation is written in the following differential form:

$$\frac{d^2 x^\sigma}{d\lambda^2} + \Gamma_{\mu\nu}^\sigma \frac{dx^\mu}{d\lambda}\frac{dx^\nu}{d\lambda} = 0 \tag{2.3.2}$$

where $\Gamma_{\mu\nu}^\sigma$ are the Christoffel symbols, and the coordinates $(t(\lambda), r(\lambda), \phi(\lambda))$ are labelled $x_\mu(\lambda)$ with λ an affine parameter.

Whilst in more complicated spacetimes one would need to use this full equation to determine the geodesic paths (see the scenarios considered in chapter 6), here one can instead use the time-translational and spherical symmetry of the metric to greatly simply the analysis. These result in the existence of two Killing vectors, $\partial/\partial t$ and $\partial/\partial\phi$, which lead to two constraints on the motion, the first is related to the energy and the second to the angular momentum:

$$E = k(r)\dot{t} \tag{2.3.3}$$

$$J = r^2 \dot{\phi} \tag{2.3.4}$$

where $\dot{} = \frac{d}{d\lambda}$.

A final independent equation for the geodesic paths can be found by extremizing the action:

$$S = \int \dot{x}^2 d\lambda \tag{2.3.5}$$

which leads to a third constraint on the motion, given by:

$$\dot{x}^2 = -k(r)\dot{t}^2 + h(r)\dot{r}^2 + r^2\dot{\phi}^2 \tag{2.3.6}$$

where $\dot{x}^2 \equiv \kappa = +1, -1, 0$ for spacelike, timelike and null geodesics respectively (note that differentiating (2.3.6) with respect to λ gives the r component of the geodesic equations).

By substituting (2.3.3) and (2.3.4) into (2.3.6), these three equations can be combined together to eliminate $\dot{t}$ and $\dot{\phi}$, giving:

$$\kappa = -\frac{E^2}{k(r)} + h(r)\dot{r}^2 + \frac{J^2}{r^2} \tag{2.3.7}$$
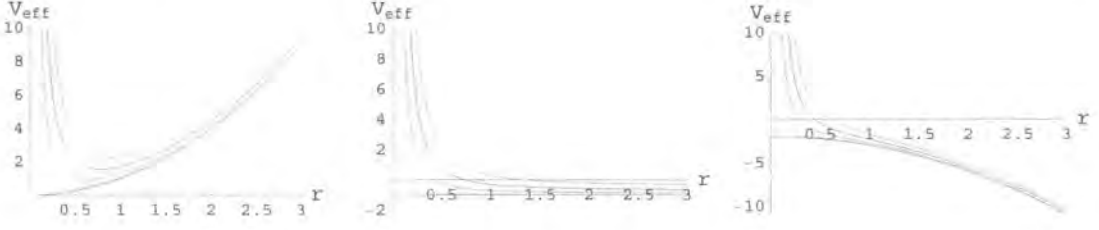
Figure 2.7: The effective potential in pure AdS (with $R = 1$) for a sample of geodesics with $E = 1$ and J ranging from 0 (red, bottom curve) to 0.8 (purple, top curve). The three plots show (from left to right) V_{eff} for timelike geodesics ($\kappa = -1$), null geodesics ($\kappa = 0$), and spacelike geodesics ($\kappa = 1$) respectively. In the null and spacelike cases, geodesics can travel in from the boundary at infinity (as $V_{eff} < 0$ at large r) and reach a minimum radius given by the largest r for which $V_{eff} = 0$.

which can be rewritten so as to introduce the concept of an effective potential for the geodesics:

$$\dot{r}^2 + V_{eff} = 0 \tag{2.3.8}$$

with

$$V_{eff} = -\frac{1}{h(r)} \left(\kappa + \frac{E^2}{k(r)} - \frac{J^2}{r^2} \right) \tag{2.3.9}$$

Note that the RHS of (2.3.8) is zero, and so any part of the effective potential which is positive represents a potential barrier, see figure 2.7. The minimum value of r obtained by spacelike and null geodesics incoming from $r = \infty$ is given by the largest solution to $V_{eff} = 0$, and is the endpoint of the ingoing part of the geodesic (and hence the starting point of the outgoing part of the geodesic). Further combining the above with (2.3.3) and (2.3.4) gives the equations:

$$\frac{dr}{dt} = \pm \frac{k(r)}{E} \sqrt{-V_{eff}} \tag{2.3.10}$$

and

$$\frac{dr}{d\phi} = \pm \frac{r^2}{J} \sqrt{-V_{eff}} \tag{2.3.11}$$

where the negative (positive) square root represents the ingoing (outgoing) part of the geodesic, and due to the independence of the metric on t and ϕ, these can both then be separated and written in integral form. In metrics with complicated $k(r)$,
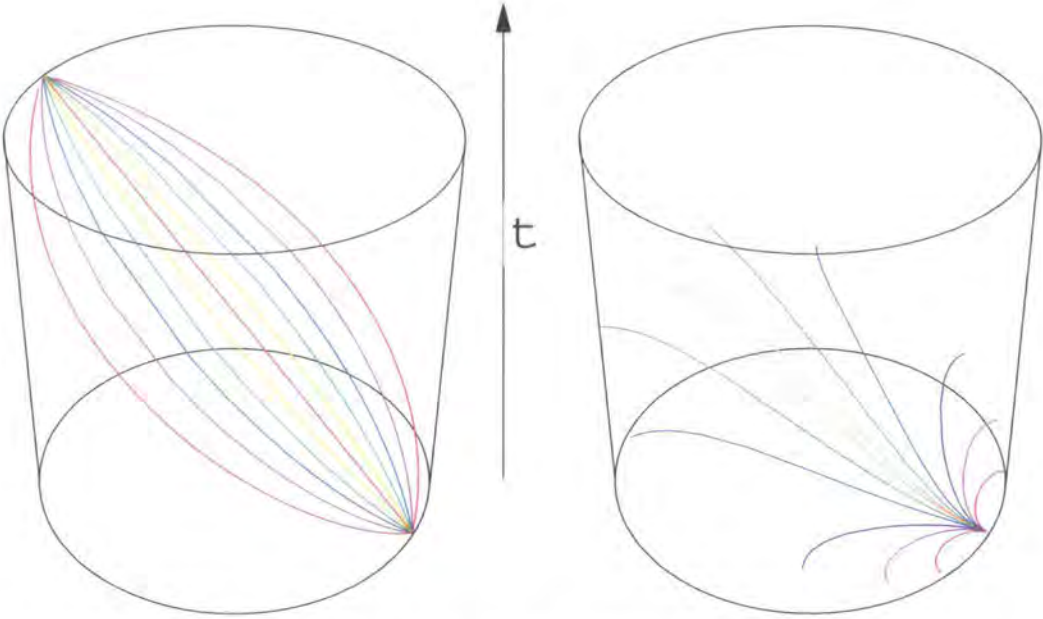
Figure 2.8: A sample of geodesic paths in AdS_3 (with $R = 1$), all beginning at the same point on the boundary, which has been compactified as in Appendix A to lie at radius $\pi/2$. The null geodesics (left) all terminate at the same (antipodal) point, whereas this is not the case for spacelike geodesics (right).

$h(r)$, the paths of geodesics can be calculated numerically using these equations, and in certain scenarios the paths can be derived analytically, see appendix A for the derivation in pure AdS.

Only null and spacelike geodesics can reach the boundary at $r = \infty$ in finite coordinate time, and as we saw in the relations to the two-point functions and the entanglement entropy, these are natural tools to work with when relating bulk physics to the boundary. The paths of a sample of null and spacelike geodesics through AdS_3 are shown in figure 2.8, where one observes that the null geodesics all terminate at the antipodal point on the boundary; this will not be the case in spacetimes which deviate from pure AdS, as we shall see in the following chapter. This is in contrast to the spacelike geodesic endpoints, where there is both an angular and temporal spread in their distribution (see Appendix A.3 for more details), obtained by varying J and E. A notable exception is the $E = 0$ case, where the geodesics are all contained in a constant time slice, as we saw in figure 2.6.

This brings us back to one of our original motivations for analysing the geodesic

behaviour, their connection to certain field theory quantities. The proper length of a geodesic is defined as:

$$\mathcal{L} = \int \sqrt{g_{\mu\nu} \frac{dx^\mu}{d\lambda} \frac{dx^\nu}{d\lambda}} \, d\lambda \qquad (2.3.12)$$

and for null geodesics is identically zero (from (2.3.6) above). What we wish to consider is the proper length of the boundary-to-boundary spacelike geodesics in AdS_3, and in particular those with zero energy.

As the metric is divergent at the boundary, in order to make the proper length finite, we introduce a cutoff r_{max} and restrict ourselves to the region $r < r_{max}$. This corresponds to the UV cutoff (the lattice spacing a) we introduced earlier in our calculation of the entanglement entropy (see section 2.2.2) via the relation $r_{max} \sim L/a$. The proper length is then given by:

$$\mathcal{L} = \int d\lambda = \int_{r_{min}}^{r_{max}} \frac{2}{\sqrt{r^2+1}\sqrt{1 - \frac{r_{min}^2}{r^2}}} \, dr = 2 \log\left(2 \, r_{max} \sin\left(\frac{\phi_{end}}{2}\right)\right) \qquad (2.3.13)$$

where we have taken the large r_{max} limit and used the relation $r_{min} = \cot(\phi_{end}) + \csc(\phi_{end})$, with $\phi_{start} = 0$. For the specific geodesic which connects the endpoints of subsystem A on the boundary we require $\phi_{end} = 2\pi l/L$, and hence we have:

$$\mathcal{L} = 2 \log\left(2 \, r_{max} \sin\left(\frac{\pi l}{L}\right)\right) \qquad (2.3.14)$$

By comparing this to the formula for the entanglement entropy (2.2.20), we see that Ryu and Takayanagi's proposal for the relationship between the two is satisfied (neglecting the constant term) if the central charge c is given by $3R/2G_N^{(3)}$. For gravitational theories on AdS_3, it has been shown [105, 106] that this is exactly the value one requires for the central charge of the dual CFT, and hence the two quantities $\mathcal{L}$ and S_A are indeed related by (2.2.21).

In subsequent chapters it will be demonstrated that one can use both this relation and that between null geodesics and two-point functions to (numerically) reconstruct the bulk metric from this boundary data in various asymptotically AdS spacetimes, thus rebuilding the hologram. We begin in the following chapter by considering the null geodesic probes.

Chapter 3

Probing the bulk geometry I

In the previous chapter we discussed the relationship between field theory data on one side of the AdS/CFT correspondence, and properties of bulk objects on the other. What we now wish to ascertain is whether one can use the field theory data to determine the actual form (in a particular gauge) of the corresponding bulk metric itself; in other words, can we recreate the holographic image from the lower dimensional starting point?

The two different sets of field theory data - the two-point correlation functions and the entanglement entropy - yield remarkably similar methods for performing this reconstruction, via null and spacelike (in the $2 + 1$ dimensional case) geodesics respectively.

In this chapter, we focus on the null geodesic approach, where we assume that we have the required two-point correlator data from the field theory and hence the endpoint data for the geodesics. We demonstrate both that the amount of information contained in the endpoint (i.e. field theory) data is sufficient to reconstruct the bulk metric and that it directly relates to the characteristic property of the corresponding null geodesics. We then explain how this leads to an iterative reconstruction of the bulk metric, where one begins at large r and systematically extracts the bulk data by using geodesics which probe incrementally deeper into the bulk. Moreover, we detail an efficient, stable and accurate algorithm by which it can be carried out in practice, including modifying the perhaps most obvious approach to formulating the method in order to eliminate an unnecessary approximation and greatly improve the

accuracy of the method at large step sizes. This is illustrated by a series of numerical examples demonstrating the algorithm at work.

Given the impressive robustness of the numerical extractor, we then provide a more detailed analysis of what causes errors to occur in the estimate and how they are kept small. One might have initially suspected that the iterative nature of the extractor would leave it vulnerable to an accumulation of errors ruining the estimate, however, we go on to demonstrate how any appearance of errors is suppressed in subsequent steps, leading to the highly accurate and stable results given in the examples section.

This metric reconstruction based upon null geodesics does have certain limitations however, as we investigate towards the end of the chapter; namely an inability to completely reconstruct the metric in spacetimes with significant central deviations from pure AdS. A large deformation manifests itself as a discontinuity in the endpoint data, and is a result of local maxima in the effective potential for the geodesics, allowing them to enter into unstable orbits. This causes a non-negligible time delay in their return out to the boundary, which leads to the discontinuity in the endpoint data and prevents further extraction of the metric beyond that radius.

3.1 Null geodesics

Supposing we are given a set of null geodesic endpoints for a general, asymptotically anti-de Sitter spacetime, as if obtained from the field theory dual - this will be the set of insertion points on the boundary of all divergent two-point correlators, as discussed in the previous chapter. Taking the spacetime to be static and spherically symmetric allows this set to be written as the endpoints of all null geodesics emanating from a single point on the boundary, or from a field theory viewpoint, the set of insertion points of all divergent two-point correlators with one coordinate fixed.

What does a plot of such endpoints look like? There are two basic forms: one where the distribution of endpoints is continuous, and which possesses both a maximum angular deviation and time delay; and one such that tending to a certain value of y (the normalised angular momentum, $y \equiv J/E$, see section 3.1.1), the endpoints

are unbounded[1] and there is a discontinuity. These two types of scenario are shown in figures 3.1 and 3.2, alongside plots of the geodesic paths through the bulk, and the difference corresponds to the severity of the deformation from pure AdS; a large deformation can give a non-monotonic effective potential for the geodesics, which results in the geodesics going into orbit around the centre before returning out to the boundary, leading to the discontinuity in the plot.[2] A small deformation leads to a bounded set of endpoints, where the distribution is continuous, and we shall begin by focussing on this case; the case of large deformations and singular spacetimes is considered in section 3.4, where we examine them in more detail and consider the effect of the discontinuity in our ability to recover the metric.

Turning now to consider the metric, what form should we expect it to take given the endpoint data we have? Even without considering the whole field theory, any symmetries of the metric are evident from the dimension of the boundary data (i.e. the endpoint plot seen above); the fact that it is a one-dimensional curve implies that the metric is a function of only one variable. If the metric had less symmetries, such as a dependence on t say, the plot of endpoints would be a two-dimensional surface, due to the now non-trivial dependence on t_{start}, as is discussed in more detail in chapter 6. Thus we are then justified in assuming time-translational invariance and spherical symmetry from the outset, and the most general static, spherically symmetric form (in five dimensions) can be written as:

$$ds^2 = -k(r)dt^2 + h(r)dr^2 + r^2 d\Omega_3^2 \tag{3.1.1}$$

where we have two unspecified functions, $k(r)$ and $h(r)$. This immediately suggests that we may not be able to fully reconstruct the metric using simply the null geodesic

---

[1] When referring to ϕ_{end} as unbounded we of course mean the unwrapped angular coordinate where ϕ is allowed to range from 0 to ∞.

[2] There is also a third form of endpoint plot, closely related to the second, where only the lower branch of the plot exists, and occurs when the central deformation is so severe as to form a singularity. In this case, any geodesics which pass behind the black hole horizon terminate at the singularity and thus do not return out to the boundary; one therefore only has the lower branch of the endpoint plot in 3.2. Finally, for even more exotic constructs, there could be several local maxima in the effective potential, which would lead to several discontinuities in the plot of the endpoints.
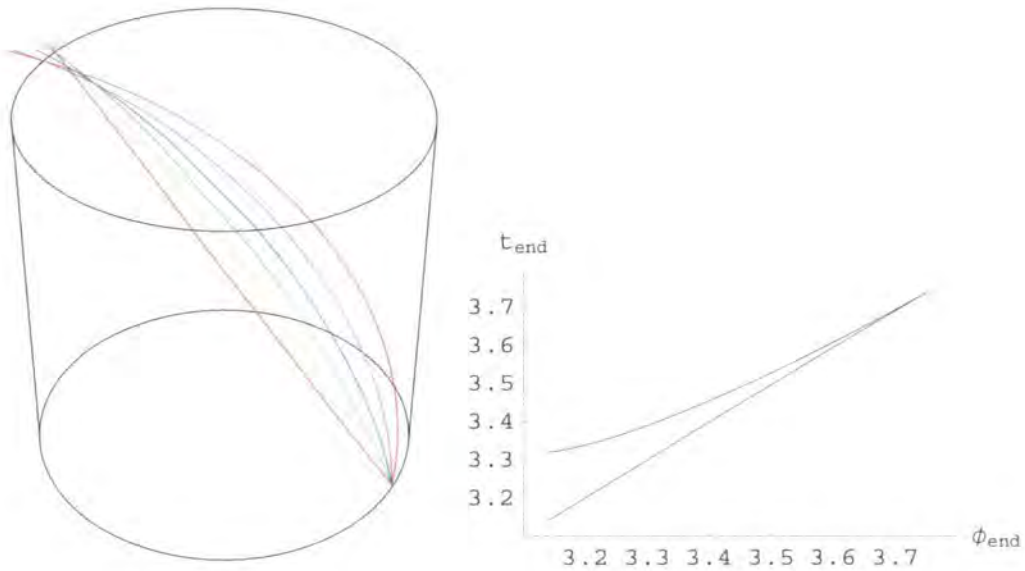
Figure 3.1: Null geodesic paths passing through a modified AdS spacetime (left plot), all starting from the arbitrary point $t_{start} = 0$, $\phi_{start} = 0$ on the boundary and with $y > 0$. The corresponding full spectrum of null geodesic endpoints for this spacetime is shown on the right, where we observe that the distribution is continuous as y varies from zero to one, with $y = 0$ the leftmost point of the upper curve. Note that all geodesics have $t_{end} \geq \pi$, which is the time taken in pure AdS - this will always be the case for deformations which satisfy certain conditions, see section 3.1.1. In the limit $y \rightarrow 1$ the endpoints approach (π, π), as the geodesics remain far from the deformation and are thus (virtually) unaffected by it.
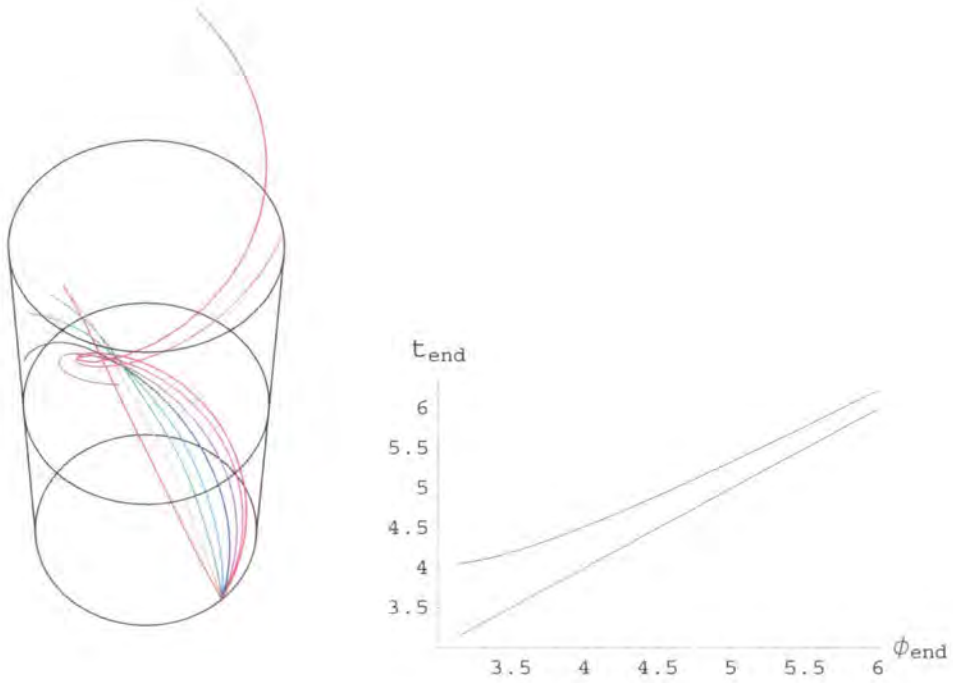
Figure 3.2: Here (left) we plot a selection of null geodesic paths in a modified AdS spacetime with a deformation so severe that geodesic orbits can occur at a specific value of y. This is evident from the corresponding spectrum of null geodesic endpoints shown on the right (for clarity, only contributions to its upper branch are shown in the left hand plot), where both the t_{end} and (unwrapped) ϕ_{end} coordinates head to infinity as y tends to this critical value. These scenarios are examined in section 3.4, where we see how this discontinuity corresponds to a non-vanishing gap ("time delay") in the spectrum, which prevents the full extraction of the metric.

probes, as they appear to only provide one "function's worth" of information (i.e. $t_{end}(\phi_{end})$, say), and not the two that are required. Note that this is assuming the two metric functions are unrelated; in a lot of more physically realistic scenarios, this is not the case, as often the corresponding stress-energy tensor will provide us with the required information, e.g. for the toy model of radiating stars considered in chapter 5. Nevertheless, we will continue assuming that we do not *a priori* know the relationship between $h(r)$ and $k(r)$ so as to provide a more general analysis.

Returning to the question of whether we have enough information to fully reconstruct the metric purely from the null geodesic endpoints, one can show that this is not possible by rewriting the above metric in a more appropriate form:

$$ds^2 = C(\tilde{r})\left(-f(\tilde{r})dt^2 + \frac{d\tilde{r}^2}{f(\tilde{r})} + \tilde{r}^2 d\Omega_3^2\right) \tag{3.1.2}$$

where we have redefined the radial coordinate $r \to \tilde{r}$ to explicitly define the conformal factor of the metric, $C(\tilde{r})$. The equivalence of the two forms is readily apparent; as we require the angular and temporal coordinates to remain unchanged we immediately have that:

$$k(r) = C(\tilde{r})f(\tilde{r}) \tag{3.1.3}$$

and

$$r = \sqrt{C(\tilde{r})}\tilde{r} \tag{3.1.4}$$

with the final transformation rule given by:

$$h(r) = \frac{C(\tilde{r})}{f(\tilde{r})\left(\sqrt{C(\tilde{r})} + \frac{\tilde{r}C'(\tilde{r})}{2\sqrt{C(\tilde{r})}}\right)} \tag{3.1.5}$$

where $C'(\tilde{r})$ represents the derivative of $C(\tilde{r})$ with respect to $\tilde{r}$. Finally, we observe that since $C(\tilde{r})$ must be positive for all $\tilde{r}$ by construction (i.e. (3.1.4) above), this transformation is well defined for any (non-zero) metric, and any singularities in the original form are equivalently manifested in the second.

As the proper length of a null geodesic is always zero, such probes cannot carry any information about this conformal factor; they cannot be used to determine $C(\tilde{r})$ as it drops out of all the relevant equations (e.g. (3.1.7)). Thus the most that can be extracted using the null geodesics alone is the single function, $f(\tilde{r})$, with the

conformal factor remaining undetermined. We will, however, see in chapter 5 how, with the addition of the spacelike geodesics, we can obtain both unknown functions $k(r)$ and $h(r)$, and thus the full metric in these more general scenarios (with certain limitations). Here we will continue to examine how effective the null geodesics are as probes of the bulk, by restricting ourselves to metrics with one unknown function as follows.

3.1.1 Asymptotically Anti-de Sitter spacetimes with a deformed interior

Using the form of the metric, (3.1.2), with the conformal factor, $C(r)$, set to one for convenience (where we also now drop the tilde ($\tilde{}$) superscript), we can consider a small modification to the pure AdS spacetime by introducing an extra term such that:

$$f(r) = 1 + \frac{r^2}{R^2} - p(r) \tag{3.1.6}$$

where $p(r)$ is an analytic function which behaves as r^2 as $r \to 0$ and tends to zero as $r \to \infty$, such that the metric is non-singular everywhere.[3]

Recall that in pure AdS, all the null geodesics terminate at their antipodal point on the boundary; the distribution of their endpoints is thus simply a single point. In a deformed spacetime, this is not the case, as we saw above; their final t and ϕ coordinates depend on the ratio of the angular momentum (J) to the energy (E). This suggests that the deviation of the endpoint distribution from the single point corresponds in some sense to the deformation term $p(r)$ (indeed, making $p(r)$ more influential simply increases the size of the "wedge", until geodesic orbits can occur and the wedge splits into two branches, see figure 3.2)

From a physical point of view this can be thought of as the extra term $p(r)$ representing an attractive modification to the centre of the spacetime, such that the geodesics follow a more curved path through the bulk, and thus "overshoot" the antipodal point. Their extra path length then also accounts for the increase in the time taken to reach the boundary at infinity. Indeed, for a generic deformation

---

[3]The r^2 behaviour of $p(r)$ at small r ensures that we avoid a conical singularity at the origin.

$p(r)$, it is not possible for null geodesics to travel from boundary to boundary in less time than in pure AdS, provided certain conditions on the spacetime (the null energy condition, null generic condition, compactness and strong causality) remain satisfied, as was proven in general in [107], and discussed in the context of asymptotically AdS bulks in [83].

How can we use this link between the endpoint plot and the deformation $p(r)$ to extract the metric? We begin by looking at the geodesic equations, which can be rewritten in integral form due to the independence of the metric on t and ϕ, as mentioned in the previous chapter. For a geodesic beginning at (t_0, ϕ_0) and ending at (t_1, ϕ_1) on the boundary, using equations (2.3.10) and (2.3.11) we have:

$$\int_{t_0}^{t_1} dt = 2 \int_{r_{min}}^{\infty} \frac{1}{f(r)\sqrt{1 - y^2 \frac{f(r)}{r^2}}} dr \qquad (3.1.7)$$

$$\int_{\phi_0}^{\phi_1} d\phi = 2 \int_{r_{min}}^{\infty} \frac{y}{r^2 \sqrt{1 - y^2 \frac{f(r)}{r^2}}} dr \qquad (3.1.8)$$

where r_{min} is minimum radius obtained by the geodesic. Note that the equations both only depend on the normalised angular momentum $y \equiv J/E$, and are independent of the absolute values. Each geodesic will penetrate to a different depth dependent on the parameter y; at the minimum radius, we have that $y^2 = \frac{r_{min}^2}{f(r_{min})}$.

Thus if we consider the set of null geodesics all beginning at the same point, (t_0, ϕ_0) on the boundary, we can obtain the full spread of endpoints by varying y from 0 to 1, as described earlier (see figure 3.1). We therefore need two pieces of information about a geodesic (namely y and r_{min}) in order to determine something about the corresponding metric function (namely $f(r_{min})$). It turns out that one of these quantities is directly available from the endpoint plot, as we now demonstrate.

For a fixed metric, the final time and angular coordinates will be functions of y only, and thus we can write:

$$\int_{t_0}^{t_1} dt = t_1 - t_0 \equiv t_{end}(y) \qquad (3.1.9)$$

$$\int_{\phi_0}^{\phi_1} d\phi = \phi_1 - \phi_0 \equiv \phi_{end}(y) \qquad (3.1.10)$$

If we define the function $g(y,r)$ as:

$$g(y,r) = \frac{1}{\sqrt{1 - y^2 \frac{f(r)}{r^2}}} \qquad (3.1.11)$$

for ease of notation, and consider the derivatives of (3.1.7) and (3.1.8) with respect to y we have:

$$\frac{dt_{end}(y)}{dy} = 2\frac{d}{dy}\left(\int_{r_{min}}^{\infty} \frac{g(y,r)}{f(r)}\,dr\right) \qquad (3.1.12)$$

$$= 2y\int_{r_{min}}^{\infty} \frac{(g(y,r))^3}{r^2}\,dr - \left(\frac{2\,g(y,r)}{f(r)}\right)\Bigg|_{r=r_{min}} \frac{dr_{min}}{dy} \qquad (3.1.13)$$

and

$$\frac{d\phi_{end}(y)}{dy} = 2\frac{d}{dy}\left(\int_{r_{min}}^{\infty} \frac{y\,g(y,r)}{r^2}\,dr\right) \qquad (3.1.14)$$

$$= 2\int_{r_{min}}^{\infty} \frac{(g(y,r))^3}{r^2}\,dr - \left(\frac{2\,y\,g(y,r)}{r^2}\right)\Bigg|_{r=r_{min}} \frac{dr_{min}}{dy} \qquad (3.1.15)$$

One can immediately see that the two integral terms differ only by a constant factor, y. We can then use the fact that at $r = r_{min}$, $y^2 = \frac{r_{min}^2}{f(r_{min})}$ to rewrite the first equation as:

$$\frac{dt_{end}(y)}{dy} = 2y\int_{r_{min}}^{\infty} \frac{(g(y,r))^3}{r^2}\,dr - y\left(\frac{2\,y\,g(y,r)}{r^2}\right)\Bigg|_{r=r_{min}} \frac{dr_{min}}{dy} \qquad (3.1.16)$$

which reveals that the other two terms are also identical upto a factor of y. Finally, to ensure the two equations are well defined, we check that the divergent piece of the integral at the lower limit r_{min} cancels with the divergent second term in (3.1.16). In order to combine the two terms, we need an expression for dr_{min}/dy, which we obtain using our expression for y in terms of the minimum radius (see the previous paragraph):

$$\frac{dr_{min}}{dy} = 1\bigg/\left(\frac{dy}{dr}\bigg|_{r=r_{min}}\right) = \frac{1}{\sqrt{f(r_{min})}}\left(1 - \frac{r_{min}f'(r_{min})}{2\,f(r_{min})}\right) \qquad (3.1.17)$$

One can then rewrite the second term of (3.1.13) as an integral from r_{min} to ∞:

$$\left(\frac{2g(y,r)}{f(r)}\right)\Big|_{r=r_{min}}\frac{dr_{min}}{dy} = \int_{r_{min}}^{\infty}\frac{(f'(r)-rf''(r))\sqrt{f(r)}\,g(y,r)}{\left(f(r)-\frac{r}{2}f'(r)\right)^2}\,dr$$
$$-\int_{r_{min}}^{\infty}\frac{f'(r)\,g(y,r)}{\left(f(r)-\frac{r}{2}f'(r)\right)\sqrt{f(r)}}\,dr$$
$$+\int_{r_{min}}^{\infty}\frac{2y\,(g(y,r))^3}{r^2}\,dr$$

and see that the third term above cancels precisely with the divergent integral in (3.1.13); after rearranging we are left with

$$\frac{dt_{end}(y)}{dy} = \int_{r_m}^{\infty}g(y,r)\frac{r\,(f'(r))^2 - 2\,rf''(r)\,f(r)}{2\left(f(r)-\frac{r}{2}f'(r)\right)^2\sqrt{f(r)}}\,dr \qquad (3.1.18)$$

Although the integral may still be infinite depending on the form of $f(r)$ as $r \to \infty$ (in asymptotically AdS spacetimes the integrand becomes constant at large r for example), the overall behaviour is well defined and can be regulated by taking the upper limit as r_{∞} say if necessary. This allows us to combine equations (3.1.16) and (3.1.15) to obtain:

$$\frac{dt_{end}(y)}{dy} = y\,\frac{d\phi_{end}(y)}{dy} \qquad (3.1.19)$$

which can be rewritten as:

$$\frac{dt_{end}}{d\phi_{end}} = y(\phi_{end}) \qquad (3.1.20)$$

Thus from the plot of the endpoints, *by taking the gradient at each point we are able to obtain the value of y for that geodesic.* Note that at no point in this derivation have we used the fact that the spacetime is asymptotically anti-de Sitter; the result holds for any static, spherically symmetric spacetime.[4] This strikingly simple equation gives a clear relation between the boundary information (the endpoint locations) and a property of the bulk objects (the ratio of angular momentum to energy of the null geodesics), and paves the way for the reconstruction of the metric, as we shall see in section 3.1.3. Before we go into the specific formalism of the extraction procedure, however, we give a brief overview of the idea.

---

[4]As suggested by our comments on the upper limit of the integrals, it is also not necessary for the boundary on which the geodesics begin and end to be at infinity; the result is valid for any spherical boundary within the bulk.

3.1.2   Overview of the extraction procedure

Each boundary-to-boundary null geodesic in our static and spherically symmetric spacetime is characterised by one parameter: the ratio of its angular momentum to its energy, y. This is directly related to the minimum radius to which the geodesic probes, and is also directly extractable from the endpoint data, as we saw above. So suppose we take a geodesic with y close to one; this will correspond to a geodesic with large minimum radius, as illustrated by the leftmost plots in figure 3.3

As the spacetime is taken to be asymptotically AdS, such a geodesic (which remains close to the boundary) will not experience any effect of the deviation from pure AdS caused by $p(r)$; we can treat it as travelling entirely through pure AdS, and hence solve for its minimum radius analytically. A geodesic which probes slightly closer will then remain mainly in pure AdS, apart from a small section near its minimum radius; this is shown in the central plots of figure 3.3.

As the unknown section can be taken to be arbitrarily small, it can be well approximated by expanding the relevant equations about the minimum radius, and this allows us to determine both the value of that radius, and the value of $f(r)$ at that point. Continuing in this fashion, we can work iteratively deeper and deeper into the spacetime (see the rightmost plots of figure 3.3), building up our knowledge of the spacetime piece by piece.

This is the general principle for reconstructing the bulk metric using the endpoint data; we will now formulate it explicitly, and investigate how accurately and reliably such a procedure works in practice.

3.1.3   Reconstructing $f(r)$: Basic Method

Having provided an overview of the procedure, we now develop the idea more rigourously. Firstly, we present a basic formalism (referred to as Method I) for the algorithm which can be used to recover the metric, introducing several approximations in the process; these are not necessarily the best approximations one can use, as we shall see in later sections, however, they provide a good starting point from which to build.
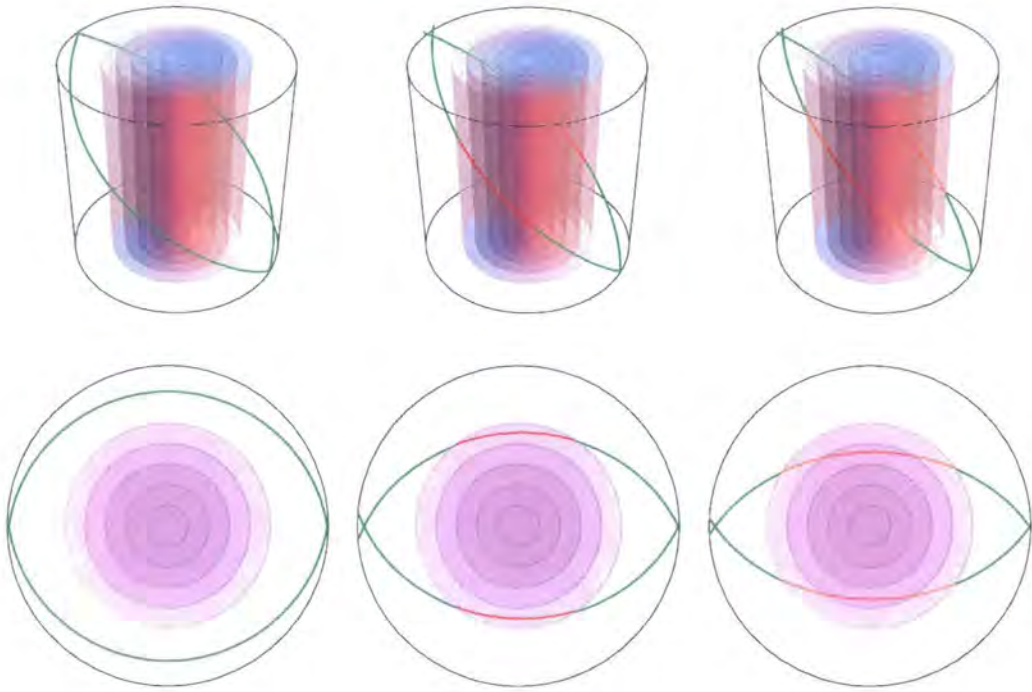
Figure 3.3: Pictorial overview of the procedure used to extract the bulk information. The top row of plots are of null geodesics in an asymptotically AdS spacetime with a deformation from pure AdS localised near the centre; the bottom row then shows a projection of the corresponding plots onto a disc of constant t, to better illustrate the different sections of the geodesics. Each plot shows not only the relevant geodesic (see below), but also the symmetric geodesic with opposite y, to help aid the visualisation. The leftmost plots show a geodesic (entirely green) which remains far away from the centre along its entire path, and can be treated as if passing through pure AdS. The central plots show a geodesic with a small part (in red) close to r_{min} experiencing the influence of the deformation, and this small section can be well approximated to enable the determining of the metric function $f(r)$ at this point. The rightmost plots show the next geodesic in the iteration, where the green section is taken to be pure AdS, the orange section has just been calculated using the previous geodesic, and the red section can again be well approximated to give $f(r)$ at this point. Depending on the nature of the deformation, this procedure can then be continued down to $r = 0$ or the point at which null geodesic orbits can occur, see section 3.4.

As mentioned above, the method involves iteratively recovering $f(r)$ starting from large radius and working down towards $r = 0$. As we are working in an asymptotically AdS spacetime, we have that as $r \to \infty$, $f(r) \to r^2/R^2 + 1$; thus we can say that for $r \geq r_n$ for some r_n which can be arbitrarily large, $f(r) \approx r^2/R^2 + 1$. We set the AdS radius (R) to one, and by considering large enough $y = y_n$ such that the minimum radius, r_{min}, corresponds to r_n, (3.1.7) becomes (setting the initial time, t_0, to be zero):

$$t_n = \int_0^{t_n} \mathrm{d}t = 2 \int_{r_n}^\infty \frac{g(y_n, r)}{f(r)} \, \mathrm{d}r \tag{3.1.21}$$

$$\approx 2 \int_{r_n}^\infty \frac{1}{(r^2 + 1)\sqrt{1 - y_n^2 \frac{r^2+1}{r^2}}} \, \mathrm{d}r = \pi \tag{3.1.22}$$

as we would expect, as geodesics remaining far from the centre of the space would not "see" the modification and thus behave as in pure AdS. In this case we can solve the equation for the minimum radius:

$$y_n^2 = \frac{r_n^2}{f(r_n)} = \frac{r_n^2}{r_n^2 + 1} \tag{3.1.23}$$

to obtain r_n in terms of y_n, which is determined from the geodesic endpoints. Thus we can determine r_n (and hence $f(r_n) = r_n^2 + 1$).

If we now consider a geodesic with slightly lower ratio of angular momentum to energy, say with $y_{n-1} = y_n - \epsilon$, where $\epsilon > 0$, we have the equation:

$$t_{n-1} = 2 \int_{r_{n-1}}^\infty \frac{g(y_{n-1}, r)}{f(r)} \, \mathrm{d}r \tag{3.1.24}$$

which can be split up as follows (noting that $r_{n-1} < r_n$):

$$t_{n-1} = 2 \int_{r_{n-1}}^{r_n} \frac{g(y_{n-1}, r)}{f(r)} \, \mathrm{d}r + 2 \int_{r_n}^\infty \frac{g(y_{n-1}, r)}{f(r)} \, \mathrm{d}r \tag{3.1.25}$$

The second integral can be evaluated by setting $f(r) = r^2 + 1$ as in (3.1.21), and we have

$$2 \int_{r_n}^\infty \frac{g(y_{n-1}, r)}{f(r)} \, \mathrm{d}r = \pi - 2 \arctan\left(\sqrt{\left(1 - y_{n-1}^2\right) r_n^2 - y_{n-1}^2} \right) \tag{3.1.26}$$

We can approximate the first integral by taking a Laurent expansion about the point r_{n-1}. This gives, to lowest order:

$$\int_{r_{n-1}}^{r_n} \frac{g(y_{n-1}, r)}{f(r)} \, dr \approx \int_{r_{n-1}}^{r_n} \frac{(r - r_{n-1})^{-1/2}}{f(r_{n-1})\sqrt{\frac{2}{r_{n-1}} - \frac{f'(r_{n-1})}{f(r_{n-1})}}} \, dr \qquad (3.1.27)$$

$$= \frac{2\sqrt{r_n - r_{n-1}}}{f(r_{n-1})\sqrt{\frac{2}{r_{n-1}} - \frac{f'(r_{n-1})}{f(r_{n-1})}}} \qquad (3.1.28)$$

where we have used that $y_{n-1}^2 = r_{n-1}^2 / f(r_{n-1})$ and integrated. This can be simplified further by writing[5]:

$$f'(r_{n-1}) \approx \frac{f(r_n) - f(r_{n-1})}{r_n - r_{n-1}} \qquad (3.1.29)$$

Thus we have:

$$t_{n-1} \approx \frac{4(r_n - r_{n-1})}{f(r_{n-1})\sqrt{\frac{2r_n}{r_{n-1}} - \frac{f(r_n)}{f(r_{n-1})} - 1}} + \pi - 2\arctan\left(\sqrt{\left(1 - y_{n-1}^2\right)r_n^2 - y_{n-1}^2}\right) \qquad (3.1.30)$$

which can be used in conjunction with $y_{n-1}^2 = r_{n-1}^2 / f(r_{n-1})$ to calculate r_{n-1} and $f(r_{n-1})$, as we know t_{n-1} and y_{n-1} from the geodesic endpoints, and r_n and $f(r_n)$ have already been calculated.

For general t_{n-i} we split the integral into several pieces; the two "end" integrals, which we evaluate as in (3.1.26) and (3.1.27), and a series of integrals in the middle which can be evaluated using the trapezium rule or similar (see figure 3.4). The formula for general t_{n-i} is then given by (for $i \geq 2$):

$$t_{n-i} = 2 \int_{r_{n-i}}^{\infty} \frac{g(y_{n-i}, r)}{f(r)} \, dr \qquad (3.1.31)$$

$$\approx A_{n-i} + B_{n-i} + C_{n-i} \qquad (3.1.32)$$

where

$$A_{n-i} = \frac{4\left(r_{n-i+1} - r_{n-i}\right)}{f(r_{n-i})\sqrt{\frac{2r_{n-i+1}}{r_{n-i}} - \frac{f(r_{n-i+1})}{f(r_{n-i})} - 1}} \qquad (3.1.33)$$

---

[5]Note that this linear approximation of the gradient is only fine whilst $r_n - r_{n-1}$ is kept small, and can cause problems with the accuracy of the estimate for the metric, see section 3.1.4 for more details.
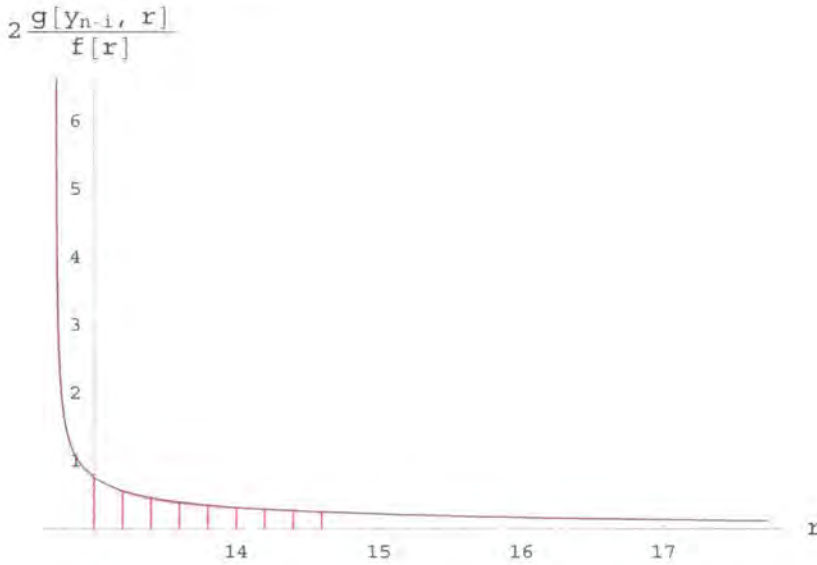
Figure 3.4: A plot showing how the integrand of (3.1.31) is split up into two end curves and a number of trapeziums in order for the integral to be well approximated. The actual curve is shown in black, with the approximations in red.

$$B_{n-i} = \sum_{j=1}^{i-1} (r_{n-j+1} - r_{n-j}) \left(\frac{g(y_{n-i}, r_{n-j+1})}{f(r_{n-j+1})} + \frac{g(y_{n-i}, r_{n-j})}{f(r_{n-j})} \right) \qquad (3.1.34)$$

$$C_{n-i} = \pi - 2 \arctan \left(\sqrt{(1 - y_{n-i}^2) \, r_n^2 - y_{n-i}^2} \right) \qquad (3.1.35)$$

For a spacetime of the form of (3.1.6) with monotonic effective potential, we can use the above to recover the function $f(r)$ down to $r = 0$. As with the majority of numerical techniques such as this, a consideration of its stability to errors which could ruin the accuracy of the estimate is important; if any error is not suppressed in subsequent iterations, the extraction will fail. It is not immediately obvious that the method is naturally stable to errors; if any error in our estimate for a particular $(r_{n-i}, f(r_{n-i}))$ was magnified in the estimate for the subsequent step, then our iteration would eventually break down, no matter how small the initial discrepancy. Thus perhaps the most obvious question now is that given the approximations we have introduced, does the method work in practice, and if so, how accurate and reliable is the estimate for $f(r)$? One of the clearest ways of demonstrating the stability is by seeing the method in action; this also provides a good indication of the overall accuracy one can expect. Before we can do so, however, we need to perform some

basic tests of the approximations and the process's efficiency in order to determine sensible values for the step size and starting choice of y.

3.1.4   Accuracy and efficiency considerations

Whilst the method just described allows the bulk metric to be fully recovered in principle (from $f(r_n)$ down to $f(0)$, with r_n arbitrarily large), there are a number of factors to take into account when performing the reconstruction in practice. For the moment we shall ignore any issues of stability (i.e. robustness to errors at each step), as this is addressed in section 3.3; instead, we concentrate here on examining the accuracy of the estimate, and obtaining a balance between this and computational effort.

Consider a setup where we divide the range of y into $N+1$ equal segments, with $y_0 = 0$ and $y_{N+1} = 1$, so that we have $N + 1$ steps in the process of recovering $f(r)$ (Note that the first step in the iteration uses y_N rather than y_{N+1}, as we want the first minimum radius to be finite).

There are a number of issues with recovering $f(r)$ in this scenario. We firstly observe that splitting y up into equal segments means that the minimum radii will not be equally separated; there will be a greater number of low radius points (due to the shape of V_{eff}, see figure 2.7 in the background section). This initially appears helpful, as we expect most of the bulk metric's deviation from pure AdS to be localised close to the centre, and so a greater number of data points in this region should improve our estimate of $f(r)$.

However, as our method for recovering $f(r)$ involves approximating integrals over r, accuracy is only maintained if the step size is kept relatively small for all r; whilst starting with y_N as close to one as possible allows $f(r)$ to be recovered from as large a radius as possible (as higher y_N means higher r_N), this also means the first few steps in r will be unacceptably large. This can be countered by ensuring the number of steps is appropriately large, however, this will then result in a longer computational time. For example, in the asymptotically AdS spacetime with $f(r)$ given by

$$f(r) = 1 + r^2 - \frac{4r^2}{(r^2 + 1)(r^2 + 8)} \tag{3.1.36}$$

if use a step size in y of 0.0005 and take the initial y_N to be 0.9995, the corresponding minimum radius $r_N \approx 31.5$. The minimum radius corresponding to $y_{N-1} = 0.999$ is only $r_{N-1} \approx 22.3$ however, and such a large jump in the radius causes problems with using our approximation of the form of (3.1.30). Whilst the original Laurent expansion of (3.1.27) is still fairly accurate over this distance, our approximation of the gradient by

$$f'(r_{n-i}) = \frac{f(r_{n-i+1}) - f(r_{n-i})}{r_{n-i+1} - r_{n-i}} \tag{3.1.37}$$

is not. For the example above, the actual value of $f'(r)$ at $r = 22.3$ is 44.5, whereas the value given by (3.1.37) is 53.8; a large discrepancy.

We can still split the y_n linearly (in order to keep the majority of the points at low radii), however, we choose the initial y_N to be be slightly lower. This enables our first step in the radius to be kept small.[6] In our example of (3.1.36), if we choose $y_N = 0.9985$ and keep the step size at 0.0005, we find that $r_N - r_{N-1} \approx 2.5$ which whilst still quite large, is much more acceptable than the value of 9.2 we had previously. Table 3.1 shows how this discrepancy in the gradient affects the extraction of $f(r)$ by the method of section 3.1.3 for the example of (3.1.36); it is worth noting at this stage that even with the lower choice of starting y the recovered estimate for $f(r)$ is still quite poor with a step size of 0.0005. This is important because although we could lower y_N even further, we must keep our initial radius reasonably large; if we choose y_N to be too low, we risk having r_N being too small, such that our assumption that the spacetime there is approximately that of pure AdS is no longer valid.[7] We can keep our choice of y_N high by reducing the step size

---

[6]This can be checked in practice by calculating r_N and r_{N-1} for a given choice of initial y_N; if the difference $r_N - r_{N-1}$ is too great, either lower y_N or increase N until it's acceptable.

[7]This poses an interesting question as to how one determines what a "reasonable" initial radius is for an unknown spacetime. If our r_N was too low, such that the metric was not approximately pure AdS at this point, how would this be apparent from the extracted estimate of $f(r)$? A simple solution is to check the behaviour of the estimate at r close to r_N; if the function does not continue

Initial y	Step size	α (4)	β (1)	γ (8)
0.9995	0.0005	0.778	0.971	0.971
0.9985	0.0005	1.39	1.52	1.52
0.9995	0.00005	2.37	2.24	2.24
0.9985	0.00005	3.42	1.13	6.18

Table 3.1: Comparing the accuracy of using two different values for y_N to recover the bulk metric information. The actual values for α, β and γ, which correspond to the three numerical factors in (3.1.36) (and are properly defined in (3.1.38)), are given in brackets. More details on how these estimates were generated is given in section 3.1.5.

(as in the lower half of Table 3.1), but at the expense of additional computational time; for more details on the numerical extraction see the examples in the next section.

Despite these potential pitfalls, the method we've outlined is remarkably stable to any such errors (see section 3.3 for an explanation of why this is so), and as the main issue of keeping the step size in r small is most important during the initial steps, one can easily tailor the starting choices of y_N and the step size to cater for the individual situation. Thus we now turn to some examples to demonstrate our ability to recover $f(r)$ in some specific scenarios.

3.1.5 Examples

Consider a small deviation from pure AdS, such as the spacetime with metric function $f(r)$ as in (3.1.36). Choosing our initial value of y to be $y_N = 0.9985$ for the reasons just given, we see how the basic method presented in section 3.1.3 fares in recovering the bulk information. Figure 3.5 shows our approximations of $f(r)$

---

as $r^2 + 1$ (i.e. pure AdS) down to say $r = r_N/2$, then the chosen initial radius was too small. It is also worth noting that in a physical situation, one would naturally expect ordinary matter to remain within a radius of order of R from the centre, due to the confining AdS potential. Finally, recall that the endpoints of the geodesics which remain far enough out to be unaffected by the deformation should be $(\pi - \phi_0, \pi - t_0)$, and thus this can also be used as a check.

generated using method I for a range of different step sizes.[8]

For this first example, the top set of curves in figure 3.5 suggest that we are easily able to extract the bulk metric using any of the step sizes, as they all appear to lie very close to the actual function $f(r)$. However, this is somewhat misleading, as we shall see. In order to more closely examine the accuracy of the recovered bulk data, we use a non-linear fit of the form:

$$f_{\text{fit}}(r) = 1 + r^2 - \frac{\alpha\, r^2}{(r^2 + \beta)(r^2 + \gamma)} \tag{3.1.38}$$

to obtain values for α, β and γ for each estimate, and the results are presented in Table 3.2. As we mentioned above, looking at the top plot of figure 3.5, all of the approximations seem very close to the original function, however, Table 3.2 shows this not to be the case. Until we go to a very small step size, we are unable to accurately extract what one might consider the important metric information; if the modification of the spacetime caused by the extra term in (3.1.36) was to correspond to some physical phenomenon, we might expect its "mass" and "extent" to be related to the quantities α, and β and γ respectively. Whilst the best fits we obtain are converging to the correct values as we take the step size smaller, we are already calculating a significant number of terms to generate these estimates.

Can we accurately recover a more complicated $f(r)$? If we consider a spacetime similar to that in (3.1.36), but which is further modified at low r by an extra term:

$$f(r) = 1 + r^2 - \frac{4r^2}{(r^2 + 1)(r^2 + 8)} + \frac{3r \sin(2r)}{r^4 + 1} \tag{3.1.39}$$

we can again generate estimates of $f(r)$ at various step sizes, and using a non-linear fit of the form of:

$$f_{\text{fit}}(r) = 1 + r^2 - \frac{\alpha\, r^2}{(r^2 + \beta)(r^2 + \gamma)} + \frac{\chi r \sin(\eta r)}{r^4 + \lambda} \tag{3.1.40}$$

---

[8]Whilst these deviations from the metric might appear rather arbitrarily chosen, with no specific origin for the deviation, they are nonetheless useful for testing the accuracy of the procedure; we shall go on to examine more physically based setups in chapter 5

Figure 3.5: Plots showing the various estimates for $f(r)$ given in Table 3.2 (i.e. produced using method I), compared to the actual metric function $f(r)$ from $(3.1.36)$. Whilst all the estimates seem good fits over a large radius (top figure), closer consideration of the curves highlights their differences (bottom figure), which lead to the inaccurate values calculated for α, β and γ from the larger step size estimates.

Initial y	Step size	α (4)	β (1)	γ (8)
0.9985	0.002	0.371	0.530	0.530
0.9985	0.001	0.797	0.995	0.995
0.9985	0.0005	1.39	1.52	1.52
0.9985	0.0002	2.18	2.11	2.11
0.9985	0.0001	2.74	1.47	3.92
0.9985	0.00005	3.42	1.13	6.18
0.9985	0.00002	3.80	1.11	7.20

Table 3.2: Best fit values (to 3 s.f.) for α, β and γ for data generated using method I, with the actual values indicated in brackets. Only in the lower half of the table do the estimates for the three unknowns really start to converge to the correct values.

we can judge the accuracy of the estimate against (3.1.39). Using the same starting value for y and the same step sizes as before, we obtain the results shown in table 3.3 and figure 3.6.

What is noticeable in this slightly more complicated example is that the presence of a more prominent feature in the metric function (in this case the small oscillation from the sine term) can obscure the finer details of the spacetime. We can clearly see that whilst the numerical factors corresponding to the sine term (χ, η and λ) are easily determined even at a large step size, it then requires a smaller step size to pick out the α, β and γ values than it did in the first example.

What can be seen from all three examples is that the method is clearly both stable to errors and capable of extracting the interior structure of the bulk with an accuracy continually improved by taking a smaller step size in the iteration. However, a slight reformulation of the integral which is split up and approximated leads to an even more accurate method.

3.2   Further analysis and method reformulation

Having established the principle behind extracting the bulk information from the geodesic endpoints, and developed a concise set of steps describing how to do so, we
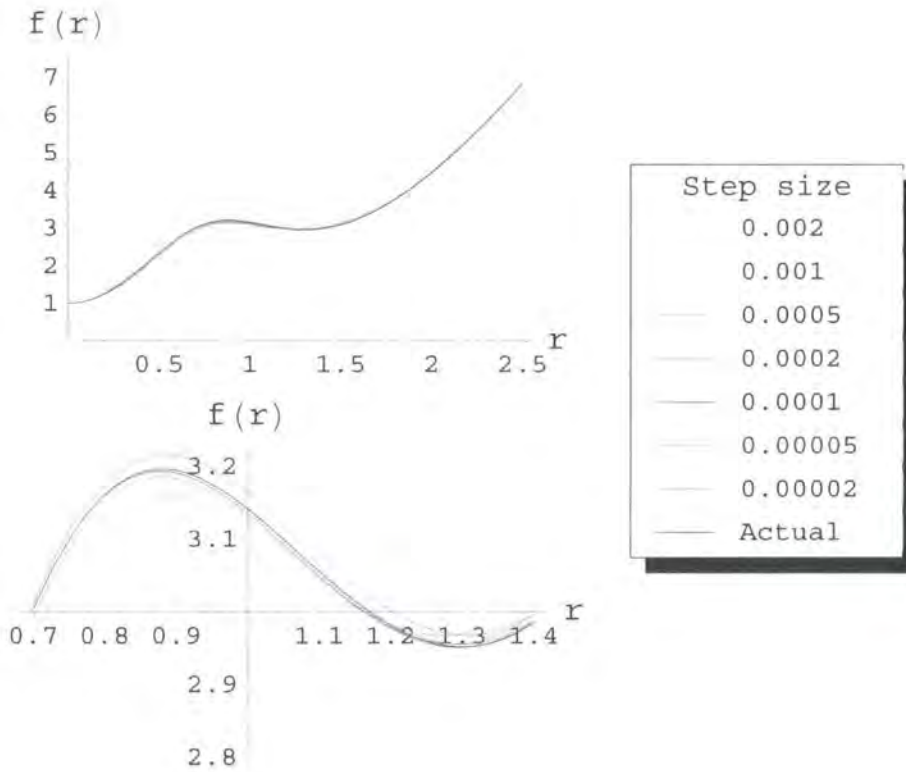
Figure 3.6: Plots showing the various estimates for $f(r)$ given in Table 3.3 (i.e. produced using method I), compared to the actual metric function $f(r)$ from (3.1.39). The convergence of the estimates to the actual curve can be seen in both plots, and whilst the values obtained for χ, η and λ are reasonably good for all step sizes, only upon using the smallest step size do we start to pick out the α, β and γ values. This is why, in the lower figure, the red curve representing the final estimate appears to be a worse fit to the actual curve than some of the others; the range of r shown highlights the accuracy of the χ, η and λ values rather than the α, β and γ ones.

Initial y	Step size	α (4)	β (1)	γ (8)	χ (3)	η (2)	λ (1)
0.9985	0.002	-1380	133	133	2.60	2.20	1.20
0.9985	0.001	0.0824	0.426	0.426	2.69	2.12	1.04
0.9985	0.0005	0.790	0.880	0.880	2.96	2.03	0.981
0.9985	0.0002	1.69	1.25	1.25	3.06	1.95	0.940
0.9985	0.0001	2.23	1.62	1.62	3.05	1.94	0.946
0.9985	0.00005	2.87	2.39	2.39	3.00	1.97	0.985
0.9985	0.00002	3.68	1.31	6.50	3.09	2.00	1.04

Table 3.3: Best fit values (to 3 s.f.) for α, β, γ, χ, η and λ for data generated using method I, with the actual values indicated in brackets. In this more complicated modification to AdS, the presence of the sine term masks the finer structure and prevents the original method from converging towards the correct values of β and γ until our smallest choice of step size.

now look at ways of modifying the method to optimise the accuracy and efficiency, and also take a more detailed look at the issue of stability.[9] Interestingly, we discover that reformulating the equations can lead to an alternative method with improved approximations, and we repeat the above examples using this new approach in order to demonstrate how this affects the accuracy.

3.2.1 Improving the approximations

We have seen numerically in the examples of the previous section how one can reduce the step size to continually improve the estimate of $f(r)$; there are several factors which might influence this accuracy: the order of the series expansion taken in equation (3.1.27), and the subsequent estimation of the derivatives of $f(r)$ necessary because of it; our trapezium approximation of the other integrals; and our taking of the far-from-centre spacetime to be pure AdS. The final one of these is was discussed further in footnote 7, and as the asymptotic form of the metric is known, this is already the least likely assumption to cause problems. The other approximations

---

[9]In addition to the issues analysed here, one might also wonder about the uniqueness of the extracted solutions; this point is discussed further in section 4.2.3.

were justified at the time by observing that they should become more accurate as our step size in r is reduced, and as this can be arbitrarily small, any errors could be eliminated by using a smaller step size; this was shown numerically to be true in the examples, and an analytic demonstration of why this so follows in section 3.3.

Firstly, however, we examine whether there are any improvements one could make to the approximations in order to improve the estimate without taking a smaller step size (to improve the efficiency of the process). The use of the trapezium rule can easily be improved upon by constructing a higher order interpolating function from the extracted data, and thus it is the series expansion approximation we examine more closely.

In our original method, after observing that the parameter y could be extracted directly from the endpoints, we then took our expression for the time t written as an integral over r, (3.1.7), and split it up into sections to be approximated. Alternatively, at this point one could equally well have used the similar expression for the angle ϕ, (3.1.8), and chosen to split that integral up instead. Continuing as before, we recall that the section closest to $r_{min} = r_{n-i}$ was approximated using a lowest order Laurent series:

$$2 \int_{r_{n-i}}^{r_{n-i+1}} \frac{g(y_{n-i}, r)}{f(r)} \, \mathrm{d}r \approx 2 \int_{r_{n-i}}^{r_{n-i+1}} \frac{(r - r_{n-i})^{-1/2}}{f(r_{n-i})\sqrt{\frac{2}{r_{n-i}} - \frac{f'(r_{n-i})}{f(r_{n-i})}}} \, \mathrm{d}r \qquad (3.2.1)$$

$$= \frac{4\sqrt{r_{n-i+1} - r_{n-i}}}{f(r_{n-i})\sqrt{\frac{2}{r_{n-i}} - \frac{f'(r_{n-i})}{f(r_{n-i})}}} = A_{n-i} \qquad (3.2.2)$$

where we have the extra unknown, $f'(r_{n-i})$. The equivalent expression for the ϕ integral is simply:

$$2 \int_{r_{n-i}}^{r_{n-i+1}} \frac{y_{n-i}\, g(y_{n-i}, r)}{r^2} \, \mathrm{d}r \approx \frac{4y_{n-i}\sqrt{r_{n-i+1} - r_{n-i}}}{r_{n-i}^2\sqrt{\frac{2}{r_{n-i}} - \frac{f'(r_{n-i})}{f(r_{n-i})}}} = \hat{A}_{n-i} \qquad (3.2.3)$$

Given the relation $y_{n-i} = r_{n-i}/\sqrt{f(r_{n-i})}$, one can immediately see that the above two equations are degenerate; namely that we have $A_{n-i} - y_{n-i}\hat{A}_{n-i} = 0$. This is what one naturally would have expected given the analysis of the endpoint gradient in section 3.1.1, and is a consequence of the previously determined relation between t and ϕ, (3.1.20). This also prevents us from using the two equations together to eliminate $f'(r_{n-i})$. What one can however do is improve the overall approximation by

taking the next-to-lowest order expansion, as at this level the equations are no longer degenerate; whilst taking this higher order expansion does introduce a $f''(r_{n-i})$ term, this is then eliminated when taking the combination $A_{n-i} - y_{n-i}\hat{A}_{n-i}$. After taking the next-to-lowest order expansion and integrating, we thus have that:

$$A_{n-i} - y_{n-i}\hat{A}_{n-i} = \frac{4}{3}\frac{(r_{n-i+1} - r_{n-i})}{f(r_{n-i})}\sqrt{\frac{2}{r_{n-i}} - \frac{f'(r_{n-i})}{f(r_{n-i})}} \qquad (3.2.4)$$

which should result in a better estimate for the metric at each step than simply using the lowest order expansion considered previously, although we still have the unhelpful introduction of the $f'(r_{n-i})$ term.

Indeed there is another problem with numerically reconstructing $f(r)$ using the approximation of the gradient by (3.1.37). If we examine the form of the term containing $f'(r)$ in the equation above, we note that the $f'(r)$ appears with a negative sign inside the square root. As our approximation of $f'(r)$ by (3.1.37) is in general an overestimation of the gradient, as for large r, $f(r) \propto r^2 + 1$, when solving for r_{n-i} and $f(r_{n-i})$ the term under the square root can become negative, leading to the estimates being imaginary. This can occur even if the overestimation is small.

There are a number of possible ways in which to resolve this problem. We can firstly consider a different approximation of the gradient to the one given in (3.1.37); the over-estimation can be avoided by using an expression such as

$$f'(r_{n-i}) = \frac{1}{2}\left(\frac{f(r_{n-i+1}) - f(r_{n-i})}{r_{n-i+1} - r_{n-i}} + \frac{f(r_{n-i}) - f(r_{n-i-1})}{r_{n-i} - r_{n-i-1}}\right) \qquad (3.2.5)$$

which takes the average of the two nearest linear tangents to the curve. Inserting this expression into either of our iterative methods for recovering $f(r)$, however, immediately raises a new problem from a computational point of view; we now cannot recover a value for r_{n-i} and $f(r_{n-i})$ at each step, as the $n - i$ term now also depends on the subsequent term, $n - i - 1$, as well as the previous. We now have to determine all the equations for the various steps and solve them together at the end to recover $f(r)$.[10] This is a much more complicated operation than numerically

---

[10]Note that the final gradient $f'(r_0)$ would have to be approximated using an expression of the form of (3.1.37)

solving at each step, and leads to a considerable increase in the computational effort required to reconstruct the metric function. Another possible approach uses the fact that the underlying structure of the spacetime is that of pure AdS; taking our deformation as that given in (3.1.6), and then taking a linear approximation to the gradient as before:

$$f'(r_{n-i}) \approx \frac{f(r_{n-i+1}) - f(r_{n-i})}{r_{n-i+1} - r_{n-i}} - (r_{n-i+1} - r_{n-i}) \qquad (3.2.6)$$

This proves to be a considerably better estimate for the gradient at large r, where the metric is close to pure AdS (and where most of our previous problems arose). In our example of section 3.1.4, with the metric given by (3.1.36), we had that $r_N = 31.5$ and $r_{N-1} = 22.3$; we then found that our original approximation, given by (3.1.37), yielded an estimate of 53.8 for the gradient at r_{N-1}, whereas the actual value was $f(r = 22.3) = 44.5$. Our new formula for the gradient gives a value of $53.8 - (31.5 - 22.3) = 44.6$, far closer than before.

Despite this huge improvement, there is another approach which solves this issue with the gradient very neatly - by avoiding introducing such a term at all! The idea follows directly from our relation between the t and ϕ endpoints, and allows a different approximation to be used to the series expansions considered thus far.

3.2.2 Reconstructing $f(r)$: Method II

Our original analysis of the endpoints in section 3.1.1 yielded a simple relation between the t and ϕ coordinates, which enabled us to determine the corresponding value of y for each geodesic. We can continue beyond this point to obtain an alternative integral with which to extract the metric. If we start from expression (3.1.19) and integrate over y we get:

$$\int^t dt' = \int y \frac{d\phi}{dy} \, dy \qquad (3.2.7)$$

which can be integrated by parts:

$$t(y) = y\,\phi(y) - \int \phi \, dy \qquad (3.2.8)$$

and then rewritten using the expression for ϕ from (3.1.8):

$$t(y) = y\,\phi(y) - \int\int_{r_{min}}^{\infty} \frac{2y}{r^2\sqrt{1 - y^2\frac{f(r)}{r^2}}}\,\mathrm{d}r\,\mathrm{d}y \tag{3.2.9}$$

We can now reverse the order of integration, and as the function $f(r)$ has no dependence on y, integrate over y:

$$t(y) = y\,\phi(y) + \int_{r_{min}}^{\infty} \frac{2}{f(r)}\sqrt{1 - y^2\frac{f(r)}{r^2}}\,\mathrm{d}r \tag{3.2.10}$$

Taking the initial conditions to be $(\phi_0, t_0) = (0, 0)$, we can say that for any endpoint (ϕ_j, t_j) on the boundary,

$$t_j - \left.\frac{dt}{d\phi}\right|_{(\phi_j, t_j)} \phi_j = \int_{r_j}^{\infty} \frac{2}{f(r)\,g(y_j, r)}\,\mathrm{d}r \tag{3.2.11}$$

where we have renamed r_{min} as r_j and used our definition for $g(y, r)$ from before. This, coupled with the equation for the minimum radius:

$$y_j^2 = \frac{r_j^2}{f(r_j)} \tag{3.2.12}$$

allows the metric function $f(r)$ to be fully reconstructed from the plot of the endpoints, say by using a method of approximating the integral similar to that in section 3.1.3. Whilst at first glance this appears almost identical to the first method, there is a significant difference between (3.1.31) and (3.2.12) (namely the position of the $g(y, r)$ term) which completely alters the shape of the integral. If one proceeds as before, by taking a series expansion at this point, one obtains exactly the same result as we saw earlier when we combined the two terms A_{n-i} and $\hat{A}_{n-i}$, namely equation (3.2.4). Explicitly, the general integral would be split into several pieces as before, and we would have:

$$t_{n-i} - y_{n-i}\phi_{n-i} = \int_{r_{n-i}}^{\infty} \frac{2}{f(r)\,g(y_{n-i}, r)}\,\mathrm{d}r \tag{3.2.13}$$

$$\approx \mathcal{A}_{n-i} + \mathcal{B}_{n-i} + \mathcal{C}_{n-i} \tag{3.2.14}$$

where

$$\mathcal{A}_{n-i} = \frac{4}{3}\frac{(r_{n-i+1} - r_{n-i})}{f(r_{n-i})}\sqrt{\frac{2}{r_{n-i}} - \frac{f'(r_{n-i})}{f(r_{n-i})}} \tag{3.2.15}$$
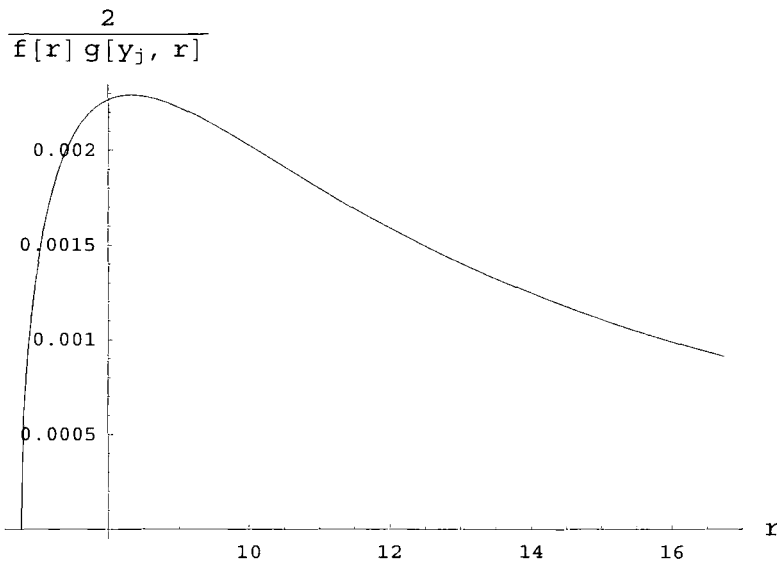
Figure 3.7: A plot showing an example curve (the integrand of (3.2.11)) to be approximated in method II. The leftmost part of the curve is initially a vertical parabola.

$$\mathcal{B}_{n-i} = \sum_{j=1}^{i-1} (r_{n-j+1} - r_{n-j}) \left(\frac{1}{f(r_{n-j+1}) \, g(y_{n-i}, r_{n-j+1})} + \frac{1}{f(r_{n-j}) \, g(y_{n-i}, r_{n-j})} \right)$$

$$(3.2.16)$$

$$\mathcal{C}_{n-i} = 2 \arctan \left(\frac{1}{\sqrt{\left(1 - y_{n-i}^2\right) r_n^2 - y_{n-i}^2}} \right) - 2 y_{n-i} \arctan \left(\frac{y_{n-i}}{\sqrt{\left(1 - y_{n-i}^2\right) r_n^2 - y_{n-i}^2}} \right)$$

$$(3.2.17)$$

where we have used $\mathcal{A}$, $\mathcal{B}$, $\mathcal{C}$ to distinguish from the A, B and C labelling used earlier.

Simply using series approximations, however, makes this reformulation a somewhat academic exercise, as they offer no improvement to the accuracy of the method compared to the original ones in section 3.1.3. What *is* different, however, is that with the new positioning of the $g(y, r)$ term, our integral (3.2.13) can instead be approximated geometrically about r_{n-i}, a process which avoids introducing the unwanted $f'(r)$ term.

Parabolic curves

Figure 3.7 shows a plot of a typical curve we are trying to approximate. The crucial difference between this type of curve and that of figure 3.4 is the behaviour at the

minimum radius, which is due to the positioning of the $g(y,r)$ term in equations (3.1.31) and (3.2.11). That $g(y,r)$ appears in the denominator of (3.2.11) rather than the numerator results in the curve of figure 3.7 having an infinite gradient at the minimum radius. We can then describe the leftmost part of the curve as following a vertical parabolic path. Thus instead of using a Laurent approximation at this point, we can make a geometric one and say that:

$$\mathcal{A}_{n-i}^{\text{parabolic}} = \frac{4}{3} \frac{(r_{n-i+1} - r_{n-i})}{f(r_{n-i+1})} \sqrt{1 - \frac{y_{n-i}^2}{y_{n-i+1}^2}} \qquad (3.2.18)$$

where we have used that the area under a parabola is 2/3 the width multiplied by the height. The gradient of the curve will always be infinite at the minimum radius, and as the other terms ($\mathcal{B}_{n-i}$ and $\mathcal{C}_{n-i}$) do not depend on $f'(r)$, we avoid the need for an approximation to the gradient of $f(r)$ of the form of (3.1.37). Importantly, we also avoid any increase in the computational effort required to recover $f(r)$, and it is worth noting that there is no similar geometric argument for such an approximation to be applied in the original method of section 3.1.3.

This formalism also has the advantage that the only unknown term in $\mathcal{A}_{n-i}^{\text{parabolic}}$ is r_{n-i}, and so one can immediately solve for this before using $y_{n-i} = r_{n-i}/\sqrt{f(r_{n-i})}$ to determine $f(r_{n-i})$. For similar step size this modification leads to a considerably more accurate estimation of $f(r)$ from the endpoints, as we shall see in the next section, where we use this new method to reconstruct $f(r)$ in the two different cases first considered in section 3.1.5.

3.2.3 Examples

To see the improvement this new formalism provides, we reconstruct the same asymptotically AdS spacetimes we considered earlier, in section 3.1.5. Our first example was the metric given by (3.1.36), which we reproduce here as a reminder:

$$f(r) = 1 + r^2 - \frac{4r^2}{(r^2 + 1)(r^2 + 8)} \qquad (3.2.19)$$

Using the same initial choice of y as before, along with an identical range of step sizes, we generate the results given in Table 3.4 and figure 3.8 in exactly the same way as in 3.1.5, using our new formalism.

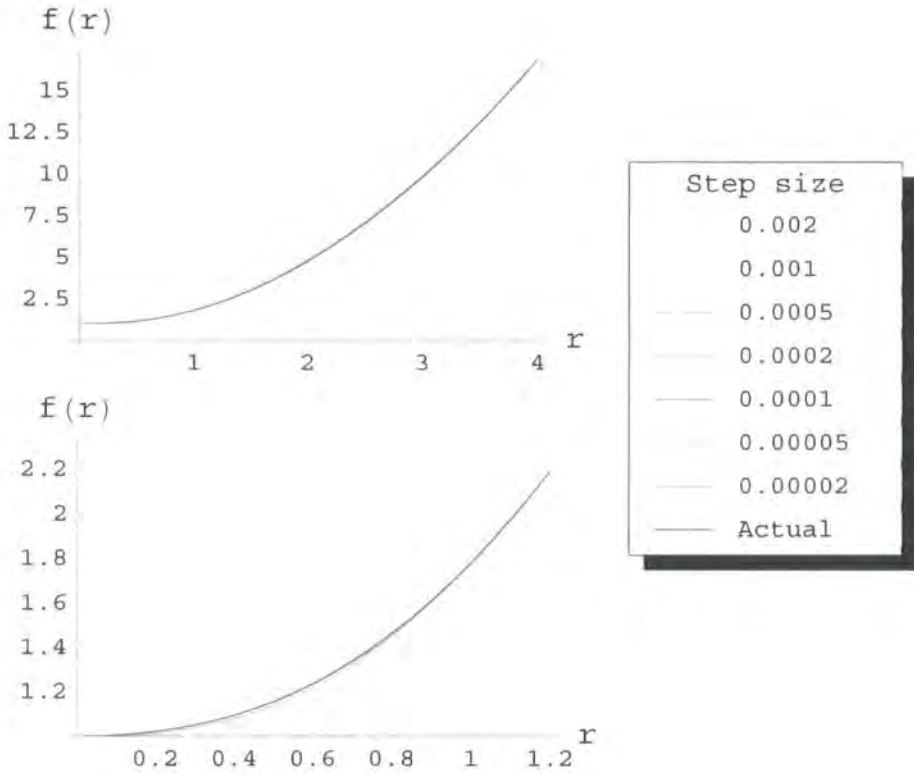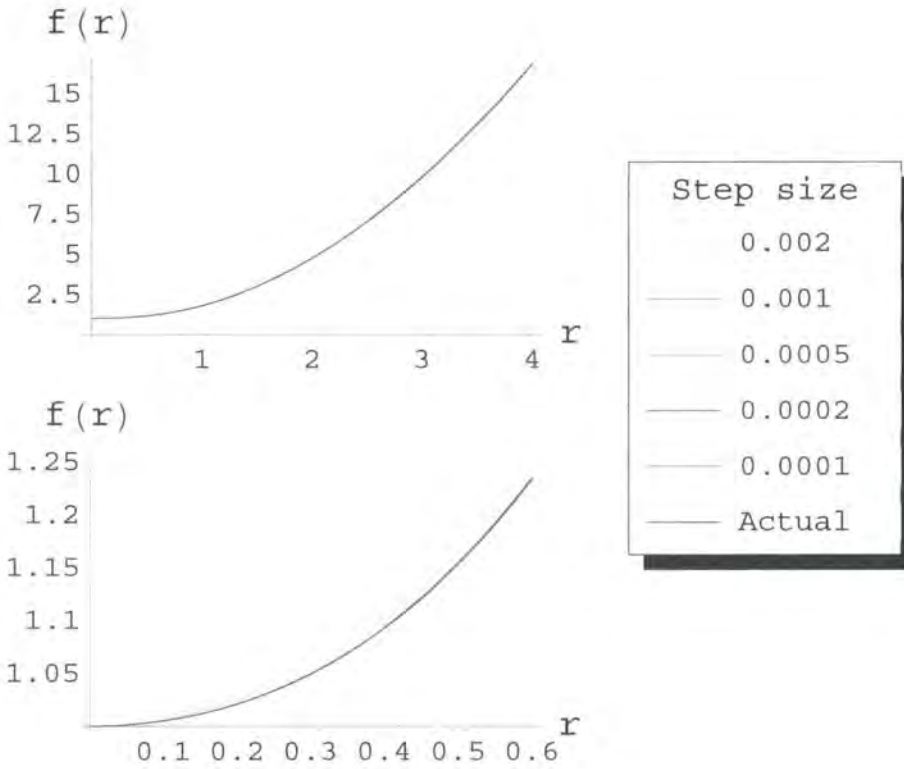**Figure 3.8:** Plots showing the various estimates for $f(r)$ given in Table 3.4 , compared to the actual metric function $f(r)$ from (3.1.36). Using method II for producing the estimates has resulted in much closer fits, both over a large radius (top figure), and at smaller scales (bottom figure). This is reflected in the highly accurate values of α, β and γ determined from the all but the largest step size estimates.

Initial y	Step size	α (4)	β (1)	γ (8)
0.9985	0.002	1.61	2.01	2.01
0.9985	0.001	3.34	1.16	6.01
0.9985	0.0005	3.92	1.01	7.77
0.9985	0.0002	3.99	1.00	7.97
0.9985	0.0001	4.00	1.00	8.00

Table 3.4: Best fit values (to 3 s.f.) for α, β and γ for data generated using method II, with the actual values indicated in brackets. Using the alternative method, we are able to pick out rough values for the three unknowns as early as with a step size of 0.001, and by a step size of 0.0001 the estimates have converged to the correct values (to 3 s.f.).

If we compare this to the fits we obtained using the data calculated via method I, we see a notable difference in the results. The estimates again all look good when plotted with the actual function $f(r)$, as we see in figure 3.8, however, as the bottom plot shows, this accuracy is now maintained at smaller scales. Table 3.4 shows the new values for α, β and γ for each step size, obtained using the same non-linear fit, (3.1.38), as before.

Comparing these estimates with those in Table 3.2, we see that the recovered values for α, β and γ are far more accurate using this alternative method, for each choice of step size. We now have a very good fit to the actual values of 4,1 and 8 in (3.1.36) obtained using a relatively low number of steps, and thus relatively quickly. Indeed, we see that to obtain the same degree of accuracy using method I we need to use step sizes which are more than twenty five times smaller, which (assuming a standard computational time per step) would therefore take at least twenty five times longer to compute. Thus using the modified second method offers a significant improvement over the original.

Whilst both method I and method II as presented here are far from optimised, as at each step one could have used higher order interpolation functions generated with already extracted terms to avoid using the trapezium approximations, for example, it is still worth presenting these computational results for each, as there was no inherent guarantee that this second method would be more efficient. Indeed, the

Initial y	Step size	α (4)	β (1)	γ (8)	χ (3)	η (2)	λ (1)
0.9985	0.002	1.17	1.46	1.46	3.47	1.94	1.12
0.9985	0.001	2.90	2.52	2.52	3.03	1.97	0.998
0.9985	0.0005	3.85	1.06	7.38	3.00	2.00	1.00
0.9985	0.0002	3.98	1.01	7.93	3.00	2.00	1.00
0.9985	0.0001	4.00	1.00	7.99	3.00	2.00	1.00
0.9985	0.00005	4.00	1.00	8.00	3.00	2.00	1.00

Table 3.5: Best fit values (to 3 s.f.) for α, β, γ, χ, η and λ for data generated using method II, with the actual values indicated in brackets. Once again, the alternative method proves much more adept at accurately estimating the unknowns, and converges to the correct values almost immediately.

very demonstration that both methods actually work in practice is also of value, as this was again not guaranteed from the outset; although one might have expected it (or at least not have been concerned about it), it is an especially important factor when using spacelike geodesics, as we shall see in the next chapter.[11] This stability of the methods to errors will be discussed shortly, after we examine the second of our examples. For a spacetime of the form (3.1.39), we obtain the results shown in table 3.5, and figure 3.9.

Once again we see that the second method produces a much better estimate of $f(r)$ than the first; the difference in the accuracy is again significant, with the estimates for the various unknowns much closer to the actual values at the larger step sizes.

We now investigate why it is that these iterative methods for estimating the metric are so robust to errors. One might have suspected beforehand that a deviation from the actual form of $f(r)$ at any step should hamper the subsequent estimate, with the cumulative effect preventing the correct small radii behaviour from being

---

[11]Interestingly, the use of simple trapezium approximations which work here lead to instabilities in the similar method involving spacelike geodesics developed in the next chapter. There one needs to use at least a second order approximation to the central parts of the integral, and the behaviour of errors is on the whole more complicated.

f(r)

f(r)

Step size
——— 0.002
       0.001
——— 0.0005
——— 0.0002
       0.0001
——— 0.00005
——— Actual
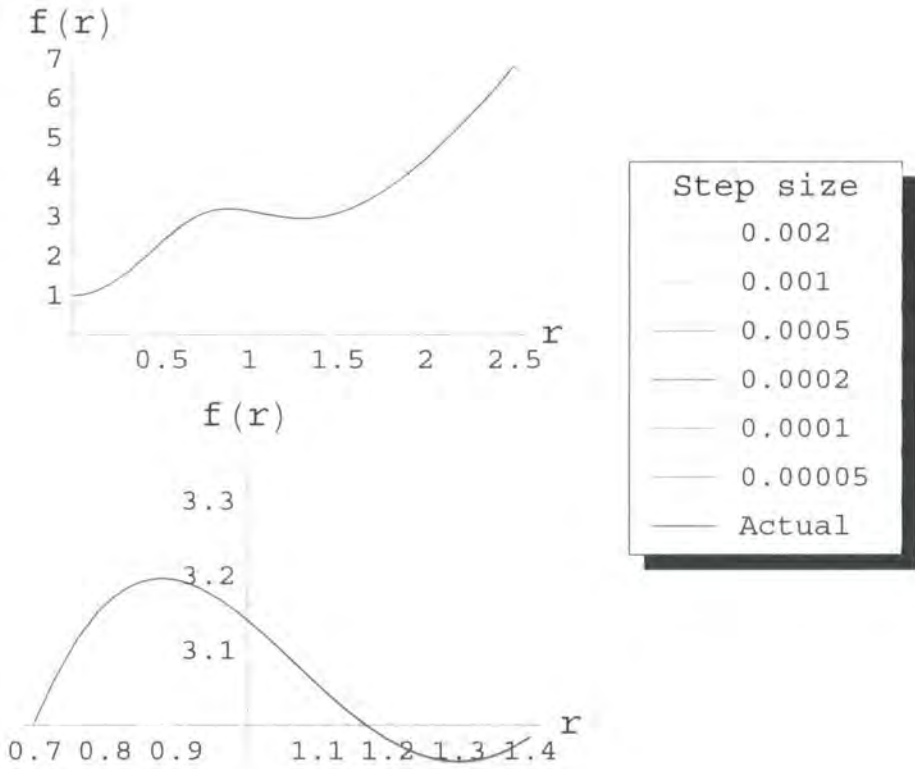
Figure 3.9: Plots showing the various estimates for $f(r)$ given in Table 3.5 (i.e. produced using method II), compared to the actual metric function $f(r)$ from (3.1.39). Only the estimates generated using the largest two step sizes are visibly distinguishable from the actual curve, as the the values of α, β, γ, χ, η and λ are all quickly picked out using this alternative method.

determined at all. Of course, we have yet to investigate those metrics with such a large central deformation that null geodesic orbits can occur, and indeed the extreme of such scenarios where the metric contains a horizon. However, the principle of extracting the metric proceeds as we have already seen, with the same stability against errors, and so we leave these cases where the metric cannot be completely determined until the subsequent section.

3.3 Error analysis

Having demonstrated numerically the considerable accuracy of the estimates for $f(r)$ generated using both methods, and in particular the second, we now look analytically as to why this iterative process is so stable against errors. As mentioned briefly earlier, one might well have expected that any errors would be cumulative, and that once the estimate deviated from the true metric, it would continue to diverge, rendering the method impossible to use in practice. The reason this is not the case is because any error term is in fact suppressed in subsequent steps.

There are three main ways errors can occur in the iteration, which are common to most numerical methods, namely:

- Data errors, where the input (i.e. the endpoint data) is inaccurate;

- Approximation errors, in our case, the approximations of the integral, and finally;

- Error propagation, where any error leads to further errors in subsequent steps of the iteration.

We shall address each in turn, explaining in what forms they manifest themselves, and how they are sufficiently suppressed to allow the accurate estimates for $f(r)$ seen in the preceding sections.

3.3.1   Errors in the original data:

If the original data from the field theory was corrupted or inaccurate in some way, this would of course lead to a false set of null geodesic endpoints from which to

attempt to estimate the metric, and would obviously affect the calculation of y and all other steps in the iteration. Although this would produce a false estimate for the metric one determines to be dual to the boundary field theory, these types of errors would not in principle prevent the method from working (unless the corruption to the data was sufficient to violate either the asymptotic behaviour one requires to be pure AdS, or is evident in some other fashion, such as by producing null geodesics with timelike separation less than π for example.

Whilst one could extend our analysis further to attempt to further account for this, we choose to focus on the errors arising from the iterative method itself, and the approximations used therein, as detailed below. We thus have consistently assumed throughout that there was no error in determining the value of y from the geodesic endpoints, and similarly that there was no error in obtaining the endpoints from the field theory data in the first place.

3.3.2 Errors in our approximations:

The next most obvious source of errors is from the approximations to the integrals used in the iteration. There were four different approximations used overall, although as two of them were alternative approximations to the same section of the integral (around the minimum radius), in any particular example only three are used: a parabolic or series expansion around r_{min}, a set of trapezium (or higher order interpolating function) approximations, and finally the condition on the asymptotic behaviour of the spacetime, with which we now begin.

In all cases, the bulk is taken to be asymptotically anti-de Sitter, and so at large radius one approximates the metric function $f(r) \approx r^2 + 1$. This is our most obviously reliable approximation, as provided a large enough choice of r_n is taken, it is accurate to as high a degree as one wishes. Given that at any step, such an approximation is only made for the final part of the integral, and that its accuracy can also be directly checked in the first instance (as one knows exactly how the geodesic should behave), we take its influence on our estimate to be both negligible and easily computable.

Now consider the other end of the integral, where the geodesic probes deepest

into the bulk; using our second formulation of the method, we applied the parabolic area formula to give:

$$\mathcal{A}_{n-i}^{\text{parabolic}} = \frac{4}{3} \frac{(r_{n-i+1} - r_{n-i})}{f(r_{n-i+1})} \sqrt{1 - \frac{y_{n-i}^2}{y_{n-i+1}^2}} \qquad (3.3.1)$$

This type of approximation, along with the alternative series expansion, were both justified earlier by claiming that they could be made arbitrarily accurate given a small enough step size, and this is indeed the case, as can be confirmed numerically. Both approximations are at least second order, and so it is no great surprise that they should be accurate enough on any particular step of the iteration, their accuracy will be more important when one considers the propagation of errors, see the following section.

Finally, the central section of the integral was approximated by a set of trapeziums, as seen in figure 3.4. Although we shall see in the next section how the effect of the total number of trapeziums affects the error[12], here we note that whilst this is only a linear approximation to the curve, for the first step in which we use such an approximation, we can take the size of the trapezium to be arbitrarily small.

Taken together, the reasoning above means that one can make the *first* error arising from our approximations arbitrarily small, however, this error will still be non-zero for any practical (i.e. non-infinitesimal) choice of step size.

What is still unclear is why the propagation of errors doesn't lead to larger and larger errors in subsequent steps of the iteration; if the small errors in the above approximations (which arise from using a finite step size) occur at every step, how is their sum continually suppressed?

---

[12]Although for a specific section of an integral (of a known curve), increasing the number of trapeziums by a factor of N decreases the error by a factor of N^2, this cannot be used to argue that the error contribution from *all* our trapeziums should be unimportant in the zero-step size limit, due to the iterative process in which our metric extraction works; at any step in the iteration, the number of trapeziums we can use in the approximation of the central curve is limited by the step size used previously.

3.3.3 Propagation of errors:

Given the iterative process by which our estimate of the metric is produced, an intrinsic concern is the propagation of errors from one step to the next. We firstly discuss how a single error at any step affects the next estimate, the behaviour of which can be analysed as follows: consider the geodesic whose actual minimum radius is r_{min}, but the estimate for which contains some small error, ϵ, such that $\bar{r}_{min} = r_{min} + \epsilon$. Note that this error is assumed to arise simply due to errors in the various approximations used in the terms of (3.2.13) (for method II), not from any earlier errors in our estimate, and as such can be made arbitrarily small (as discussed above). Then we have that our estimate for the metric at this point will also be slightly out, and this is given by:

$$\bar{f} \equiv f(\bar{r}_{min}) = \frac{(r_{min} + \epsilon)^2}{y^2} = f(r_{min}) \left(1 + \frac{2\epsilon}{r_{min}} + \frac{\epsilon^2}{r_{min}^2} \right) \qquad (3.3.2)$$

where we recall that y is the corresponding ratio of J to E for that geodesic and we have kept the order ϵ^2 terms for the moment. We can immediately see from the above that any error in the estimate for r_{min} corresponds to an error in $f(r_{min})$ suppressed by a factor of r_{min}. Thus in the initial steps at larger r, one can (if necessary) accommodate a relatively large error from the approximations to the relevant integral in the value for r_{min}, and still extract a good estimate for the metric function. Indeed, as we would expect the error (from the approximations) in r_{min} to always be significantly smaller than the magnitude r_{min}, this should be true even for small r_{min}; what we wish to consider is how the above errors in both r and $f(r)$ appear in the next step of the iteration.

Using method II, and denoting the erroneous estimates from the current step as $\bar{r}_{m+1}$ and $\bar{f}_{m+1}$, we have that the next estimate uses these values in two terms of our approximation of the integral (3.2.13): the parabolic term and the trapezium[13]

---

[13]Although the trapezium approximations could be replaced with a higher order interpolation function in order to provide a better fit, as the methods both work with the rougher trapezium fits, we perform the stability analysis for this scenario; interestingly, this is not true for our method involving spacelike geodesics developed in the following chapter, see section 4.2.1.

closest to r_m. We thus have that

$$t_m - y_m \phi_m = \frac{4}{3} \frac{(\bar{r}_{m+1} - \bar{r}_m)}{\bar{f}_{m+1}} \sqrt{1 - \frac{y_m^2}{y_{m+1}^2}}$$

$$+ (r_{m+2} - \bar{r}_{m+1}) \left(\frac{1}{f(r_{m+2}) \, g(y_m, r_{m+2})} + \frac{1}{\bar{f}_{m+1} \, g(y_m, \bar{r}_{m+1})} \right)$$

$$+\text{error-free terms} \tag{3.3.3}$$

where the labelling $\bar{r}_m$ in the above reminds us that our estimate for the minimum radius r_m will contain error terms. Now suppose for the moment that the only appearance of the error was in the first term, so ignoring the trapezium contribution. If this were the case, after combining the error-free terms and the endpoint data on the LHS into a single (numerical) term, denoted Z, and rearranging to solve for $\bar{r}_m$, we would have:

$$\bar{r}_m = \bar{r}_{m+1} - \frac{3\bar{f}_{m+1}Z}{4\sqrt{1 - \frac{y_m^2}{y_{m+1}^2}}} \tag{3.3.4}$$

By using our expressions for the errors given above, namely that $\bar{r}_{m+1} = r_{m+1} + \epsilon$, and $\bar{f}_{m+1}$ as in (3.3.2), we can then rewrite this as:

$$\bar{r}_m = r_{m+1} - \frac{3f(r_{m+1})Z}{4\sqrt{1 - \frac{y_m^2}{y_{m+1}^2}}} + \epsilon \left(1 - \frac{3f(r_{m+1})Z}{2r_{m+1}\sqrt{1 - \frac{y_m^2}{y_{m+1}^2}}} \right) \tag{3.3.5}$$

The first two terms on the RHS are simply equivalent to r_m, and the question that remains is to the size of the coefficient of ϵ. If this number were larger than one, any error would thus be increased at subsequent steps, and the estimate for $f(r)$ would diverge away from the correct function. From the form of the coefficient, however, we see that its value will tend to one from below as the step size in y tends to zero (note that although the square root in the denominator tends to zero as $y_{m+1} \rightarrow y_m$, this divergence is suppressed by the numerator also tending to zero). This behaviour, whilst easily shown numerically, is also obvious from the form of the final term; it is simply twice the step size in r, divided by r_{m+1}. As the step size in r must decrease to zero as the step size in y does the same, this final term must therefore vanish[14] and the coefficient of the error tends to one.

---

[14]There appears to be a small loophole in this argument, which is due to the presence of the

Thus if one only had the error occurring in the one term of our equation (3.2.13), any error would either be suppressed, or at worst kept constant in subsequent steps. How is this affected by the appearance of the error in the neighbouring trapezium approximation, which we mentioned earlier but then temporarily ignored? Returning to (3.3.3), after a similar rearranging to solve for $\bar{r}_m$ and use of our expressions for $\bar{r}_{m+1}$ and $\bar{f}_{m+1}$ as before we have:

$$\bar{r}_m = r_m + \epsilon \left(\frac{1}{4} - \frac{3f(r_{m+1}) \left(2f(r_{m+2})Z + (3r_{m+1} - 2r_{m+2})\sqrt{1 - \frac{y_m^2}{y_{m+2}^2}} \right)}{4r_{m+1}f(r_{m+2})\sqrt{1 - \frac{y_m^2}{y_{m+1}^2}}} \right) + O(\epsilon^2)$$

$$(3.3.6)$$

where we have kept only first order terms in ϵ, and recall that Z is defined as the LHS of (3.3.3) minus the sum of the error-free terms from the RHS (and as such, isn't exactly the same as the Z in (3.3.4) and (3.3.5), where all the trapezium terms were taken to be error-free). Analysing the behaviour of the ϵ coefficient as the step size in y tends to zero, we have that the term containing Z goes to zero for precisely the same reasons stated in the previous case, for the similar term in (3.3.5). For the final term we note that in the methods proposed in sections 3.1.3 and 3.2.2, we took a constant step size in y. Thus if we denote this step size by σ, we have that:

$$\frac{\sqrt{1 - \frac{y_m^2}{y_{m+2}^2}}}{\sqrt{1 - \frac{y_m^2}{y_{m+1}^2}}} = \frac{\sqrt{1 - \frac{y_m^2}{(y_m + 2\sigma)^2}}}{\sqrt{1 - \frac{y_m^2}{(y_m + \sigma)^2}}} \to \sqrt{2} \quad \text{as} \quad \sigma \to 0 \qquad (3.3.7)$$

As we can also write $r_{m+2}/r_{m+1} \to 1$ and $f(r_{m+1})/f(r_{m+2}) \to 1$ as $\sigma \to 0$, we can therefore say that the error in the r_m term in the small step size limit is given by:

$$\bar{r}_m = r_m + \epsilon \left(\frac{1}{4} - \frac{3}{2\sqrt{2}} \right) \approx r_m - 0.81\epsilon \qquad (3.3.8)$$

which means that the error is further suppressed in subsequent steps than if one didn't include the error in the trapezium term!

Another subtle point to consider is that we have gone from having a small positive error in our estimate for r_{m+1} to a smaller, *negative* error in our estimate for r_m.

---

r_{m+1} term in the denominator, as surely when $r \to 0$ this will also diverge? However, as this radial value is that for the previous step in the iteration, it necessarily must be greater than zero for there to be a subsequent step! Thus as one needs to take ever smaller step sizes in order to probe to $r = 0$, this term is naturally overcome.
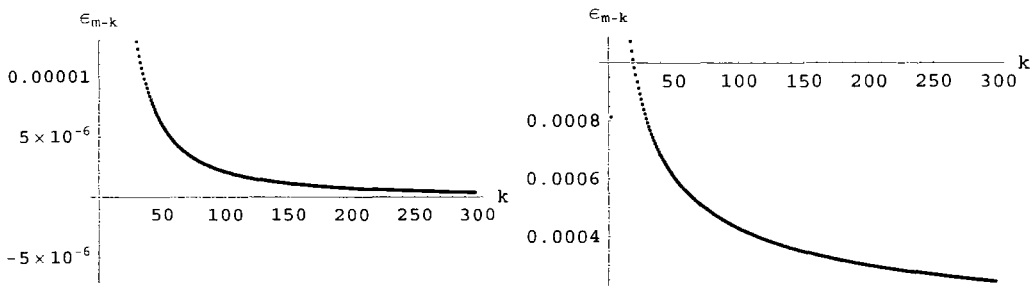
Figure 3.10: Plots of the error term ϵ_{m-k} against the number of steps k with initial error $\epsilon_{m+1} = 1/10$. The left hand plot shows the behaviour for $\epsilon_{m-k}^{approx} = 0$, i.e. purely error propagation with no additional contribution from the approximations. In the right hand plot, we have assumed a constant additional error at each step, $\epsilon_{m-k}^{approx} = \epsilon_{m+1} = 1/10$. In both cases, the overall error is heavily suppressed as k becomes large.

The reason this is important is that one could well suppose that whatever generated the original ϵ error in r_{m+1} could generate another, similar sized error in our second step, in addition to the error carried over. If this were the case, we would have a new error in r_m of $-0.81\epsilon + \epsilon = 0.19\epsilon$, and although the coefficient is still less than one, to complete the analysis one must consider the possible issue of the accumulation of errors.

We now have errors in the estimates for r_{m+1} and r_m; what about the next step, r_{m-1}, or in general, r_{m-j}? In the limit $\sigma \to 0$, the first order (neglecting powers of ϵ^2 or higher) expression for the error at step $m - j$ is given by the formula:

$$\epsilon_{m-k} = \epsilon_{m-k+1} + \frac{3}{4} \sum_{j=0}^{k} \left((\epsilon_{m-j+2} - \epsilon_{m-j+1}) \left(\sqrt{1+k-j} + \sqrt{2+k-j} \right) \right) + \epsilon_{m-k}^{approx}$$

$$(3.3.9)$$

which includes contributions both from previous steps (note that ϵ_{m+2} is taken to be zero, as our original error was only introduced at step ϵ_{m+1}) and the error introduced at the current step from inaccuracies in the approximations, denoted ϵ_{m-k}^{approx}. As can be seen in figure 3.10, the error is heavily suppressed for k large (i.e. after numerous subsequent steps), and this remains true even if a relatively large contribution from inaccurate approximations is included.

This analysis has confirmed what we already knew numerically from the examples

in sections 3.1.5 and 3.2.2: that the metric extractor is both intrinsically stable with a natural suppression of errors, and that the estimates for the metric produced should be highly accurate after sufficient steps. What we have not yet addressed is limitations to the procedure for determining the metric which arise not from numerical issues, but from situations where the data from the geodesic probes itself is insufficient.

3.4   Limitations: Metrics with a non-monotonic effective potential

At the beginning of this chapter, we asked what the form of the endpoint information would be for null geodesics in a static, spherically symmetric bulk with a central deformation; for the set of geodesics all emanating from the same point on the boundary, it can be plotted as t_{end} vs ϕ_{end}, as we saw in figures 3.1 and 3.2. The subsequent analysis was focused on the case where this plot was continuous, i.e. figure 3.1, which is the case corresponding to relatively small deformations from pure AdS, and allows for the metric to be estimated down to the centre of the spacetime. For larger deformations, the plot becomes discontinuous, and for a black hole metric, the top branch disappears entirely, as discussed in footnote 2, and in both cases there is a problem with our numerical method for reconstructing $f(r)$.

What is happening from a geodesic point of view? If the deformation to the metric is large enough, for some critical value of the (normalised) angular momentum y the null geodesics can go into an unstable orbit, as we saw in 3.2. This results in the discontinuity seen in the endpoint plot where the (unbounded) ϕ_{end} coordinate heads off to infinity; there is also a jump in the time taken by the geodesics with $y < y_{crit}$ compared with those with $y > y_{crit}$, as indicated in figure 3.11.

The reason for these unstable orbits is because the effective potential for the metric isn't monotonic; the orbits occur when the greatest radius (r_p say) for which $dV_{eff}/dr = 0$ corresponds with that for which $V_{eff} = 0$, see figure 3.12. This non-monotonicity also explains the time delay for those geodesics with angular momentum lower than y_{crit}, indicated by the gap between the asymptotes in figure
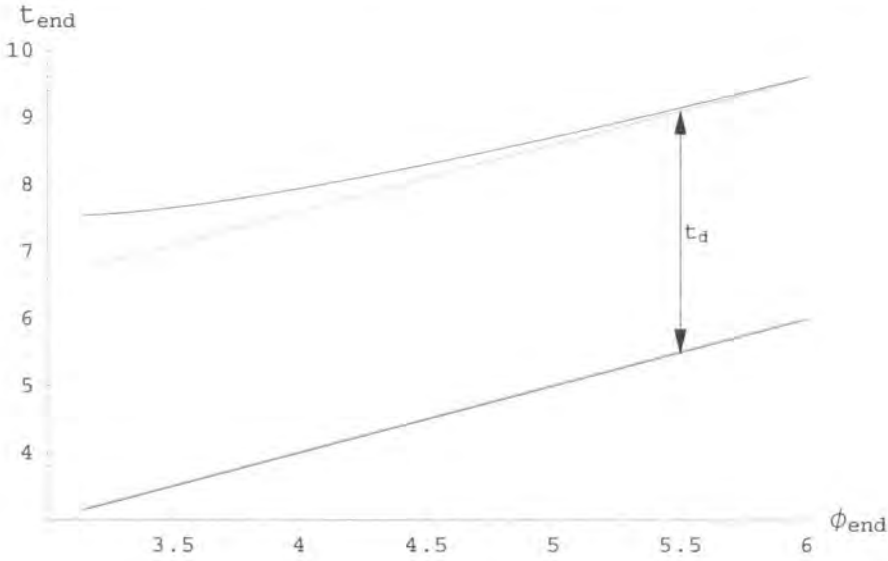
Figure 3.11: Plot of the endpoints of null geodesics which all begin from the same point on the boundary and pass through an AdS-like space time with non-monotonic V_{eff}. The red lines indicate the limits to which the black curves tend as $y \to y_{crit}$

3.11: those with slightly lower y have an effective potential of the form shown as the dashed blue curve in figure 3.12, and travel down to minimum radius r_{p-1}, whereas those with $y \geq y_{crit}$ have minimum radius greater than or equal to r_p, indicated by the dashed red curve. The extra (non-negligible) distance $r_p - r_{p-1}$ travelled by the geodesics results in the time delay seen in the endpoints.

We thus have the situation where we have no geodesics with minimum radius r_q, where $r_{p-1} < r_q < r_p$, and this is where our iterative methods break down. Although we can begin by using one of the methods from earlier to recover $f(r)$ down to $r = r_p$, which corresponds to using the endpoints in the "lower branch" of figure 3.11, we cannot continue past this point. Using method I, say, the final term of the iteration will be:

$$t_p = 2 \int_{r_p}^{\infty} \frac{1}{f(r)\sqrt{1 - y_p^2 \frac{f(r)}{r^2}}} \, \mathrm{d}r \approx A_p + B_p + C_p \qquad (3.4.1)$$

with A_p, B_p and C_p defined as in section 3.1.3. As the next term would involve an integration over the range r_{p-1} to r_p, which cannot necessarily be taken to be small, it cannot be well approximated by the methods we have used previously.
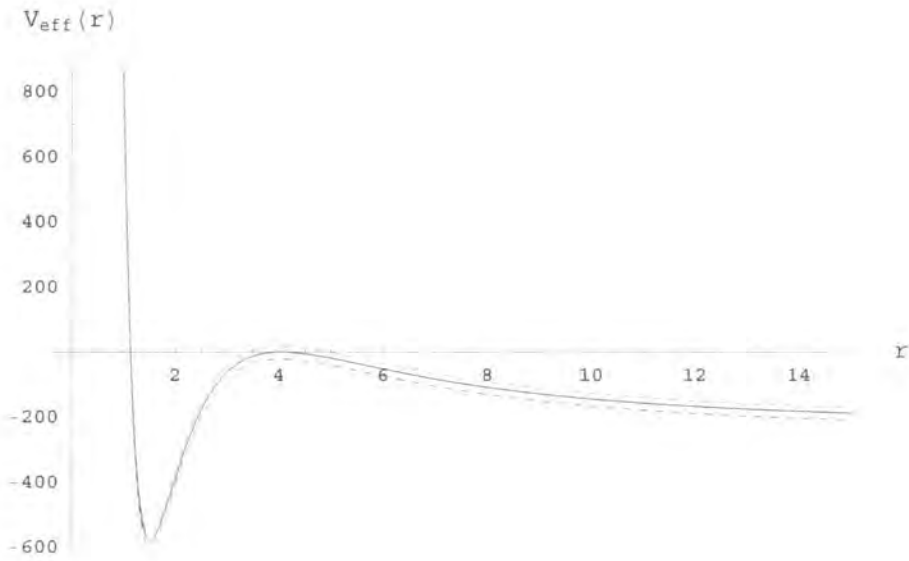
Figure 3.12: Plot of the effective potential for three null geodesics: one with the critical angular momentum, y_{crit} (the solid black curve), one with $y < y_{crit}$ (the lowest curve, dashed blue), and one with $y > y_{crit}$ (top curve, dashed red). The null probe which follows the solid effective potential will go into circular orbit due to the local maximum; the geodesic with slightly lower y (dashed blue line) then has significantly lower r_{min}, and this finite jump in the minimum radius causes the iterative extraction method to break down.

The gap between the upper and lower branches of figure 3.11 tends to a constant time delay, t_d, as $\phi \to \infty$, and it is this which corresponds to the integral we are unable to well approximate:

$$t_d = 2 \int_{r_{p-1}}^{r_p} \frac{1}{f(r)\sqrt{1 - y_{p-1}^2 \frac{f(r)}{r^2}}} \, \mathrm{d}r \qquad (3.4.2)$$

where we note that in the limit $\phi \to \infty$ we have that $y_{p-1} = y_p$.

We are left with the situation where we do not have enough information to carry on recovering $f(r)$ past the rightmost maximum in the effective potential; there is no approximation we could attempt to make without already knowing more about the form of V_{eff}. Although we have the extra endpoint data (i.e. the top branch of figure 3.11), we are unable to use it to extract f(r).

Having discovered this apparent limitation in the extraction of the bulk metric, we should ask ourselves how often we would expect to find metrics which give non-monotonic effective potentials for the null geodesics. In other words, how often do we find spacetimes which allow stable orbits of light rays? Whilst it is very easy to construct metrics by hand which allow this, in physical systems[15] circular orbits of light rays are a rarity. Indeed, recent work by Hubeny *et al.*, [83], indicates that for metrics corresponding to a gas of radiation in AdS, it is impossible for circular null geodesics to occur.

One scenario in which null geodesics can go into circular orbits is around black holes, e.g. in Schwarzschild-AdS. We again cannot recover the entirety of $f(r)$, as the geodesics which pass behind the horizon will not return out to the boundary, and we are left with a reduced spectrum of endpoints from which to recover $f(r)$. The endpoints we do obtain are again those with (normalised) angular momentum above some critical value, and so we can use the above iterative method to recover $f(r)$ down to a certain critical radius (which will be greater than the horizon radius,

---

[15]Admittedly our restrictive case of metrics of the form of (3.1.2) with $C(\tilde{r}) = 1$ are unrealistic, as any metric of this form necessarily has opposite sign pressure and energy density components of the stress tensor. We shall see, however, in chapter 5 how with the addition of spacelike probes one can determine the form of the most general static, spherically symmetric metrics, i.e. (3.1.1).

r_h).

For a final example, we show this explicitly for Schwarzschild-AdS, in which the metric function $f(r)$ is given by (with $R = 1$ as usual):

$$f(r) = 1 + r^2 - \frac{r_h^2}{r^2}\left(r_h^2 + 1\right) \qquad (3.4.3)$$

and the effective potential for null geodesics is given by:

$$V_{eff} = \left(1 + r^2 - \frac{r_h^2}{r^2}\left(r_h^2 + 1\right)\right)\frac{J^2}{r^2} - E^2 \qquad (3.4.4)$$

For a null geodesic to avoid hitting the singularity at $r = 0$, we require $V_{eff} = 0$ for some $r > r_h$, and the closest r for which this will happen will be when the gradient of V_{eff} is also zero. Differentiating (3.4.4) with respect to r, and setting equal to zero gives

$$\frac{2J^2}{r^5}\left(2\left(r_h^2 + r_h^4\right) - r^2\right) = 0 \qquad (3.4.5)$$

which is equal to zero when $r = \sqrt{2}\sqrt{r_h^2 + r_h^4}$. Thus for the case where $r_h = 1$ say, the minimum r which can be probed by the null geodesics is $r = 2$, and hence we can obtain information about the metric function $f(r)$ from $r = \infty$ down to $r = 2$.

The most interesting observation about these scenarios is that in both metrics with small central deformations (i.e. giving a monotonic V_{eff}) and those with very large deformations (i.e. black holes) we can use all the information available to us; although we cannot fully recover the $f(r)$ in the BH setup using our numerical extractor, this is because we do not have any further boundary information to use as input. In the "in between" case of reasonably large deformations, we have the extra information but are currently unable to use it to determine anything further about the metric. Whilst one can argue this is what one should expect, as the discontinuity effectively breaks our chain of working inwards from our known boundary conditions of being asymptotically AdS, the presence of the "upper branch" of information suggests that more details of the metric could be determined.

3.5 Summary

In the above chapter we investigated how the set of null geodesic endpoints (previously shown to be obtainable, in principle, from the field theory) could be used to extract significant information about the bulk. Restricting ourselves to static, spherically symmetric spacetimes, the general metric has two unknown functions of r, only one of which is accessible as the null geodesics are not sensitive to the overall conformal factor of the metric. We demonstrated how they can be used in a remarkably simple manner to extract the single remaining function ($f(r)$), and here we summarise the main ideas behind the method:

- Each null geodesic probes to a certain minimum radius dependent only on the ratio of angular momentum to energy, $y \equiv J/E$, with:

$$y = \frac{r_{min}}{\sqrt{f(r_{min})}} \qquad (3.5.1)$$

- For a static, spherically symmetric bulk, with pure AdS asymptotics, the set of null geodesic endpoints can plotted as a function t_{end} vs ϕ_{end}, such as that seen in figure 3.1, which is continuous for small enough deviations from pure AdS.

- The gradient at any point on the plot immediately yields the corresponding value of y for that geodesic, i.e.

$$\frac{dt_{end}}{d\phi_{end}} = y \qquad (3.5.2)$$

- After noting that for a choice of y sufficiently close to one such that the geodesic remains close to the boundary and is not affected by the central deformation, on can setup an iterative method for determining r_{min} (and hence $f(r_{min})$ via (3.5.1)) by choosing geodesics with smaller and smaller y.

- The iteration is very accurate with only basic approximations, even more so when one avoids introducing $f'(r)$ terms which then require further approximation. This accuracy and overall stability to errors can be explained analytically, and is a result of a suppression rather than simple propagation of error terms in subsequent iterations.

- For large deformations from pure AdS, however, the endpoint information is not continuous, and in the extreme case where a horizon forms, is incomplete. The discontinuity is due to a local maximum in the effective potential for the geodesic at some critical value of y, which results in a circular orbit and an unbounded value for t_{end} and ϕ_{end}. Nonetheless, one can still use the data from geodesics with y larger than this value to extract part of the metric.

In the following chapter, we uncover strong parallels between the ideas presented above and the probing of the bulk by zero-energy spacelike geodesics.

Chapter 4

Probing the bulk geometry II

In the previous chapter we used the relation between insertion points of two-point functions on the boundary and the endpoints of null geodesics to propose a numerical method for extracting the bulk structure. Given the boundary data, we were able to extract one function's worth of information ($f(r)$) about the bulk metric, however, due to the proper length of null geodesics being zero the conformal factor of the metric, $C(r)$, remained undetermined. We now turn to a different relation involving the entanglement entropy of a subsystem of the boundary field theory and the area of minimal surfaces in the bulk, as proposed in [80,81] and discussed in the background chapter. In three bulk dimensions, this minimal surface area is simply the proper length of a zero-energy (i.e. static) spacelike geodesic, and we thus consider in this chapter whether a similar procedure for determining the bulk structure can be constructed using such probes.

Although the setup is very similar to the one considered in the previous chapter, there is an obvious difference between null and spacelike geodesics observable from a plot such as figure 2.8; in pure AdS, the null geodesics are naturally convergent (to the point antipodal to their starting point), whereas this is not the case for spacelike ones. One might then wonder whether this natural divergence of the endpoints would affect the stability of any iterative attempt to reconstruct the bulk involving spacelike geodesics.

We find, however, that this is not the case; one can indeed devise an algorithm to extract the metric, although with some important differences to that for the null

geodesics. We give an analysis of the method, with further details in appendix B.1, and follow this with some numerical examples demonstrating both its stability and high level of accuracy. Significantly, the information one recovers about the metric is complementary to that extracted via the null geodesics; whilst the static spacelike geodesics are not sensitive to the timelike component of the metric, $k(r)$ in (3.1.1), they can be used to extract $h(r)$, which is related to the conformal factor by (3.1.5). Hence one can use the two methods in conjunction to extract both unknown functions $k(r)$ and $h(r)$; this is demonstrated for a toy model of a "star" in AdS_3 in the following chapter.

Before this combining of the two methods, however, we provide further analysis (section 4.2) of how this method involving spacelike geodesics differs from that given in the previous chapter, especially with regard to its stability to errors. Interestingly, whilst in the previous chapter we were able to reformulate the algorithm to eliminate the need for a series expansion approximation of the integral around r_{min} (see section 3.2.2), this same reformulation does not prove as useful here; although one can still rewrite the relevant equations for the spacelike geodesics in similar form, see the end of section 4.2.1, attempting to then use the parabolic approximation leaves the equations without any remaining unknowns! Using a series expansion in this reformulation instead is also problematic, as it leads to the method becoming unstable to errors, completely ruining the extraction.

We conclude the section with a brief comment on how one can confirm the validity of the solution obtained by our numerical algorithms, and also present an intriguing link between the two different types of geodesic (null and static spacelike) that allows the endpoint data for null geodesics in one spacetime to be viewed as the boundary information of static spacelike geodesics in an alternative spacetime, although it is unclear how this duality could be applied in the context of AdS/CFT.

4.1 Spacelike geodesics

We saw in the background chapter how the entanglement entropy of a subsystem of a two-dimensional CFT was related to the proper length of the zero-energy space-

like geodesic connecting the endpoints of that subsystem, via (2.2.21) (see section 2.2.2), shown visually in figure 2.6. For an asymptotically anti-de Sitter spacetime, one then wonders whether one can use this proper length information to extract information about the bulk. For the specific cases of static, spherically symmetric deformations (in three dimensions), the minimal surfaces are still the zero-energy spacelike geodesics seen in the pure AdS case, with a different set of boundary data. Thus we have a scenario much the same as in the previous chapter; we have a set of geodesics which can probe to increasing depths in the bulk, from large r down to the centre at $r = 0$ (or r_h for metrics containing a horizon, see below), by varying the endpoint coordinates on the boundary.

When considering the null geodesics we had two boundary coordinates, t_{end} and ϕ_{end}, as the path travelled both spatially and temporally through the bulk, and by plotting these endpoints we could see qualitatively the difference from pure AdS, where the set of endpoints was a single point. As we are now considering *static* spacelike geodesics, this scenario is slightly different; there is only the angular component to the endpoints, as the geodesics all lie in a constant time slice (and hence $t_{end} = t_{start} \equiv 0$). We still have two pieces of information from the field theory, however, as we also have the proper length for each geodesic. Thus our "endpoints" (or rather our two coordinates) are now $\mathcal{L}$ and ϕ_{end}, and by plotting $\mathcal{L}$ vs ϕ_{end} one can again see the difference from pure AdS, where the corresponding relation is $\mathcal{L}(J) = 2\log(2r_{max}\sin(\frac{\phi_{end}(J)}{2}))$ as computed at the end of section 2.3, see figure 4.1. Note that once again we have one parameter specifying the geodesic path; in the null case it was y, the normalised angular momentum, here it is simply the angular momentum, J, itself.

There is already an interesting difference between the ability of the null and (static) spacelike geodesics to probe the bulk; for larger deformations of the interior, the method involving null geodesics ran into problems extracting the metric past a certain radius, where the effective potential became non-monotonic. This does not
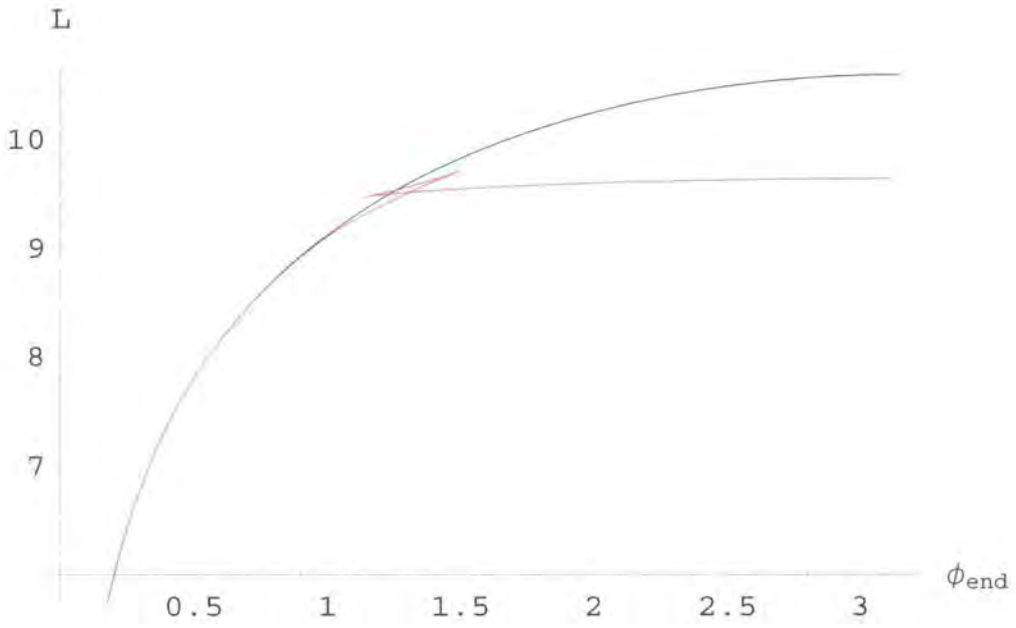
Figure 4.1: A plot of the proper length, $\mathcal{L}$, vs the angular separation of the endpoints, ϕ_{end}, for static spacelike geodesics in an asymptotically AdS spacetime (red, lower curve), and in pure AdS (black, upper curve). When the angular separation is small, the geodesics remain far from the centre, away from the deformation, and hence both curves coincide.

happen for spacelike geodesics with zero energy; working in a metric of the form,[1]

$$ds^2 = -k(r)dt^2 + h(r)dr^2 + r^2 d\Omega_3^2 \tag{4.1.1}$$

from (2.3.7) with E set to zero we have that:

$$\dot{r}^2 - \frac{1}{h(r)}\left(1 - \frac{J^2}{r^2}\right) = 0 \tag{4.1.2}$$

and hence

$$V_{eff} = -\frac{1}{h(r)}\left(1 - \frac{J^2}{r^2}\right) \tag{4.1.3}$$

For V_{eff} to be non-monotonic, one requires $dV_{eff}/dr = 0$ for some r; differentiating (4.1.3) w.r.t r gives:

$$\frac{dV_{eff}}{dr} = \frac{h'(r)}{h(r)^2}\left(1 - \frac{J^2}{r^2}\right) - \frac{2J^2}{r^3 h(r)} \tag{4.1.4}$$

and given that when V_{eff} equals zero (i.e. at $r = r_{min}$) we have that $r_{min} = J$, the first term disappears, leaving us with:

$$\left.\frac{dV_{eff}}{dr}\right|_{V_{eff}=0} = -\frac{2}{r_{min}\, h(r)} \tag{4.1.5}$$

As $r_{min} \neq 0$ (except for the radial geodesic), in order for dV_{eff}/dr to be zero we require $h(r) = \infty$, which only occurs at the horizon, and hence one can always use the static spacelike geodesics to probe infinitely close to this point; thus for the example of a black hole considered in section 3.4, we would be able to probe down to $r = r_h$, the horizon radius.

All this is getting a little ahead of ourselves, however, as we have yet to actually formulate a numerical method for extracting the information; this is done as follows.

4.1.1   Reconstructing the metric

Proceeding as we did in the previous chapter with null geodesics, equation (4.1.2) can be combined with the angular momentum conservation equation $J = r^2\dot{\phi}$ to give:

$$\frac{dr}{d\phi} = \frac{r}{\sqrt{h(r)}}\sqrt{\frac{r^2}{J^2} - 1} \tag{4.1.6}$$

---

[1]As the static spacelike geodesics cannot probe the timelike part of the metric, it makes sense to use this form of the metric, rather than the conformal form used in the previous chapter.

This can then be re-cast as an integral equation along the geodesic path, where we note that the final angular separation will be a function of J only:

$$\phi_{end}(J) \equiv \int_0^{\phi_{end}} \mathrm{d}\phi = 2 \int_{r_{min}}^{r_{max}} \frac{\sqrt{h(r)}}{r\sqrt{\frac{r^2}{J^2} - 1}} \mathrm{d}r \qquad (4.1.7)$$

where r_{min} is the minimum radius obtained by the geodesic, and in the zero energy case is given simply by $r_{min} = J$. Note that by the spherical symmetry of the metric, we can fix the starting point of the geodesic to an arbitrary value, and we choose $\phi_{start} = 0$. As the metric is divergent at the boundary $r = \infty$, we introduce a cut-off r_{max} and restrict ourselves to the region $r < r_{max}$.[2] We also have that the proper length of the geodesic (also dependent only on J) is given by:

$$\mathcal{L}(J) = 2 \int_{r_{min}}^{r_{max}} \frac{\sqrt{h(r)}}{\sqrt{1 - \frac{J^2}{r^2}}} \mathrm{d}r \qquad (4.1.8)$$

We thus have two equations, (4.1.7) and (4.1.8) (analogous to equations (3.1.7) and (3.1.8) in the previous chapter) with which to determine the function $h(r)$ at each r.

Given that the spacetime in which we are working is asymptotically AdS, we can begin as before by taking $h(r) \approx (r^2 + 1)^{-1}$ for $r \geq r_n$ for some r_n which can be arbitrarily large (but still below the cut-off r_{max}). Thus all static spacelike geodesics with angular momentum $J \geq J_n \equiv r_n$ will remain sufficiently far from the central deformation $p(r)$ such that they remain undisturbed by its effects, and in the limiting case $J = r_n$ we can write:

$$\phi_n = 2 \int_{r_n}^{r_{max}} \frac{1}{r\sqrt{r^2 + 1}\sqrt{\frac{r^2}{r_n^2} - 1}} \mathrm{d}r \qquad (4.1.9)$$

$$= \frac{\pi}{2} - \arctan\left(\frac{2r_n^2 + (r_n^2 - 1) r_{max}^2}{2r_n \sqrt{r_{max}^4 - (r_n^2 - 1) r_{max}^2 - r_n^2}}\right) \qquad (4.1.10)$$

$$\approx \frac{\pi}{2} - \arctan\left(\frac{r_n^2 - 1}{2r_n}\right) \quad \text{for } r_{max} \gg r_n \qquad (4.1.11)$$

where $\phi_n = \phi_{end} - \phi_{start}$, and is the length of section B of the boundary in figure 2.6. Hence from the ϕ endpoints, which are specified by our choice of region A in

---

[2]This cut-off corresponds to the ratio between the UV cutoff (or equivalently the lattice spacing) in the CFT and the total length of the system: $r_{max} \sim L/a$, see section 2.2.2.

the CFT, we can determine r_n and we have that $h(r_n) = (r_n^2 + 1)^{-1}$. As in the null geodesic case, this is then the starting point for an iterative method which will recover the metric from r_n down to zero (in the non-singular case).

The naive way in which to continue (supposing we were ignorant of the approach taken in the previous chapter; indeed, a similar approach could have been taken there) is by taking a slightly smaller choice of minimum radius, $r_{n-1} < r_n$, and splitting up the relevant integrals in (4.1.7) and (4.1.8) into two pieces, one from r_{n-1} to r_n and one from r_n to r_{max}. These integrals could then both be well approximated, the first by taking a series expansion about the minimum radius r_{n-1}, and the second by approximating the spacetime as pure AdS, as in (4.1.9). We would thus end up with two simultaneous equations which could be solved to give r_{n-1} and $h(r_{n-1})$, and could then proceed in a similar fashion to obtain the the entire bulk metric, to an arbitrary level of accuracy determined by our choice of step size in r (which is determined by our choice of boundary region $\phi_{end} - \phi_{start}$). However, it turns out there is a significant problem with this setup which prevents it being applied in practice; the iterative process is unstable, with any errors in the estimates for r_{n-i} and $h(r_{n-i})$ leading to greater errors in subsequent steps. This results in a rapid divergence of the estimate from the actual metric, and the iteration quickly breaks down.

This unstable setup, where we solve for the two unknowns simultaneously at each step can be avoided entirely, however, simply by applying what we observed in section 3.1.1. The scenario we have above, with the two equations (4.1.7) and (4.1.8) is very closely related to the situation we found ourselves in with the null geodesics. We have two unknowns, r_{min} and $h(r_{min})$, and we have already noted that for the static spacelike geodesics, $r_{min} = J$, the angular momentum of the geodesic. Thus if one could somehow determine J from the "endpoint" data, one would immediately have r_{min}, and one could then easily proceed to recovering $h(r)$. The natural question to then ask is: does the gradient of the spacelike "endpoints" provide us with any further information. We find that indeed it does, in exactly the same way as it did previously, as we now show explicitly.

Consider the equations (4.1.7) and (4.1.8) above; they both have very similar

forms, and there is in fact a strikingly simple yet powerful relation between the two quantities, $\mathcal{L}$ and ϕ_{end}. Taking the derivative of both with respect to J, the angular momentum, we have that:

$$\frac{d\mathcal{L}(J)}{dJ} = 2 \int_{r_{min}}^{r_{max}} \frac{J\sqrt{h(r)}}{r^2 \left(1 - \frac{J^2}{r^2}\right)^{3/2}} \, dr - \left(\frac{2\sqrt{h(r)}}{\sqrt{1 - \frac{J^2}{r^2}}}\right)\Bigg|_{r=r_{min}} \frac{dr_{min}}{dJ} \qquad (4.1.12)$$

and

$$\frac{d\phi_{end}(J)}{dJ} = 2 \int_{r_{min}}^{r_{max}} \frac{\sqrt{h(r)}}{r^2 \left(1 - \frac{J^2}{r^2}\right)^{3/2}} \, dr - \left(\frac{2 J \sqrt{h(r)}}{r^2 \sqrt{1 - \frac{J^2}{r^2}}}\right)\Bigg|_{r=r_{min}} \frac{dr_{min}}{dJ} \qquad (4.1.13)$$

Using the fact that $J = r_{min}$, and noting that the divergent part of the integral cancels with the divergent second term in each equation[3], we can see that the two equations are identical upto a factor of J, and we therefore have that:

$$\frac{d\mathcal{L}(J)}{dJ} = J \frac{d\phi_{end}(J)}{dJ} \qquad (4.1.14)$$

which can be rewritten as

$$\frac{d\mathcal{L}}{d\phi_{end}} = J = r_{min} \qquad (4.1.15)$$

Thus we have the remarkable fact that the minimum radius[4] of the static spacelike geodesic connecting any two points on the boundary is immediately calculable from the gradient of a plot of the proper length, $\mathcal{L}$ versus angular separation ϕ_{end} (figure 4.1). The form of (4.1.15) and its obvious similarities with (3.1.20), where the gradient of the null geodesic endpoints yielded y, suggests a possible link between null and spacelike geodesics (and in particular between the time taken t_{end}^{null} and the proper length $\mathcal{L}_{space}$), and this comparison is further investigated in section 4.2.4.

Returning to the present question of reconstructing the bulk, (4.1.15) immediately provides us with one of the two unknowns we need at each step, and leaves

---

[3]See the equivalent calculation in section 3.1.1.

[4]Note that equation (4.1.15) holds in any static, spherically symmetric spacetime; in those with less symmetry, such as angular variation of the metric as well as radial, one finds that the gradient $\frac{d\mathcal{L}}{d\phi_{end}}$ gives the final angular momentum of the geodesic, but as this will not be conserved, it is not necessarily equal to r_{min}, see chapter 6.

us with only needing to calculate $h(r_{min})$. This can be done iteratively as in the null case, beginning at large r, by splitting up (4.1.7) (or (4.1.8)) and taking various approximations to each part of the integral. Whilst there are still issues of stability to errors to consider (as we mention briefly below and examine in detail in section 4.2.1), we note that this does now lead to a working metric extractor, the full details of which are given in Appendix B.1.

The relation (4.1.15) also allows one to more precisely determine the radii at which the metric deviates from pure AdS, directly from the endpoints and without any knowledge of $h(r)$. We can now explicitly check the radii at which the pure AdS assumption holds for a given tolerance, as we can now determine the value of r_{min} corresponding to each ϕ separation of the endpoints, and hence plot r_{n-i} vs ϕ_{n-i} for each i. In pure AdS, we know that the relation is given analytically by $r_{min} = \cot(\frac{\phi_{end} - \phi_{start}}{2})$, and at small enough angular separation, the two plots should coincide (this is also of course true on the plot of $\mathcal{L}$ vs ϕ_{end}, see figure 4.1).

An interesting point which is worth mentioning now concerns the series expansion of the relevant integral around r_{min}. Recall that in the original formulation of the null method (section 3.1.3), taking the lowest order expansion in (3.1.27) introduced an $f'(r_{n-i})$ term, which then also required approximating. Here, because there is no $h(r)$ term in the denominator of (4.1.7), we have that to lowest order:

$$2 \int_{r_{n-i}}^{r_{n-i+1}} \frac{\sqrt{h(r)}}{r\sqrt{\frac{r^2}{r_{n-i}^2} - 1}} \, dr \approx 2\sqrt{2\, h(r_{n-1})} \sqrt{\frac{r_{n-i+1} - r_{n-1}}{r_{n-1}}} \qquad (4.1.16)$$

and there is no $h'(r_{n-i})$ term present. Thus we can avoid introducing a gradient term if we so wish, although in practice one finds the better approximation offered by taking a next-to-lowest order expansion is worth the extra approximation of $h'(r)$ then needed.

At this juncture one might well ask why we haven't immediately continued to develop the method as we did in the previous chapter, where we reformulated the equations to allow for better approximations to be used; it turns out that one cannot use the parabolic approximation as it leaves the equation with no unknowns, and with a series approximation, this reformulation ruins the stability of the iteration to errors (see section 4.2.1)! Hence one has to be very careful, as although the iterative

methods for the two types of geodesic are seemingly very similar (and thus one might expect them to be similarly stable to any errors), this is not the case due to some subtle differences in their behaviour. Indeed, the situation is somewhat more delicate now; the method is in fact unstable if one uses a linear approximation to the central parts of the integral (i.e. the trapezium rule), even though this worked fine in the null case. One instead has to use (at least) a second order polynomial fit in order for the errors to be eliminated. Before giving an analytical explanation for why this is the case, we first demonstrate numerically the stability and accuracy of the method as described in appendix B.1 in a set of examples; further discussion and analysis follows in section 4.2.1.

4.1.2 Examples

To illustrate the procedure for metric extraction, we begin by considering some examples of deformations of the pure AdS metric. In the cases considered we have taken the proper length and angular separation of the endpoints to be known from the relevant field theory, and taken a linear step size in J (and hence r_{min}). The method of Appendix B.1 is then applied for a variety of step sizes, and the resulting estimates for $h(r)$ are plotted alongside the actual curve.[5] The three deviations from pure AdS we consider are the following:

$$1/h_1(r) = 1 + r^2 - \frac{4\,r^2}{(r^2 + 1)(r^2 + 8)} + \frac{3r\sin(2\,r)}{r^4 + 1} \qquad (4.1.17)$$

$$1/h_2(r) = 1 + r^2 + \frac{10\sin^2(3\,r)}{r^3 + 1} \qquad (4.1.18)$$

$$1/h_3(r) = 1 + r^2 + \frac{10\sin^2(10\,r)}{r^3 + 1} \qquad (4.1.19)$$

where each gives a non-singular, asymptotically AdS spacetime. These functions were chosen as tests of the extraction method because they provide clearly visible deviation from the pure AdS metric of $h(r) = (r^2 + 1)^{-1}$. The first example also corresponds to one used in section 3.1.5 (c.f. equation (3.1.39)) in the null geodesic

---

[5]To aid with the visualisation, and given the comparisons we wish to make with the previous chapter, the example functions are defined as $1/h(r) = 1 + r^2 + \dots$, and are plotted as such.

Step size	α (4)	β (1)	γ (8)	χ (3)	η (2)	λ (1)
0.1	3.75	0.70	7.99	3.03	1.99	1.00
0.05	3.81	0.79	7.95	3.02	1.99	1.00
0.01	3.94	0.85	8.19	3.01	2.00	1.00
0.005	3.95	0.93	8.01	3.01	2.00	1.00

Table 4.1: Best fit values (to 2 d.p.) for the $h_{\text{fit}1}(r)$ parameters α, β, γ, χ, η and λ, with the actual values indicated in brackets.
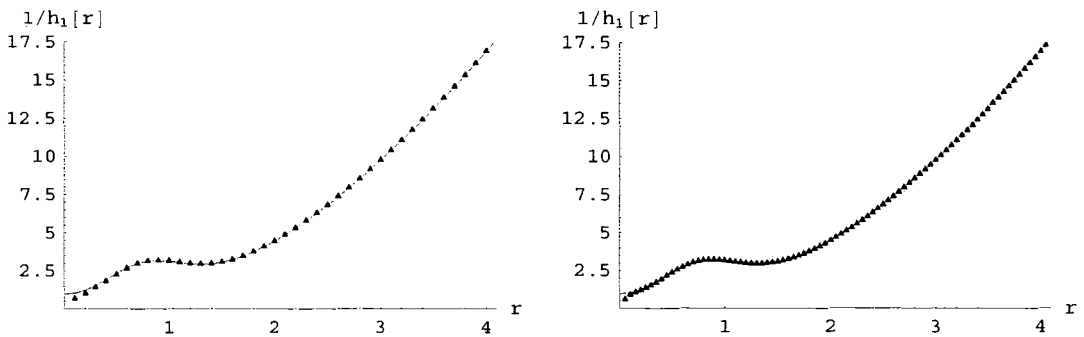
Figure 4.2: The data points for the largest two step size estimates for $h_1(r)$, compared with the actual curve (in blue). Whilst both give good estimates to the curve, the step size of 0.1 (left) deviates at a higher r than when using a step size of 0.05 (right).

based method for extracting the bulk information, and despite the similarities between $h_2(r)$ and $h_3(r)$, we shall see a noticeable difference in the accuracy of their extraction for larger step sizes.

For the first example we use four choices of step size in r, namely $\triangle r \approx 0.1, 0.05, 0.01$ and 0.005, and compare the accuracy of the generated curves to the actual function; this is done by considering best fits to the numerical estimates, obtained by using a non-linear fit to the following function:

$$1/h_{\text{fit}1}(r) = 1 + r^2 - \frac{\alpha\, r^2}{(r^2 + \beta)(r^2 + \gamma)} + \frac{\chi r \sin(\eta r)}{r^4 + \lambda} \qquad (4.1.20)$$

to give values for the various parameters. The results are shown in Table 4.1, with the corresponding data points plotted in figures 4.2 and 4.3.

From Table 4.1, which contains the data for the estimates of $h_1(r)$ we see that
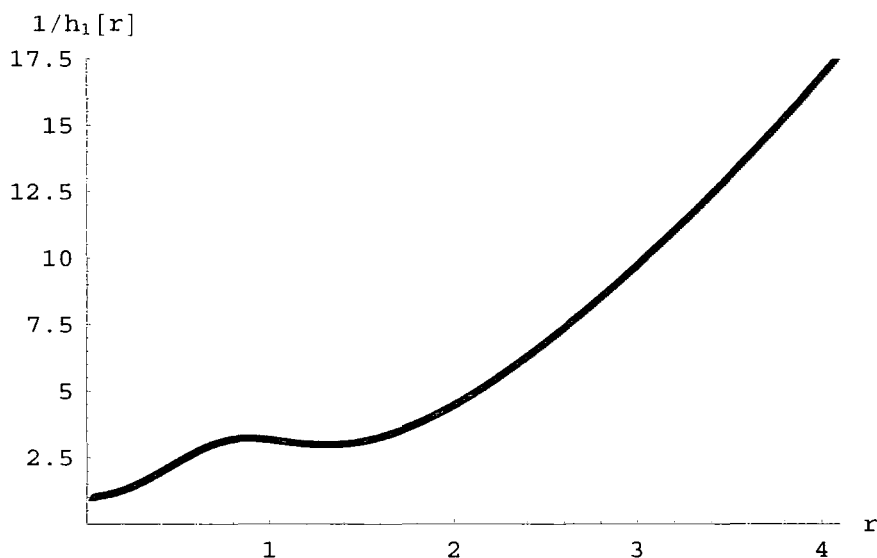
Figure 4.3: The data points for the next-to-smallest step size estimate for $h_1(r)$, compared with the actual curve (in blue). The fit here appears very good even close to $r = 0$, however, Table 4.1 shows that we still need to go to a smaller step size in order to accurately extract values for α, β and γ.

there is a very good fit to the actual values of the six parameters from our non-linear fit (4.1.20), even at the largest step size we consider. Indeed, by eye it is hard to tell any difference between the accuracy of the estimates except at very small radii. This is mainly due to the relatively slow variation of $h_1(r)$ with r, which ensures the various approximations we take in order to produce the estimates remain good even for the larger step sizes. Whilst it appears that taking a smaller step size is rather superfluous, it should be noted that the finer structure parameters (namely α, β and γ) would need the smaller step size data in order to be determined to a high level of confidence. Our choice of non-linear fit function is also rather specifically chosen to match the example; if one did not know beforehand the form of $h_1(r)$ one would want to take smaller step size estimates in order to obtain data down as close to $r = 0$ as possible (as is discussed at the end of the section), to ensure that any finer structure was not being masked, and also as a check on the validity of the previous estimate.

We see similar behaviour in the second example, where we have chosen a slightly more fluctuating function to attempt to recover. Here we use the three largest
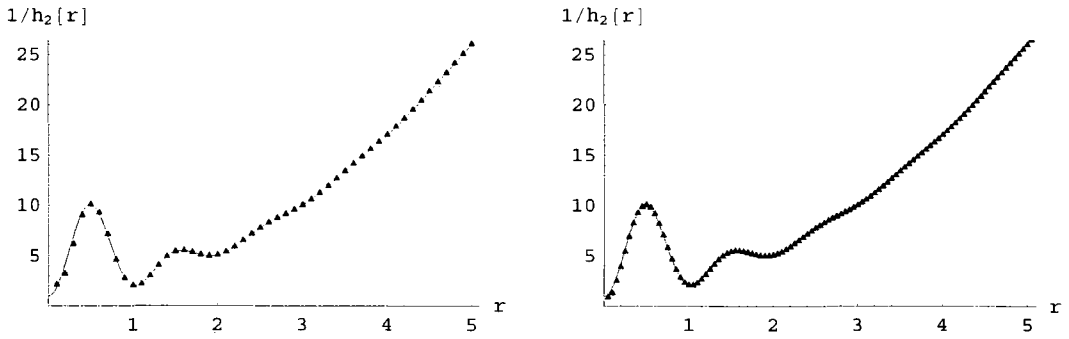
Figure 4.4: The data points for the largest two step size estimates for $h_2(r)$, compared with the actual curve (in blue). Despite the larger deviation from pure AdS than in example 1, both the estimates here provide good fits to the curve.

Step size	χ (10)	η (3)	λ (1)
0.1	10.32	2.99	1.06
0.05	10.08	3.00	1.01
0.01	10.05	3.00	1.01

Table 4.2: Best fit values (to 2 d.p.) for the $h_{\text{fit2}}(r)$ parameters χ, η and λ, with the actual values indicated in brackets.

choices of step size in r, and the data generated in each estimate is shown in figures 4.4 and 4.5, where we also include a plot of the actual function $h_2(r)$ as comparison.

We can again use a non-linear fit to evaluate the estimate; in this case we use a function of the form:

$$1/h_{\text{fit2}}(r) = 1 + r^2 + \frac{\chi \sin^2(\eta\, r)}{r^3 + \lambda} \qquad (4.1.21)$$

and the results are shown in Table 4.2.

Thus far everything is progressing as expected: the smaller step sizes are producing closer fits to the curve, and better estimates for the values of the various parameters. In these first two examples, we even have that the largest step sizes produce good fits to the curves; do we ever see a large increase in accuracy over our choice of step size? If we consider the third example (which was obtained by increasing the value of η from the second example), where the function oscillates more wildly at low r, we do see a significant improvement in the estimates as the
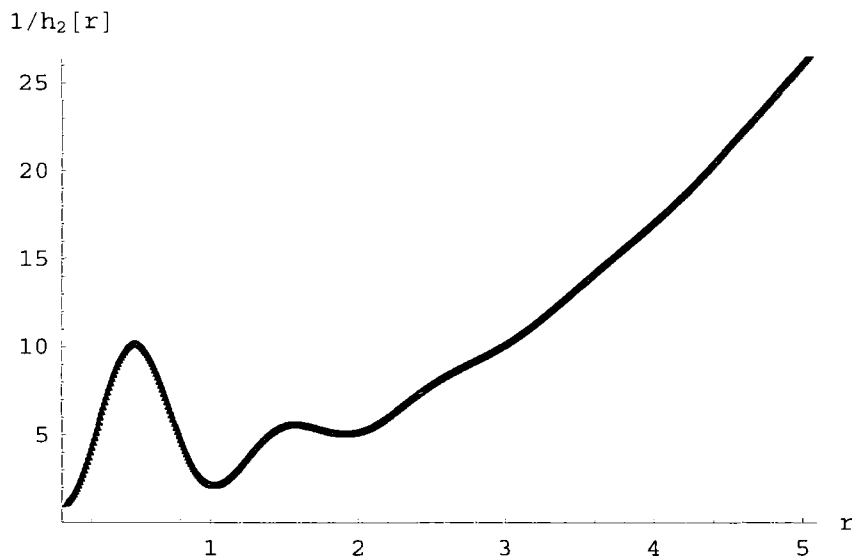
Figure 4.5: At a step size of 0.01, the estimate data for $h_2(r)$ matches the actual curve (in blue) almost exactly, even close to $r = 0$.

Step size	χ (10)	η (10)	λ (1)
0.1	7.49	8.03	0.29
0.05	11.60	10.00	1.25
0.01	9.96	9.99	0.99

Table 4.3: Best fit values (to 2 d.p.) for the $h_{\text{fit3}}(r)$ parameters χ, η and λ, with the actual values indicated in brackets.

step size decreases. Proceeding as before, we see that for the largest step size of 0.1, the method has difficultly in following the rapid oscillations at low r; this is then significantly improved upon in the subsequent estimates, as shown in figures 4.6 and 4.7, and in the non-linear fit data given in Table 4.3.

As expected, the smaller step size again produces a closer fit to the actual curve, however, in this third example, the largest step size fail to give accurate data for the unknowns χ, η and λ, although it does make a reasonably close fit to the curve until the iterative process breaks down.

Finally, one should comment on the fact that the deviation of the estimate from the actual curve does not apparently prevent the iteration from continuing to give
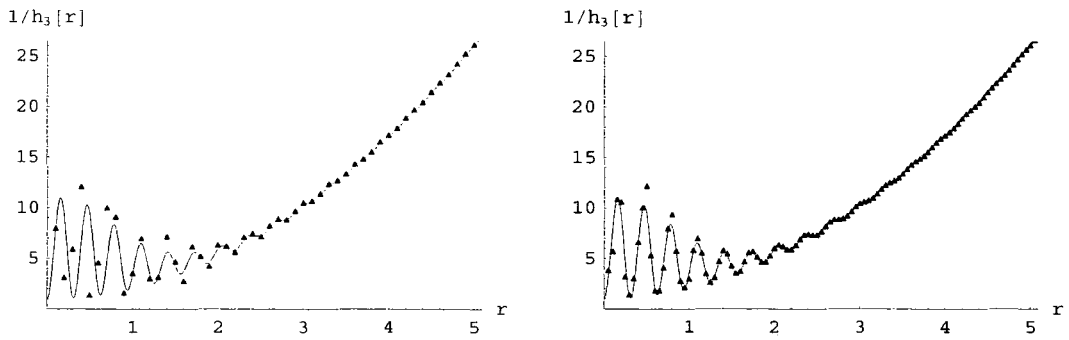
Figure 4.6: The data points for the largest two step size estimates for $h_3(r)$, compared with the actual curve (in blue). The reduction in step size from 0.1 (left) to 0.05 (right) gives a marked improvement in the fit of the points to the curve at low r.
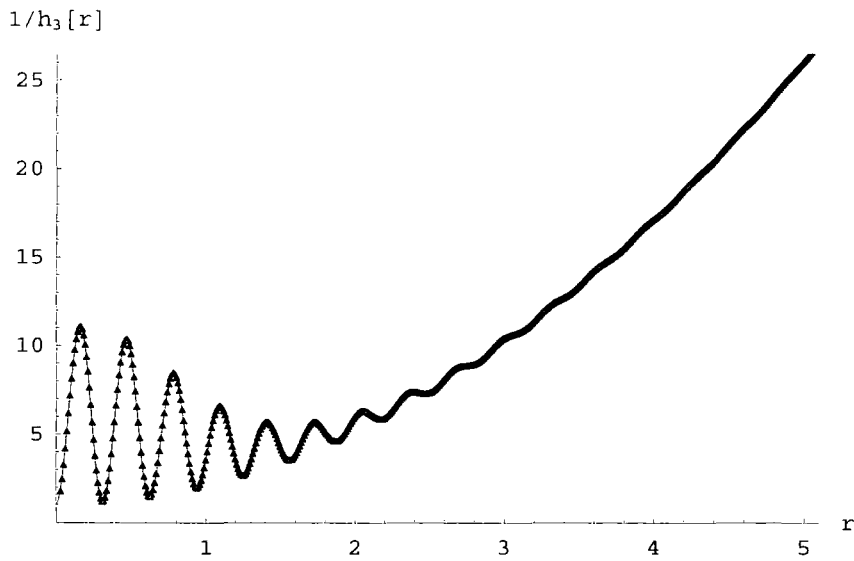
Figure 4.7: The data points for the smallest step size estimate for $h_3(r)$, compared with the actual curve (in blue). This level of precision gives a very good fit to the curve, and this is mirrored in the highly accurate estimates for the function parameters, given in Table 4.3

sensible looking (although erroneous) values in subsequent steps. Whilst appearing to allow for an incorrect determination of the metric, applying the checks described in section 4.2.3 (reconstructing the field theory data using the metric estimate) will quickly highlight any areas in which the estimate for $h(r)$ has deviated from the correct function. As stated before, this merely indicates that the step size in r was too great for the iterative method to properly be effective in extracting the information using the approximations chosen in Appendix B.1. Aside from simply reducing the step size, or using better approximations (such as at each step creating an interpolating function estimate for $h(r)$ using the already determined data), there are other possible resolutions of this problem to further optimise the extraction. One could take either a non-linear step size in r to include more terms near $r = 0$, or simply take appropriately varying step sizes depending on the fluctuations of the metric; where the metric is varying rapidly with r the step size could be reduced. Thus by making several passes, reducing the step sizes at appropriate r each time, the estimate of $h(r)$ can be significantly improved without considerably increasing the computation time.

The third example above has shown that in wildly fluctuating spacetimes one needs smaller step sizes in order to guarantee accuracy of the estimate for $h(r)$ down to small r. If we significantly increase the frequency of the oscillations, how does this affect our estimate? One would naturally expect that for large enough oscillations, the linear approximation of the gradient $h'(r)$ used in the extraction would introduce significant errors, especially around the turning points of $h(r)$, which may ruin the subsequent estimate. We shall see in the next section how the introduction of errors affects the estimate, and how the propagation of such errors are suppressed in subsequent steps by the iterative algorithm, however, to conclude this examples section we give some brief numerical observations. The two curves shown in figure 4.8 come from considering modifications to example 3 where the $\sin^2(10\,r)$ term is replaced by first $\sin^2(20\,r)$ and then $\sin^2(30\,r)$; one still obtains a relatively good fit to the curve using the smallest step size, although in the more rapidly oscillating case the fit does deviate away from the correct curve, especially near the peaks at low r, as was predicted.
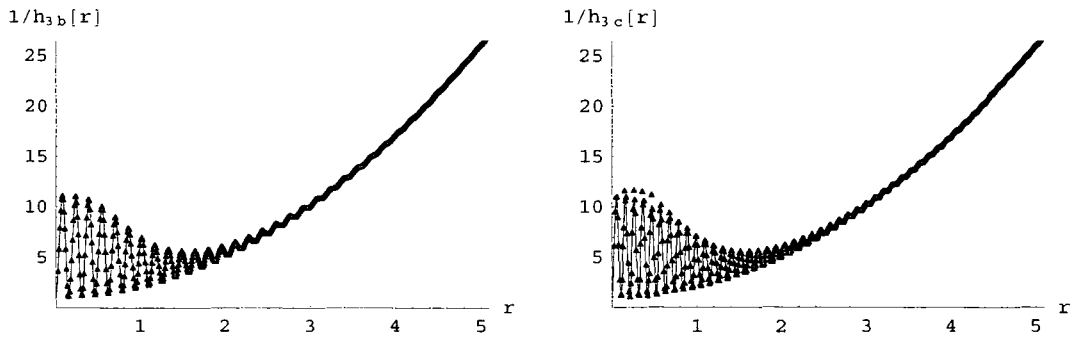
Figure 4.8: Plots of $h_3(r)$ with the $\sin^2(10\,r)$ term replaced by $\sin^2(20\,r)$ (left) and $\sin^2(30\,r)$ (right), along with estimates generated with a step size of 0.01. Interestingly, whilst sufficiently increasing the frequency of the metric oscillations does reduce the depth to which the metric is accurately extracted, it does not adversely affect the accuracy of the fit to that point.

Perhaps most importantly, the obtained estimate is still accurate until one reaches the deep interior where the amplitude of the oscillations is large. Thus even in metrics with a large and rapidly varying interior, one can use a reasonable step size to extract the metric with confidence down to a fairly close distance to the centre. After checking the estimate by recreating the field theory data, one can then continue the extraction from that point with better approximations, and a smaller step size (beginning slightly further out than the final terms so as to give some overlap with the initial estimate and check the consistency of the estimates) in order to fully reconstruct the metric function.

In any case, the more exotic spacetimes one might wish to consider may not have only one independent metric function $h(r)$ to extract, and in order to fully determine the metric in these more general cases, one would need to consider a combination of the methods involving null and spacelike probes, as is detailed in chapter 5.

4.2 Further discussion

Despite the similarities between the two alternative approaches to extracting bulk information demonstrated in this and the previous chapter, the are some differences, and for completeness we provide an error analysis of the stability of the spacelike

geodesic method (c.f. the analysis in section 3.3).

As we have already seen, both sets of boundary data directly yield information about the connecting geodesic (and hence the bulk) via their gradients; in each case one recovers the (normalised) angular momentum. However, in the spacelike case, this then immediately allows us to determine r_{min} for each geodesic and so in the numerical iterations one is solving for only one unknown (namely $h(r_{min})$) at each step. This is in contrast to the null case, where the endpoint gradient gave us $y = r_{min}/\sqrt{f(r_{min})}$, leaving us to solve for both r_{min} and $f(r_{min})$ at each step.

This has a number of interesting consequences with regards to our approximations, as we shall see. Firstly, we note that if the information from the field theory (i.e. the plot of $\mathcal{L}$ vs ϕ_{end}) is assumed to be free from error, then our estimates for the minimum radius at each step must also be completely accurate. Hence any errors which enter into our estimate arise solely in the $h(r_{n-i})$ terms - contrast this with the null case where both our estimates for r_{n-i} and $f(r_{n-i})$ could be inaccurate.

4.2.1 Error analysis

We wish to consider how the propagation of errors through our new iterative algorithm might be different to the behaviour seen in the error analysis of the previous chapter. Suppose then that at some point in the extraction, r_{m+1} say, our estimate $\bar{h}_{m+1}$ for the metric has picked up an error from one of the approximations we introduced, which we can write as (we introduce the error term in this form to simplify the resulting algebra):

$$\sqrt{\bar{h}_{m+1}} = \sqrt{h(r_{m+1})} + \epsilon \qquad (4.2.1)$$

Our estimate for $h(r_m)$, which we denote $\bar{h}_m$ can then be calculated for the next step of the iteration by considering various approximations to equation (4.1.7) (our integral for ϕ):

$$\phi_m = 2\sqrt{2\bar{h}_m}\sqrt{\frac{r_{m+1} - r_m}{r_m}} + \sqrt{\bar{h}_{m+1}}\left(\frac{r_{m+2} - r_{m+1}}{r_{m+1}\sqrt{\frac{r_{m+1}^2}{r_m^2} - 1}}\right) \qquad (4.2.2)$$

$$+ \text{ error-free terms} \qquad (4.2.3)$$

where we have used the lowest order approximation for the series expansion (in-

troduced in section 4.1.1) for simplicity[6]. In this case, most terms are error-free; the only term involving $\bar{h}_{m+1}$ is from our approximation of the interval from r_{m+1} to r_{m+2} via the trapezium rule (the effect of using a higher order approximation is discussed below). We can now substitute in for $\bar{h}_{m+1}$ from (4.2.1), and rearrange to solve for $\bar{h}_m$:

$$\sqrt{\bar{h}_m} = Z - \sqrt{\bar{h}_{m+1}} \left(\frac{(r_{m+2} - r_{m+1}) \, r_m^{3/2}}{2\sqrt{2} \, r_{m+1} \sqrt{r_{m+1} - r_m} \sqrt{r_{m+1}^2 - r_m^2}} \right) \qquad (4.2.4)$$

$$= \sqrt{h(r_m)} - \epsilon \left(\frac{(r_{m+2} - r_{m+1}) \, r_m^{3/2}}{2\sqrt{2} \, r_{m+1} \sqrt{r_{m+1} - r_m} \sqrt{r_{m+1}^2 - r_m^2}} \right) \qquad (4.2.5)$$

where we have defined $Z \equiv (\phi_m - \text{error-free terms})$, and then used the fact that the combination of all the error-free terms is simply $\sqrt{h(r_m)}$. Now by taking the step size in r to be linear, i.e. such that both $r_{m+2} - r_{m+1} = r_{m+1} - r_m = \sigma$, we have that

$$\sqrt{\bar{h}_m} = \sqrt{h(r_m)} - \epsilon \left(\frac{r_m^{3/2}}{2\sqrt{2} \, r_{m+1} \sqrt{r_{m+1} + r_m}} \right) \qquad (4.2.6)$$

and hence we see that for the step size tending to zero, the error term does not vanish, it tends to the constant $\epsilon_m \to -\epsilon/4$ as $\sigma \to 0$. This mirrors what we saw in the null case (in our analysis of the error in $\bar{r}_m$), however, there we found the coefficient of the error to be ≈ -0.81. One could take this to suggest that if the null geodesic method was stable, then the spacelike one should also be so; given the differences in the two algorithms, however, we need to make a more thorough analysis of the propagation of errors than a simple comparison of this coefficient.

The reason the coefficient does not vanish in (4.2.6) is because the factor of σ in the numerator one might have hoped would cause the suppression has been cancelled by a similar factor in the denominator. However, we note that it is heavily suppressed at small r, where the numerator dominates, and is approximately constant at large r; for a linear step size $\sigma = 0.01$, the coefficient of the error is plotted against r in figure 4.9.

---

[6]Whilst in the method given in appendix B.1 we use a next to lowest order expansion, it suffices here to demonstrate that the method is stable at lowest order; although the introduction of the $h'(r)$ term would also involve the error from $\bar{h}_{m+1}$ in its approximation, it is sufficiently suppressed at small step size to not affect the stability.
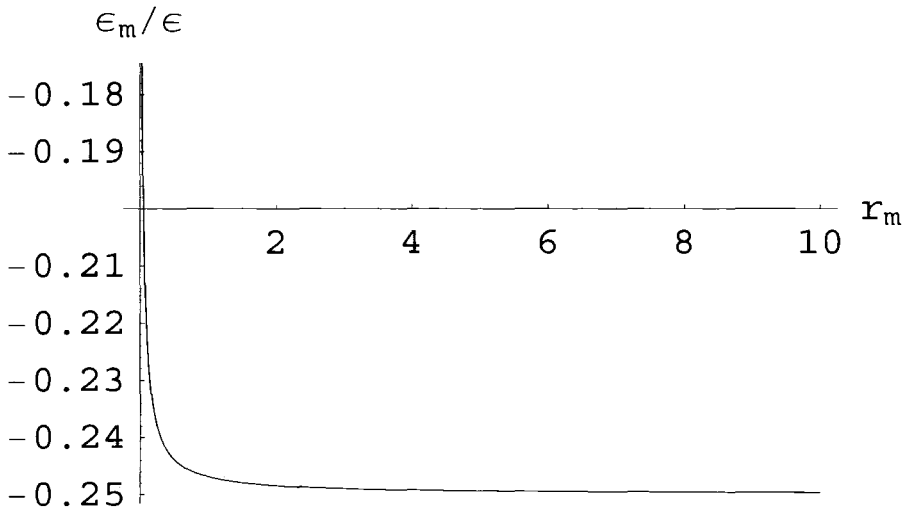
Figure 4.9: Introducing an error of order ϵ at step $m + 1$ results in a smaller error at step m which (for non-zero step size) has a coefficient that depends on the radius, although for r_m large it is approximately constant. Interestingly, this coefficient of the error is smaller than that seen in our analysis of the method involving null geodesics.

Using a second order polynomial fit in (4.2.2) instead, given by Simpson's rule (as in the appendix), does not eliminate this term, it simply reduces the expression for the new error in (4.2.6) by a factor of 2/3, assuming a linear step size in r.

As the error is not suppressed in the limit $\sigma \to 0$, this could result in an instability from the accumulation of the error terms over hundreds of iterations; to analyse this we need to consider the size of the error after k subsequent iterations, which is given by:

$$\epsilon_{m-(k+1)} = -\left(\frac{\epsilon_{m-k}}{4} + \sum_{j=0}^{k-1} \frac{\epsilon_{m-j}}{2\sqrt{k+1-j}} + \epsilon_{m-(k+1)}^{approx} \right) \qquad (4.2.7)$$

in the limit $\sigma \to 0$, where we have also included a constant additional error at each step (denoted $\epsilon_{m-(k+1)}^{approx}$ as we did in (3.3.9) in the equivalent expression in the error analysis of the previous chapter. As shown in figure 4.10a, where the error $\epsilon_{m-(k+1)}$ is plotted against the number of steps with $\epsilon_{m-(k+1)}^{approx} = 0$, despite not being suppressed by σ, the error still appears to die away to zero after a sufficient number of steps. Even including a non-zero constant additional error at each step does not prevent this suppression, see figure 4.10b.
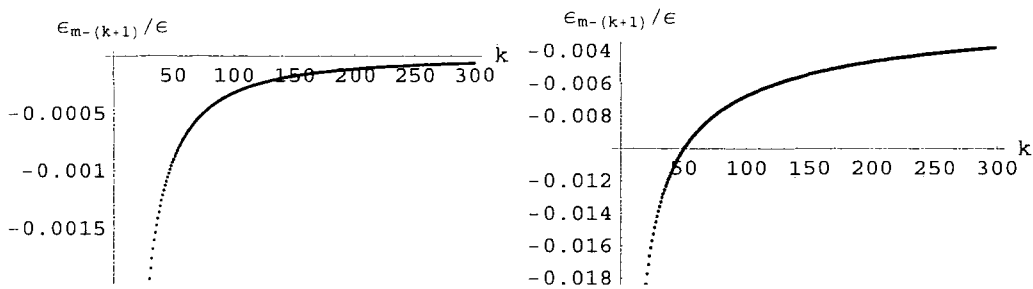
Figure 4.10: Plots of the error term $\epsilon_{m-(k+1)}/\epsilon$ against the number of steps k with initial error $\epsilon = 1/10$. The left hand plot shows the behaviour for $\epsilon^{approx}_{m-(k+1)} = 0$, i.e. purely error propagation with no additional contributions. In the right hand plot, we have assumed a constant additional error at each step, $\epsilon^{approx}_{m-(k+1)} = 1/10$. In both cases, the overall error is continually suppressed as k becomes large.

Earlier (in section 4.1.1), however, it was claimed that the method was *unstable to errors* when only a linear approximation to the central parts of the integral for ϕ was used; how does this reconcile with the above? In figure 4.11, which shows an attempt to recover a sample metric with this setup, we see that the metric extractor does indeed break down if the trapezium rule is used in the approximations; although the estimate does converge towards $h(r)$ initially, there is a sudden divergence which severely corrupts the estimates at subsequent iterations.

Although given the simplicity of our model for the error, one might have expected the actual numerical behaviour to be more complex, we can still look at what may have caused the breakdown and why it wasn't predicted by our error analysis. Indeed, what is perhaps most important is to ascertain why the null method was stable with this trapezium rule approximation, and why the spacelike method is not. Our analysis thus far has shown strong parallels between the propagation of the errors in the two different cases, and we must examine why our basic expressions for the errors in equations (3.3.9) and (4.2.7) might be misleading.

One natural explanation for this is because our formula for the error, (4.2.7), does not correctly incorporate the continual errors arising from our approximations of the integrals. Whilst we have attempted to include this by adding a constant term $\epsilon^{approx}_{m-(k+1)}$ at each step, we find that in fact a better estimate of such a term is
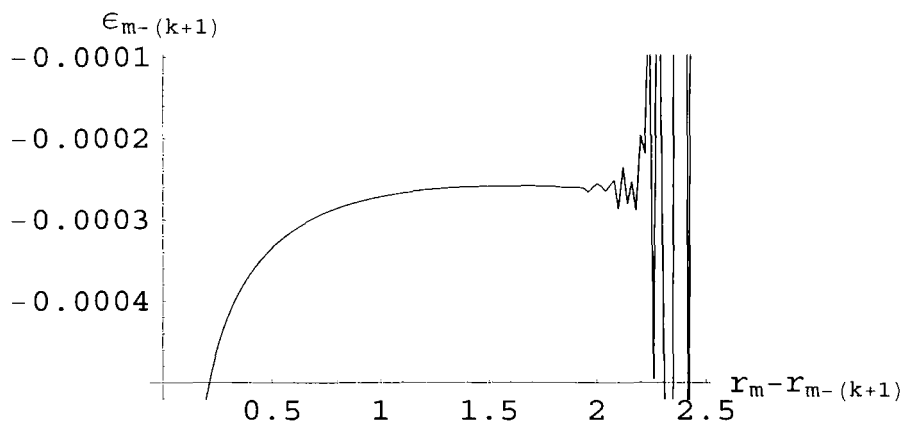
Figure 4.11: A plot of the actual errors arising from a use of the trapezium rule approximation in the metric extractor. For a step size of $\sigma = 0.02$, and with $r_{m+1} = 10$ (where we took the correct value for $h(r_{m+1})$ as our first step), we see that the suppression of the errors does not continue indefinitely, as the model of (4.2.7) would suggest. Instead we see a gradual decline in the suppression, until the turning point at $r_m - r_{m-(k+1)} \sim 1.7$. This is then followed by a complete breakdown in the algorithm resulting in massive errors and ruining the extraction.

more complicated. Crucially, the contribution from the use of the linear trapezium rule has been neglected; there is an extra term at order $\sqrt{\sigma}$, which will appear as a constant contribution to the error terms for each integral approximated in this way, and hence must be included inside the summation over j. This extra error, which is not present in the null case for reasons explained below, results in the divergence of the overall error after sufficient steps in the iteration.

The error arising from the use of the trapezium rule on a general integral is given by:

$$\int_a^b f(x)\,\mathrm{d}x = \frac{b-a}{2}(f(a) + f(b)) - \frac{(b-a)^3}{12}\frac{d^2 f(x)}{dx^2}\bigg|_{x=\chi} \qquad (4.2.8)$$

where $\chi \in (a,b)$, and on first impressions it appears that, in our case, the error term for each trapezium is proportional to σ^3, and hence heavily suppressed as $\sigma \to 0$. As, however, the value of χ will also depend on both σ and the number of iterations k, it is not quite so simple, and we must evaluate the error term fully in powers of

σ. We have that the error in our case is given by:

$$\epsilon^{\text{trap}} \sim -\frac{\sigma^3}{12}\frac{d^2}{dr^2}\left(\frac{2\sqrt{h(r)}}{r\sqrt{\frac{r^2}{r_{min}^2}-1}}\right)\Bigg|_{r=\chi} \tag{4.2.9}$$

Choosing χ to be the midpoint of each interval, such that $\chi = r_{min} + a\sigma$ (where $a = 1/2, 3/2, \dots$), and expanding in powers of σ we find that the lowest order contribution is given by:

$$\epsilon^{\text{trap}} \sim -\frac{\sqrt{\sigma}}{8\sqrt{2}a^{5/2}}\sqrt{h(\chi)}r_{min} + O(\sigma^{3/2}) \tag{4.2.10}$$

When solving for the error at the current step, the above contribution from each trapezium will be multiplied by a factor of $\sqrt{r_{min}}/2\sqrt{2}\,\sigma$, and hence will appear as a succession of terms proportional to $\sqrt{h(\chi)}/a^{5/2}$. Thus whilst they are suppressed with distance away from r_{min} by the factor of $a^{-5/2}$, they do not vanish in the limit $\sigma \to 0$. Returning to our previous notation, our expression for the error, (4.2.7), can be modified to include such terms:

$$\epsilon_{m-(k+1)} = -\left(\frac{\epsilon_{m-k}}{4} + \sum_{j=0}^{k-1}\frac{\epsilon_{m-j}}{2\sqrt{k+1-j}} + \sum_{j=0}^{k}\frac{\sqrt{h(\chi_j)}}{2\,(k+1-j)^{5/2}} - \epsilon_{m-(k+1)}^{approx}\right) \tag{4.2.11}$$

One can then get an idea of the behaviour of such an error by taking the $h(\chi_j)$ terms to be approximately given by $1/(\chi_j^2 + 1)$, and calculating the above for a small step size we find the error $\epsilon_{m-(k+1)}$ is no longer suppressed; after sufficient steps in the iteration, the error starts to diverge, even in the case $\epsilon_{m-(k+1)}^{approx} = 0$ (see figure 4.12). This then matches what we see in the early stage of the plot of the actual error for an example spacetime given in figure 4.11. Although the true behaviour is more complicated still, with this divergence of the error leading to a rapid breakdown of the algorithm such that highly erroneous estimates for $h(r_{n-i})$ are produced, we now have an explanation for why the error is not continually suppressed.

This extra error is naturally absent from higher order approximations than the linear trapezium rule (such as the second order Simpson's rule described in appendix B.1), and thus is consistent with our numerical results of section 4.1.2, where we used such an approximation to produce the highly accurate examples seen there.

Finally, we note that this analysis is also consistent with that of section 3.3 because a contribution to the error such as that described above does not appear in

$$\in_{m-(k+1)} / \in$$
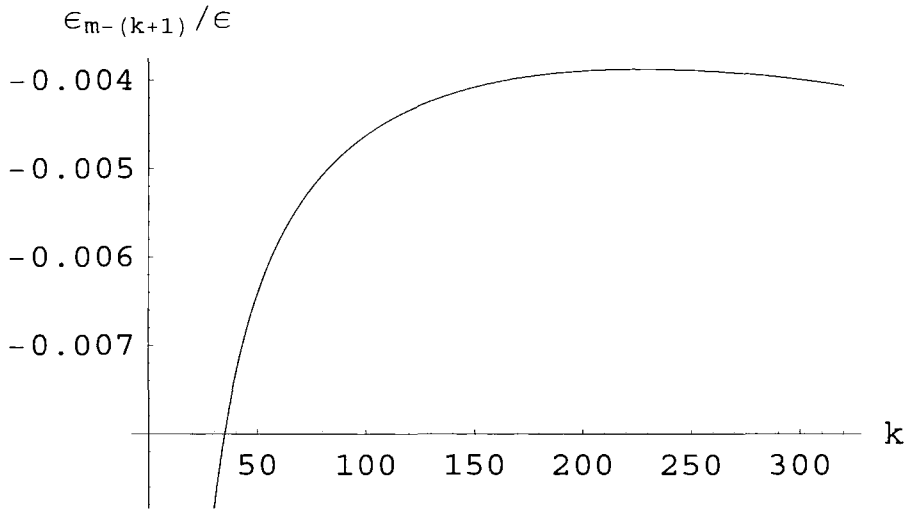
Figure 4.12: After properly including the contribution to the error from the trapezium terms, we now observe behaviour more closely matching that of figure 4.11; the suppression stops after a finite number of steps (indicated by the turning point at $k \sim 230$), after which the error starts to diverge. Although the actual behaviour is more complicated still, we now have clear evidence that the trapezium rule does not allow for an accurate estimate of the metric to be produced.

our expression (3.3.9), as in that case the lowest order contribution from the error in the trapezium rule approximation of (4.2.8) is of order $\sigma^{3/2}$. Hence this error is suppressed in the low σ limit, and we obtain the continual convergence of the estimates for the metric indicated by (3.3.9) and as seen in the examples of section 3.2.3.

What we have yet to consider is the reformulation of the method that was used in the previous chapter to eliminate the need for a series approximation entirely; in the spacelike case such a reformulation proves unhelpful, as we shall now see.

4.2.2 Method reformulation

We can again reformulate our equations in a similar manner to that given in the analysis of section 3.2.2: beginning with expression (4.1.14) and integrating over J gives

$$\int^{\mathcal{L}} \mathrm{d}\mathcal{L}' = \int J \frac{d\phi}{dJ} \, \mathrm{d}J \tag{4.2.12}$$

This can then be integrated by parts:

$$\mathcal{L}(J) = J\,\phi_{end}(J) - \int \phi\,\mathrm{d}J \tag{4.2.13}$$

and rewritten using (4.1.7):

$$\mathcal{L}(J) = J\,\phi_{end}(J) - \int\int_{r_{min}}^{r_{max}} \frac{2\sqrt{h(r)}}{r\sqrt{\frac{r^2}{J^2}-1}}\,\mathrm{d}r\,\mathrm{d}J \tag{4.2.14}$$

For some specific geodesic with proper length $\mathcal{L}_{n-i}$ and angular separation ϕ_{n-i} on the boundary (to continue with the notation from earlier) we thus have that:

$$\mathcal{L}_{n-i} = r_{n-i}\,\phi_{n-i} + \int_{r_{n-i}}^{r_{max}} 2\sqrt{h(r)}\sqrt{1 - \frac{r_{n-i}^2}{r^2}}\,\mathrm{d}r \tag{4.2.15}$$

where we have also used that $r_{min} = J$ and relabeled the minimum radius as r_{n-i}.

After splitting up the integral into pieces as usual, if we attempt to apply our parabolic area formula from section 3.2.2 to the integral around r_{n-i}, we have that:

$$A_{n-i}^{\text{parabolic}} = \frac{4}{3}\left(r_{n-i+1} - r_{n-i}\right)\sqrt{h(r_{n-i+1})}\sqrt{1 - \frac{r_{n-i}^2}{r_{n-i+1}^2}} \tag{4.2.16}$$

and we can immediately see that there is no dependence on $h(r_{n-i})$; as this is our only unknown, the above expression is no use in our metric extractor!

What happens if instead we use a series approximation? The lowest order approximation to the integral at r_{n-i} is given by:

$$A_{n-i}^{\text{series}} = \frac{4\sqrt{2}}{3}\left(r_{n-i+1} - r_{n-i}\right)^{3/2}\sqrt{\frac{h(r_{n-i})}{r_{n-i}}} \equiv r_{n-i}A_{n-i} - \mathcal{A}_{n-i} \tag{4.2.17}$$

where A_{n-i} and $\mathcal{A}_{n-i}$ are as defined in Appendix B.1; note that we now have the required $h(r_{n-i})$ term, and that this combination of the two series expansions from the appendix has eliminated the dependence on $h'(r_{n-i})$. However, applying this method in practice leads to some serious stability problems, and it fails to generate any reliable estimate for $f(r)$ at any step size. This can be easily explained by analysing the behaviour of the errors as before; suppose again that at the point r_{m+1}, our estimate $\bar{h}_{m+1}$ acquires an error of the form of (4.2.1). The error at the next step is then given by:

$$\sqrt{\bar{h}_m} = \sqrt{h(r_m)} - \frac{\epsilon}{2\sqrt{2}}\left(\sqrt{r_{m+1} + r_m}\sqrt{\frac{r_m}{r_{m+1}}}\right) \tag{4.2.18}$$

where we have taken the small step size limit, $\sigma \to 0$, and we see that the error coefficient is now much larger than one (at large radius). This completely ruins the extraction, as it means any non-zero error in the first few steps (which is unavoidable given the approximations) is immediately blown up in the following steps. Hence we are unable to use this reformulation of the ϕ_{end} and $\mathcal{L}$ equations to improve the metric extractor.

Having discussed the suppression of errors in our estimate, we now address the issue of how confident one can be that the extracted solution matches the actual metric, $h(r)$.

4.2.3 Validating the extracted solution

A natural question to ask at this point is on the uniqueness of the solution, i.e. is there more than one possible $h(r)$ (or equivalently $f(r)$ in the null case) which gives the same boundary data for the geodesics? Then if there is a unique $h(r)$, does this proposal for reconstructing the metric always find it, and not some alternative set of points $(r_{n-i}, h(r_{n-i}))$ which also solve equations (B.1.4) and (B.1.10) without being the actual metric function?

Considering the second question, it is quite simple to show that if the metric function $h(r)$ corresponding to the boundary data is unique, then the iterative method must recover it (up to a level of accuracy determined by the number of steps). We will show that if this is not the case, then either the metric function was not unique, contradicting our assumption, or the estimate does not in fact correspond properly to the boundary data.

Take the extracted points $(r_{n-i}, h(r_{n-i}))$ for $i = 0, \ldots, n$, and use them to construct an interpolation function, which is then our estimate for the metric function. We can then use this estimate to compute the proper length and angular separation of all spacelike geodesics passing through the spacetime. If the generated data matches with the original data from the field theory, we have successfully produced an estimate for an actual bulk metric, and by our assumption of uniqueness, this function must be $h(r)$.

If the generated data fails to match correctly to that from the field theory, we

can deduce that we haven't in fact produced an estimate for $h(r)$, but instead that our $(r_{n-i}, h(r_{n-i}))$ are simply a set of points which solve the equations (B.1.4) and (B.1.10). In this case, the iterative step size used to produce the estimate was too large, and the extraction procedure should be repeated with a smaller step size. Once the new estimate has been produced, the above test can again be applied; this can continue until an actual estimate of $f(r)$ is recovered.

Finally, one should note that at an infinitesimally small step size, one will use the complete[7] set of spacelike geodesics to probe the spacetime, generating a continuous estimate for $h(r)$ from r_n down to zero. As such the data generated from our estimate must correspond to that from the field theory, as it was all used in its production. Thus, by uniqueness, the estimate must correspond to $h(r)$.

A basic argument for the uniqueness of the bulk metric corresponding to the field theory data (in our case, the proper length of the static spacelike geodesics as a function of the angular separation of the endpoints) follows from a comparison of the local degrees of freedom on each side, by noting that this data and the geometry of the constant time slice we wish to recreate contain the same amount of information, as $h(r)$ is a function of the radial coordinate only. When coupled with knowledge of the asymptotic behaviour of the spacetime (that it approaches pure AdS at large r), we have the boundary conditions needed to ensure that the metric function is unique. In less symmetric cases one has more freedom in the metric, but correspondingly one also has more information with which to determine this, as we see in chapter 6.

4.2.4 A duality between the boundary data of null and zero-energy spacelike geodesics

The strong parallels between the two approaches to probing the bulk seen in the previous chapters suggest a possible link between null geodesics passing through one bulk, and zero-energy spacelike geodesics passing through another, at least in static, spherically symmetric metrics. The use of the boundary data is almost identical

---

[7]By complete, we mean all geodesics which have minimum radius $r_{min} \leq r_n$, where r_n can be taken arbitrarily large

in both cases, namely (t_{end}, ϕ_{end}) giving $dt_{end}/d\phi_{end} = y$ for the null geodesics, and $(\mathcal{L}, \phi_{end})$ giving $d\mathcal{L}/d\phi_{end} = J$ for the static spacelike ones, and immediately suggests identifying the time taken for the null geodesic to traverse the bulk with the (regularised) proper length of the zero energy spacelike probes. We also have that each set of geodesics is only sensitive to one part of the metric; the null geodesics cannot probe the conformal factor, the static spacelike geodesics are independent of the timelike component, hence the integral equations for the geodesics can be expressed in terms of only one metric function in each case; specifically, in our notation, these are $f(r)$ for the null geodesics, and $h(r)$ for the spacelike ones.

The question then, is for what background metrics does the above hypothesis hold? To get a general indication of how the two bulks should be related, consider the t and ϕ equations for the null geodesics (choosing $t^{null}_{start} = \phi^{null}_{start} = 0$ without loss of generality):

$$t^{null}_{end} = 2 \int_{r_{min}}^{\infty} \frac{1}{f(r)\sqrt{1 - y^2 \frac{f(r)}{r^2}}} \, dr \qquad (4.2.19)$$

$$\phi^{null}_{end} = 2 \int_{r_{min}}^{\infty} \frac{y}{r^2\sqrt{1 - y^2 \frac{f(r)}{r^2}}} \, dr \qquad (4.2.20)$$

recalling that $y = J/E$ is the normalised angular momentum, and the minimum radius obtained by the geodesic is denoted r_{min}. If we make the substitution $r^2/f(r) \rightarrow \tilde{r}^2$, we have that:

$$\frac{d\tilde{r}}{dr} = \frac{1}{\sqrt{f(r)}} \left(1 - \frac{r}{2 f(r)} \frac{df(r)}{dr} \right) \qquad (4.2.21)$$

and thus we can rewrite (4.2.19) and (4.2.20) as:

$$t^{null}_{end} = 2 \int_{\tilde{r}_{min}}^{\tilde{r}_{max}} \frac{\sqrt{h(\tilde{r})}}{\sqrt{1 - \frac{y^2}{\tilde{r}^2}}} \, d\tilde{r} \qquad (4.2.22)$$

$$\phi^{null}_{end} = 2 \int_{\tilde{r}_{min}}^{\tilde{r}_{max}} \frac{y\sqrt{h(\tilde{r})}}{\tilde{r}^2\sqrt{1 - \frac{y^2}{\tilde{r}^2}}} \, d\tilde{r} \qquad (4.2.23)$$

where we have defined:

$$\sqrt{h(\tilde{r})} \equiv 1 \bigg/ \left(\sqrt{f(r)} - \frac{r}{2\sqrt{f(r)}} \frac{df(r)}{dr} \right) \qquad (4.2.24)$$

and we note that the limit $\tilde{r}_{max}$ will depend on the form of $f(r)$. Comparing the above equations (4.2.22) and (4.2.23) with those for the proper length and angular separation of static spacelike geodesics, we see that they are identical! In other words we have that:

$$t_{end}^{null} = \mathcal{L}_{space} \tag{4.2.25}$$

and

$$\phi_{end}^{null} = \phi_{end}^{space} \tag{4.2.26}$$

We thus have the apparent duality that the (t, ϕ) endpoints of null geodesics in a background defined by $f(r)$ can be equivalently viewed as the $(\mathcal{L}, \phi)$ information of static spacelike geodesics in a background defined by $h(\tilde{r})$, with the appropriate relation between $f(r)$ and $h(\tilde{r})$ given above. For example, considering $f(r) = 1 + r^2/R^2$ (i.e. pure AdS behaviour, where they all terminate at the antipodal point on the boundary $\phi_{end}^{null} = t_{end}^{null}/R = \pi$), we have $r \to \tilde{r}R/\sqrt{R^2 - \tilde{r}^2}$ which gives:

$$h(\tilde{r}) = \frac{R^2}{R^2 - \tilde{r}^2} \tag{4.2.27}$$

and for the limits we note that $r = 0 \Rightarrow \tilde{r} = 0$ and $r = \infty \Rightarrow \tilde{r} = R$.

A simple comparison of the geodesic equations, however, is not sufficient to fully determine the forms of the two background metrics. Recall that in defining the null geodesic equations (4.2.19) and (4.2.20) above, we have been working in a metric of the form:

$$ds^2 = C(r) \left(-f(r)dt^2 + \frac{dr^2}{f(r)} + r^2 d\Omega_3^2 \right) \tag{4.2.28}$$

where the conformal factor cancels out due to their zero proper length. Thus for the case of $f(r) = 1 + r^2/R^2$, we obtain the spectrum of endpoints identical to that for pure AdS irrespective of the conformal factor $C(r)$. Making the transformation $r^2/f(r) = r^2/(1 + r^2/R^2) \to \tilde{r}^2$ which as we recall implies $r \to \tilde{r}R/\sqrt{R^2 - \tilde{r}^2}$ the metric becomes:

$$ds^2 = C(r) \left(-\frac{R^2}{R^2 - \tilde{r}^2}dt^2 + \frac{R^4}{(R^2 - \tilde{r}^2)^2}d\tilde{r}^2 + \frac{\tilde{r}^2 R^2}{R^2 - \tilde{r}^2}d\Omega_3^2 \right) \tag{4.2.29}$$

where we see that in order for the definition of $h(r)$ given above in (4.2.27) to be true, we must multiply the metric by a factor of $1 - \tilde{r}^2/R^2$, which is equivalent to

choosing the conformal factor:

$$C(r) = \frac{R^2}{R^2 + r^2} \left(= \frac{1}{f(r)} \right) \tag{4.2.30}$$

in our original metric (4.2.28), and gives us:

$$ds^2 = -dt^2 + \frac{R^2}{R^2 - \tilde{r}^2} d\tilde{r}^2 + \tilde{r}^2 d\Omega_3^2 \tag{4.2.31}$$

in terms of $\tilde{r}$. Thus we can say that our original spectrum of null geodesic endpoints which all terminate at the antipodal point on the boundary can equivalently be thought of as the set boundary data (i.e. $\mathcal{L}$ and ϕ_{end}^{space}) of static spacelike geodesics provided the conformal factor of the metric is given by (4.2.30).

Unfortunately, an immediate translation of this into the AdS/CFT picture is somewhat difficult, as the conversion of the radial coordinate from r to $\tilde{r}$ doesn't allow both sets of geodesics to be in asymptotically anti-de Sitter bulks, as the form of (4.2.31) indicates. Thus it appears that one cannot pin both sets of geodesics to the boundary, and hence we are unable to use the above to relate the corresponding CFT quantities of each type of geodesic.

Finally, we observe that this relationship between the (static) spacelike and null geodesics is trivially true in a flat spacetime, where the metric functions are all identically equal to unity; one can see that equations (4.2.25) and (4.2.26) are immediately satisfied. This can be seen to arise by recalling that the distinction between the geodesics is manifest from the condition on extremising the action, and for a flat spacetime we have (from equation (2.3.7)):

$$\kappa = -E^2 + \dot{r}^2 + \frac{J^2}{r^2} \tag{4.2.32}$$

which for static spacelike geodesics becomes:

$$1 = \dot{r}^2 + \frac{J^2}{r^2} \tag{4.2.33}$$

as $\kappa = 1$ and $E = 0$. This is exactly the same, however, as we obtain for the null geodesics, where $\kappa = 0$ and as they are parameterised by $y \equiv J/E$ we are free to choose $E = 1$, which also gives $dt/d\lambda = 1$ and thus makes the relation between t_{end}^{null} and $\mathcal{L}_{space}$ explicit.

4.3   Summary

In this chapter we have seen how the bulk geometry can be extracted (in asymptotically AdS spacetimes) using the entanglement entropy information obtained from the corresponding field theory. In the three dimensional case, the entanglement entropy of a subsection A of the boundary is proportional to the proper length of the static spacelike geodesic connecting the endpoints of A (see figure 2.6). One thus has boundary information $(\mathcal{L}, \phi_{end})$ for all the geodesics with fixed starting point, and this data allows the minimum radius, r_{min}, of the geodesic to be immediately determined, via a consideration of the gradient, which yields $d\mathcal{L}/d\phi_{end} = J = r_{min}$.

We used this to construct an iterative algorithm by which to determine our one remaining unknown, $h(r_{min})$, by considering various approximations to the integral equation for ϕ; by starting at large r, where the metric is approximately pure AdS, one can probe further and further into the bulk using geodesics with progressively smaller minimum radius, and hence determine $h(r)$ down to $r = 0$ (or $r = r_h$ if the metric contains a horizon). This was demonstrated numerically in a set of examples.

Although this iterative method was developed in an analogous way to those involving null geodesics (presented in chapter 3), there were some subtle differences in the stability of each method to errors; specifically, the trapezium approximation which worked extremely well previously was now shown to lead to an unstable algorithm when used with the spacelike geodesic equations. Furthermore, our analysis demonstrated that the parabolic approximation used in chapter 3 was also not applicable to our new procedure for extracting the metric.

We concluded the chapter by briefly describing the rather intriguing observation that the endpoint information $(t_{end}^{null}, \phi_{end}^{null})$ of the null geodesics could also be viewed as the boundary information $(\mathcal{L}^{space}, \phi_{end}^{space})$ of the static spacelike geodesics in an alternative spacetime. Unfortunately, it is not entirely clear how this apparent duality can be used in the context of AdS/CFT, due to the transformation of the radial coordinate that is required.

The next chapter begins by demonstrating how the null and spacelike methods can be used in conjunction to extract both unknown functions $k(r)$ and $h(r)$ in a metric of the form of (4.1.1).

Chapter 5

Probing the bulk geometry III

In the previous two chapters we saw how intrinsically different bulk probes (namely null and static spacelike geodesics) could be used to recover significant information about the bulk. The motivations for using each type of geodesic were also rather different (two-point correlators and entanglement entropy), yet the algorithms presented for extracting the bulk information were remarkably similar; this apparent link between the two approaches was discussed further in section 4.2.4, albeit somewhat briefly, where we saw an intriguing connection between the proper length of the static spacelike geodesics and the time taken for the null geodesics to traverse the bulk.

Returning to the algorithms, the obvious question that arises from having two different methods for probing the bulk is whether they can be used in conjunction to recover more information about the metric than either can individually. This is indeed the case, due to the already observed fact that the geodesics probe the bulk in different ways; the null geodesics are not sensitive to the overall conformal factor of the metric, whereas the static spacelike geodesics have by definition, zero energy, and thus cannot access the timelike component of the metric. The function obtained by the spacelike probes, $h(r)$, is related to the conformal factor, however, and so once determined, leaves the null geodesics to simply extract the timelike component, $k(r)$.

This is the essence of the method described in the first part of the chapter: one begins by using the spacelike geodesics to estimate $h(r)$, then applies a slightly

modified version of the null geodesic method (which incorporates this estimate) to determine $k(r)$.

Clearly the limitations from each individual method carry over to this case, as we are not altering the way in which we probe the bulk; the null geodesics still cannot be used to extract the metric past the radius at which they go into circular orbit, for example. Given that one applies the spacelike method first, however, one should always be able to extract the maximum amount of information available using the two methods combined in this way, as the spacelike geodesics can always probe to the same, if not greater depth than the null ones. Thus for a three dimensional bulk with slight deviation from pure AdS, one should be able to recover both $k(r)$ and $h(r)$ down to the centre, and fully determine the geometry of the central deformation (in the chosen coordinates); we demonstrate this extraction of both metric functions for a radiating perfect fluid "star" in AdS_3.

The most significant limitation, however, is that in higher dimensions, the area of the minimal surface related to the entanglement entropy will no longer be the proper length of static spacelike geodesics. Restricting ourselves to three dimensions, whilst fine theoretically[1], does limit the physical realism of our bulk structures, given the non-dynamical nature of gravity in such scenarios (for example).

Since Ryu and Takayanagi's initial proposal for the holographic entanglement entropy formula was put forward, there have been a number of subsequent papers on the subject, as given in chapter 2. Specifically, work by Hubeny *et al.* [82] has examined the question of what the correct minimal surface to consider should be in dimension greater than three; in principle, one can imagine using the equations for these minimal surfaces to iteratively probe the bulk. This requires a significant extension to the proposals given here, including the rewriting of our iterative algorithms in differential (rather than integral) form, as typically this form of the equations will either be necessary or simply easier to work with. This process is begun in the next chapter, although instead of examining these alternative minimal surfaces we consider metrics with reduced symmetry, which also requires the

---

[1] Although naturally one would prefer not to have such a restriction!

use of differential equations. We conclude this chapter, however, by examining the behaviour of our toy model of a star in higher dimensions, noticing some interesting developments as one increases the spacetime dimension (see section 5.2), motivated by the following observation.

A surprising feature noticed previously in a study of bulk-cone singularities in AdS/CFT [83] is that in five bulk dimensions, the total mass of a radiating perfect fluid star does not increase monotonically with increasing central density, ρ_0 (as one might have expected), rather it oscillates about its asymptotic value. Extending our model to encompass this and higher dimensions (by considering the star model in general dimension d, including non-integer values), we find that this behaviour is limited to a certain range of dimensionality; there is a critical dimension above which the oscillations disappear, see figure 5.5. Analysing this behaviour first numerically and then analytically (via a dynamical systems approach), we develop a model for the self-similar behaviour of the total mass at large ρ_0, and obtain both a value for the critical dimension and an expression for the dependence of the saturation density (the density at which the first peak in the oscillations occurs) on the dimension d. Thus whilst our original three dimensional model had a clear unphysicality, these oscillations in the total mass suggest other instabilities in the model of the star, and a breakdown in the physical realism of the model even in dimensions where gravity does fall off with distance.

5.1 Sequential extraction of the two metric functions

Having developed the two methods individually, we now demonstrate how to use them in conjunction with one another to determine both unknown functions of a metric of the form (3.1.2), repeated here for convenience:

$$ds^2 = -k(r)dt^2 + h(r)dr^2 + r^2 d\phi^2 \tag{5.1.1}$$

when we restrict ourselves to the (2+1)-dimensional case as in the previous chapter.[2]

Whilst it is not obvious that a field theory in which it is easy to determine the locations of singularities in two-point correlation functions will also allow a simple computation of the entanglement entropy, we can nonetheless ask the question of how much information about the corresponding spacetime one can extract if one assumes one has access to such data.

We begin with the spacelike geodesics, where we use our iterative method of the previous chapter to determine $h(r)$; specifically, for each r_i we estimate the corresponding $h(r_i)$, and from this we generate a best fit curve, $h_{\text{fit}}(r)$. We then use the null geodesic method applied to a metric of the form of (5.1.1) above to recover $k(r)$, with the relevant equation being:

$$t_j - \frac{dt}{d\phi}\bigg|_{(\phi_j,t_j)} \phi_j = \int_{r_j}^{\infty} 2\sqrt{h(r)} \sqrt{\frac{1}{k(r)} - \frac{y_j^2}{r^2}}\, dr \tag{5.1.2}$$

for a null geodesic probing down to r_j. With the estimate for $h(r)$, this becomes:

$$t_j - \frac{dt}{d\phi}\bigg|_{(\phi_j,t_j)} \phi_j = \int_{r_j}^{\infty} 2\sqrt{h_{\text{fit}}(r)} \sqrt{\frac{1}{k(r)} - \frac{y_j^2}{r^2}}\, dr \tag{5.1.3}$$

which, when coupled with the equation for the minimum r,

$$y_j^2 = \frac{r_j^2}{k(r_j)} \tag{5.1.4}$$

allows the metric function $k(r)$ to be reconstructed via the same iterative method described in chapter 3: for the general term r_{n-i}, one approximates the integral from r_{n-i} to r_{n-i+1} by the parabolic area formula; the integral from r_n to $r = \infty$ by taking the spacetime to be pure AdS; and the remaining $i - 1$ integrals by the trapezium rule, to obtain (c.f. equations (3.2.13)-(3.2.17)):

$$t_{n-i} - \frac{dt}{d\phi}\bigg|_{(\phi_{n-i},t_{n-i})} \phi_{n-i} \approx A_{n-i} + B_{n-i} + C_{n-i} \tag{5.1.5}$$

where

$$\mathcal{A}_{n-i} = \frac{4}{3} \left(r_{n-i+1} - r_{n-i} \right) \eta(y_{n-i}, r_{n-i+1}) \tag{5.1.6}$$

---

[2]The procedure presented here can of course be applied to spacetimes of larger bulk dimension, however, as mentioned above, it is less well motivated to do so since the spacelike geodesic boundary data is no longer available from the field theory via the entanglement entropy.

$$\mathcal{B}_{n-i} = \sum_{j=1}^{i-1} \left(r_{n-j+1} - r_{n-j} \right) \left(\eta(y_{n-i}, r_{n-j+1}) + \eta(y_{n-i}, r_{n-j}) \right) \tag{5.1.7}$$

and

$$\mathcal{C}_{n-i} = 2 \arctan\left(\frac{1}{\sqrt{\left(1 - y_{n-i}^2\right) r_n^2 - y_{n-i}^2}} \right) - 2y_{n-i} \arctan\left(\frac{y_{n-i}}{\sqrt{\left(1 - y_{n-i}^2\right) r_n^2 - y_{n-i}^2}} \right) \tag{5.1.8}$$

where we have defined the function $\eta(y_j, r_k)$ as:

$$\eta(y_j, r_l) \equiv \sqrt{h_{\mathrm{fit}}(r_l)} \sqrt{\frac{1}{k(r_l)} - \frac{y_j^2}{r_l^2}} \tag{5.1.9}$$

The only area of concern numerically with this procedure would be whether significant errors in recovering $k(r)$ appear unless the estimate function for $h(r)$ is highly accurate; one can investigate whether this is so by running the extraction of $k(r)$ several times using a different estimate for $h(r)$ in each case. We see how this affects the results in the first example below.

We also note that as we have simply applied the methods sequentially, the stability of the iteration to errors is unaffected; the same error analysis carried out in the two previous chapters is equally valid here. The fact that the null method is so robust to errors, and indeed seeks to suppress them in subsequent steps is a great benefit, as it helps ensure that any numerical anomalies that might have appeared in the estimate for $h(r)$ do not ruin the subsequent estimate of $k(r)$.

Finally, we reiterate that the depth to which the metric can be recovered is subject to the same restrictions as before (see section 3.4): for example in singular spacetimes, whilst the spacelike geodesics can probe down to the horizon radius, r_h (and we thus obtain $h(r)$ down to $h(r_h)$), the null geodesics can only probe as far as the first local maximum in the effective potential (figure 3.12), at some $r_{h2} > r_h$, leaving $k(r)$ undetermined for $r < r_{h2}$. Nevertheless, by combining the two different approaches to probing the bulk, we have obtained more information than is possible using either individually.

5.1.1 Example 1: Accuracy test

Consider a spacetime where the two metric functions $k(r)$ and $h(r)$ are given by the following:

$$k(r) = 1 + r^2 - \frac{7\,r^2}{(r^2 + 1)(r^2 + 13)} + \frac{2r\sin(5\,r)}{r^4 + 15} \qquad (5.1.10)$$

$$h(r) = \left(1 + r^2 - \frac{4\,r^2}{(r^2 + 1)(r^2 + 8)} + \frac{3r\sin(2\,r)}{r^4 + 1}\right)^{-1} \qquad (5.1.11)$$

Whilst this is in no way meant to be a representation of any physical deformation of the bulk, it is a good test of the combined extraction method, as it provides a monotonic effective potential for the null geodesics, and so allows us to probe down to $r = 0$.

One can also use the similarity between this spacetime and that described in the first example of section 4.1.2, namely that we have $h(r) \equiv h_1(r)$. This was deliberately chosen so the part of the metric probed by the spacelike geodesics is exactly as it was in that case; the change in $k(r)$ has no effect on the results, and thus the best fit estimates for $h(r)$ are exactly those specified by the values of the parameters in Table 4.1. We therefore have four different estimates for $h(r)$ (one for each of the four choices of step size used), and we label them $h_{0.1}(r)$ through to $h_{0.005}(r)$, where the subscript refers to the step size. All that is left to do is to attempt to recover $k(r)$ via the null geodesic data[3] for each fit to $h(r)$, and compare it firstly to the actual values, and also to those obtained using the exact function $h(r)$ rather than an estimate. The results are analyzed using a best fit of the form of (4.1.20) and are presented in Table 5.1.

We see quite clearly from the table of results that even using our roughest estimate for $h(r)$, namely $h_{0.1}(r)$, we obtain a highly accurate estimate for $k(r)$. Indeed, the limiting factor is not the accuracy of the estimate for $h(r)$, rather it is the choice of step size and starting y in the null geodesic part of the extraction (see footnote 3).

---

[3]As we saw in chapter 3, one can use a range of different step sizes in y to obtain varied levels of accuracy in the metric extraction; as we are not intending to specifically analyze the null geodesic method here, we simply choose a starting value of $y = 0.9985$, and a step size of $\triangle y = 0.0005$, as these are sensible values for the example given.

$h_{\text{fit}}(r)$	α (7)	β (1)	γ (13)	χ (2)	η (5)	λ (15)
$h_{0.1}(r)$	6.81	1.03	12.49	2.00	4.99	14.92
$h_{0.05}(r)$	6.81	1.03	12.48	2.00	4.99	14.92
$h_{0.01}(r)$	6.80	1.03	12.48	2.00	4.99	14.92
$h_{0.005}(r)$	6.80	1.03	12.48	2.00	4.99	14.92
$h(r)$	6.80	1.03	12.48	2.00	4.99	14.92

Table 5.1: Best fit values (to 2 d.p.) for the $k_{\text{fit}}(r)$ parameters α, β, γ, χ, η and λ, with the actual values indicated in brackets. We see that even our roughest estimate for $h(r)$ is close enough for the extraction of $k(r)$ to be highly accurate.

5.1.2   Example 2: Radiation in AdS_3, a toy model

As the two extraction methods give such good fits when applied sequentially, we now turn our attention to a less trivial example, where we consider a gas of radiation in AdS_3. There have been numerous papers exploring this and other closely related geometries in various dimensions, such as [83, 108–110], and we focus here purely on our ability to recover the metric information via our numerical extraction methods. Firstly, recall that although restricting ourselves to three bulk dimensions does make our spacelike geodesic method fully applicable, it also restricts the physical realism of the model due to the non-dynamical nature of gravity; we shall investigate the behaviour of similar models in higher dimensions in the following section. Nevertheless, it provides a good toy model for radiating "stars" in AdS spacetimes, and allows us to demonstrate how well the pertinent information (e.g. the "star's" mass and density profiles) about the bulk can be recovered.

We consider a perfect fluid solution to Einstein's equations, with the pressure $P(r)$ set equal to half the density, $\rho(r)/2$, as for radiating matter the stress-energy tensor is traceless. For a metric of the form of (4.1.1), we find that[4]:

$$h(r) = \left(1 + r^2 - m(r)\right)^{-1} \tag{5.1.12}$$

---

[4]We set $R = 1$ and $8\pi G_3 \equiv 1$ for convenience.

and

$$k(r) = \left(\frac{\rho_\infty}{\rho(r)}\right)^{2/3} \tag{5.1.13}$$

where the mass function[5] is defined by:

$$m(r) = 2\int_0^r \rho(\acute{r})\acute{r}\,\mathrm{d}\acute{r} \tag{5.1.14}$$

and ρ_∞ is the leading coefficient of $\rho(r)$ at large r, and is given by $\rho_\infty \approx \rho(r)r^3$ as $r \to \infty$. We obtain from the field equations a pair of coupled ODEs for $m(r)$ and $\rho(r)$:

$$m'(r) = 2\rho(r)r \tag{5.1.15}$$

$$\frac{6 + 3\rho(r)}{1 + r^2 - m(r)} + \frac{2\rho'(r)}{\rho(r)r} = 0 \tag{5.1.16}$$

which when combined with the relevant boundary conditions $m(0) = 0$ and $\rho(0) = \rho_0$ can be numerically solved to allow us to generate the geometry of the spacetime (see figure 5.1). The condition $\rho(0) = \rho_0$ specifies the internal density of the gas, and ρ_0 is the single free parameter of the system: pure AdS is recovered when $\rho_0 = 0$.

Before we begin with the metric extraction, we should make a comment about the features of such spacetimes at large radius, as there are significant differences in the asymptotic behaviour of the metric depending on the choice of ρ_0. For $\rho_0 \neq 0$, we have that the asymptotic behaviour of the metric functions is given by

$$h(r) \to \left(1 + r^2 - M\right)^{-1} \quad \text{and} \quad k(r) \to 1 + r^2 - M \quad \text{as } r \to \infty \tag{5.1.17}$$

where $M > 0$ is a constant. If $M > 1$ we have that the metric becomes the BTZ black hole solution at large r (see [53,111, for example] for more details); this poses a problem for the method involving null geodesics, as we can no longer use them to probe the full range of r. Whilst this is due to the form of the effective potential (see figure 5.2), it is not due to the local maximum problem we saw in section 3.4. Here we no longer have geodesics which can usefully probe the spacetime *away* from the centre: for the full set of null geodesics (obtained by varying y for zero to one), the minimum radius reached by the geodesics is bounded from above. We thus cannot

---

[5]Note that the mass function used here is a rescaling of the actual mass; a constant factor from the integral over ϕ does not appear in our definition of $m(r)$ due to our definition of $h(r)$.
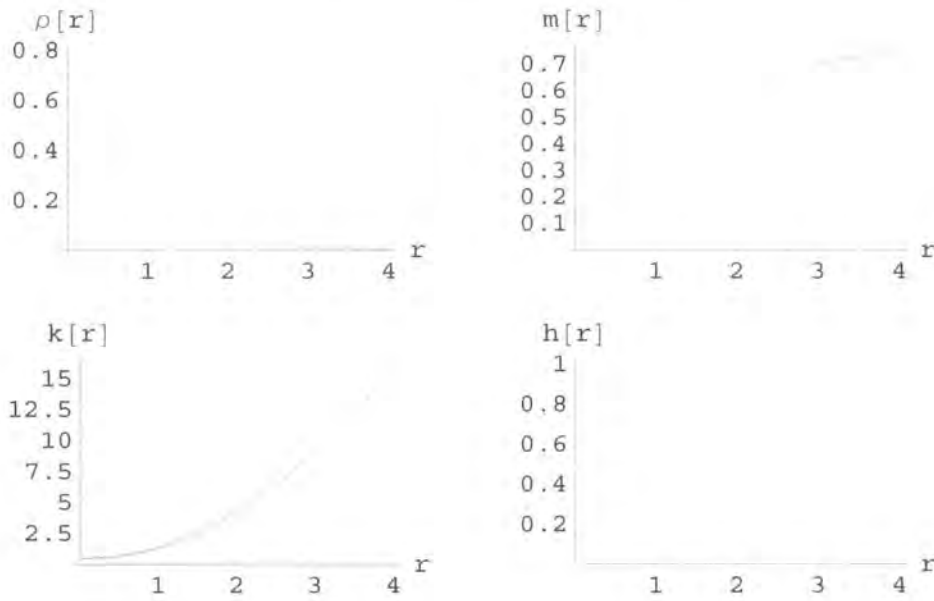
Figure 5.1: The density and mass profiles (top plots) for a "star" with central density $\rho_0 = 0.8$, along with plots of the corresponding metric functions $k(r)$ and $h(r)$ (bottom).

take r_{min} to be arbitrarily large on the first step of our iteration, which was necessary for us to begin extracting the metric (although we should note that we could still apply the spacelike method to extract $h(r)$ in this scenario). Instead however, we will consider the region $0 < M < 1$, corresponding to conical defects, in which both methods are applicable and is obtained by taking ρ_0 to be small.[6]

Let us then proceed with recovering the metric in the specific example shown in figure 5.1, where we have set $\rho_0 = 0.8$. Bearing in mind that our goal is to firstly reconstruct the functions $k(r)$ and $h(r)$, and then use these to determine the mass and density profiles ($m(r)$ and $\rho(r)$ respectively) of the star, we begin by applying the spacelike geodesic method (with step sizes of 0.1, 0.05 and 0.01) to produce three estimates for $h(r)$, the most accurate of which, $h_{0.01}(r)$, is shown in figure 5.3.

In the previous example, we defined $h(r)$ explicitly by hand, and so knew the

---

[6]One should also note from (5.1.17) that our iterative equations for recovering the metric need to be modified to take into account the new asymptotic behaviour, as we no longer have that $k(r) \approx r^2 + 1$ at large r. Thus we say that for $r \geq r_n$ we have that $k(r)$ and $h(r)$ are given by (5.1.17), and modify the approximations to the integrals for ϕ_{n-i} and $\mathcal{L}_{n-i}$ accordingly.
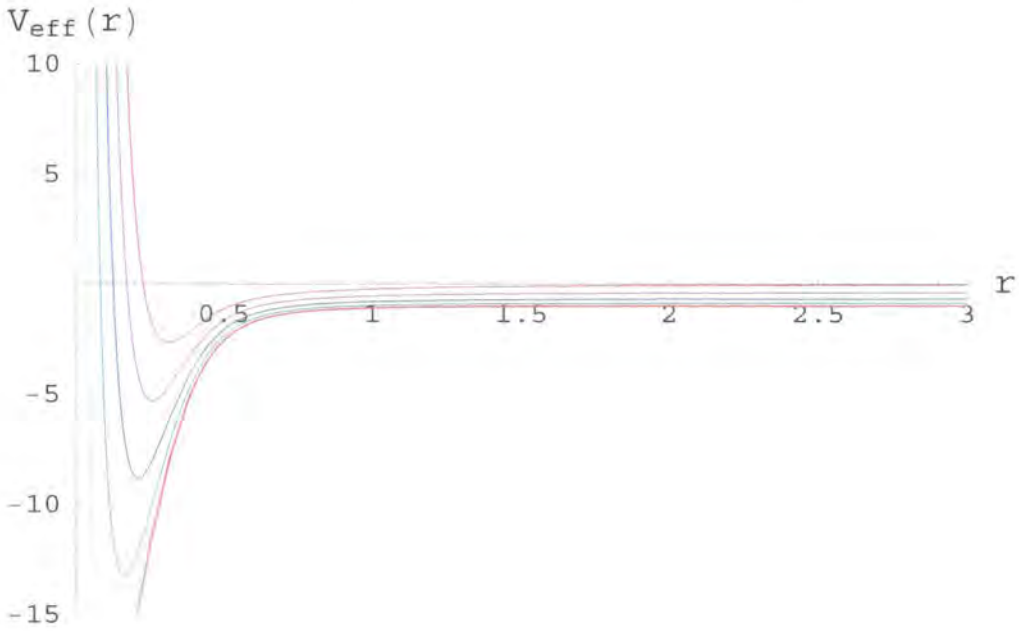
Figure 5.2: Effective potentials for null geodesics in a spacetime with $M = 8$. The upper (red) potential is for $y \equiv J/E = 0.9999$; no matter how close to one the ratio J/E becomes, the minimum radius (defined by $V_{eff} = 0$) remains small.

form of the function with which to apply the non-linear fit to generate the best fit curve $h_{\text{fit}}(r)$, however here we do not have such a starting point. Instead, we use the data points $(r_{n-i}, h(r_{n-i}))$ to generate an interpolating function which will serve as our $h_{\text{fit}}(r)$. Thus although we cannot write down an explicit form for $h_{\text{fit}}(r)$, we can use the interpolating function to then carry out the next part of the extraction process, namely using the null geodesic probes to recover $k(r)$.

Using the third (and most accurate) estimate for $h(r)$, we produce the estimate for $k(r)$, $k_{\text{fit}}(r)$, also shown in figure 5.3: we have now reconstructed the star metric. Although if we so wished we could have taken smaller step sizes to improve both the estimate of $h(r)$ and that of $k(r)$, we now continue with the ones we have.

How do we use the metric functions to determine the mass and density information for the star? From (5.1.12) it is immediately obvious: we can rearrange the equation to solve for $m(r)$, and substitute in our interpolating function $h_{\text{fit}}(r)$ to give an estimate for the mass profile:

$$m_{\text{fit}}(r) = 1 + r^2 - \frac{1}{h_{\text{fit}}(r)} \tag{5.1.18}$$
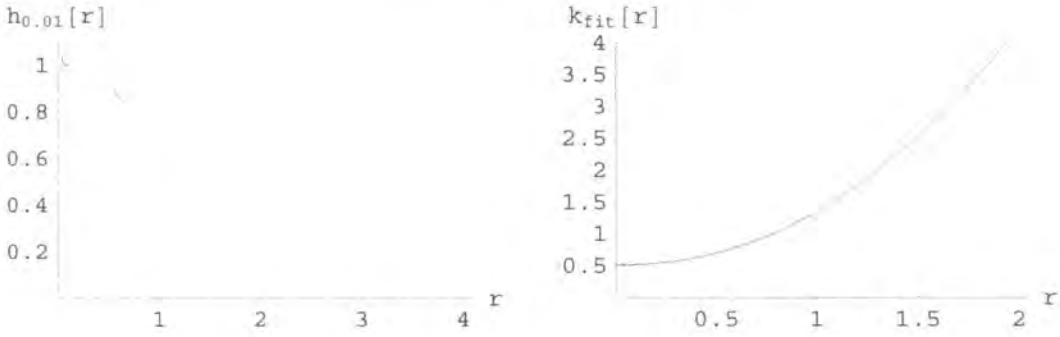
Figure 5.3: The third (and most accurate) estimate for $h(r)$, where the fit is good down to $r \sim 0.1$ (left plot). The estimate for $k(r)$ generated using this approximation to $h(r)$ is given in the right plot, and we see that it too appears accurate down to very low r.

and we obtain a fit for the density profile in similar fashion, by using the above estimate for $m(r)$ in (5.1.15), to give:

$$\rho_{\text{fit}}(r) = \frac{m'_{\text{fit}}(r)}{2r} \qquad (5.1.19)$$

These two fits are plotted against the actual functions $m(r)$ and $\rho(r)$ in figure 5.4, and we see that by using the metric function data $h_{\text{fit}}(r)$ we have obtained reasonably good estimates of the mass and density profiles of the star, aside from at very small r, where the errors from the estimate of $h(r)$ become noticeable. What is noticeable is that the estimate for $\rho(r)$ fails at higher r than any of the others; this is due to the use of the derivative of the interpolating function $m_{\text{fit}}(r)$ in its construction, and is dealt with later (see below).

One now asks the obvious question of why it was necessary to extract the function $k(r)$ at all, seeing as we have apparently just reconstructed the information about the star simply by using $h_{\text{fit}}(r)$. This is where we recall that we should be assuming that *a priori* we knew nothing about the origin of the metric's deviation from pure AdS. In fact, this has not been the case. Whilst our expressions for $h(r)$ in terms of $m(r)$ and the mass $m(r)$ in terms of the density $\rho(r)$, (5.1.12) and (5.1.15), stem from the dimensionality of the bulk (e.g. in higher dimensions one would have the $m(r)$ term multiplied by some negative power of r), in defining $k(r)$ by (5.1.13) we have already taken the matter content to be a gas of radiation, which sets $P(r) = \rho(r)/2$ and removes the pressure profile as an unknown. Given this knowledge, one could
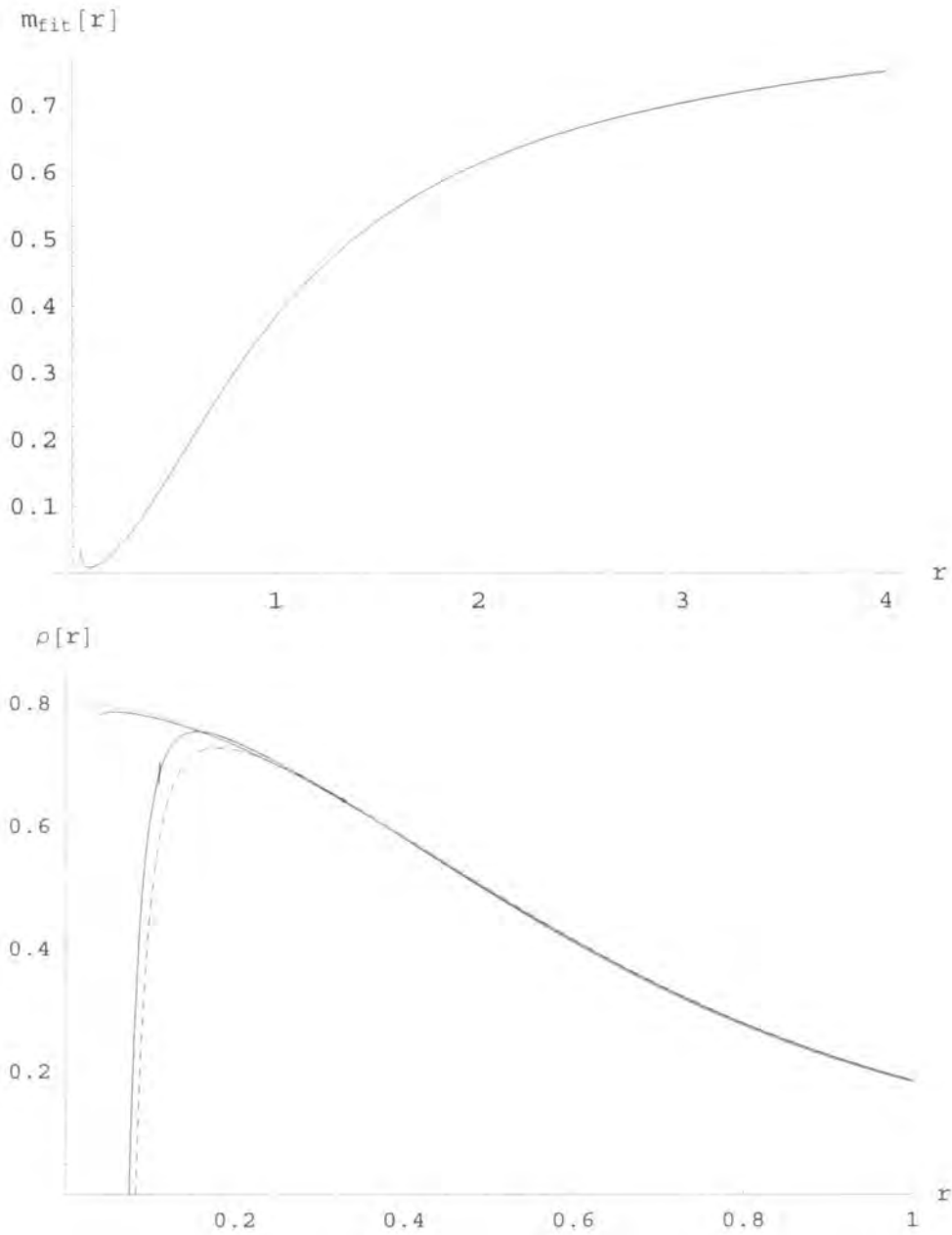
Figure 5.4: Estimates for the mass and density profiles for our "star". As with $h_{0.01}(r)$ and $h_{\text{fit}}(r)$, these match the actual curves closely until low r, although the density estimate $\rho_{\text{fit}}(r)$ (dashed) fails at noticeably higher r than the others. Included in the lower plot are alternative estimates for for the density profile, obtained from (5.1.13) (closest fit) and (5.1.20) (solid)

indeed have simply used the spacelike geodesic method say to extract the information about the star, as $h(r)$ gives $m(r)$, and $m(r)$ gives $\rho(r)$. Extracting $k(r)$ becomes a necessity, however, if one removes the assumption about the matter content; then one also has to compute the pressure profile. It is most easily determined (once we have our fits for $k(r)$ and $h(r)$) from the G_{rr} component of Einstein's equations, and we have that:

$$P_{\text{fit}}(r) = \frac{k'_{\text{fit}}(r)}{2\,r k_{\text{fit}}(r) h_{\text{fit}}(r)} - 1 \qquad (5.1.20)$$

which in our example corresponds to $\rho_{\text{fit}}(r)/2$. Therefore by also plotting $2\,P_{\text{fit}}(r)$ in figure 5.4, we can see how close the fits generated by the two different expressions (5.1.19) and (5.1.20) match, and this provides a check that the matter content is indeed that of a gas of radiation and confirms that our expression, (5.1.13), for $k(r)$ is correct.

Interestingly, we see that this expression provides a slightly better fit to $\rho(r)$ at small r than that from (5.1.19). This is simply because (5.1.20) includes $k_{\text{fit}}(r)$ terms, and the non-linear step size in r in the null extraction method generates a greater amount of data points at low r for the estimate for $k(r)$, thus allowing the derivative of the interpolation function to be more accurately determined. We can obtain the best fit at low r by using $k_{\text{fit}}(r)$ in (5.1.13) and solving for $\rho(r)$ (see figure 5.4), where we have avoided using derivatives.[7]

Finally, we can use the estimates to give a numerical value for our free parameter ρ_0. Taking ρ_∞ as having been calculated from the asymptotic fall off, and approximating the value of $k(0)$ as 0.525, we obtain a value of 0.76, compared with the actual value of $\rho_0 = 0.8$. Whilst the match is fairly good, this is where the accuracy of the estimates for $k(r)$ and $h(r)$ become very important; in taking $k(0) = 0.525$ we have discarded the final few iterations of $k_{\text{fit}}(r)$ at small r, which lead to a kink in the curve, as being erroneous and due to an incomplete recovery of $h(r)$. This is a reasonable assumption to make, as in our previous examples we saw that for too large a step size the method of generating $h_{\text{fit}}(r)$ fails to quite reach down to

---

[7]One should note this does firstly require the value of ρ_∞ to be determined from the fall off of $\rho(r)$ at large r; this is however available from our earlier fit to ρ given in (5.1.19).

$r = 0$. We also have the data from the higher step size fits ($h_{0.1}(r)$ and $h_{0.05}(r)$) with which to analyse the accuracy of our estimates for $h(r)$ at low r. However, as it is the small r region from which the numerical value of ρ_0 is calculated, in order for it to be confidently extracted one must ensure the estimates $h_{\text{fit}}(r)$ and $k_{\text{fit}}(r)$ are thoroughly checked for r close to zero.

5.2 Stability analysis of "star" geometries

The restriction to three dimensions imposed in the above example was done so as to allow the use of spacelike geodesics to probe the bulk, as only in this dimension is their proper length calculable from the entanglement entropy. However, we observed that the behaviour of gravity is non-dynamical in only three dimensions; there is no fall off with distance and as such one could question the physical appropriateness of our model of a "star".

Recent work [82] has made progress in detailing the correct minimal surfaces corresponding to the entanglement entropy to consider in higher dimensions; this leads one to believe our procedure for extracting the metric should be applicable in these higher dimensions, using these minimal surfaces to probe the bulk. Whilst we make headway in generalising the algorithms to use differential rather than integral equations in the following chapter, this presents us with another avenue of interest; one could also ask the question of how the behaviour of the "star" geometries changes as the number of dimensions increases. We have already mentioned how it is different for the case of $d = 3$, but perhaps surprisingly, we find that there is another critical dimension affecting the stability of such scenarios.

Here we present a brief analysis into the stability of radiating perfect fluid stars. We begin by extending the three dimensional equations for a star given in the previous section to d-dimensions, before analysing the behaviour of the star's total mass. We consider the variation of the total mass as a function of the central density, and observe that for large enough dimensionality, the mass increases monotonically with the density. However in the lower dimensional cases, oscillations appear (this was originally noted in the $d = 5$ case in [83]), indicating that the perfect fluid model of

the star is becoming unrealistic. We numerically find the critical dimension separating these two regimes to be 11.0 (to three significant figures), and give an explicit relation, (5.4.11), between the spacetime dimension d and the "saturation density" ρ_c, see section 5.4.1. We also provide a numerical analysis of the behaviour at large central density, in particular the self-similar behaviour that appears in dimension $d < d_c$; several parameters of our numerical model are then also determined analytically from a dynamical systems analysis of the behaviour, where we consider the expansion about a fixed point of the zero-cosmological constant solution.

There are already some instances of such dimension dependent phenomena within general relativity[8]; for example, the Gregory-Laflamme instability [113,114] of black strings, and the work of Belinsky, Khalatnikov and Lifshitz (BKL) [115] and its extensions [116–118], where the dynamics of a spacetime in the vicinity of a cosmological singularity were studied.[9] In these extensions they found that the general behaviour of the relevant Einstein solutions changed from "chaotic" in the low dimensional cases ($d < 11$) to non-chaotic in higher dimensions ($d \geq 11$), in much the same manner as we observe the transition from oscillatory to monotonic total mass behaviour in the radiating star case considered here. It is interesting that their work also reveals a critical dimension of eleven, and a more detailed comparison of the two different scenarios (including an analysis to determine the exact (possibly non-integer) value of d_c for their transition) may yield further insight.

Before we present our findings, we note that this feature (namely the appearance of a critical dimension) of higher dimensional radiating stars has also been simultaneously investigated in two other works. In [4], Vladislav Vaganov analyses the behaviour of radiating perfect fluid models in d-dimensional AdS spacetimes; he

---

[8]Of course, dimension dependent behaviour is not restricted to GR, it is seen in a wide variety of fields, e.g. correlation energies in atomic physics [112].

[9]Briefly, their analysis of the setup was performed using the mixmaster model, where the dynamical behaviour is governed by Kasner exponents and conditions upon them, and in which the evolution continues until the system reaches a stability region where the Kasner exponents remain constant. They observed that such a stability region could only exist for $d \geq 11$, and thus the evolution continues indefinitely for any lower number of dimensions. This has interesting consequences not elaborated on here, which are discussed in detail in the papers cited above.

notes (as we do here) that there is a significant change in the behaviour of the total mass for $d > 11$ (where it becomes a monotonic rather than oscillatory function of the central density), and demonstrates this not only for the mass but also the temperature and entropy.

He also presents a dynamical systems analysis (based on that given in [119]) of the behaviour for a general linear equation of state, $P(r) = q\rho(r)$, which includes the radiation case. This analysis complements the numerical results presented here, providing an analytic derivation of the critical density, which is determined to be $d_c = 10.964\ldots$, consistent with our relation (5.4.11). The specific analysis for the radiation case is given in section 5.5, where we give not only the derivation of the critical density, but also demonstrate how the dynamical systems technique gives analytical expressions for other parameters introduced in our numerical investigation into the self-similar behaviour for $d < d_c$.

The second related paper, [84] by Pierre-Henri Chavanis, presents an in-depth study of the behaviour of general stars ("isothermal spheres") with a linear equation of state in an asymptotically flat background. His results are again complementary, finding that there is monotonic behaviour for $d \geq 11$, in contrast to the oscillatory behaviour observed in lower dimensions. By asymptotic analysis he also finds the value for the critical dimension in the radiation case to be very close to eleven, and although there initially appeared to be a discrepancy between the two alternative calculations of the critical dimension in [4] and [84], the latter was subsequently corrected to agree with the value of $d_c = 10.964\ldots$ found in [4]. His paper also includes a comprehensive investigation into the stability of the different regimes, looking at a number of alternative stellar configurations and considering the behaviour of other thermodynamic parameters (entropy, temperature,...), in addition to the mass.

5.3 Perfect fluid models

We begin by extending the analysis of perfect fluid models from the three-dimensional case given in section 5.1.2 to higher dimensions. Consider a general static, spheri-

cally symmetric d-dimensional AdS spacetime with metric:

$$ds^2 = -k(r)dt^2 + h(r)dr^2 + r^2 d\Omega_{d-2}^2 \tag{5.3.1}$$

By considering a perfect fluid of a gas of radiation, one can obtain implicit expressions for $k(r)$ and $h(r)$ for a simple model of a "star" geometry. For a perfect fluid we have that the stress tensor is of the form:

$$T_{ab} = \rho(r)u_a u_b + P(r)(g_{ab} + u_a u_b) \tag{5.3.2}$$

where u^a is the d-velocity of a co-moving gas, and upon which we impose the further constraint that the matter be purely radiating; this sets $\rho(r) = (d-1)P(r)$ as it requires that T_{ab} be traceless. One obtains the required metric by solving Einstein's equation: $G_{ab} + \Lambda g_{ab} = 8\pi G_d T_{ab}$, with the above stress tensor and a negative cosmological constant, as follows. The relevant components of Einstein's equations in general dimension d are given by:

$$G_{rr} = \left(\frac{d-2}{2}\right)\frac{(d-3)(k(r)-k(r)h(r))+rk'(r)}{r^2 k(r)} = \left(\frac{\rho(r)}{d-1} + \frac{(d-1)(d-2)}{2R^2}\right)h(r) \tag{5.3.3}$$

$$G_{tt} = k(r)\left(\frac{d-2}{2}\right)\frac{(d-3)(h^2(r)-h(r))+rh'(r)}{r^2 h^2(r)} = \left(\rho(r) + \frac{(d-1)(d-2)}{2R^2}\right)k(r) \tag{5.3.4}$$

where we have used that $\Lambda = -(d-1)(d-2)/(2R^2)$, $P(r) = \rho(r)/(d-1)$, and set $8\pi G_d \equiv 1$ for convenience[10]. We can infer the form of $h(r)$ from (5.3.4), as the $k(r)$ dependence cancels, and we find that $h(r)$ is given by:

$$h(r) = \left(1 + \frac{r^2}{R^2} - \frac{m(r)}{r^{d-3}}\right)^{-1} \tag{5.3.5}$$

where $m(r)$ is a mass function (see footnote 5) related to the density via:

$$m(r) = \frac{2}{d-2}\int_0^r \rho(\acute{r})\acute{r}^{d-2}\,\mathrm{d}\acute{r} \tag{5.3.6}$$

---

[10]In the numerical results presented shortly we also set $R = 1$; we include it here to ease comparison with the dynamical systems analysis of the $\Lambda = 0$ (and hence $R = \infty$) case given in section 5.5.

In order to specify a form for $k(r)$, we recall the energy-momentum conservation equation, $\nabla_\mu T^{\mu\nu} = 0$, which for a general perfect fluid without the radiation condition gives:

$$P'(r) + \frac{k'(r)}{2\,k(r)}(P(r) + \rho(r)) = 0 \qquad (5.3.7)$$

which can be re-arranged to give

$$k(r) = \left(\frac{\rho_\infty}{\rho(r)}\right)^{2/d} \qquad (5.3.8)$$

in the radiation case, where we have introduced ρ_∞, which is the leading coefficient of $\rho(r)$ at large r, and is given by $\rho_\infty \approx \rho(r)r^d$ as $r \to \infty$. Substituting $h(r)$ from (5.3.5) into (5.3.3) and eliminating $k'(r)/k(r)$ using (5.3.7) then gives an equation in terms of $m(r)$, $\rho(r)$ and $\rho'(r)$,.

$$\frac{(d-3)}{r^2}\left(1 - \frac{1}{1 + \frac{r^2}{R^2} - \frac{m(r)}{r^{d-3}}}\right) - \frac{2\rho'(r)}{r\,\rho(r)\,d} = \frac{2\rho(r) + (d-1)^2(d-2)/R^2}{(d-1)(d-2)\left(1 + \frac{r^2}{R^2} - \frac{m(r)}{r^{d-3}}\right)} \qquad (5.3.9)$$

which couples with our equation for $m'(r)$:

$$m'(r) = \frac{2}{d-2}\,\rho(r)\,r^{d-2} \qquad (5.3.10)$$

to give a pair of ODEs which generalise (5.1.15) and (5.1.16) to d dimensions. For specified dimension d, these allow the geometry of the spacetime to be numerically generated when they are combined with the relevant boundary conditions: $m(0) = 0$ and $\rho(0) = \rho_0$. The condition $\rho(0) = \rho_0$ specifies the central density of the gas, and we have that for fixed R, ρ_0 is the single free parameter of the system (pure AdS is recovered when $\rho_0 = 0$).

5.4 Total mass as a function of central density

Whilst mathematically one can work with this perfect fluid setup in any number of dimensions (including non-integer ones), one would also like to consider the appropriateness of doing so, given that we wish to use the geometry as the setup for a toy model of a star. In other words, is there any significant change in behaviour as the dimensionality of the model is altered. A particular quantity of interest in analysing the stability of the model is the total mass M of the star, and as we have
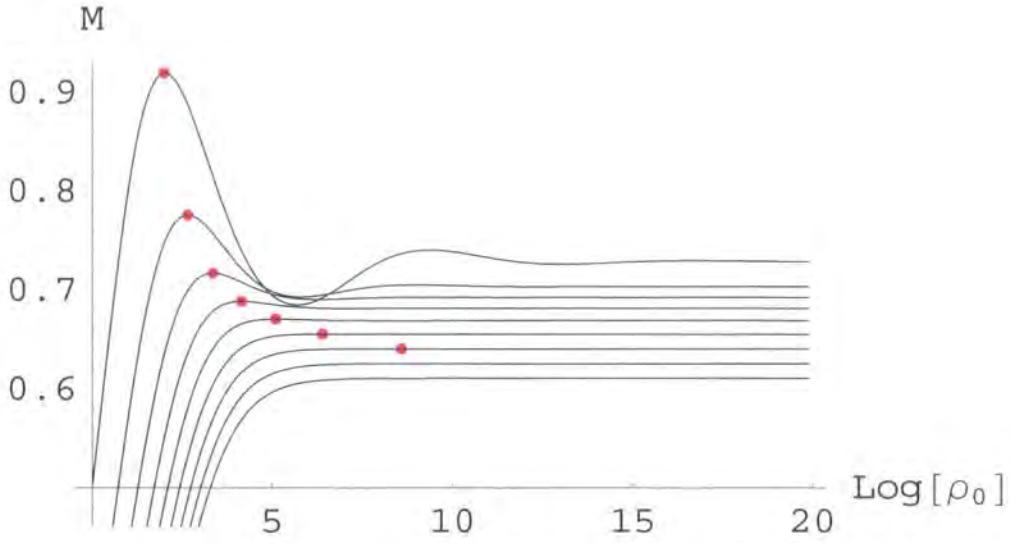
Figure 5.5: Total mass vs density for the radiating perfect fluid model in various dimensions, from $d = 4$ (top curve) through to $d = 12$ (bottom curve). The saturation point for each dimension is indicated by the red dots; these correspond to the maximum value of the total mass in the relevant dimension, at the critical density ρ_c (see section 5.4.1). For d large, there is no local maximum and hence no finite saturation point; in these cases, the maximum total mass is given by the asymptotic value, η_d.

just seen, the mass and density profiles of our gas of radiation are determined by a single parameter: the central density of the gas, ρ_0.

To avoid possible instabilities such as those considered in the asymptotically flat case (in four dimensions) in [120], one would expect the total mass to increase monotonically with ρ_0. One could also expect the total mass to be bounded from above by some maximum value, analogous to the $4d$ asymptotically flat case where we have that for a fixed size R_{star} of star, the maximum possible mass such a star can have is given by $M_{max} = 4R_{star}/9$, [121].

In our scenarios the total mass is indeed bounded from above, however, this maximum is not always the asymptotic value of the total mass at large density. Although we observe that as $\rho_0 \to \infty$ we have $M(\rho_0) \to \eta_d$, where η_d is some finite constant dependent on the dimension d (see section 5.4.2 below for more details), what we do not find in all cases is the total mass approaching this constant monotonically, see figure 5.5. When the dimensionality is low, there are sizable
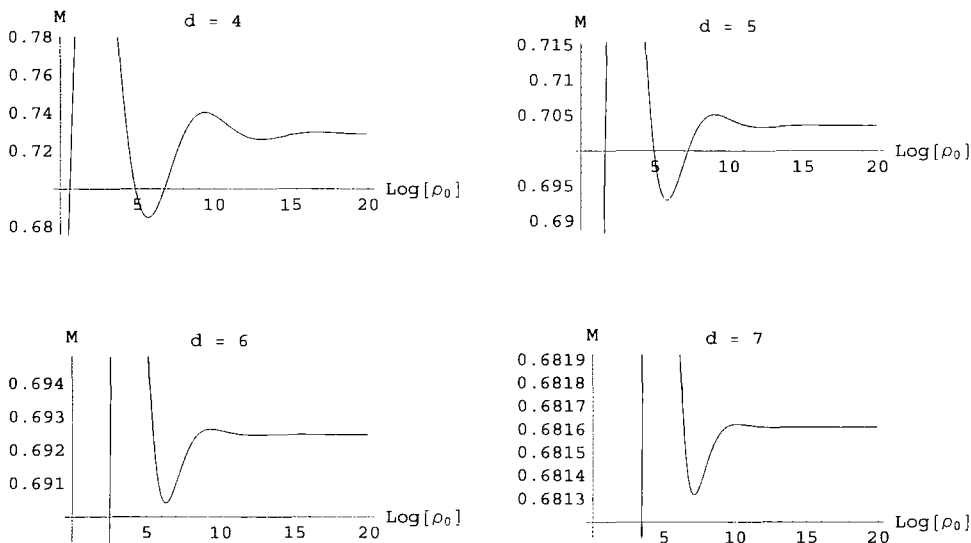
Figure 5.6: The oscillations in the total mass M: as the central density ρ_0 is increased, M does not simply increase monotonically towards its final value η_d. Instead, it reaches a larger maximum before undergoing damped oscillations towards η_d. Note that the amplitude of the oscillations becomes smaller as the dimensionality d is increased.

oscillations about the final value η_d before the curve settles down (see figure 5.6), as was noted in the $d = 5$ case in [83], and in other similar scenarios, e.g. [122], and the star's maximum mass is given by some value greater than η_d. As the dimension is increased, however, these oscillations become less pronounced, and for d sufficiently high they disappear altogether, see figure 5.7.

Ideally one would like to analytically determine the dependence of the shape of the curve on both the dimension d and the density ρ_0, however, due to the complexity of the equations, the exact behaviour must be computed numerically. One can nevertheless use this data to construct models of the various features of the star's behaviour: for example, in section 5.4.2 below, we give an analysis of the total mass at large ρ_0 (where it approaches a constant, dependent on d) in different dimensions.

One particularly interesting feature is the appearance of the turning points in the total mass seen in figure 5.6, and specifically the locations of the local maxima in different dimensions. One can see from the figures that as the dimensionality is increased, the appearance of the first maximum moves to larger ρ_0; by analysing this
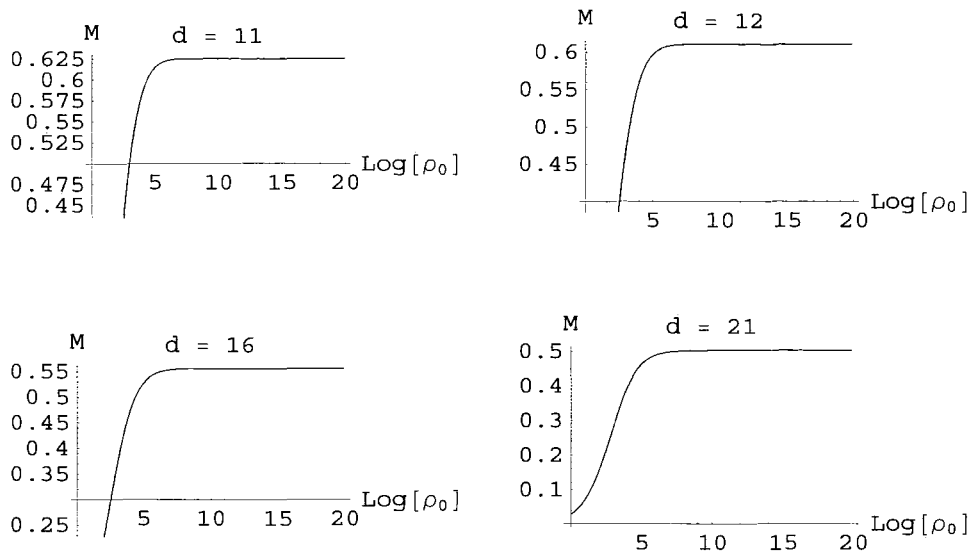
Figure 5.7: For larger d, there are no oscillations in the total mass: M is now a monotonic function of the central density ρ_0, and its maximum is also its asymptotic value as $\rho_0 \to \infty$, namely η_d.

progression one can obtain a remarkably simple relation which immediately gives a value for the critical dimension, above which the oscillations do not exist, and hence the total mass is a monotonic function of ρ_0.

5.4.1 A critical dimension

The saturation point, ρ_c, which we define as being the location of the first local maximum when increasing ρ_0, can be seen to progress to larger and larger ρ_0 as the dimension d is increased, see figure 5.5. What we wish to determine is whether this saturation point appears for all dimension d (for sufficiently large ρ_0), or whether there is a cut-off dimension, d_c, such that for larger d, there is no local maximum and hence no saturation point. Figure 5.8 shows how the saturation point varies with dimension; numerical analysis then finds (to 3 significant figures) that this behaviour is given by the following model:

$$\log \rho_c \approx 0.500\, d + \frac{5.75}{\sqrt{11.0 - d}} - 2.20 \tag{5.4.11}$$
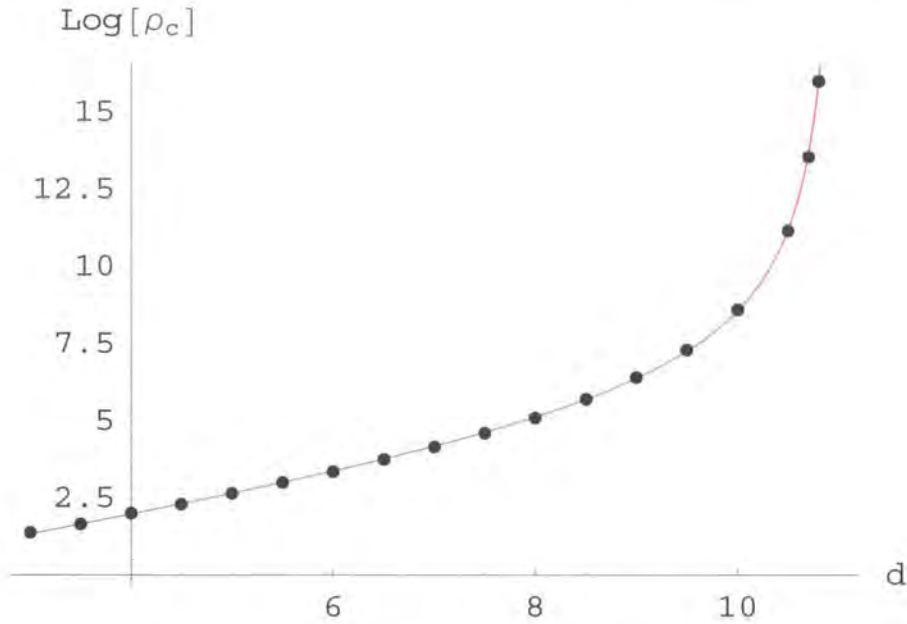
Figure 5.8: The change in the saturation point ρ_c with increasing dimension d. The points plotted are the calculated values for the saturation point for the star model in the corresponding dimension, the red best fit line is the curve given by (5.4.11). The divergent behaviour as d approaches eleven indicates that for $d > 11$ there is no saturation point, and hence no apparent instability in the perfect fluid model of the "star".

which gives a critical dimension $d_c = 11.0.$[11] What is perhaps rather surprising is the simplicity of (5.4.11): not only do we have a critical dimension appearing so clearly, the overall dependence on d is remarkably simple, and the co-efficient of the linear term appears to be exactly one half.

As we shall see in section 5.5, the value of the critical dimension can also be determined by an analytical consideration of the radiating perfect fluid system with zero cosmological constant (i.e. in the limit $R \to \infty$). Although such a solution is singular at $r = 0$, and has infinite mass, by confining the radiation to finite sized box

---

[11]As mentioned earlier, correspondence with V. Vaganov and P. H. Chavanis suggested that the critical dimension in the radiating perfect fluid case is very close to (but not exactly) eleven, and this is indeed the case as we see in the dynamical systems analysis approach in section 5.5, where we obtain a value complementary to the numerical estimate of 11.0 given here. Interestingly, the exact value of $d_c = 11$ appears in the case of Newtonian isothermal spheres, as noticed by Sire and Chavanis in 2002 [123].
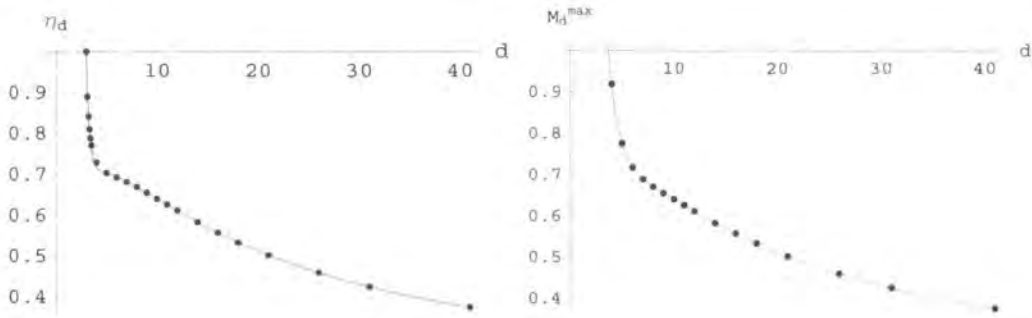
Figure 5.9: The plot on the left shows η_d for various dimensions, with the approximation given in (5.4.12) shown in red. The data points are all at integer values for the dimension, with the addition of points at $d = 3.1, 3.2, ..., 3.5$ to highlight the behaviour of the curve at low d. The righthand plot shows the behaviour of M_d^{max}; this is identical to that of η_d for $d \geq 11$, however for $d < 11$, the maximum is given by the value of the total mass at the saturation point, ρ_c. The best fit approximation (red curve) for each is simple in terms of its d dependence, and provides a good fit over a large range of d.

one can obtain finite mass solutions. The features determined in this configuration can be related to equivalent behaviour in the asymptotically anti-de Sitter case (where the (finite) mass is confined by the AdS potential), and indeed exact values for certain parameters can also be computed. This same analysis is not restricted to the star geometries considered here, it can be used with any linear equation of state [4], or even more generally [119]. Before giving the analysis for our case of perfect fluid radiation, however, we firstly present further numerical results.

5.4.2   Total mass at large ρ_0

In addition to considering the variation of the saturation point for the star with dimension, one can also investigate the asymptotic behaviour of M as ρ_0 becomes large. As mentioned in section 5.4, at large ρ_0, the value of the total mass tends to a constant, η_d, which is then only dependent on the dimension; the value of this constant decreases as d increases. The values are plotted in figure 5.9 and despite the complicated appearance of the plot, a remarkably close fit for all dimensions is given by:

$$\eta_d \approx 0.716 + \exp\left[9.85 - 3.72\,d\right] - \exp\left[-0.603 - \frac{20.3}{d}\right] \qquad (5.4.12)$$

which is also shown in the figure. Checks show that the function continues to give accurate predictions for larger d, and although there is perhaps slightly more complicated behaviour for $d \sim 4$, we do not attempt to investigate this further here[12]; despite the relative compactness of the expression, there is little intuitive origin for any of the constants involved. Nonetheless, it is impressive that the behaviour of the mass at large ρ_0 can be expressed in such simple powers of the dimension.

One can perform a similar analysis of the behaviour of the maximum value of the total mass as the dimension increases; the results are also shown in figure 5.9. For $d > 11$, the maximum total mass corresponds to the asymptotic value, η_d, however, for lower dimension, the maximum is given by the mass at the saturation point. A good fit to the curve is given by:

$$M_d^{max} \approx 0.712 + \exp\left[2.74 - 1.07\,d\right] - \exp\left[-0.592 - \frac{20.5}{d}\right] \qquad (5.4.13)$$

which differs (significantly) from (5.4.12) only in the second term, as to be expected as the curves differ only at low d. Again, however, their is little apparent significance about the values of the numerical constants involved in the expression, and although we have produced fits with relatively simple dependence on d which give accurate predictions for η_d and M_d^{max} over a large range of dimensions, we now turn to an analysis of the oscillatory behaviour, which can be considered both numerically and analytically.

5.4.3 Self-similarity analysis for $d < 11$

Another interesting feature of the plots of the total mass seen in figures 5.5 and 5.6 is the self-similarity exhibited by the oscillatory behaviour as $\rho_0 \to \infty$. A numerical

---

[12]Whilst in the dynamical systems analysis (section 5.5) the $d = 3$ case (where we have $\eta_3 = 1$) needs considering separately, as there is different asymptotic behaviour involved due to the non-dynamical nature of gravity in such a scenario (see section 5.1.2), we find that we can include it both here (in the analysis of η_d) and also in our earlier result for the critical dimension (see section 5.4.1).

d	α_d	β_d	μ_d	ν_d
3.1	0.305	0.184	8.33	0.66
4	0.383	0.371	8.44	0.86
5	0.400	0.601	9.35	0.98
6	0.415	0.825	10.3	1.03
7	0.431	1.03	11.4	1.07

Table 5.2: Numerical estimates for α_d, β_d, μ_d and ν_d (to three significant figures) for the model of the total mass given in (5.4.14) .

analysis of the periodicity and damping of the oscillations seen for $3 < d < 11$ leads us to propose the following model for the total mass:

$$M_d(\rho_0) \approx \eta_d + \alpha_d \exp\left[-\beta_d \log(\rho_0)\right] \cos\left[\mu_d - \nu_d \log(\rho_0)\right] \qquad (5.4.14)$$

which gives a good approximation for the behaviour in the region $\rho_0 > \rho_c$. In (5.4.14), η_d is the asymptotic value of the mass discussed above, and the four parameters α_d, β_d, μ_d and ν_d are constants dependent only on the dimension d. Approximate values for these constants for $d = 3.1, 4, 5, 6$ and 7 are given in Table 5.2.

Although the values given in table 5.2 are only approximate, we nonetheless see interesting dependencies on d emerging. For example, β_d appears to increase roughly linearly with dimension ($\beta_d \approx 0.22d - 0.51$), as do α_d and μ_d for $d \geq 4$. We will see below in the dynamical systems analysis how this linear behaviour of β_d on d is only an approximation to the true behaviour, and the same analysis also provides exact values for the parameter ν_d.

5.5   Dynamical systems analysis

By considering the behaviour of the system of coupled ODEs given in section 5.3 in the limit $R \to \infty$, we can obtain analytical results for some of the interesting features of the radiating perfect fluid star geometries described above. The analysis presented here follows that detailed in both [4] and [119], where it is given in more

general settings; by focusing on the radiation case (where $\rho(r) = (d-1)P(r)$) we can give a good explanation of why the numerical behaviour seen above is so, without excessive over-complication.

The basic idea is to rewrite the equations for $\rho'(r)$ and $m'(r)$ in terms of dimensionless (compact) variables and perform an analysis of the fixed points. The corresponding eigenvalues and eigenvectors obtained by linearising about these fixed points give a complete description of the nearby behaviour (Hartman-Grobman theorem, [124]) on the new state space, which can then be translated back to the physical picture by inverting the transformations given below. Interestingly, for the perfect fluid stars, the dependence of the total mass (as well as other quantities, e.g. the entropy) on the central density, ρ_0, is governed by the behaviour around (and hence the eigenvalues of) a single fixed point. Specifically for our case we will see how this gives both an exact value for the critical dimension d_c, and a clear analytical explanation for the observed behaviour in the two regimes $d < d_c$ (oscillatory) and $d > d_c$ (monotonically increasing). We will also obtain expressions for the β_d and ν_d parameters introduced earlier.

To proceed, we thus set $R = \infty$, and our equations (5.3.9) and (5.3.10) become:

$$\rho'(r) = -\frac{\rho(r)\,d\left((d-3)(d-2)(d-1)m(r) + 2r^{d-1}\rho(r)\right)}{2(d-2)(d-1)(r^{d-2} - r\,m(r))} \tag{5.5.15}$$

$$m'(r) = \frac{2}{d-2}\,\rho(r)\,r^{d-2} \tag{5.5.16}$$

where $8\pi G_d$ has again been set equal to one. Note that we do not include the $d = 3$ example of section 5.1.2 here, as it is a special case (due to the non-dynamical nature of gravity, as discussed previously). We can now introduce the dimensionless variables:

$$u = \frac{2\,r^{d-1}\rho(r)}{(d-2)m(r)} \tag{5.5.17}$$

and

$$v = \frac{(d-1)\,m(r)}{2\,r^{d-3}}\left(1 - \frac{m(r)}{r^{d-3}}\right)^{-1} \tag{5.5.18}$$

which allow equations (5.5.15) and (5.5.16) to be rewritten in the form:

$$\frac{du}{d\xi} = -u\left(1 - d + u + \left(d - 3 + \frac{u}{d-1}\right)\left(\frac{v\,d}{d-1}\right)\right) \tag{5.5.19}$$

$$\frac{dv}{d\xi} = -v\left(d - 3 - u + (d - 3 - u)\left(\frac{2v}{d-1}\right)\right) \tag{5.5.20}$$

where we have also introduced the new independent variable $\xi = \ln(r)$. For the case of positive mass and density we're considering here, both u and v are greater than zero (for non-zero r), and we make a final change of variables to the bounded U and V defined by[13]:

$$U = \frac{u}{1+u}, \qquad V = \frac{v}{1+v} \tag{5.5.21}$$

which gives the system of equations:

$$\frac{dU}{d\lambda} = U(1-U)\left(d - 1 - dU - \left(2d - 4 + \frac{d-3}{d-1}\right)V + \left(2d - 3 + \frac{d(d-5)+3}{(d-1)^2}\right)UV\right) \tag{5.5.22}$$

$$\frac{dV}{d\lambda} = V(1 - V)(3 - d + (d - 2)U)\left(1 + \left(\frac{2}{d-1} - 1\right)V\right) \tag{5.5.23}$$

where we have also introduced the independent variable λ, defined by:

$$\frac{d\lambda}{d\xi} = \frac{1}{(1 - U)(1 - V)} \qquad \left(= (1 + u)(1 + v)\right) \tag{5.5.24}$$

The fixed points of the system (5.5.22) and (5.5.22) are calculated in the usual fashion, by setting both $dU/d\lambda$ and $dV/d\lambda$ to zero and solving for U and V; there are six in total, with eigenvalues then obtained from

$$\frac{d}{d\lambda}\begin{pmatrix} U \\ V \end{pmatrix} = \left.\begin{pmatrix} \frac{\partial}{\partial U}\left(\frac{dU}{d\lambda}\right) & \frac{\partial}{\partial V}\left(\frac{dU}{d\lambda}\right) \\ \frac{\partial}{\partial U}\left(\frac{dV}{d\lambda}\right) & \frac{\partial}{\partial V}\left(\frac{dV}{d\lambda}\right) \end{pmatrix}\right|_{fp} \begin{pmatrix} U - U_{fp} \\ V - V_{fp} \end{pmatrix} \tag{5.5.25}$$

where the matrix components are evaluated at the particular fixed point under consideration. A table of such eigenvalues is given in [4], where they are labelled $T_1, \ldots, T_6$; we do not list them all again here, however, as orbits in the interior of the state space $[0,1]^2$ originate from either T_2 or T_4 and converge to the fixed point T_3 (as is shown in [119]). This fixed point corresponds to the singular self-similar solution given by equation (2.14) of [4], and due to the scale invariance of the system

---

[13]Although the range of both U and V is defined as being $(0, 1)$, in order to perform the fixed point analysis of the asymptotic behaviour, it is necessary that the boundary points also be included; this requires the system given by (5.5.22) and (5.5.23) be C^1 on $[0, 1]^2$, which is manifestly so.

one can consider the entire set of (positive mass) solutions as being represented by a single orbit from T_2 to T_3 (this is true for any linear equation of state, $P(r) = q\rho(r)$).

Although one cannot write an analytic expression for this orbit, one can obtain approximations by linearising about the fixed points. As discussed briefly earlier, as this zero-cosmological constant solution is singular, in order to produce finite mass solutions the radiation must be confined to an (unphysical) box; the two fixed points T_2 and T_3 thus represent solutions with $\rho_0 = 0$ and in the limit $\rho_0 \to \infty$ respectively. The behaviour described by the linearisation about T_3 then reveals aspects of the large ρ_0 limit of the radiating stars (where the confining AdS potential results in the finite mass solutions without the need for any unphysical box), exactly what we analysed numerically in sections 5.4.2 and 5.4.3. This linearisation gives an explanation for the existence of a critical dimension and the differing behaviour seen in higher and lower dimensions, including quantitative expressions for d_c and the β_d and ν_d parameters of Table 5.2, as we shall now show.

Fixed point T_3 corresponds to the following values of U and V:

$$U_{T_3} = \frac{d-3}{d-2}, \qquad V_{T_3} = \frac{2(d-1)^2}{2 - 4\,d + (d-1)d^2} \tag{5.5.26}$$

and has eigenvalues:

$$T_3^{\pm} = \frac{d(d-3)}{2 - 4\,d + (d-1)d^2}\left(1 - d \pm \sqrt{\frac{(d-12)d^2 + 13\,d - 18}{d-2}}\right)$$

$$\equiv k_d\left(1 - d \pm \sqrt{\frac{(d-12)d^2 + 13\,d - 18}{d-2}}\right) \tag{5.5.27}$$

where we denote the coefficient k_d and observe that it is strictly positive for $d > 3$. These eigenvalues govern the behaviour of the solution, and we immediately see that there are two distinct regimes; one where the expression inside the square root is negative, corresponding to the oscillatory behaviour seen in figure 5.6, and one where the expression is positive, resulting in the monotonic behaviour seen in figure 5.7.[14] We thus obtain a value for the critical dimension given by the solution to:

$$(d_c - 12)d_c^2 + 13\,d_c - 18 = 0 \tag{5.5.28}$$

---

[14]The fact that $k_d > 0$ ensures that the fixed point T_3 is a stable focus for the oscillatory behaviour in the $d < d_c$ case; for $d > d_c$, we have that $T_3^{\pm}$ is strictly less than zero, and hence acts as a stable node.

which yields $d_c = 10.964\ldots$, complementary to the value of $d_c = 11.0$ obtained numerically, although with the significance of being non-integer rather than exactly 11; interestingly for any linear equation of state the value of d_c is always in the range $10 \leq d_c \leq 11$, see [4].

We can relate the asymptotic behaviour obtained from the state space picture to the physical quantities of mass and density via several auxiliary equations to those given above, specifically:

$$\frac{dr}{d\lambda} = (1 - U)(1 - V)r\,, \quad \frac{dm}{d\lambda} = U(1 - V)m \qquad (5.5.29)$$

and

$$\frac{d\rho}{d\lambda} = -\frac{V\,d}{d-1}\left(1 - U + \frac{U}{d-1}\right)\rho \qquad (5.5.30)$$

Given expressions for U and V in terms of λ (as obtained from an analysis of the behaviour around the fixed points, say), one can integrate the above to determine corresponding expressions for the mass, radius and density in terms of λ. There is, however, a simple way to see the dependence of the total mass M_d on the central density ρ_0, which also reveals the origin of the β_d and ν_d parameters of our numerical model in section 5.4.3.

Focusing then on the case where $d < d_c$, how does the imaginary term in (5.5.27) lead to the (self-similar) oscillatory behaviour manifest in the total mass at large ρ_0? This can be seen directly from the linearisation about T_3, where we observe similar oscillations in the expressions for $U(\lambda)$ and $V(\lambda)$ (see below); as mentioned above, it is the behaviour around T_3 that governs the behaviour of the physical quantities in the large ρ_0 limit. By considering the behaviour of $U(\lambda)$ and $V(\lambda)$ in terms of ρ_0, we can extract the coefficients which should then match those in (5.4.14) (as argued more fully in [119]). The solutions of (5.5.22) and (5.5.23) in the large λ limit (i.e. about the fixed point T_3) can be expressed as:

$$Re(U(\lambda)) = U_{T_3} + \exp\left(-(d-1)k_d\lambda\right)\cos\left(k_d\lambda\sqrt{\frac{18 - (d - 12)d^2 - 13\,d}{d - 2}}\right) \qquad (5.5.31)$$

$$Re(V(\lambda)) = V_{T_3} + \exp\left(-(d-1)k_d\lambda\right)\cos\left(k_d\lambda\sqrt{\frac{18 - (d - 12)d^2 - 13\,d}{d - 2}}\right) \qquad (5.5.32)$$

d	β_d	ν_d
3.1	$231/1240 \approx 0.186$	$\sqrt{695519}/1240 \approx 0.672$
4	$3/8 = 0.375$	$\sqrt{47}/8 \approx 0.857$
5	$3/5 = 0.6$	$2\sqrt{6}/5 \approx 0.980$
6	$5/6 \approx 0.833$	$\sqrt{13/3}/2 \approx 1.04$
7	$15/14 \approx 1.07$	$2\sqrt{215}/5 \approx 1.05$

Table 5.3: Exact values (alongside decimal equivalents) obtained from the dynamical systems analysis for β_d and ν_d for the model of the total mass (5.4.14).

where we have only kept the real angular term as we are only interested in the period of the oscillations (ν_d) and the coefficient of the damping (β_d); the extra factors (namely α_d and μ_d) cannot be extracted directly from this analysis.[15]

For sufficiently high density stars (i.e. with large ρ_0), we have $\lambda \propto \frac{1}{2}\frac{d\lambda}{d\xi}\big|_{T_3} \log(\rho_0)$, and we thus obtain:

$$\beta_d = \frac{(d-1)k_d}{2(1 - U_{T_3})(1 - V_{T_3})} = \frac{d}{4} + \frac{1}{2d} - \frac{3}{4} \tag{5.5.33}$$

and

$$\nu_d = \frac{k_d}{2(1 - U_{T_3})(1 - V_{T_3})}\sqrt{\frac{18 - (d-12)d^2 - 13d}{d-2}}$$
$$= \frac{1}{4d}\sqrt{(d-2)(18 - (d-12)d^2 - 13d)} \tag{5.5.34}$$

which give the values shown in Table 5.3, provided as a comparison to the numerical estimates obtained in section 5.4.3. We see that they match very closely, with any discrepancies most likely due to a combination of numerical imprecision in the original data for the mass at large ρ_0 and the use of oscillations at insufficiently large ρ_0 for the asymptotic dependence to be totally dominant.

---

[15]Technically, for a solution of this form one should first make a linear change of coordinates such that the matrix on the RHS of (5.5.25) is in diagonal form. This only manifests itself, however, as extra multiplicative constants which do not affect the decay term β_d or oscillation period ν_d, and hence can be ignored.

5.6 Summary

In this chapter we have brought together the two iterative algorithms developed previously, showing how they can be applied sequentially to extract firstly $h(r)$ via the zero-energy spacelike probes, and then $k(r)$ via the null geodesics. This procedure required us to use the estimate for $h(r)$ in our extraction of $k(r)$, and so our first numerical example (section 5.1.1) demonstrated that the ability of the null geodesics to accurately recover $k(r)$ was not affected by any small errors in the estimate for $h(r)$. We thus proceeded to consider a more interesting example, that of a toy model of a radiating (perfect fluid) star in AdS_3, where the restriction to three bulk dimensions was a necessary condition for the boundary information of the spacelike geodesics to be obtainable from the field theory.

This restriction to three dimensions forces a natural unphysicality onto our model of the star, due to the non-dynamical manifestation of gravity, and we would hope in future to be able to develop these numerical techniques for extracting the bulk information to higher dimensions by considering the appropriate minimal surfaces discussed in [82]. Even in these higher dimensions however, the radiating model of a star contains instabilities indicating further unphysicalities, as we saw in the second half of the chapter. By considering the total mass of the star as a function of its central density, ρ_0, we revealed the presence of a "critical dimension", below which the total mass does not increase monotonically with ρ_0 as one might expect for a stable model. Instead, oscillations appear, and by analysing the progression of the corresponding maxima, we numerically computed the critical dimension to be $d_c = 11.0$, see equation (5.4.11). These oscillations also demonstrated self-similar behaviour at large ρ_0, and we presented further numerical analysis for various dimensionality.

These findings were also made in work by two other authors [4, 84], where analytical results (giving a value of $d_c = 10.964\ldots$ for the case of radiating perfect fluid stars) were derived in addition to the numerical evidence. Prompted by the methods developed in [4] and [119], we presented a dynamical systems analysis of our numerical findings which yielded expressions for both the critical dimension and certain parameters of the self-similar model described in section 5.4.3.

Finally, we noted that this change in behaviour from oscillatory to stable, due

to the increase of d past a certain critical dimension, is not confined to the cases of perfect fluids; extensions [116–118] to the work of Belinsky, Khalatnikov and Lifshitz which studied the dynamics of a spacetime in the vicinity of a cosmological singularity found a similar transition; intriguingly they also discovered a critical dimension of eleven.

In the next chapter we go on to consider generalisations of our iterative algorithms for extracting the bulk metric to less symmetric cases, where we can no longer write the geodesic equations in integral form.

Chapter 6

Extensions to less symmetric cases

In all of the previous chapters we have taken the spacetime metric to be both static and spherically symmetric, however, we now consider how the methods for extracting the bulk presented here could be extended to include more general cases.

Reducing the amount of symmetry removes conserved quantities from the geodesics; spherical symmetry gives us conservation of angular momentum, time translational symmetry gives us energy conservation. Consequently, there will be additional unknowns introduced in our analysis of the geodesic path, as we will need to know more details about its route through the bulk; this is not necessarily problematic, however, as there will also be further information available from the geodesic equations, i.e. the geodesic probes will carry more information to the boundary. One important consequence is that the geodesic equations are no longer expressible in integral form, and we have to work with the coupled second order ODEs. Although naturally more complicated, our methods for extracting the bulk involve considering their expansions around the geodesic's minimum radius; this gives significant simplifications, as we shall see in section 6.2.2 where we consider a spacetime which is no longer spherically symmetric.

Rewriting the iterative procedures for extracting the metric in differential form is important both for the generalisations to specific cases with less symmetry, and for the development of a fully covariant method for using the boundary data of the two-point correlation functions and the entanglement entropy to ascertain the geometric structure of the corresponding bulk dual. As we mentioned previously, working

with the differential equations will also generally be necessary when considering the higher dimensional cases, where the use of minimal surfaces rather than spacelike geodesics is required.

Whilst such a coordinate independent method is not presented here, as further analysis of the boundary data in these less symmetric cases is required in order to fully make use of the extra information available, the workings in the following sections provide a good basis from which to begin the construction of one, and perhaps most importantly, give a feel for how such a method could be constructed.

6.1 The boundary data

Our first task then is to analyse the boundary data in the less symmetric cases. Previously, for each type of geodesic (null or static spacelike), we obtained a single (one-dimensional) function's worth of information, in the form of t_{end} vs ϕ_{end} or $\mathcal{L}$ vs ϕ_{end} (figures 3.1 and 4.1). This was obtained by fixing one end of the geodesics on the boundary and varying the single remaining parameter, the (normalised) angular momentum.

For each reduction of symmetry, we introduce an extra dependence to the metric, and add an extra dimension to the information available at the boundary. For example, if one relaxes time-translational invariance, then one has to consider all possible starting values for the geodesic along the time axis. Thus the plot of t_{end} vs ϕ_{end} for the null geodesics is extended along a transverse direction parameterised by t_{start}, resulting in a two-dimensional surface, as shown in figure 6.1a. A similar surface plot arises in the static but non-spherically symmetric case (where the metric is allowed to depend on one of the angular coordinates, ϕ say). Relaxing both symmetries would give a three-dimensional volume of information, which could be viewed as a series of surface plots in much the same way as the surface plots can be thought of as a series of one-dimensional plots (see figure 6.1b). One of the natural questions to now ask is how are our equations for the "gradient" of the boundary information, $dt_{end}/d\phi_{end} = y$ from chapter 3 and $d\mathcal{L}/d\phi_{end} = J$ from chapter 4 modified in these new scenarios?
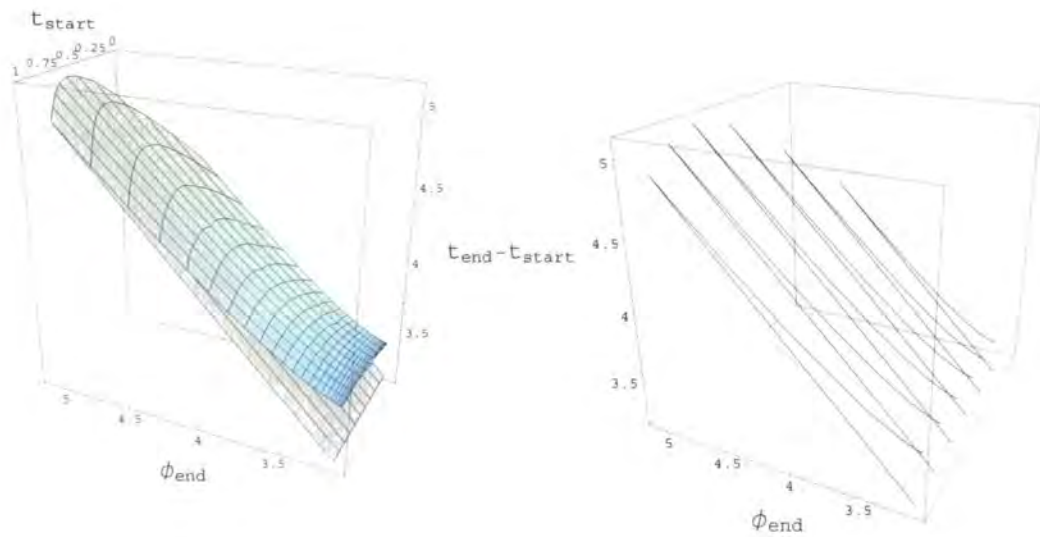
Figure 6.1: The endpoints of null geodesics in a spacetime with reduced symmetry (specifically, with the introduction of time-dependence to the metric). The plot of $(t_{end} - t_{start})$ vs ϕ_{end} is extended along a transverse direction parameterised by t_{start}, resulting in the two-dimensional surface seen on the left. By fixing t_{start} at different values, this surface plot can be viewed as a series of one-dimensional plots, as shown on the right. Each one represents the spread of endpoints obtained by varying y_{start} from zero to one for that particular t_{start}; in the static case, they are all identical.

The first point to note is that we no longer have the integral equations for $dt/d\lambda$ (or $d\mathcal{L}/d\lambda$) and $d\phi/d\lambda$ which led to the analytical derivation of the above expression for the gradients given in sections 3.1.1 and 4.1.1. We can still construct endpoint plots similar to those seen in the symmetric cases by fixing the starting point $(t_{start}, \phi_{start})$ and varying y_{start} (or J_{start}) from 0 to 1 (0 to J_{cutoff}), as mentioned above, however, whilst we might still expect the gradient to be related to the (normalised) angular momentum in some sense, it is not immediately obvious how, as we no longer necessarily have conservation of either energy or angular momentum along the geodesics.

Although we have to compute the paths of the geodesics (and hence their endpoints) via the coupled second order ODEs, we can still investigate numerically what the gradients $dt_{end}/d\phi_{end}$ and $d\mathcal{L}/d\phi_{end}$ represent. A natural guess, given what we know about the symmetric case, would be that they should give some average of the (normalised) angular momentum over the whole path, such as:

$$\frac{dt_{end}}{d\phi_{end}} \overset{?}{=} \frac{\int y(\lambda)\mathrm{d}\lambda}{\int \mathrm{d}\lambda} \tag{6.1.1}$$

and

$$\frac{d\mathcal{L}}{d\phi_{end}} \overset{?}{=} \frac{\int J(\lambda)\mathrm{d}\lambda}{\int \mathrm{d}\lambda} \tag{6.1.2}$$

Initial numerical studies show, however, that this guess appears to be incorrect; plotting the mean value of the (normalised) angular momentum against the value of the gradient does not result in the linear correlation one would expect if the above relations were true. Interestingly, one obtains a very close fit to the gradient by considering the *final* value of the (normalised) angular momentum as the geodesic reaches the boundary; these results are shown in figure 6.2. The seeming correlation is made all the more meaningful when one observes that the curve for y_{mean} is clearly not coincident with the gradient $dt_{end}/d\phi_{end}$, nor are the curves for y_{start} or $y|_{r_{min}}$.[1] Whilst this numerical justification is not to be taken as a proof, there appears sufficient correlation for the gradient of the endpoints to be used to extract

---

[1]Note that whilst the curve for y_{mean} is almost identical to that for $y|_{r_{min}}$ (in figure 6.2), this will not necessarily be true in general, although it would be interesting to determine how often and how closely it holds.
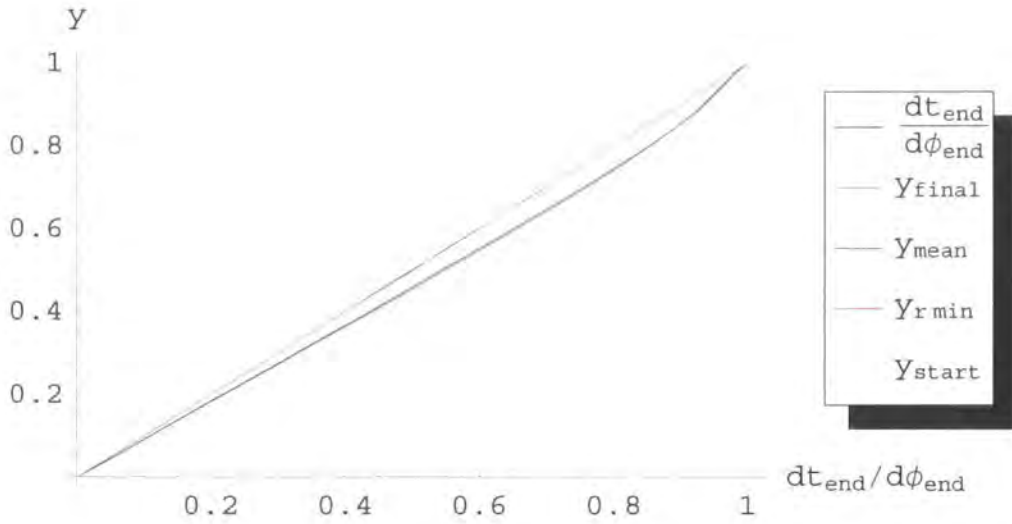
Figure 6.2: For null geodesics in a time dependent (isotropic) spacetime, the figure shows four curves plotting different measures of their normalised angular momentum y: its initial value at ϕ_{start} (lowest curve, in orange), its value at r_{rmin} (red), its average over the whole path (blue), and finally its value at ϕ_{end} (green). Note that each is plotted as a function of the actual endpoint gradient $dt_{end}/d\phi_{end}$, and hence we are looking to determine which choice of y gives the closest match to a straight line through the origin, also included (black); it is the third curve which is coincident with this line, thus implying $dt_{end}/d\phi_{end} = y_{final}$.

y_{final} for the whole set of null geodesics. A similar numerical argument gives that $d\mathcal{L}/d\phi_{end} = J_{final}$ for the case of a static but non-spherically symmetric spacetime.

Given the close fit of the gradients to y_{final} and J_{final}, we thus consider in the following sections how it is possible to use this information to extract the metric functions via both the spacelike and null geodesics.

We do not give any further numerical analysis of the gradients' possible relation to $y(\lambda)$ and $J(\lambda)$, however, we make further comments about their possible form at the end of section 6.2. This is motivated by our discovery that without certain restrictions being placed on the form of the metric one attempts to recover (or, in other words, without further knowledge of the metric), any such extraction is rendered impossible by the presence of a large number of unknowns, directly related to the coefficient of $d\phi^2$ in the metric, which of course is intrinsically linked to the

definition of the angular momentum.

In addition to the gradients from the set of one-dimensional plots in figure 6.1b, which were obtained from the two-dimensional surface by fixing the starting point of the geodesic, one could also ask what the gradients in the new direction (i.e. along t_{start} in the time-dependent case) represent, for fixed t_{end} or fixed y_{final}. As all gradients of this type are identically zero for the static case, one should expect them to somehow encode information about the time-dependence of the metric functions. Identifying what this gradient represents is difficult, however, both analytically, as one has no obvious starting point for how to write down dt_{end}/dt_{start} for example, nor any useful comparison with the static case (other than that the expression should vanish in the time-independent limit), and numerically, due to the vast range of possible models one could use to fit to the curve, and the difficulty in completely eliminating errors from the data for the geodesics generated via the ODEs. The presence of this extra gradient information and the fact that it is currently unused provides further indication that one might be able to resolve the aforementioned problem of an excessive number of unknowns if one could better access the information contained in this extra dimension of the surface plot.

Having thus seen how the boundary data can be described as higher dimensional surfaces in the less symmetric cases, and how the gradients $dt_{end}/d\phi_{end}$ and $d\mathcal{L}/d\phi_{end}$ give the final value of the (normalised) angular momentum, we now consider in detail how introducing an angular dependence to the metric affects the geodesic equations. We show in a simplified case how the extra unknowns then introduced are accompanied by sufficient extra equations such that one can still construct an iterative algorithm by which to extract the metric information.

6.2 Introducing angular dependence to the metric

The full consideration of a generic, non-symmetric metric in arbitrary dimension is beyond the scope of this work, and indeed is both unwieldy from a formulaic point of view (as the geodesic equation (2.3.2) becomes increasingly complicated) and loses much of the intuitive feel for the principles of reconstructing the metric

which we have built in earlier chapters. Thus rather than immediately removing all symmetry from the bulk, and attempting to analyse the generalisation of the methods to these more complex scenarios, we begin by considering the loss of only one such symmetry (isotropy) by introducing an angular dependence to the metric, and restrict ourselves to three dimensions so as to keep the entanglement entropy relation of chapter 4 applicable. This scenario is particularly helpful as keeping time-translational invariance ensures that the relevant spacelike geodesic (i.e. the minimal surface whose area is dual to the entanglement entropy) is still the zero-energy geodesic used in previous chapters.

Even in such a simple case, the completely arbitrary generalisation of (4.1.1) to include angular dependence should include three unknown functions (after choosing a gauge which eliminates three of the original six), which could then be written as[2]:

$$ds^2 = -k(r, \phi)dt^2 + h(r, \phi)dr^2 + j(r, \phi)d\phi^2 \qquad (6.2.1)$$

Unfortunately, however, we shall see at the end of this section how attempting to recover such a general form of the metric appears to introduce too many unknowns than can be determined from the boundary information we can currently utilise (namely the series of one-dimensional plots of figure 6.1b). It is unclear whether this is due to the endpoint data not containing enough information to fully determine the metric in such cases, or rather that it does and it is instead our use of the data that is not sufficiently developed; as we mentioned above, there is the currently untapped information contained in the 2nd dimension of the surface plot in figure 6.1a.

Interestingly, however, if one specifies the form of $j(r, \phi)$ explicitly the analysis is greatly simplified, with the result that one can construct an iterative method for determining $h(r, \phi)$ via the static spacelike geodesic probes, and $k(r, \phi)$ via the null

---

[2]Often in practice it is simpler from a notational point of view to keep cross terms such as $drd\phi$ rather than write the metric in this form, however, the main concern is the presence of the three unknown functions k, h and j. Also, one should note that although one can often combine these to write the metric in a simpler form (using an integrating factor) which overall only has two unknown functions, this is not necessarily guaranteed.

ones. Thus if at some point in the future the endpoint information[3] could be used to a greater degree (to determine either the form of $j(r, \phi)$ when it is not specified explicitly, or provide further coupled equations to those given below), the method presented here could be applied in the more general case.

Consider then the following modification to the metric, where we have set $j(r, \phi) = r^2$:

$$ds^2 = -k(r, \phi)dt^2 + h(r, \phi)dr^2 + r^2 d\phi^2 \tag{6.2.2}$$

This is simply the original metric (4.1.1) with the new freedom that the two functions k and h can depend on the angular coordinate ϕ in addition to the radial coordinate r, and we follow our previous approach (see chapter 5) of firstly using the spacelike geodesics to determine h, then the null geodesics to determine k.

For the above metric, the geodesic equation (2.3.2) yields the following set of second order differential equations:

$$h(r, \phi)\frac{d^2 r}{d\lambda^2} = r\left(\frac{d\phi}{d\lambda}\right)^2 - \frac{1}{2}\frac{\partial k(r, \phi)}{\partial r}\left(\frac{dt}{d\lambda}\right)^2 - \frac{1}{2}\frac{\partial h(r, \phi)}{\partial r}\left(\frac{dr}{d\lambda}\right)^2 - \frac{\partial h(r, \phi)}{\partial \phi}\frac{dr}{d\lambda}\frac{d\phi}{d\lambda} \tag{6.2.3}$$

$$\frac{d^2 t}{d\lambda^2} + \frac{1}{k(r, \phi)}\left(\frac{\partial k(r, \phi)}{\partial r}\frac{dt}{d\lambda}\frac{dr}{d\lambda} + \frac{\partial k(r, \phi)}{\partial \phi}\frac{dt}{d\lambda}\frac{d\phi}{d\lambda}\right) = 0 \tag{6.2.4}$$

$$\frac{d^2 \phi}{d\lambda^2} + \frac{1}{2r^2}\left(\frac{\partial k(r, \phi)}{\partial \phi}\left(\frac{dt}{d\lambda}\right)^2 - \frac{\partial h(r, \phi)}{\partial \phi}\left(\frac{dr}{d\lambda}\right)^2 + 4r\frac{dr}{d\lambda}\frac{d\phi}{d\lambda}\right) = 0 \tag{6.2.5}$$

As there is no time-dependence in the metric, we again have energy conservation, encapsulated by (6.2.4) above, which can be integrated over λ as before to give:

$$E = k(r, \phi)\frac{dt}{d\lambda} \tag{6.2.6}$$

Finally, the constraint from extremizing the action:

$$\kappa = -k(r, \phi)\left(\frac{dt}{d\lambda}\right)^2 + h(r, \phi)\left(\frac{dr}{d\lambda}\right)^2 + r^2\left(\frac{d\phi}{d\lambda}\right)^2 \tag{6.2.7}$$

---

[3]Whilst the most obvious additional use of the endpoint information is the consideration of the gradient along the extra dimension, there may also be further information in the gradients $dt_{end}/d\phi_{end}$ and $d\mathcal{L}/d\phi_{end}$, as these are directly related to y and J, and hence the coefficient of $d\phi^2$, $j(r, \phi)$. Although our numerical results indicate that the gradient simply gives the *final* value of the (normalised) angular momentum, there could be hidden subtleties we have not unearthed which yield greater information about the metric. See the end of the section for further discussion.

provides the distinction between the null ($\kappa = 0$) and spacelike ($\kappa = 1$) geodesics used to probe the bulk. With the introduction of an angular dependence to the metric, our approach to extracting the metric must now be concerned with not only the radial direction, but also this angular direction; as we shall now see, there is a natural generalisation of the methods of the previous chapters which retains the idea of probing the bulk in incremental steps in the radius, and hence the essence of our iterative algorithms.

6.2.1 Overview of the extraction procedure

Recall the setup we had before, when there was no angular dependence in the metric: we considered a series of geodesics which probed deeper and deeper into the bulk - in other words, we had one which probed down to each r_{n-i}. These were specified by the angular separation of the endpoints on the boundary, and the actual values of the ϕ_{start} and ϕ_{end} were unimportant. This allowed us to reconstruct the bulk step by step, one value of $f(r_{n-i})$ at a time.

Now, what is the analogous method in the non-spherically symmetric case? At each step of the iteration we can still consider some fixed angular separation of the endpoints, however, we must also vary ϕ_{start} from 0 to 2π (with some choice of slicing sufficient to give an accurate estimate), such that for each iterative step we recover a "ring" of information about the metric. The subsequent steps then recover smaller and smaller rings, extracting the metric function down to lower and lower radii. An important point to note is that although each ring is specified by a label $n - i$, they will *not* be rings of constant radius, and hence the r_{n-i} will also depend on ϕ. This is because geodesics with the same separation of endpoints on the boundary but different ϕ_{start} will *not* necessarily probe to the same depth in the bulk, due to the angular dependence of the metric.

We originally saw in chapter 3 how one could use the null geodesics to recover one function's worth of information about the metric, and then in chapter 4 how one could use the static spacelike geodesics to recover a complementary function's worth of information; in combination they could then be used to recover both unknown functions $k(r)$ and $h(r)$. Here we again have two unknown functions $k(r, \phi)$

and $h(r, \phi)$, and by firstly considering the spacelike geodesics, one can recover the function $h(r, \phi)$, proceeding as follows.

6.2.2 Determining $h(r, \phi)$

As the metric has no time dependence and we are working in three bulk dimensions, the pertinent minimal surface in the bulk for the entanglement entropy relation, equation (2.2.21), is again a static, spacelike geodesic connecting the endpoints of region A, as shown in figure 2.6. Thus we are free to choose the zero energy slice as before and set $E = 0$ in the geodesic equations. However, given the new ϕ dependence of the metric, this geodesic will no longer (necessarily) have conserved angular momentum, and hence $J_{start} \neq J_{final}$. Note that we are still using the same definition of the angular momentum as before, namely $J = r^2 \dot{\phi}$, but since $\dot{\phi}$ is no longer a Killing vector, J is not necessarily constant over the entire geodesic path.

This has important consequences for our extraction of $h(r, \phi)$, as we can no longer immediately determine the minimum radius of the geodesic, r_{min} from the plot of proper length vs ϕ_{end}, as $d\mathcal{L}/d\phi_{end} = J_{final} \neq J|_{rmin}$. The additional information encapsulated within the geodesic equations is, however, sufficient to overcome this added complication (in the case where we have specified $j(r, \phi) = r^2$). How then do we proceed? As in the spherically symmetric cases considered earlier, we again focus on the properties of the geodesics at their minimum radii: for a static, spacelike geodesic we have the following relations,

$$\frac{dt}{d\lambda} = 0 \quad \text{from choosing the zero energy slice} \tag{6.2.8}$$

$$\left.\frac{dr}{d\lambda}\right|_{r_{min}} = 0 \quad \text{by definition} \tag{6.2.9}$$

$$\left.\frac{d\phi}{d\lambda}\right|_{r_{min}} = \frac{1}{r_{min}} \quad \text{from the definition of } J \text{ and that } J|_{rmin} = r_{min} \tag{6.2.10}$$

which then allow the full geodesic equations (6.2.3) and (6.2.5) to be considerably simplified at the point $r = r_{min}$:

$$\left.\frac{d^2\phi}{d\lambda^2}\right|_{r_{min}} = 0 \tag{6.2.11}$$

and

$$\frac{d^2r}{d\lambda^2}\bigg|_{r_{min}} - \frac{r_{min}}{h(r_{min}, \phi|_{r_{min}})}\left(\frac{d\phi}{d\lambda}\bigg|_{r_{min}}\right)^2 = 0 \tag{6.2.12}$$

which implies:

$$\frac{d^2r}{d\lambda^2}\bigg|_{r_{min}} = \frac{1}{r_{min}h_{min}} \tag{6.2.13}$$

where we have defined $h_{min} \equiv h(r_{min}, \phi|_{r_{min}})$ for convenience. By differentiating the geodesic equation with respect to λ, we can obtain similarly compact expressions for the higher order derivatives of r and ϕ:

$$\frac{d^3\phi}{d\lambda^3}\bigg|_{r_{min}} = -\frac{2}{r_{min}^3 h_{min}} \quad, \quad \frac{d^4\phi}{d\lambda^4}\bigg|_{r_{min}} = \frac{5}{r_{min}^4 h_{min}^2}\frac{dh(r, \phi)}{d\phi}\bigg|_{r_{min}} \tag{6.2.14}$$

and

$$\frac{d^3r}{d\lambda^3}\bigg|_{r_{min}} = -\frac{2}{r_{min}^2 h_{min}^2}\frac{dh(r, \phi)}{d\phi}\bigg|_{r_{min}} \tag{6.2.15}$$

This immediately shows that the $\partial h(r, \phi)/\partial\phi$ term which embodies the non-isotropy of the metric appears in the fourth derivative of ϕ and the third derivative of r (with respect to λ); this is a consequence of our definition of J, where we have that both:

$$\frac{dJ}{d\lambda} = r^2\frac{d^2\phi}{d\lambda^2} + 2r\frac{dr}{d\lambda}\frac{d\phi}{d\lambda} \tag{6.2.16}$$

and

$$\frac{d^2J}{d\lambda^2} = r^2\frac{d^3\phi}{d\lambda^3} + 2r\frac{d^2\phi}{d\lambda^2} + 2\frac{dr}{d\lambda}\frac{d\phi}{d\lambda} + 2r\frac{d^2r}{d\lambda^2}\frac{d\phi}{d\lambda} + 2r\frac{dr}{d\lambda}\frac{d^2\phi}{d\lambda^2} \tag{6.2.17}$$

are identically zero at $r = r_{min}$ (by relations (6.2.10), (6.2.11), (6.2.13) and (6.2.14) above). Hence in order to incorporate correctly the non-conservation of J along the geodesic, we must Taylor expand to order $d^3J/d\lambda^3$, where we have:

$$\frac{d^3J}{d\lambda^3} = \frac{1}{r_{min}^2 h_{min}^2}\frac{dh(r, \phi)}{d\phi}\bigg|_{r_{min}} \tag{6.2.18}$$

which is clearly proportional to both $d^4\phi/d\lambda^4$ and $d^3r/d\lambda^3$. The general behaviour of J over the geodesic path is depicted in figure 6.3; it is constant at large and small λ (as the geodesic is near the boundary and away from the deformation), and although it varies as it approaches the minimum radius, at the point r_{min} (indicated by the dashed red line) the gradient is again zero.

With these equations in mind, we now look to expand the coordinates r and ϕ, around this minimum radius r_{min}; our idea is the same as previously, to approximate
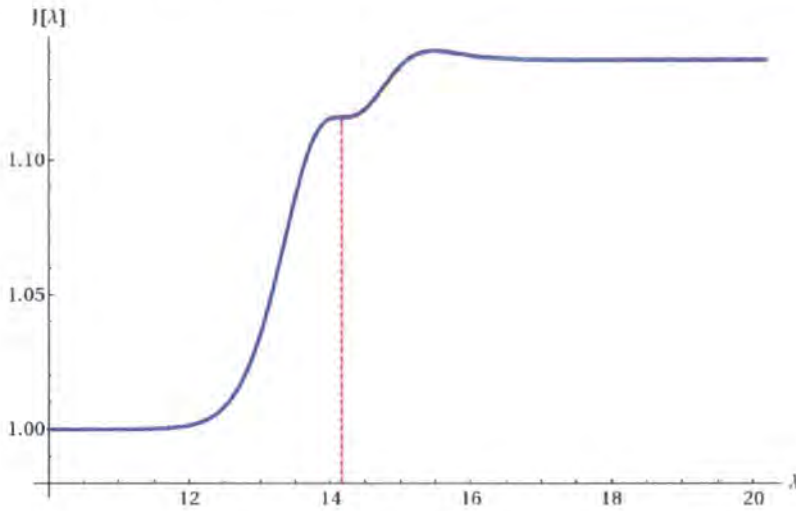
Figure 6.3: Plot showing the variation of the angular momentum $J(\lambda)$ over a typical (zero-energy spacelike) geodesic path; it is constant at large and small λ, when the geodesic is near the boundary and far from the deformation. The dashed red line indicates when the geodesic is at its minimum radius, where $dJ/d\lambda = d^2J/d\lambda^2 = 0$.

a small area around r_{min} up to some slightly larger radius, where the metric is already known (we again use the assumption that the metric is approximately pure AdS near the boundary for the first step).

Before continuing, there is an important distinction to make between this current setup and the spherically symmetric case, when Taylor expanding away from the minimum radius. In the original case, where the metric had only radial dependence, it did not matter in which direction along the geodesic one expanded along away from r_{min} as the paths were both identical (the geodesic was symmetric about r_{min}), as evident from figure 2.6. With the addition of an angular dependence to the metric, one now has to consider the two directions away from r_{min} independently, and we thus introduce additional labels a and b for the different directions.[4] Returning to our notation of chapter 3, where we denote the current step of the iteration as $n - i$ (and hence $r_{min} = r_{n-i}$ etc), the values of the angular momentum at r^a_{n-i+1} and

---

[4]This is in addition to the idea that we now need vary the starting point of the geodesic all around the boundary in order to recover a ring of information at each step, as described in section 6.2.1 above.

r^b_{n-i+1} will be different: we shall denote then J^a_{n-i+1} and J^b_{n-i+1} respectively.

Now consider our proposed iterative process for recovering the metric: at each step, we shall recover a ring of information, which can be used to generate an interpolating function estimate for $h(r, \phi)$. So for the ith step, where the geodesics have minimum radius r_{n-i} (for ϕ ranging from 0 to 2π), the bulk can be taken to be known from r_{n-i+1} outwards.[5]

We then proceed as follows: begin by choosing some specific ϕ_{start} from which the geodesics all originate, and which results in a corresponding plot of $\mathcal{L}$ vs ϕ_{end}. We thus have that $d\mathcal{L}/d\phi_{end} = J_{final} = J^b_n$, where the last equality comes from our taking the spacetime to be pure AdS for $r \geq r_n$, and hence J is conserved from this point to the boundary. By using the extracted estimate for the metric function $h(r, \phi)$, one can use this known value for the final angular momentum to determine J^b_{n-i+1} (the value of J at r^b_{n-i+1}) by numerical evaluating the coupled ODEs given in equations (6.2.5) and (6.2.7), with the appropriate boundary condition on $d\phi/d\lambda$, down to r^b_{n-i+1}.

This leaves us with J^a_{n-i+1} as an apparent unknown; we currently don't know $J_{start} = J^a_n$, and hence can't work along the geodesic to r^a_{n-i+1}. We can easily obtain the value of J_{start}, however, by considering a second set of field theory data in conjunction with the first. Our current geodesic has angular separation $\phi_{end} - \phi_{start} = \gamma$ say, and we used this and the proper length data (from the entanglement entropy) to determine J_{final}. By simply using our current endpoint for the geodesic as the starting point for a different set of geodesics, $\theta_{start} := \phi_{end}$, as illustrated in figure 6.4, we obtain a new set of endpoints, with a corresponding plot of proper length vs θ_{end}. The point we are interested in is where the angular separation on this new plot is the same as before, i.e. when $\theta_{end} - \theta_{start} = \gamma$; these must then be connected by our original geodesic. By taking the gradient at this point, we can obtain the final value of angular momentum, $\mathcal{J}$, for this geodesic, which by

---

[5]Recall that the rings of recovered information will not be at constant radius; the value of r_{n-i+1} (and r_{n-i}) will vary around the ring.
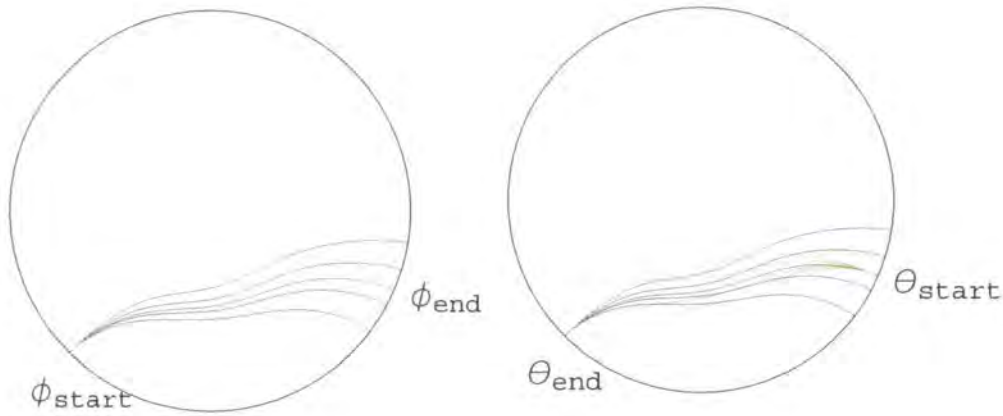
Figure 6.4: For our geodesic currently under consideration (the green curve), which begins at ϕ_{start} and ends at ϕ_{end}, we can determine the value of J_{final} from our knowledge of the neighbouring geodesics which all began at ϕ_{start} (grey curves) as usual. By considering the corresponding set of geodesics which all begin at $\theta_{start} := \phi_{end}$ (orange curves), we obtain a second set of endpoint data from which we can determine J_{start}, by identifying the geodesic with $\theta_{end} = \phi_{start}$.

construction must be equal to the value of J_{start} we required. Hence we have:

$$\frac{d\mathcal{L}}{d\theta_{end}} = \mathcal{J}_{final} \equiv J_{start} = J_n^a \tag{6.2.19}$$

and we can use this to determine J_{n-i+1}^a. We thus have values for J_{n-i+1}^a and J_{n-i+1}^b for the geodesic, and can now consider the expansions of the geodesic equation around $r_{min} = r_{n-i}$.

We begin with the angular coordinate ϕ, and as we have been working with the angular momentum J, we use an expansion of $d\phi/d\lambda$ to give:

$$\begin{aligned}
\left.\frac{d\phi}{d\lambda}\right|_{r_{n-i+1}^b} &\approx \left.\frac{d\phi}{d\lambda}\right|_{r_{n-i}} + \left.\frac{d^2\phi}{d\lambda^2}\right|_{r_{n-i}} (\lambda_{n-i+1}^b - \lambda_{n-i}) \\
&\quad + \left.\frac{d^3\phi}{d\lambda^3}\right|_{r_{n-i}} \frac{(\lambda_{n-i+1}^b - \lambda_{n-i})^2}{2} + \left.\frac{d^4\phi}{d\lambda^4}\right|_{r_{n-i}} \frac{(\lambda_{n-i+1}^b - \lambda_{n-i})^2}{6} \\
&= \frac{1}{r_{n-i}} - \frac{(\lambda_{n-i+1}^b - \lambda_{n-i})^2}{r_{n-i}^3 h_{n-i}} + \frac{5(\lambda_{n-i+1}^b - \lambda_{n-i})^3}{6 r_{n-i}^4 h_{n-i}^2} \frac{\partial h_{n-i}}{\partial \phi} \tag{6.2.20}
\end{aligned}$$

where we have used the appropriate relations for the derivatives of ϕ w.r.t λ at r_{min} given earlier. As we can expand in both directions, we also have an additional

expression with $b \to a$. Note that we have to include terms down to $d^4\phi/d\lambda^4$ as this is the first order at which the change in the angular momentum J at the minimum radius appears, as mentioned earlier.

Finally therefore, using our definition of J, we can express $d\phi/d\lambda$ at r^b_{n-i+1} as $J^b_{n-i+1}/(r^b_{n-i+1})^2$ and write:

$$\frac{J^b_{n-i+1}}{(r^b_{n-i+1})^2} \approx \frac{1}{r_{n-i}} - \frac{(\lambda^b_{n-i+1} - \lambda_{n-i})^2}{r^3_{n-i}h_{n-i}} + \frac{5(\lambda^b_{n-i+1} - \lambda_{n-i})^3}{6r^4_{n-i}h^2_{n-i}}\frac{\partial h_{n-i}}{\partial\phi} \qquad (6.2.21)$$

and similarly for J^a_{n-i+1}.

For the radial expansion we have:

$$\begin{aligned}
r^b_{n-i+1} &\approx r_{n-i} + \frac{dr}{d\lambda}\bigg|_{r_{n-i}}(\lambda^b_{n-i+1} - \lambda_{n-i}) \\
&\quad + \frac{d^2r}{d\lambda^2}\bigg|_{r_{n-i}}\frac{(\lambda^b_{n-i+1} - \lambda_{n-i})^2}{2} + \frac{d^3r}{d\lambda^3}\bigg|_{r_{n-i}}\frac{(\lambda^b_{n-i+1} - \lambda_{n-i})^2}{6} \\
&= r_{n-i} + \frac{(\lambda^b_{n-i+1} - \lambda_{n-i})^2}{2r_{n-i}h_{n-i}} - \frac{(\lambda^b_{n-i+1} - \lambda_{n-i})^3}{3r^2_{n-i}h^2_{n-i}}\frac{\partial h_{n-i}}{\partial\phi} \qquad (6.2.22)
\end{aligned}$$

and similarly for r^a_{n-i+1}. Note that these approximations reduce to the correct behaviour in the spherically symmetric case (as they must): the extra terms contain a factor of $\partial h(r,\phi)/\partial\phi$, thus if there is no angular dependence in the metric, $\partial h(r,\phi)/\partial\phi = 0$ and angular momentum is again conserved.

What we now have should then be enough to determine the metric at this point, as we have four equations, (6.2.21) and (6.2.22) for both a and b expansions, and four unknown parameters associated with the minimum radius, namely: r_{n-i}, h_{n-i}, $\partial h_{n-i}/\partial\phi$ and λ_{n-i}. We saw above how the quantities J^a_{n-i+1} and J^b_{n-i+1} could both be calculated from the boundary information, and the two remaining factors, λ^a_{n-i+1} and λ^b_{n-i+1} are immediately obtainable in much the same way; we have boundary conditions for λ from our knowledge of $\mathcal{L}$; the definition of proper length is simply the integral over all λ along the path. Thus by choosing $\lambda_{start} = 0$ and $\lambda_{end} = \mathcal{L}$ and using our knowledge of the bulk down to r^a_{n-i+1} and r^b_{n-i+1}, by evaluating the geodesic equations we can determine λ^a_{n-i+1} and λ^b_{n-i+1}.

We thus have an estimate for the metric function $h(r,\phi)$ and its partial derivative $\partial h(r,\phi)/\partial\phi$ at the point (r_{n-i}, ϕ_j) (although ϕ_j was not explicitly calculated, it is easily determined once r_{n-i} and λ_{n-i} are known, for example by considering a series

expansion for ϕ similar to those in (6.2.20) and (6.2.22)).[6] By varying ϕ_{start} from 0 to 2π (whilst keeping the angular separation of the endpoints fixed) and repeating the above, one can obtain estimates for $h(r_{n-i}, \phi)$ for an arbitrarily large number of ϕ_j and use these to construct an interpolating function estimate for $h(r_{n-i}, \phi)$ for all ϕ, thus extracting the "ring" of information described in section 6.2.1.

One can then repeat this whole process with geodesics with slightly larger $\phi_{end} - \phi_{start}$, which have longer proper length and which probe down to a slightly smaller set of minimum radii denoted r_{n-i-1}, and obtain $h(r_{n-i-1}, \phi)$. Continuing iteratively through the bulk, this results in an interpolation function estimate for $h(r, \phi)$ over the whole range of r and ϕ, constructed from the discrete lattice of points whose separation can be made arbitrarily small by our choices of step size in both radial and angular directions.

Determining $h(r, \phi)$ with an arbitrary $j(r, \phi)$

Before we turn to the second stage of the extraction involving the null geodesics, we further discuss why keeping the function $j(r, \phi)$ as an unknown is so problematic (recall that we set $j(r, \phi) = r^2$ in section 6.2). For arbitrary $j(r, \phi)$, the r and ϕ components of the geodesic equation for the zero-energy spacelike geodesics become:

$$h(r, \phi)\frac{d^2 r}{d\lambda^2} = \frac{1}{2}\frac{\partial j(r, \phi)}{\partial r}\left(\frac{d\phi}{d\lambda}\right)^2 - \frac{1}{2}\frac{\partial h(r, \phi)}{\partial r}\left(\frac{dr}{d\lambda}\right)^2 - \frac{\partial h(r, \phi)}{\partial \phi}\frac{dr}{d\lambda}\frac{d\phi}{d\lambda} \quad (6.2.23)$$

---

[6]Interestingly, in the above method we have avoided introducing the unknown $\partial h(r, \phi)/\partial r$ into the equations, a fact that mirrors what we saw in the spherically symmetric case described in chapter 4 and Appendix B.1. There we found that the lowest order series expansion to the relevant integral did not contain a $dh(r)/dr$ term, see equation (4.1.16), however, in our numerical study it transpired that using a next-to-lowest order expression (equation (B.1.2) in the appendix) with a linear approximation for $dh(r)/dr$ proved more accurate. Returning to the non-spherically symmetric case being investigated here, avoiding any $\partial h(r, \phi)/\partial r$ terms came by our stopping of the series expansions in (6.2.20) and (6.2.22) at orders $d^4\phi/d\lambda^4$ and $d^3 r/d\lambda^3$ respectively; if one goes to the next order, one introduces terms involving both $\partial h(r, \phi)/\partial r$ and $\partial^2 h(r, \phi)/\partial \phi^2$. Thus in order to use these higher order series expansion one must use approximations to *both* these extra unknowns; further numerical study is required to determine which route is more efficient at extracting an accurate estimate.

$$j(r,\phi)\frac{d^2\phi}{d\lambda^2} = \frac{1}{2}\frac{\partial h(r,\phi)}{\partial \phi}\left(\frac{dr}{d\lambda}\right)^2 - \frac{1}{2}\frac{\partial j(r,\phi)}{\partial \phi}\left(\frac{d\phi}{d\lambda}\right)^2 - \frac{\partial j(r,\phi)}{\partial r}\frac{dr}{d\lambda}\frac{d\phi}{d\lambda} \qquad (6.2.24)$$

with the further constraint now giving:

$$h(r,\phi)\left(\frac{dr}{d\lambda}\right)^2 + j(r,\phi)\left(\frac{d\phi}{d\lambda}\right)^2 = 1 \qquad (6.2.25)$$

which gives:

$$\frac{d\phi}{d\lambda}\bigg|_{r_{min}} = \frac{1}{\sqrt{j(r_{min},\phi|_{r_{min}})}} \qquad (6.2.26)$$

The problem which now arises is when one calculates the derivatives of ϕ and r with respect to λ required to obtain the series expansions about $r_{min} = r_{n-i}$. Whilst we earlier demonstrated that the $\partial h_{n-i}/\partial \phi$ term only appears at order $d^3\phi/d\lambda^3$ and $d^4\phi/d\lambda^4$, from the equations above we find that:

$$\frac{d^2\phi}{d\lambda^2}\bigg|_{r_{n-i}} = -\frac{1}{2\,j_{n-i}^2}\frac{\partial j_{n-i}}{\partial \phi} \qquad (6.2.27)$$

and

$$\frac{d^2r}{d\lambda^2}\bigg|_{r_{n-i}} = \frac{1}{2\,h_{n-i}\,j_{n-i}}\frac{\partial j_{n-i}}{\partial r} \qquad (6.2.28)$$

and hence both derivatives of $j(r,\phi)$ immediately appear at second order! Whilst this itself wouldn't necessarily be an issue if we could simply use these second order expansions to recover the metric, the problem is that they won't reduce to the correct expressions if j has no dependence on ϕ but h does. Thus if we want to allow for this possibility by allowing not assuming anything about the form of $h(r,\phi)$ and $j(r,\phi)$ beforehand, we have to go to third and fourth order in r and ϕ respectively in our expansions about r_{n-i}. This then introduces several further derivatives of j which results in far too many unknowns than can be determined by the equations.

There are a number of possible resolutions to this problem, which have been briefly mentioned earlier but we now recap:

- Further simplification of the form of the metric given in (6.2.1); whilst this is the most general form of the metric one could write, it may be possible to simplify further to eliminate one of the unknown functions, for example by transforming to different coordinates. The main issue with this is that in order to make this transformation one requires the use of an integrating factor, which is not guaranteed to be definable for arbitrary metric. It may

be that the cases when we cannot make such a simplification have some other signature in the boundary field theory which would indicate this, and if so, one then knows when it is possible to use the metric in the simplified form.

- A more detailed analysis of what the gradients $dt_{end}/d\phi_{end}$ and $d\mathcal{L}/d\phi_{end}$ represent; our numerical study indicated that the two gradients give the final values of y and J for the corresponding geodesic, however, it is possible that the true relation is more complex, and if so, this would naturally provide a link to the function $j(r, \phi)$. For example, if they were related to a function of the average angular momentum (perhaps weighted so as to give a greater y_{final} dependence), then this would relate directly (via an equation of the form of (6.1.1)) to the function $j(r, \phi)$ (and its derivatives).

- Finally, and perhaps most notably, we have the gradient in the alternative direction (ϕ_{start} here, t_{start} in the discussion of section 6.1), which is currently completed ignored in the method developed above. As this gradient must be identically zero when the metric has only radial dependence, it is natural to assume it is some way related to the ϕ derivatives of the metric functions (for a bulk with angular dependence). Thus if one could determine an explicit relation (either numerically or analytically), this would provide significant further information about the bulk, which may be enough to allow for the extraction to proceed in the case of general $j(r, \phi)$.

Despite the limitations of working with fixed $j(r, \phi)$, it is worth completing the analysis of the case currently under investigation (with $j(r, \phi) = r^2$), as if in future it is discovered how to incorporate an arbitrary $j(r, \phi)$ into the equations, this analysis will provide a useful starting point. We thus proceed by considering how to extract $k(r, \phi)$ via the null geodesic probes.

6.2.3 Determining $k(r, \phi)$

Thus far we have used the zero-energy spacelike geodesics to recover $h(r, \phi)$ in our non-spherically symmetric spacetime, albeit with the specific choice of $j(r, \phi) = r^2$. Given this knowledge, we now demonstrate how one can then use the null geodesic

probes to extract the remaining unknown metric function, $k(r, \phi)$. The principles of the method are much the same as those used in determining $h(r, \phi)$; for fixed choice of ϕ_{start}, we take series expansions around $r_{min}(= r_{n-i})$ and use our knowledge of the bulk at larger r to solve the simultaneous equations and obtain an estimate for $k(r, \phi)$ at r_{n-i}. This is then repeated with a number of other choices of ϕ_{start}, so as to give estimates for $k(r_{n-i}, \phi)$ around the whole "ring", $0 \leq \phi_{start} < 2\pi$, with a smaller slicing of ϕ (i.e. a larger number of different ϕ_{start}) giving a more accurate overall estimate of the metric at this radius.

To what order do we need to take the series expansions in order to include the variation of $k(r, \phi)$ in the ϕ direction? The relevant components of the geodesic equation ((6.2.3) and (6.2.5)) give the following expressions when evaluated at r_{min}:

$$\frac{d^2 r}{d\lambda^2}\bigg|_{r_{min}} = \frac{E^2}{k(r_{min}, \phi|_{r_{min}})h(r_{min}, \phi|_{r_{min}})} \left(\frac{1}{r_{min}} - \frac{1}{2k(r_{min}, \phi|_{r_{min}})} \frac{\partial k(r, \phi)}{\partial r}\bigg|_{r_{min}} \right) \tag{6.2.29}$$

and

$$\frac{d^2 \phi}{d\lambda^2}\bigg|_{r_{min}} = -\frac{1}{2} \left(\frac{E}{r_{min} k(r_{min}, \phi|_{r_{min}})} \right)^2 \frac{\partial k(r, \phi)}{\partial \phi}\bigg|_{r_{min}} \tag{6.2.30}$$

where we have used the energy conservation equation, (6.2.6), to eliminate $dt/d\lambda$, and (6.2.7) evaluated at r_{min} to eliminate $d\phi/d\lambda$. From this we see that the terms $\partial k(r, \phi)/\partial r$ and $\partial k(r, \phi)/\partial \phi$ appear immediately, without the need for calculating further derivatives of ϕ and r, and thus our series expansions need only go to second order.

For our null geodesics, their paths through the bulk are characterised by the parameter y, the normalised angular momentum, which in the static case was conserved over the whole path and obtainable directly from the geodesic endpoints (see section 3.1.1). In the static but non-isotropic case being analysed here, y has a dependence on λ from the non-conservation of angular momentum: $y(\lambda) \equiv J(\lambda)/E$, where E remains a constant. This is related to the metric at the minimum radius in the same way as before; from our constraint (6.2.7) evaluated at r_{min} we find $y(\lambda)|_{r_{min}} = r_{min}/\sqrt{k(r_{min}, \phi|_{r_{min}})}$. Unlike in the spherically symmetric case, however, we no longer have the value of y at r_{min} available directly from the endpoints, as the gradient $dt_{end}/d\phi_{end}$ now gives y_{final}.

Nonetheless, if the metric is known down to some ring r_{n-i+1}, this value of y_{final}

can be used to calculate the value of y at r^b_{n-i+1}, denoted y^b_{n-i+1} (following exactly the same reasoning as in section 6.2.2 above). The superscript is used as before to distinguish between this case, where the outgoing part of the geodesic reaches r_{n-i+1} after it reaches r_{n-i}, and the case where the ingoing part of the geodesic reaches r_{n-i+1} before reaching r_{n-i}, labelled r^a_{n-i+1}. Again running in parallel to the method described in the previous section (in particular figure 6.4), the value of y^a_{n-i+1} can be computed by considering the alternative set of two-point functions with coordinate (t_{end}, ϕ_{end}) fixed, and the starting points allowed to vary; from a plot of these starting points, the gradient will give the corresponding values of y_{start} for the geodesics. The geodesic with the matching coordinate ϕ_{start} is then the one currently under consideration, and we can use the particular value of y_{start} to determine y^a_{n-i+1}.

Consider then the following series expansions:

$$
\begin{aligned}
r^b_{n-i+1} &\approx r_{n-i} + \left.\frac{dr}{d\lambda}\right|_{r_{n-i}} (\lambda^b_{n-i+1} - \lambda_{n-i}) + \left.\frac{d^2 r}{d\lambda^2}\right|_{r_{n-i}} \frac{(\lambda^b_{n-i+1} - \lambda_{n-i})^2}{2} \\
&= r_{n-i} + \left(\frac{1}{r_{n-i}} - \frac{1}{2\,k_{n-i}}\frac{\partial k_{n-i}}{\partial r}\right) \frac{E^2 (\lambda^b_{n-i+1} - \lambda_{n-i})^2}{2\,k_{n-i}\,h_{n-i}}
\end{aligned}
\tag{6.2.31}
$$

and

$$
\begin{aligned}
y^b_{n-i+1} &\approx y_{n-i} + \left.\frac{dy}{d\lambda}\right|_{r_{n-i}} (\lambda^b_{n-i+1} - \lambda_{n-i}) \\
&= y_{n-i} + \left.\frac{1}{E}\frac{dJ}{d\lambda}\right|_{r_{n-i}} (\lambda^b_{n-i+1} - \lambda_{n-i}) \\
&= y_{n-i} + \left.\frac{r^2_{n-i}}{E}\frac{d^2\phi}{d\lambda^2}\right|_{r_{n-i}} (\lambda^b_{n-i+1} - \lambda_{n-i}) \\
&= y_{n-i} - \left.\frac{E}{2\,(k_{n-i})^2}\frac{\partial k_{n-i}}{\partial \phi}\right|_{r_{n-i}} (\lambda^b_{n-i+1} - \lambda_{n-i})
\end{aligned}
\tag{6.2.32}
$$

where we have used the definition of y and equations (6.2.29) and (6.2.30) to obtain the final expressions, and we have two further equations with the superscript $b \rightarrow a$.

At first appearance, it seems that we have a far greater number of unknowns than before, as unlike in the spacelike case we cannot determine the λ values from the boundary information; this is quickly resolved, however, when one considers that they were given from our knowledge of the proper length - for the null geodesics the analogous parameter is the time taken to traverse the bulk. We note that each RHS contains the term $E(\lambda^b_{n-i+1} - \lambda_{n-i})$, and from the energy conservation equation

(6.2.6) this can be rewritten as $k_{n-i}(t^b_{n-i+1} - t_{n-i})$. Thus we have:

$$r^b_{n-i+1} \approx r_{n-i} + \left(\frac{k_{n-i}}{r_{n-i}} - \frac{1}{2}\frac{\partial k_{n-i}}{\partial r} \right) \frac{(t^b_{n-i+1} - t_{n-i})^2}{2\, h_{n-i}} \qquad (6.2.33)$$

and

$$y^b_{n-i+1} \approx y_{n-i} - \frac{1}{2\, k_{n-i}}\frac{\partial k_{n-i}}{\partial \phi}\bigg|_{r_{n-i}} (t^b_{n-i+1} - t_{n-i}) \qquad (6.2.34)$$

plus the similar expressions with $b \to a$. As we can eliminate y_{n-i} using $y_{n-i} = r_{n-i}/\sqrt{k_{n-i}}$, we are left with the above four equations involving the five unknowns: r_{n-i}, t_{n-i}, k_{n-i}, $\partial k_{n-i}/\partial r$ and $\partial k_{n-i}/\partial \phi$. Thus in order to extract an estimate to the metric, we must consider a further approximation to one of these unknowns.

Compare this with status of the equivalent expressions ((6.2.21) and (6.2.22)) in the spacelike case; there we had four equations but only four unknowns, as the series expansions had not introduced a $\partial h_{n-i}/\partial r$ term. As we noted in the footnote at the end of the section, this ties in with what we saw in the original, symmetric case considered in chapter 4, where the lowest order series expansion did not include a $dh(r)/dr$ term. For these null geodesics, we are unable to avoid the $\partial k_{n-i}/\partial r$ term, which again mirrors what we saw in the spherically symmetric case, where our lowest order series expansion (equation (3.1.27)) *did* introduce the unknown $df(r)/dr$.[7] There we used a linear approximation to the derivative term, and we can look to do the same here with $\partial k_{n-i}/\partial r$, however, we must be careful with our choice of ϕ in such an approximation, as strictly we want:

$$\frac{\partial k(r_{n-i}, \phi|_{r_{n-i}})}{dr} \approx \frac{k(r_{n-i+1}, \phi|_{r_{n-i}}) - k(r_{n-i}, \phi|_{r_{n-i}})}{r_{n-i+1} - r_{n-i}} \qquad (6.2.35)$$

Unfortunately, to specify $k(r_{n-i+1}, \phi|_{r_{n-i}})$ we require a knowledge of $\phi_{r_{n-i}}$, which we currently don't have. One option is to use an estimate for the value of $\phi|_{r_{n-i}}$ by considering where one expects it to be, given that one knows the value of ϕ which the geodesic with slightly larger (normalised) angular momentum with the same value

---

[7]After further analysis of the static, spherically symmetric case, we reformulated the method so as to use a parabolic approximation (see section 3.2.2) to the relevant integral which then removed the need for an estimate of $df(r)/dr$ entirely; in the less symmetric cases, it is not obvious how one could use a similar reformulation to eliminate $\partial k(r, \phi)/\partial r$, as there is no direct application of the parabolic approximation to the differential equations.

of ϕ_{start} (which gave us the estimate for k_{n-i+1}) reached at it's minimum radius, r_{n-i+1}. Provided one takes a small enough step size in the parts of the bulk where the metric varies most significantly with ϕ, this still gives a very good estimate, with any deviance from the correct gradient vanishing as the step size tends to zero.[8]

With this approximation of $\partial k_{n-i}/\partial r$, we now have sufficient equations to determine the remaining unknowns, and by performing the above with geodesics with different ϕ_{start}, can obtain the ring of information about the metric at radius r_{n-i}. Continuing inwards using geodesics with lower and lower y, by this process one can produce an estimate for $k(r, \phi)$ over the whole bulk.

6.3 Summary

In this chapter we have begun the process of generalising the previously developed methods for extracting the bulk information via the geodesic probes to spacetimes with less symmetry. We discussed what the form of the boundary information in such cases should be, and observed that a reduction in the amount of symmetry in the metric results in a corresponding increase in the dimensionality of the boundary data. Figure 6.1 gave a pictorial representation of this, where we have a two-dimensional surface plot for an isotropic but non-static metric; the figure also shows how this two-dimensional surface can be viewed as a series of one dimensional curves of the form seen previously in the static case.

An important consequence of the reduction in symmetry is that the angular momentum and energy associated with the geodesics are no longer necessarily conserved. An analysis of the gradient $dt_{end}/d\phi_{end}$ at fixed t_{start} (which previously yielded the conserved quantity $y = J/E$ in the static, spherically symmetric bulks, see section 3.1.1) for such cases revealed a rather surprising result. Rather than

---

[8]Whilst basic tests of equations (6.2.33) and (6.2.33) (along with their $b \to a$ counterparts) with this approximation to $\partial k_{n-i}/\partial r$ indicate that they can be used to give an accurate estimate of $k(r_{n-i}, \phi|_{r_{n-i}})$, further testing is required to determine whether one could proceed to accurately extract the complete function $k(r, \phi)$ via the iterative application of the above, due to possible implications for the stability of the method to errors.

the gradient being proportional to some average of y over the geodesic's path, our numerical study found that:

$$\frac{dt_{end}}{d\phi_{end}} = y_{final} \quad \text{for fixed} \ \ t_{start} \tag{6.3.36}$$

where y_{final} is the value of y as it reaches the boundary. Similarly for the spacelike geodesics we found that $d\mathcal{L}/d\phi_{end} = J_{final}$; again the gradient yields the final value of the angular momentum rather than some average.

Our methods for iteratively extracting the bulk in the previous chapters had made use of the fact that one could write the geodesics in integrable form; this led naturally to the idea of splitting up these integrals into pieces which could then be well approximated. In the less symmetric cases, one must use the full second order geodesic equation to compute the paths through the bulk, and thus it appears at first that one could not use a direct generalisation of the methods to these scenarios. The basic idea of the method (both for the null and spacelike geodesics), however, centred around taking a series expansion around the minimum radius, r_{min}, and using previously determined information about the bulk to compute the remainder of the integral. This is exactly the procedure followed here in the less symmetric cases, but recast in the form of differential equations. One also now has to consider slices in ϕ as well as in r (for a static but non-spherically symmetric metric), as described in section 6.2.1.

We analysed in more detail the specific case of a static but non-spherically symmetric three dimensional bulk with an asymptotically anti-de Sitter boundary, with metric given by (6.2.2). We found that the two unknown functions $h(r, \phi)$ and $k(r, \phi)$ can be determined sequentially via the zero-energy spacelike geodesics and the null geodesics respectively (c.f. the equivalent procedure in section 5.1).

For the spacelike geodesics, we used series expansions about the minimum radius to generate four simultaneous equations: (6.2.21), (6.2.22) for both directions away from $r_{min} = r_{n-i}$ (labelled a and b). This expansion in both directions is also a new feature of the less symmetric cases, and we now have to use two sets of boundary information (see figure 6.4) to determine J_{start} and J_{final} via the gradient relation described above. One could then use these values along with a knowledge of the spacetime for $r \geq r_{n-i+1}$ to obtain values for J^a_{n-i+1} and J^b_{n-i+1} to use in the series

expansions, and similarly for λ^a_{n-i+1} and λ^b_{n-i+1}, with λ_{start} and λ_{final} calculable from the knowledge of the geodesic's proper length.

The simultaneous equations could then be used to compute the four unknowns r_{n-i}, h_{n-i}, $\partial h_{n-i}/\partial\phi$ and λ_{n-i}, and we thus have our estimate for the metric at this step in r and for this particular choice of ϕ_{start}. By keeping the distance on the boundary $\phi_{end} - \phi_{start}$ fixed whilst varying ϕ_{start}, one obtains the ring of information described in section 6.2.1. One can then proceed to lower r by slightly increasing the distance $\phi_{end} - \phi_{start}$ and repeating the estimation process.

After a discussion of why keeping the most general form of the metric given in (6.2.1) is problematic, due to the significant number of extra unknowns introduced by keeping the function $j(r,\phi)$ unspecified, we then gave a similar description of how one could use the null geodesics to determine $k(r,\phi)$.

Although we have only considered the loss of one such symmetry, the methods presented here give a basis from which to build a fully covariant method for extracting the bulk, although further research into both better use of the extra information available in the higher dimensional surface plots and an extraction method involving the minimal surfaces related to the entanglement entropy in more than three bulk dimensions is required.

Chapter 7

Summary and Conclusions

The main focus of this thesis has been in devising methods by which one can use information located on the boundary of some asymptotically anti-de Sitter spacetime in order to determine the geometrical structure of the bulk interior. This was motivated by the inspirational duality conjectured by Maldacena just over ten years ago, named the AdS/CFT correspondence, which related these anti-de Sitter geometries to (lower dimensional) conformal field theories living on their boundary at infinity. As discussed in the introduction, this example of holography has led to a great deal of new research in a variety of directions, greatly expanding our knowledge of both non-perturbative string theory and field theories at strong coupling.

As we saw in the background chapter, this duality provides a direct link between physics in the CFT and properties of bulk objects; we saw how the insertion points of two-point correlation functions in the field theory correspond to the endpoints of null geodesic paths through the bulk. Thus a natural question to ask is whether one can extract the form of the metric these null geodesics propagate through in their traversing of the bulk simply from a knowledge of their endpoints. As null geodesics have zero proper length, they are intrinsically blind to the overall conformal factor of the metric, and as such one cannot expect to be able to recover the full metric; the question then becomes one of how much of the non-conformal part can be determined. As we saw at the start of chapter 3, a general static, spherically symmetric metric can be expressed in terms of two independent functions of the radial coordinate; thus if one of these is the overall conformal factor, we are left

with one function's worth of information to extract (which we denoted $f(r)$). By considering the geodesic endpoints as a function $t_{end}(\phi_{end})$, we saw in figures 3.1 and 3.2 how our boundary information in such a symmetric case also appears as a "function" of one variable (although only numerically).

In order to relate this boundary data to the metric function $f(r)$, we considered how the endpoints related to the depth to which the geodesic reaches in its path through the bulk. Null geodesics are parameterised by $y \equiv J/E$, which is related to the minimum radius by $y = r_{min}/\sqrt{f(r_{min})}$, and we demonstrated (section 3.1.1) how this quantity is available directly from the endpoints simply by taking the gradient $dt_{end}/d\phi_{end}$. This observation led to the development of an iterative method to extract $f(r)$, based on an approximation of the geodesic equation (written in integral form) which provided the second equation needed to solve simultaneously with $y = r_{min}/\sqrt{f(r_{min})}$ to give r_{min} and $f(r_{min})$. Using the asymptotically AdS boundary conditions at large r to solve at the first step, we continued by taking geodesics with slightly lower y to probe to smaller and smaller r, and determine the entire metric function $f(r)$. Our numerical studies revealed that such a procedure for reconstructing the bulk metric from the endpoint information is both remarkably stable to errors and yields highly accurate estimates for $f(r)$; this was then supported by an analytical consideration of the affect of introducing error terms into the algorithm.

This stability to errors, whilst perhaps not unexpected, was not guaranteed; it is impressive that even when using the rather rough estimate of a linear approximation to the central parts of the integral, the accuracy was not adversely affected. Our modification to the method described in 3.2.2 was a neat way by which to greatly improved the efficiency of the extraction, as it considerably improved the accuracy without requiring any extra computation.

One important class of spacetimes in which this iterative method breaks down before reaching $r = 0$ is those with severe deformations from pure AdS, such that for a certain critical value of y, the null geodesics can go into a circular orbit. We considered this problem in section 3.4, where we noted that these orbits occur when the location of a local maximum in the effective potential coincides with the

effective potential being zero, see figure 3.12. This results in a non-negligible time delay for the geodesics with $y < y_{crit}$, which is too large for our approximations used in the iterative algorithm to hold. For physically realistic models of the central deformation, however, there is evidence to suggest that null geodesic orbits are highly unlikely to occur; recent work by Hubeny *et al.* [83] demonstrated that for a gas of radiation in an asymptotically AdS background, it is impossible for null geodesics to enter into such orbits.

Our numerical procedure contrasts with other approaches to extracting information about the bulk via boundary information in that it provides a very detailed reconstruction of the deep interior of the spacetime. For example, the information contained within the expectation values of certain one-point functions in the field theory was shown in [56] to allow the size of a spherical source to be estimated, and hence a way (in principle) to distinguish between star and black hole geometries. Such a distinction is made immediately here, however, given the endpoint information of the null geodesics; for a star geometry, one has a complete set of endpoints, whose gradient will yield values of y from zero to one. A black hole geometry, on the other hand, will result in a reduced spectrum of endpoints due to the geodesics which pass behind the horizon not travelling back out to the boundary, and thus not appearing on the endpoint plot.[1] Furthermore, our iterative method then gives the structural form of this geometry, to an arbitrarily high level of accuracy, and with apparently no "wasted" information; we have used the endpoint function $t_{end}(\phi_{end})$ to give $f(r)$ by numerically constructing a one-to-one correspondence between the two.

Somewhat remarkably, a very similar process for extracting bulk information can be performed via zero-energy spacelike geodesics, motivated by the relationship between their proper length and the entanglement entropy of the corresponding boundary subsystem (a manifestation of the "area law" relation of Ryu and Takayanagi [80, 81] described in chapter 2). Their proposal allows the entanglement entropy to be calculated holographically, by a knowledge of the corresponding bulk

---

[1]For further discussion of using null geodesic endpoints as signatures of horizon formulation see [83].

physics; what we demonstrated here was a solution to the inverse problem, of using the entanglement entropy data to reconstruct the unknown bulk geometry. We began by considering the static, spherically symmetric case, as in chapter 3, and we also noted that we are restricted to working in three bulk dimensions, in order for the pertinent minimal surface to be the zero-energy spacelike geodesic.

The boundary data for the static spacelike geodesics then available from the field theory takes the form of a function $\mathcal{L}(\phi_{end})$, in much the same fashion as the null endpoints were written as a function $t_{end}(\phi_{end})$. Indeed the parallels extend yet further; a calculation of the gradient $d\mathcal{L}/d\phi_{end}$ reveals that once again we are able to obtain the relevant parameter for the corresponding geodesic, namely J, the angular momentum.

In fact, in certain situations one can view the endpoint data of the null geodesics as that of zero-energy spacelike geodesics! In section 4.2.4 we showed that a simple transformation of coordinates resulted in the (t, ϕ) endpoints of null geodesics in a background defined by $f(r)$ being equivalent to the $(\mathcal{L}, \phi)$ information of static spacelike geodesics in a background defined by $h(\tilde{r})$ (with the relationship between $f(r)$ and $h(\tilde{r})$ given by (4.2.24)). Unfortunately, as we also noted, such a transformation does not allow both spacetimes to be asymptotically anti-de Sitter, and it is rather unclear how this apparent duality relates to the holographic picture of AdS/CFT. Nonetheless, it is an intriguing observation, and given the perhaps surprising nature of the developments in holography made in recent years, is perhaps worthy of further investigation.

Returning to our numerical extraction of the bulk, we observed that despite this link between the two types of geodesic, there were some interesting differences between the respective iterative methods. With regards to their stability against error propagation, the linear approximation which worked extremely well for the null geodesics had to be replaced with (at least) a second order fit in our new algorithm for the spacelike probes. Our analytical analysis of the error terms explained to some extent why this was so, demonstrating that a linear approximation no longer sufficiently suppresses the errors in subsequent steps; whilst the error converges towards zero initially, after a number of iterations it begins to diverge (see figure

4.12). This divergence mirrors the behaviour seen in the actual errors shown in figure 4.11, and although the behaviour there is more complicated (with severe corruption then occurring), this is due to extra instabilities in the numerics which were not modelled by our estimate of the error.

What is important, however, is that this use of a second (or higher) order approximation costs virtually nothing in terms of extra computation, and so in no way affects the efficiency of the method, which was seen to be broadly comparable with that in chapter 3. One area in which the efficiency could not be improved was by reformulating the method as we did for the null geodesics, due to the fact that in the spacelike case, the gradient of the boundary function $\mathcal{L}(\phi_{end})$ immediately yields the minimum radius of the geodesic, r_{min}. This leaves us with only needing to calculate $h(r_{min})$ from our integral equation, a term which is absent from the parabolic approximation used in the reformulation.

The major result of both chapters 3 and 4 (which are based on work in [1, 2]) is that one can use the boundary information to determine one function's worth of information about the bulk, in the highly symmetric geometries considered. What is then even more helpful is the fact that the two methods uncover different information about the bulk structure; the null geodesics have zero proper length, and hence are not sensitive to the overall conformal factor of the metric, whereas the static spacelike geodesics by definition cannot probe the timelike part. This complementary nature of the two numerical algorithms thus allowed us to consider the situation where we had access to both sets of boundary data, and as the most general static, spherically symmetric metric has only two unknown functions, a sequential application of the algorithms allowed us to determine both.

In demonstrating how this allowed one to extract the pertinent information about a radiating perfect fluid model of a star in AdS_3, we took a slight detour from our main investigation to consider how these perfect fluid models behaved in higher dimensions. Motivated by an observation in [83] that the total mass of such stars does not increase monotonically with central density in AdS_5, we performed a numerical study of the behaviour over a wide range of dimensions, which revealed the presence of a critical dimension for the stability of such stars, as originally presented in [3].

Whilst this research was being conducted, it transpired that similar work was also being carried out separately by two other authors, Vladimir Vaganov in [4] and Pierre-Henri Chavanis in [84]. This resulted in some fruitful discussions about the origin of the critical dimension, and an analytical explanation for both its value of $d_c = 10.964\ldots$ and the different types of behaviour seen in the higher and lower dimensions. Their analysis extended beyond the radiating case considered here to encompass a general linear equation of state $P = q\rho$, with the interesting result that for any value of q between zero and one, the critical dimension is always between ten and eleven, with $q = 0$ giving $d_c = 11$ and $q = 1$ giving $d_c = 10$. We concluded chapter 5 with a dynamical systems analysis yielding the aforementioned $d_c = 10.964\ldots$, as well as values for other parameters of our numerical model of the self-similar oscillations for the specific case of the radiating perfect fluid star.

How does this relate to the wider field? Dimension dependent phenomena occur in a wide variety of subjects, and are often related to the stability of the system, with objects undergoing a significant change in behaviour at the critical dimension; in the area of general relativity, we discovered that almost exactly the same type of scenario is found in extensions [116–118] to the work of Belinsky, Khalatnikov and Lifshitz (BKL) [115], where they examine the dynamics of a spacetime in the vicinity of a cosmological singularity. It would be very interesting to compare these two situations more closely, especially given the value of the critical dimension in their case also being between ten and eleven.[2]

Returning to the primary goal of the thesis, that of reconstructing the bulk from the boundary, the double extraction (using the two types of geodesic) is unfortunately only well motivated in scenarios with three bulk dimensions, as otherwise the proper length information of the spacelike geodesics is not readily available from the field theory data; instead one must consider using the appropriate minimal surfaces which correspond to the entanglement entropy. Furthermore, one must also have some method for calculating this entanglement entropy in the field theory, which in higher dimensions poses considerable difficulties. As already noted, how-

---

[2]Their study only considered integer value dimensions, and hence the exact (non-integer) value of the critical dimension is not currently known (if indeed it is a non-integer).

ever, subsequent research [82] has detailed the correct minimal surfaces one should use in Ryu and Takayanagi's area formula, (2.2.21), and there has been progress both numerically [79] and analytically [99, 100] in the higher dimensional entropy calculations.

What will almost certainly be necessary, however, in generalising our methods to include minimal surfaces is the use of coupled differential equations rather than the integral forms we had been using up to this point. This would also be the first step towards developing a coordinate independent algorithm for extracting the bulk, which could be applied to metrics more general than the highly symmetric cases considered in chapters 3, 4 and 5. Whilst producing a covariant method will require further research, we began this process in chapter 6 by considering spacetimes with less symmetry.

Our first observation was that for each loss of symmetry (i.e. each extra coordinate dependence in the metric) there was a corresponding increase in the dimensionality of the boundary information of the geodesics (see figure 6.1). One also has that the previously conserved quantities of angular momentum and energy can now vary along each geodesic. This presented us with two obvious questions about the boundary data; firstly, what do our gradients $dt_{end}/d\phi_{end}$ and $d\mathcal{L}/d\phi_{end}$ now represent, and secondly, what information is contained in the new, transverse, directions of the higher-dimensional plots of the boundary data.

We were unable to ascertain a precise answer to the second question, simply noting that as the gradient in these extra directions must be zero in the more symmetric cases, one can conclude that whatever information they encode must be related in some sense to the new dependencies in the metric. Our analysis of the first question was somewhat more revealing, however, as a numerical study yielded the rather surprising result that gradients $dt_{end}/d\phi_{end}$ and $d\mathcal{L}/d\phi_{end}$ give y_{final} and J_{final} respectively; the *final* values of the (normalised) angular momenta as the geodesics reach the boundary. Intuitively, one might have expected the gradients to encode some more complicated average of the (normalised) angular momenta over the whole geodesic path; nonetheless, our numerical study clearly indicated this wasn't the case (see figure 6.2).

Given this analysis of the boundary data, we then focused on the specific case of a static, non-isotropic spacetime in three bulk dimensions, and a restricted form of the metric. By expanding the differential forms of the geodesic equation about the minimum radius, we demonstrated how it was possible to obtain sufficient equations to extract the metric functions $h(r, \phi)$ and $k(r, \phi)$ via the zero-energy spacelike and null geodesics respectively, although we noted that one has to consider not simply a radial slicing of the bulk (as in the symmetric metrics), but also an angular one: on the ith step of the radial iteration, after obtaining $h(r_{n-i}, \phi_j)$ for some particular ϕ_j, one has to vary ϕ_{start} in order to obtain estimates for $h(r_{n-i}, \phi)$ for all ϕ, i.e. the "ring" of information described in section 6.2.1.

Moreover, we observed that if one uses the most general form of the metric corresponding to such scenarios, one is faced with significantly more unknowns than one can determine from these equations. Although a problem, we discussed several possible ways in which it might be resolved, the most promising of which being that the boundary information has yet to be exploited to its full potential, as we have currently only utilized the gradients $dt_{end}/d\phi_{end}$ and $d\mathcal{L}/d\phi_{end}$ in the method presented here.

Despite this limitation, the analysis presented in chapter 6 provides a solid basis from which to continue generalising the work presented in this thesis to both less symmetric metrics, and to the higher-dimensional cases, with the hope that eventually, a fully covariant (or even analytic) map between the boundary information and the bulk can be found.

Thus to conclude: since Maldacena's proposal for a duality between conformal field theory and anti-de Sitter bulk there has been a remarkable amount of progress in refining and expanding on this duality, and others of its type, such as AdS/QCD. Building up a dictionary of relationships between field theory and bulk has resulted in remarkable new ways for calculating properties on both sides of the correspondence.

Here, we have taken two of these relationships and applied them in a novel manner in order to "recreate the hologram"; by taking the field theory data as input, we have demonstrated how one can systematically build up a highly accurate picture

of the geometrical interior of the bulk, working inwards from the boundary to determine the metric functions to arbitrarily high accuracy. The impressive stability of the two algorithms was immediately apparent numerically, and given the field theory data, one can easily apply them to perform the metric extraction rapidly and efficiently. The limitations in the applicability of the methods (using geodesics) were minor; the only one of note was the issue with non-monotonic effective potentials in the null method preventing a complete reconstruction of the metric. This primarily occurs, however, in unphysical metrics, constructed by hand, or in black hole scenarios where one has a limited set of endpoint data with which to perform the reconstruction in the first place.

The major limitation came not from any inability of the geodesics to probe the metric, but in that the use of spacelike geodesics is only well motivated in bulks with three spacetime dimensions. There is a natural resolution to this problem, namely to use the minimal surfaces described in [82] to probe the metric, however, this avenue was not explored further here, as it raises the additional question of how one computes the entanglement entropy in these higher dimensional cases.

Although the availability of the field theory data was not discussed in detail here, we observed that there are several techniques for calculating the entanglement entropy in a two-dimensional CFT, as required for the spacelike geodesic method. We also commented on how there has been significant progress in applying certain numerical techniques (e.g. DMRG [79]) to these higher dimensional cases, and also those with time-dependence. If these yield further developments in the future, this provides extra motivation for producing not only methods applicable in higher dimensions, but also ones which can be applied to the time-dependent (or generally non-symmetric) cases.

Our final chapter thus focused on making the first steps towards developing such a generally applicable method, by considering the addition of an angular dependence to the three dimensional metrics used previously. After finding that the gradient relations (which had proven so crucial in developing the methods in the symmetric case) now yielded the final values of y and J (which are no longer conserved) as the geodesics return to the boundary, we described how one could use the differential

forms of the geodesic equation to iteratively extract the bulk. Our analysis emphasised how the approach of using geodesics with progressively smaller minimum radii can be applied in more general cases, and that the complex nature of the geodesic behaviour is considerably simplified when considering expansions about these minimum radii.

Overall, we have demonstrated how one can indeed reconstruct the bulk from the boundary, in a highly accurate and efficient manner, and with hope that after further research, the techniques detailed here could be generalised to help construct explicit maps between the two sides of the AdS/CFT correspondence in a covariant manner.

Appendix A

Auxiliary Results: Pure AdS

A.1 The structure of Anti-de Sitter space

The d-dimensional Anti-de Sitter spacetime, AdS_d may be defined as the hyperboloid with isometry $SO(2, d-1)$ given by:

$$Y_0^2 + Y_d^2 - \sum_{i=1}^{d-1} Y_i^2 = R^2 \qquad \text{(A.1.1)}$$

embedded in $\mathbb{R}^{d+1}$ with induced metric

$$ds^2 = -dY_0^2 - dY_d^2 + \sum_{i=1}^{d-1} dY_i^2 \qquad \text{(A.1.2)}$$

We can obtain a solution to (A.1.1) by setting:

$$Y_0 = R \cosh \rho \cos \tau, \quad Y_d = R \cosh \rho \sin \tau, \quad \text{and} \quad Y_i = R \Omega_i \sinh \rho \qquad \text{(A.1.3)}$$

with $i = 1, \ldots, d-1$ and $\sum_i \Omega_i^2 = 1$, which gives the metric on AdS_d as:

$$ds^2 = R^2 \left(-\cosh^2 \rho \, d\tau^2 + d\rho^2 + \sinh^2 \rho \, d\Omega_{d-2}^2 \right) \qquad \text{(A.1.4)}$$

where R is the radius of curvature. As taking $0 \leq \rho$ and $0 \leq \tau \leq 2\pi$ results in the above solution covering the entire hyperboloid once, we term (τ, ρ, Ω_i) the global co-ordinates of AdS_d. However, we are left with closed timelike curves due to the periodic nature of τ (see figure A.1); to obtain a causal spacetime, one must unwrap
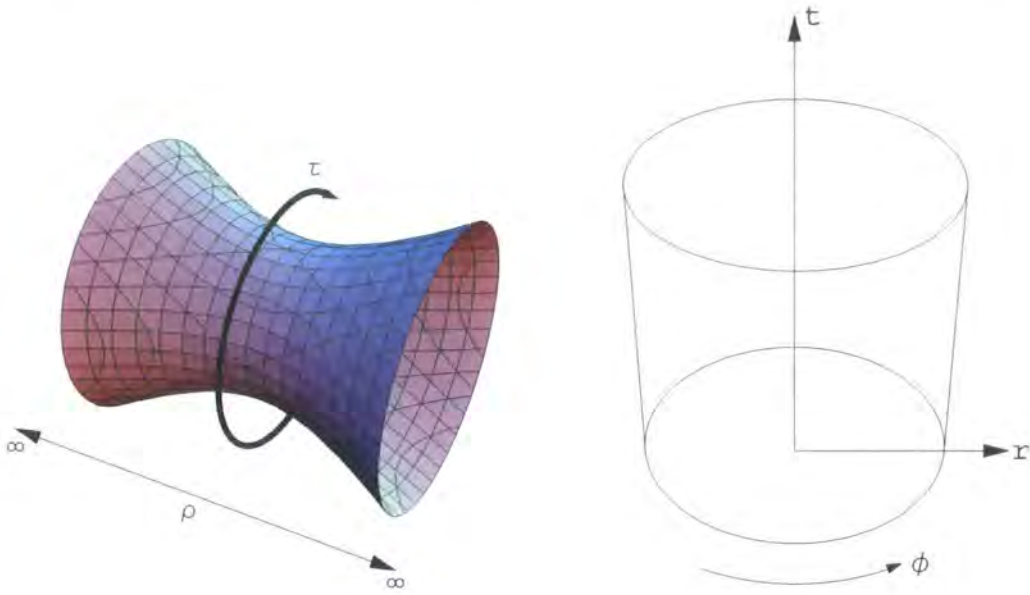
Figure A.1: AdS_d pictured as a hyperboloid in $\mathbb{R}^{d+1}$ (left figure), where the time coordinate τ is periodic, and we have closed timelike curves; by unwrapping in this direction and allowing τ to range over the whole of $\mathbb{R}$ we obtain a causal spacetime. Changing coordinates to the (t, r, Ω_i) used in (A.1.12) results in the cylindrical representation given on the right (where one angular coordinate is pictured, labelled ϕ). This has a timelike conformal infinity at radius $r = \pi/2$, and is equivalent to one half of the Einstein static universe.

the time co-ordinate (by taking $-\infty < \tau < \infty$) to obtain the universal covering space.[1]

One can use various different coordinate systems in which to write such a metric; we saw in chapter 2 the product of AdS_5 and S^5 written as:

$$ds^2 = \frac{R^2}{z^2}(-dt^2 + dx_1^2 + dx_2^2 + dx_3^2 + dz^2) + R^2 d\Omega_5^2 \qquad (A.1.5)$$

These Poincaré coordinates $z, t, \vec{x}$ can be obtained from (A.1.2) by first defining the light cone coordinates:

$$u \equiv \frac{(Y_0 - Y_{d-1})}{R^2} \quad \text{and} \quad v \equiv \frac{(Y_0 + Y_{d-1})}{R^2} \qquad (A.1.6)$$

---

[1]For the rest of this thesis, when we refer to AdS_d we refer to this universal cover, with no closed timelike curves.

with a simultaneous redefinition of the other coordinates:

$$x^i \equiv \frac{Y_i}{u R} \quad \text{and} \quad t \equiv \frac{Y_d}{u R} \tag{A.1.7}$$

One can then express (A.1.1) in the form:

$$R^4 uv + R^2 u^2 (t^2 - \vec{x}^2) = R^2 \tag{A.1.8}$$

where $\vec{x}^2$ is the sum over the $(x^i)^2$ components. This results in the identifications:

$$Y_0 = \frac{1}{2u} \left(1 + u^2 \left(R^2 + \vec{x}^2 - t^2\right)\right), \quad Y_{d-1} = \frac{1}{2u} \left(1 + u^2 \left(\vec{x}^2 - t^2 - R^2\right)\right)$$

$$Y_d = Rut, \quad \text{and} \quad Y_i = Rux^i \tag{A.1.9}$$

which with the substitution $z = 1/u$ give:

$$Y_0 = \frac{1}{2z} \left(z^2 + R^2 + \vec{x}^2 - t^2\right), \quad Y_{d-1} = \frac{1}{2z} \left(z^2 + \vec{x}^2 - t^2 - R^2\right)$$

$$Y_d = \frac{Rt}{z}, \quad \text{and} \quad Y_i = \frac{Rx^i}{z} \tag{A.1.10}$$

which then yields the AdS_5 part of (A.1.5) from our original AdS metric (A.1.2).

The coordinates used in the majority of this thesis are (t, r, Ω_i), and in which the metric for AdS_5 is given by:

$$ds^2 = -\left(\frac{r^2}{R^2} + 1\right) dt^2 + \frac{dr^2}{\left(\frac{r^2}{R^2} + 1\right)} + r^2 d\Omega_3^2 \tag{A.1.11}$$

which we obtain by defining $r/R = \sinh(\rho)$ and $t/R = \tau$ and substituting into A.1.4. Finally, the cylindrical visualisations of anti-de Sitter space seen throughout this work, including the right hand plot in figure A.1 above are obtained by rescaling these new radial and time coordinates ($r \to R\tan(r)$ and $t \to Rt$) to give:

$$ds^2 = R^2 \left(-\sec^2(r)dt^2 + \sec^2(r)dr^2 + \tan^2(r)d\Omega_3^2\right) \tag{A.1.12}$$

A.2 Null geodesics

For the case of pure AdS, much can be computed analytically, and here we calculate the paths of null geodesics, showing explicitly that those which travel from boundary-to-boundary must always terminate at the point antipodal to where they start,

regardless of their ratio of angular momentum to energy. We shall work in the metric given by (A.1.12) above, where we suppress two of the angular coordinates as before (see section 2.3), and denote the remaining such coordinate ϕ. This leads to the modified constraint equations:

$$E = R^2 \sec^2(r)\dot{t} \tag{A.2.13}$$

$$J = R^2 \tan^2(r)\dot{\phi} \tag{A.2.14}$$

$$R^2 \left(-\sec^2(r)\dot{t}^2 + \sec^2(r)\dot{r}^2 + \tan^2(r)\dot{\phi}^2 \right) = 0 \tag{A.2.15}$$

which combine together to give:

$$-\frac{E^2}{R^2 \sec^2(r)} + R^2 \sec^2(r)\dot{r}^2 + \frac{J^2}{R^2 \tan^2(r)} = 0 \tag{A.2.16}$$

Rearranging, and again using (A.2.13) to eliminate the dependence on λ gives:

$$\sqrt{\frac{E^2}{(R^2 \sec^2(r))^2} - \frac{J^2}{R^4 \tan^2(r)\sec^2(r)}} = \dot{r} = \frac{dr}{dt}\frac{dt}{d\lambda} = \frac{dr}{dt}\frac{E}{R^2 \sec^2(r)} \tag{A.2.17}$$

and so

$$\frac{dr}{dt} = \sqrt{1 - \frac{J^2}{E^2 \sin^2(r)}} \tag{A.2.18}$$

Using the substitution $x = \frac{\cos(r)}{\sqrt{1-y^2}}$, where we define y as being the ratio of angular momentum to energy, $y \equiv J/E$, this equation becomes:

$$\frac{dx}{dt} = -\sqrt{1 - x^2} \tag{A.2.19}$$

which implies $x = -\sin(t - const)$ and thus that

$$\cos(r) = -\sqrt{1 - y^2}\sin(t - const) \tag{A.2.20}$$

where the choice of constant is given by the starting point of the geodesic; for $t_{start} = 0$ we require the constant to be zero. Note also that at the minimum radius of the geodesic, $y^2 = \sin^2(r)$ and so $t|_{r_{min}} = t_{start} + \pi/2$ regardless of the value of y. As the null geodesics are symmetric about the minimum radius, this implies that the overall time taken by the geodesic to reach the bulk must be $t_{end} - t_{start} = \pi$. One can also calculate the dependence of ϕ on t:

$$\frac{J}{R^2 \tan^2(r)} = \dot{\phi} = \frac{d\phi}{dt}\frac{dt}{d\lambda} = \frac{d\phi}{dt}\frac{E}{R^2 \sec^2(r)} \tag{A.2.21}$$

thus:

$$\frac{d\phi}{dt} = \frac{y}{\sin^2(r)} \tag{A.2.22}$$

which can be combined with (A.2.20) to give:[2]

$$\tan(\phi - const) = y \tan(t - t_{start}) \tag{A.2.23}$$

where the choice of constant on the LHS merely fixes the angular starting point of the geodesic. Thus at the minimum radius, when $t|_{r_{min}} - t_{start} = \pi/2$, we require $\phi|_{r_{min}} - \phi_{start} = \pi/2$. By symmetry we must then have that $\phi_{end} - \phi_{start} = \pi$, and hence any null geodesic beginning on the boundary must necessarily end at its antipodal point irrespective of the choice of y. This is not the case for spacelike geodesics, as we shall now see.

A.3 Spacelike geodesics

Unlike the null geodesics, which are specified simply by the ratio of their angular momentum to the energy, $y = J/E$, spacelike geodesics are parameterised by both E and J, and this results in a significantly more varied set of possible endpoints for the geodesics, even in pure AdS.

This was alluded to in the background section, where we saw in figure 2.8 that the paths of spacelike geodesics all starting from the same point on the boundary do not all converge to the antipodal point as they traverse the bulk, rather they diverge to form a "disc" of endpoints on the boundary, each with different t_{end} and ϕ_{end}, in stark contrast to the null geodesics. In the particular case shown in figure 2.8 the geodesics shown all started with the same energy but with different angular momenta, resulting in the corresponding spread of endpoints along the boundary.

By varying the value of the energy, one can shift this set of endpoints, as we see in figure A.2; in this plot each curve corresponds to a set of geodesics with J ranging from 0 to ∞ at a fixed energy. The points close to the starting point of $t = 0$, $\phi = \pi$ (from which all the geodesics originated) are from those with high

---

[2]Note that the dependence of the geodesics on the AdS radius of curvature has been scaled out in (A.2.20) and (A.2.23) by the choice of coordinates.
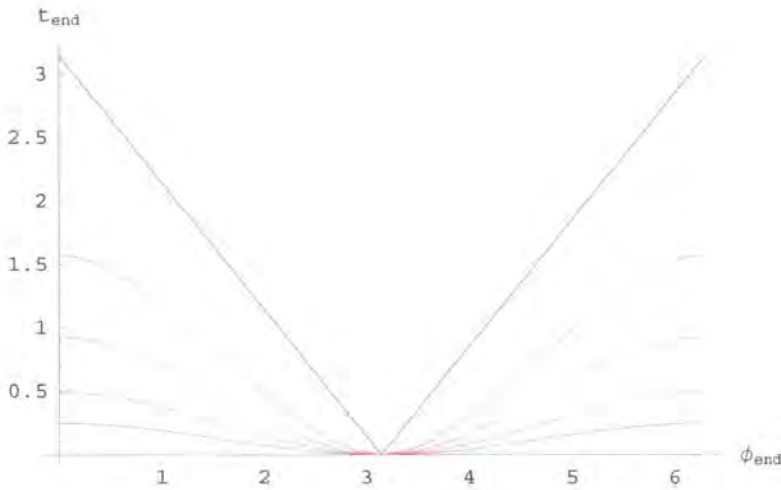
Figure A.2: Sets of boundary-to-boundary spacelike geodesic endpoints, obtained by fixing the value of E and varying J (each colour corresponds to a different energy). All the geodesics originated at the point $(\pi, 0)$, the sets with lower values of E have lower time delays in traversing the bulk; in the limit $E = 0$, the geodesics remain pinned to the $t = 0$ slice.

angular momentum, whereas the points close to the edge of the plot are from low angular momentum geodesics. The black curve illustrates the upper limit of the coloured curves as E increases, and one can in fact connect any two points below this line by a spacelike geodesic with a particular choice of J and E.

Clearly, fixing E and varying J is not the only way one can define a "set" of spacelike geodesics. If we consider again the ratio $y = J/E$, and look at the endpoints of the discs of geodesics when this ratio is fixed, there is significantly different behaviour for the regions where $|y| > 1$ and $|y| < 1$.

Curves with $y = const$ are illustrated below (figure A.3); the red curves represent $|y| = const < 1$, and the green curves represent $|y| = const > 1$. The black lines indicate the upper limit of the coloured curves, and the blue lines represent the critical values $y = \pm 1$, where the energy is equal to $\pm$ the angular momentum.[3]

Whilst the paths of spacelike geodesics in general metrics need to be computed numerically, in the case of pure AdS their behaviour can also be determined analytically. In the background chapter we saw that the constraint equations (2.3.3),

---

[3]Note: There is no correlation between the colours used in figures A.2 and A.3.
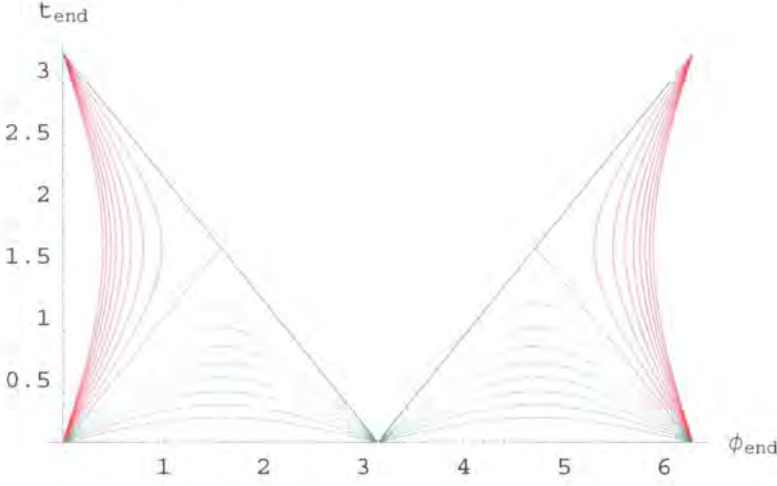
Figure A.3: The endpoints of sets of spacelike geodesics with $y = const$; the red curves represent $|y| = const < 1$, and the green curves represent $|y| = const > 1$. The black lines indicate the upper limit of the coloured curves, and the blue lines represent the critical values $y = \pm 1$. Note the fact apparent from both this and the previous plot: any point below the black lines can be reached with a spacelike geodesic with a particular choice of J and E.

(2.3.4) and (2.3.6) could be combined to introduce an effective potential for the geodesics, such that:

$$\dot{r}^2 + V_{eff} = 0 \qquad (A.3.24)$$

where V_{eff} was defined in (2.3.9). For the spacelike geodesics in pure AdS (with $R = 1$), we then have

$$\dot{r} = \pm\sqrt{r^2 + 1 + E^2 - J^2 - \frac{J^2}{r^2}} \qquad (A.3.25)$$

where the negative square root represents the ingoing part and the positive square root the outgoing part. We can use the above with (2.3.3) and (2.3.4) to obtain the following expressions for r in terms of t and ϕ:

$$r = \frac{\sqrt{1 + J^2 + E \tan(t - c_1)(E \tan(t - c_1))}}{\sqrt{E^2 - J^2 - 1 + 2E \tan(t - c_1)}} \qquad (A.3.26)$$

$$r = \frac{J \sec(\phi - c_2)}{\sqrt{E^2 - J^2 + 1 + 2J \tan(\phi - c_2)}} \qquad (A.3.27)$$

For our analysis of the endpoints, we wish to consider solutions to these equations at the boundary, i.e. in the limit $r \to \infty$; this requires the denominators of these

equations to be zero:

$$E^2 - J^2 - 1 + 2E\tan(t_{end} - c_1) = 0 \qquad (A.3.28)$$

$$E^2 - J^2 + 1 + 2J\tan(\phi_{end} - c_2) = 0 \qquad (A.3.29)$$

The constants c_1 and c_2 can be determined from the initial conditions of the ingoing geodesics; for the case where $t_{start} = 0$ and $\phi_{start} = \pi$ this requires that $c_1 = n\pi - \frac{\pi}{2}$ and $c_2 = m\pi - \frac{\pi}{2}$ with n and m integers. Equations (A.3.28) and (A.3.29) can be solved for J and combined to give:

$$E\tan\left(\frac{\pi}{2} - t_{end}\right) = 1 + \left(\sqrt{E^2 + \sec^2\left(\phi_{end} + \frac{\pi}{2}\right)} + \tan\left(\phi_{end} + \frac{\pi}{2}\right)\right)\tan\left(\phi_{end} + \frac{\pi}{2}\right)$$
$$(A.3.30)$$

for $0 \le \phi_{end} \le \pi$, and

$$E\tan\left(\frac{\pi}{2} - t_{end}\right) = 1 + \left(\sqrt{E^2 + \sec^2\left(\frac{\pi}{2} - \phi_{end}\right)} + \tan\left(\frac{\pi}{2} - \phi_{end}\right)\right)\tan\left(\frac{\pi}{2} - \phi_{end}\right)$$
$$(A.3.31)$$

for $\pi \le \phi_{end} \le 2\pi$, which reproduces exactly the plots such as those in figure A.2. To reintroduce the dependence on R we can just rescale the time coordinate in (A.3.30) and (A.3.31) such that $t_{end} \to t_{end}/R$; in other words, t_{end} runs linearly with the AdS radius R, $t_{end} = Rfunc(\phi_{end})$.

We can also consider the situations where $E = aJ$ in order to investigate the plots seen in figure A.3. Returning to (A.3.28) and (A.3.29), it is clear to see that in the case $E = J$, the equations become simply (with appropriate choice of n and m):

$$t_{end} = \pi - \phi_{end} \qquad (A.3.32)$$

Using the substitution of $E = aJ$ produces the only slightly more complicated formula:

$$t_{end} = \text{arccot}\left(\frac{\sqrt{1 - a^2 + \cot^2(\phi_{end})}}{a}\right) \qquad (A.3.33)$$

which allow the plots of $E/J = constant$ to be produced, as seen in figure A.3. From this plot we can see the presence of turning points in all the curves where $a \ne \pm 1$. For the $|y^{-1}| \equiv |a| > 1$ curves, the turning points occur at $t_{end} = \pi/2$ (easy to check by solving (A.3.33) for ϕ_{end} and differentiating w.r.t t_{end}). The formula for these

turning points is then given by substituting in the value $t_{end} = \pi/2$ to (A.3.33). We get two solutions for the region $0 \leq \phi_{end} \leq 2\pi$, as expected from figure A.3:

$$\phi_{end} = \text{arccot}\left(\sqrt{-1 + a^2}\right) \quad \text{and} \quad \phi_{end} = 2\pi - \text{arccot}\left(\sqrt{-1 + a^2}\right) \qquad \text{(A.3.34)}$$

Similarly, the turning points for the $|y^{-1}| \equiv a < 1$ curves all occur at $\phi_{end} = 3\pi/2$ and $\phi_{end} = \pi/2$, with the t_{end} coordinate given by:

$$t_{end} = \arctan\left(\frac{a}{\sqrt{1 - a^2}}\right) \qquad \text{(A.3.35)}$$

and thus we can see analytically how all the features of the boundary-to-boundary spacelike geodesics arise. In more complicated spacetimes, or ones where the form of the metric is not specified explicitly, one must perform the calculations numerically, although definite features such as the turning points seen here often allow the equations to be simplified sufficiently for some analytical expression to be determined. These features are often manifest when one considers certain subsets of the complete range of geodesics whose endpoints cover the entire lower triangles in figures A.2 and A.3, and in this work we have focused on a particularly special set of such spacelike geodesics: the zero-energy ones, whose paths lie entirely in the $t = 0$ plane, and which are thus characterised by only one parameter, their angular momentum, J.

The properties of these particular geodesics, and in particular their relationship to quantities in the boundary field theory not only makes them useful probes of the bulk structure (see chapter 4), but also suggests links with the null geodesics analysed in chapter 3, which are also only characterised by one parameter, their normalised angular momentum, y.

Appendix B

Auxiliary Results: Probing the bulk

B.1 Metric extraction via spacelike probes

In section 4.1.1 we outlined the principle behind the iterative technique of metric extraction: determining r_{min} from the gradient $d\mathcal{L}/d\phi_{end}$ and then calculating an estimate for $h(r_{min})$ at each step by splitting up the integral in (4.1.7) and approximating each piece separately, beginning the whole process at large r, where the metric is approximately pure AdS and we can take $h(r) \approx (r^2 + 1)^{-1}$. Here we go on to give further details of how to set this up, and explicitly write down the equations used in the approximations[1].

Having taken the first step which chooses an r_n large enough so the metric is approximately pure AdS, and hence $h(r_n) = (r_n^2 + 1)^{-1}$, we can continue as follows. For a geodesic with slightly lower angular momentum J_{n-1} (which can be obtained by taking a slightly larger region B on the boundary), we can split up the integral

---

[1]The procedure used here is only one of a number of possible methods for discretizing the integral; for the purposes of illustrating the principle, this method is both brief and accurate to a good degree. For discussion on the stability of the iteration to errors, see section 4.2.1

over r in (4.1.7) into two pieces:

$$\phi_{n-1} = 2 \int_{r_{n-1}}^{r_n} \frac{\sqrt{h(r)}}{r\sqrt{\frac{r^2}{J^2} - 1}} \, dr + 2 \int_{r_n}^{r_{max}} \frac{\sqrt{h(r)}}{r\sqrt{\frac{r^2}{J^2} - 1}} \, dr \qquad (B.1.1)$$

The first integral in the above can be well approximated by taking a next-to-lowest order series expansion about the point $r = r_{n-1} (= J_{n-1})$, as the distance $r_n - r_{n-1}$ is small. For the second integral, we can again use our assumption that $h(r) = (r^2 + 1)^{-1}$ for $r \geq r_n$, and overall we obtain for the angular separation of the endpoints:

$$\begin{aligned}
\phi_{n-1} \approx \quad & 2\sqrt{2h(r_{n-1})} \sqrt{\frac{r_n - r_{n-1}}{r_{n-1}}} + \frac{2\,r_{n-1}h'(r_{n-1}) - 5h(r_{n-1})}{3\sqrt{2h(r_{n-1})}} \left(\frac{r_n - r_{n-1}}{r_{n-1}}\right)^{3/2} \\
& + \arctan\left(\frac{2r_{n-1}^2 + \left(r_{n-1}^2 - 1\right) r_n^2}{2r_{n-1}\sqrt{r_n^4 - \left(r_{n-1}^2 - 1\right) r_n^2 - r_{n-1}^2}}\right) \\
& - \arctan\left(\frac{r_{n-1}^2 - 1}{2r_{n-1}}\right) \qquad\qquad\qquad\qquad\qquad\qquad\qquad\qquad (B.1.2)
\end{aligned}$$

where we have again taken the limit $r_{max} \gg r_n > r_{n-1}$. Alternatively, one could perform similar approximations on the equation for the proper length, (4.1.8), to obtain:

$$\begin{aligned}
\mathcal{L}_{n-1} \approx \quad & 2\sqrt{2r_{n-1}h(r_{n-1})}\sqrt{r_n - r_{n-1}} + \frac{3h(r_{n-1}) + 2\,r_{n-1}h'(r_{n-1})}{3\sqrt{2\,r_{n-1}\,h(r_{n-1})}} \left(r_n - r_{n-1}\right)^{3/2} \\
& + 2\log\left(2\,r_{max}\right) - 2\log\left(\sqrt{r_n^2 - r_{n-1}^2} + \sqrt{r_n^2 + 1}\right) \qquad\qquad (B.1.3)
\end{aligned}$$

In the above expressions we have introduced a further unknown, namely the gradient of the function $h(r)$ at the point $r = r_{n-1}$, which can be approximated linearly as described in section 3.1.3, which holds provided the radial distance $r_n - r_{n-1}$ is kept small.[2] Taking the entanglement entropy as a known quantity from the CFT

---

[2]The presence of an $h'(r)$ term deserves further comment: one can avoid introducing it by using the lowest order expansion, however, this reduces the overall accuracy of the method. The detrimental effect of the approximation to the gradient on the accuracy of the estimates is not as pronounced as in the method of chapter 3 due to the use of linear step size in J (and hence

(which then gives us $\mathcal{L}$), along with the angular separation of the endpoints (which is given simply from the length of the subsystem in the CFT) one can calculate the corresponding minimum radius r_{n-1} from (4.1.15), and so our only remaining unknown in both (B.1.2) and (B.1.3) is $h(r_{n-1})$. We can thus numerically solve either for $h(r_{n-1})$, and determine the metric function at this point. Continuing in a similar fashion, by taking geodesics with progressively smaller angular momenta and numerically solving at each step, we can iteratively extract the complete metric.

For general ϕ_{n-i} and $\mathcal{L}_{n-i}$ the integrals are split up into $(i + 1)$ pieces; two are approximated as in (B.1.2) and (B.1.3), with the remaining terms evaluated using Simpson's rule (a polynomial fit to the curve). The general expression for ϕ_{n-i} can then be written as:

$$\phi_{n-i} \approx A_{n-i} + B_{n-i} + C_{n-i} \tag{B.1.4}$$

where

$$A_{n-i} = 2\sqrt{2h(r_{n-i})}\sqrt{\frac{r_{n-i+1} - r_{n-i}}{r_{n-i}}} + \frac{2\,r_{n-i}h'(r_{n-i}) - 5h(r_{n-i})}{3\sqrt{2h(r_{n-i})}}\left(\frac{r_{n-i+1} - r_{n-i}}{r_{n-i}}\right)^{3/2} \tag{B.1.5}$$

$$C_{n-i} = \arctan\left(\frac{2r_{n-i}^2 + \left(r_{n-i}^2 - 1\right)r_n^2}{2r_{n-i}\sqrt{r_n^4 - \left(r_{n-i}^2 - 1\right)r_n^2 - r_{n-i}^2}}\right) - \arctan\left(\frac{r_{n-i}^2 - 1}{2r_{n-i}}\right) \tag{B.1.6}$$

are the two approximations we had before, and the B_{n-i} term is given by:

$$B_{n-i} = \sum_{j=1}^{i/2} \frac{\left(r_{n-2j+3} - r_{n-2j+1}\right)}{3}\left(g_{n-i}(r_{n-2j+3}) + 4\,g_{n-i}(r_{n-2j+2}) + g_{n-i}(r_{n-2j+1})\right) \tag{B.1.7}$$

for i even[3], and by

$$B_{n-i} = \sum_{j=1}^{(i-1)/2} \frac{\left(r_{n-2j+2} - r_{n-2j}\right)}{3}\left(g_{n-i}(r_{n-2j+2}) + 4\,g_{n-i}(r_{n-2j+1}) + g_{n-i}(r_{n-2j})\right) \tag{B.1.8}$$

---

r), see section 4.1.2. Surprisingly, an alternative integral one might consider when setting up the iteration, which allows the higher order series expansions to be combined to eliminate $h'(r)$ leads to an unstable method, rather than a more accurate one, see section 4.2.2.

[3]Using this definition requires a value for the r_{n+1} term, which can be obtained in an identical way to that used in determining r_n

for i odd, where we have defined the function

$$g_{n-i}(r) \equiv \frac{\sqrt{h(r)}}{r\sqrt{\frac{r^2}{r_{n-i}^2} - 1}} \tag{B.1.9}$$

for ease of notation. For the proper length we similarly have that:

$$\mathcal{L}_{n-i} \approx \mathcal{A}_{n-i} + \mathcal{B}_{n-i} + \mathcal{C}_{n-i} \tag{B.1.10}$$

with

$$\mathcal{A}_{n-i} = 2\sqrt{2r_{n-i}h(r_{n-i})}\sqrt{r_{n-i+1} - r_{n-i}} + \frac{3h(r_{n-i}) + 2r_{n-i}h'(r_{n-i})}{3\sqrt{2r_{n-i}h(r_{n-i})}}(r_{n-i+1} - r_{n-i})^{3/2} \tag{B.1.11}$$

$$\mathcal{C}_{n-i} = 2\log(2r_{max}) - 2\log\left(\sqrt{r_n^2 - r_{n-i}^2} + \sqrt{r_n^2 + 1}\right) \tag{B.1.12}$$

$$\mathcal{B}_{n-i} = \sum_{j=1}^{i/2} \frac{(r_{n-2j+3} - r_{n-2j+1})}{3}\left(\zeta_{n-i}(r_{n-2j+3}) + 4\zeta_{n-i}(r_{n-2j+2}) + \zeta_{n-i}(r_{n-2j+1})\right) \tag{B.1.13}$$

for i even, and

$$\mathcal{B}_{n-i} = \sum_{j=1}^{(i-1)/2} \frac{(r_{n-2j+2} - r_{n-2j})}{3}\left(\zeta_{n-i}(r_{n-2j+2}) + 4\zeta_{n-i}(r_{n-2j+1}) + \zeta_{n-i}(r_{n-2j})\right) \tag{B.1.14}$$

for i odd, with the function ζ defined by

$$\zeta_{n-i}(r) \equiv \frac{\sqrt{h(r)}}{\sqrt{1 - \frac{r_{n-i}^2}{r^2}}} \tag{B.1.15}$$

Thus we can continue the metric extraction down to $r = 0$ in the non-singular case, or down to $r = r_h$ in the black hole case, as described in section 4.1.

To clarify one further point, we note that the original (naive) method of section 4.1.1 can be stabilised by introducing a particular regularisation of the proper length, where one subtracts off the proper length of a corresponding geodesic in pure AdS which probes down to the same depth, r_{min}. Although this appears to not introduce any new information, one should remember that we are working from the field theory data, and as such, one does not in fact know the proper length of this geodesic, but rather the one which has the same angular separation of the endpoints. Thus using

this regularisation is actually equivalent to determining the minimum radius from (4.1.15), using this to determine the length of the corresponding geodesic in pure AdS, and then treating r_{min} as an unknown again in (B.1.4) and (B.1.10). This excessive over complication considerably reduces the efficiency of the method, as the equations are considerably more complicated to solve for (even numerically) at later steps.

Bibliography

[1] J. Hammersley, *"Extracting the bulk metric from boundary information in asymptotically AdS spacetimes"*, JHEP **0612**, 047 (2006) [arXiv:hep-th/0609202].

[2] J. Hammersley, *"Numerical metric extraction in AdS/CFT"*, GRG, to appear, [arXiv:0705.0159].

[3] J. Hammersley, *"A critical dimension for the stability of radiating perfecct fluid stars"*, arXiv:0707.0961

[4] V. Vaganov, *"Self-gravitating radiation in AdS(d)"*, arXiv:0707.0864

[5] S. L. Glashow, *"Partial Symmetries of Weak Interations"*, Nucl. Phys. **22** (1961) 579-588.

[6] M. Gell-Mann and S. L. Glashow, *"Gauge Theories of Vector Particles"*, Annals of Physics **15** (1961) 437-460.

[7] J. Bjorken and S. L. Glashow, *"Elementary Particles and $SU(4)$"*, Phys. Lett. **11** (1964) 255-257.

[8] A. Salam and J. C. Ward, *"Electromagnetic and Weak Interations"*, Phys. Lett. **13** (1964) 168-171.

[9] S. Weinberg, *"A Model of Leptons"*, Phys. Rev. Lett. **19** (1967) 1264-1266.

[10] D. J. Gross and F. Wilczek, *"Asymptotically Free Gauge Theories 1."*, Phys. Rev. D **8** (1973) 3633-3652.

[11] D. Politzer, *"Reliable Perturbative Results for Strong Interactions?"*, Phys. Rev. Lett. **30** (1973) 1346-1349.

[12] S. Hawking, *"A Brief History of Time"*, Bantam Books (1988)

[13] M. B. Green, J. H. Schwarz and E. Witten *"Superstring Theory"*, in 2 volumes, Cambridge Univ. Press (1987)

[14] J. Polchinski, *"String Theory"*, in 2 volumes, Cambridge Univ. Press (1998)

[15] B. Zweibach, *"A First Course in String Theory"*, Cambridge Univ. Press (2004)

[16] For a brief introduction to superstring theory, see J. H. Schwarz *"Introduction to Superstring Theory"*, arXiv:hep-ex/0008017.

[17] T. Thiemann, *"Lectures on loop quantum gravity"* Lect. Notes Phys. **631**, 41-135. (2003) [arXiv:gr-qc/0210094].

[18] A. Ashtekar and J. Lewandowski *"Background independent quantum gravity: a status report"* Class. Quant. Grav. **21**, R53 (2004), [arXiv:gr-qc/0404018].

[19] T. P. Sotiriou, *"Modified Actions for Gravity: Theory and Phenomenology"*, arXiv:0710.4438

[20] P. Brax and C. van de Bruck *"Cosmology and Brane worlds: A Review"*, Class. Quant. Grav. **20** (2003) R201-R232, [arXiv:hep-th/0303095].

[21] T. Kaluza, *"On the problem of unity in physics"*, Sitzungsber. Preuss. Akad. Wiss. Berlin (Math. Phys.) 966-972 (1921).

[22] C. N. Yang and R. Mills *"Conservation of Isotopic Spin and Isotopic Gauge Invariance"*, Phys. Rev. **96**, 191195i (1954).

[23] For an up-to-date graduate level introduction to the Standard Model, see W. N. Cottingham and D. A. Greenwood, *"An Introduction to the Standard Model of Particle Physics"*, Cambridge Univ. Press (2007)

[24] M. Dine, *"Supersymmetry and String Theory: Beyond the Standard Model"*, Cambridge Univ. Press (2007)

[25] S. T. Yau, *"Calabi's Conjecture and some new results in algebraic geometry"* Proc. Nat Acad. Sci. **74**, 1798-1799 (1977)

[26] P. Candelas, G. T. Horowitz, A. Strominger and E. Witten, *"Vacuum Configurations for Superstrings"* Nucl. Phys. B. **258**, 46-74 (1985)

[27] D. Lust, *"String Landscape and the Standard Model of Particale Physics"*, arXiv:0707.2305

[28] R. Bousso and J. Polchinski, *"Quantization of four-form fluxes and dynamical neutralization of the cosmological constant"*, JHEP **0006**, 006 (2000) [arXiv:hep-th/0004134].

[29] M. R. Douglas, *"The statistics of string / M theory vacua"*, JHEP **0305**, 046 (2003) [arXiv:hep-th/0303194].

[30] P. Candelas, X. de la Ossa, Y. He and B. Szendroi, *"Triadophilia: A Special Corner in the Landscape"*, arXiv:0706.3134

[31] P. Woit, *"Not Even Wrong: The Failure of String Theory and the Continuing Challenge to Unify the Laws of Physics"*, Jonathan Cape (2006)

[32] L. Smolin, *"The Trouble with Physics: The Rise of String Theory, the Fall of a Science and What Comes Next"*, Allen Lane (2007)

[33] L. Susskind, *"The anthropic landscape of string theory"*, arXiv:hep-th/0302219.

[34] E. Witten, *"String theory dynamics in various dimensions"*, Nucl. Phys. B **443**, 85-126 (1995) [arXiv:hep-th/9503124]; see also E. Witten, *"Some comments on string dynamics"*, in "Los Angeles 1995, Future Perspectives in string theory", (501-523), [arXiv:hep-th/9507121].

[35] J. M. Maldacena, *"The large N limit of superconformal field theories and super-gravity"*, Adv. Theor. Math. Phys. **2**, 231 (1998) [Int. J. Theor. Phys. **38**,1113 (1999)][arXiv:hep-th/9711200].

[36] E. Witten, *"Anti-de Sitter space and holography"*, Adv. Theor. Math. Phys. **2**, 253 (1998) [arXiv:hep-th/9802150].

[37] S. S. Gubser, I. R. Klebanov and A. M. Polyakov, *"Gauge theory correlators from non-critical string theory"*, Phys. Lett. B **428**, 105 (1998) [arXiv:hep-th/9802109].

[38] O. Aharony, S. S. Gubser, J. M. Maldacena, H. Ooguri and Y. Oz, *"Large N field theories, string theory and gravity"*, Phys. Rept. **323**, 183 (2000) [arXiv:hep-th/9905111].

[39] J. Polchinski, *"Dirichlet-branes and Ramond-Ramond charges"*, Phys. Rev. Lett. **75** (1995) 4724 [arXiv:hep-th/9510017].

[40] G. 't Hooft, *"Dimensional reduction in quantum gravity"*, arXiv:gr-qc/9310026.

[41] L. Susskind, *"The World as a hologram"*, J. Math. Phys. **36**, 6377 (1995) [arXiv:hep-th/9409089].

[42] S. W. Hawking, *"Information loss in black holes"*, Phys. Rev. D **72**, 084013 (2005) [arXiv:hep-th/0507171].

[43] J. Louko, D. Marolf and S. F. Ross, *"On geodesics propagators and black hole holography"*, Phys. Rev. D **62**, 044041 (2000) [arXiv:hep-th/0002111].

[44] V. E. Hubeny, *"Precursors see inside black holes"*, arXiv:hep-th/0208047.

[45] P. Kraus, H. Ooguri and S. S. Shenker, *"Inside the horizon with AdS/CFT"*, arXiv:hep-th/0212277.

[46] T. S. Levi and S. F. Ross, *"Holography beyond the horizon and cosmic censorship"*, arXiv:hep-th/0304150.

[47] L. Fidkowski, V. Hubeny, M. Kleban and S. Shenker, *"The Black Hole Singularity in AdS/CFT"*, hep-th/0306170.

[48] J. Kaplan, *"Extracting data from behind horizons with the AdS/CFT correspondence"*, arXiv:hep-th/0402066.

[49] V. Balasubramanian and T. S. Levi, *"Beyond the veil: Inner horizon instability and holography"*, arXiv:hep-th/0405048.

[50] A. Hamilton, D. Kabat, G. Lifschytz and D. A. Lowe, *"Local bulk operators in AdS/CFT: A boundary view of horizons and locality"*, arXiv:hep-th/0506118.

[51] G. Festuccia and H. Liu, *"Excursions beyond the horizon: Black hole singularities in Yang-Mills theories (I)"*, arXiv:hep-th/0506202.

[52] K. Maeda, M. Natsuume and T. Okamura, *"Extracting information behind the veil of horizon"*, arXiv:hep-th/0605224.

[53] T. Banks, M. R. Douglas, G. T. Horowitz and E. J. Martinec, *"AdS dynamics from conformal field theory"*, arXiv:hep-th/9808016.

[54] V. Balasubramanian, P. Kraus, A. E. Lawrence and S. P. Trivedi, *"Holographic probes of anti-de Sitter space-times"*, Phys. Rev. D **59**, 104021 (1999) [arXiv:hep-th/9808017].

[55] U. H. Danielsson, E. Keski-Vakkuri, and M. Kruczenski, *"Black hole formation in AdS and thermalisation on the boundary"*, JHEP **0002**, 039 (2000) [arXiv:hep-th/9912209].

[56] G. T. Horowitz and V. E. Hubeny, *"CFT Description of Small Objects in AdS"*, JHEP **0010**, 027 (2000) [arXiv:hep-th/0009051].

[57] B. Freivogel, S. B. Giddings and M. Lippert, *"Towards a theory of precursors"*, Phys. Rev. D **66**, 106002 (2002) [arXiv:hep-th/0207083].

[58] M. Porrati and R. Rabadan, *"Boundary rigidity and holography"*, JHEP **0401**, 034 (2004) [arXiv:hep-th/0312039].

[59] V. A. Kazakov, A. Marshakov, J. A. Minahan and K. Zarembo, *"Classical/quantum integrability in AdS/CFT "*, JHEP **0405**, 024 (2004) [arXiv:hep-th/0402207].

[60] A. Strominger, *"The ds/CFT Correspondence"*, JHEP **0110**, 034 (2001) [arXiv:hep-th/0106113].

[61] A. Strominger, *"Inflation and the ds/CFT Correspondence"*, JHEP **0111**, 049 (2001) [arXiv:hep-th/0110087].

[62] B. P. Schmidt *et al.*, *"The High-Z Supernova Search: Measuring Cosmic Deceleration and Global Curvature of the Universe Using Type Ia Supernovae"*, Astrophys. J. **507**, 46-63 (1998) [arXiv:astro-ph/9805200].

[63] A. G. Riess *et al.* [Supernova Search Team Collaboration], *"Observational Evidence from Supernovae for an Accelerating Universe and a Cosmological Constant"*, Astrophys. J. **116**, 1009-1038 (1998) [arXiv:astro-ph/9805201].

[64] S. Perlmutter *et al.* [Supernova Cosmology Project Collaboration], *"Measurements of Omega and Lambda from 42 High-Redshift Supernovae"*, Astrophys. J. **517**, 565-586 (1999) [arXiv:astro-ph/9812133].

[65] A. J. M. Medved, *"How Not to Construct an Asymtotiaclly de Sitter Universe"*, arXiv:hep-th/0203191.

[66] K. Peeters and M. Zamaklar, *"The string/gauge theory correspondence in QCD"*, arXiv:0708.1502

[67] D. Mateos, *"String theory Quantum Chromodynamics"*, arXiv:0709.1523

[68] B. Muller and J. L. Nagle, *"Results from the relativistic heavy ion collider"*, Ann. Rev. Nucl. Part. Sci **56** 93-135 (2006) [arXiv:nucl-th/0602029].

[69] F. Wilczek, *"Diquarks as inspiration and as objects"*, arXiv:hep-ph/0409168

[70] J. D. Bekenstein, *"Black holes and entropy"*, Phys. Rev. D **7**, 2333-2346 (1973)

[71] S. W. Hawking, *"Particle Creation by Black Holes"*, Commun. Math. Phys. **43**, 199-220 (1975) [Erratum-ibid. **46** 206 (1976)]

[72] A. Strominger and C. Vafa, *"Microscopic Origin of the Bekenstein-Hawking Entropy"*, Phys. Lett. B **379**, 99 (1996) [arXiv:hep-th/9601029].

[73] A. Einstein, B. Podolsky and N. Rosen, *"Can Quantum-Mechanical Description of Physical Reality Be Considered Complete?"*, Phys. Rev. **47**, 777-780 (1935).

[74] J. S. Bell, *"On the Einstein Podolsky Rosen paradox"*, Physics **1**, 195-200 (1964).

[75] G. Jaeger, *"Quantum Information: An Overview"*, Berlin: Springer (2006).

[76] P. Calabrese and J. Cardy, *"Entanglement entropy and quantum field theory"*, J. Stat. Mech. **0406**, P002 (2004) [arXiv:hep-th/0405152].

[77] P. Calabrese and J. Cardy, *"Entanglement entropy and quantum field theory: A non-technical introduction"*, Int. J. Quant. Inf. **4**, 429 (2006) [arXiv:quant-ph/0505193].

[78] S. R. White, *"Density matrix formulation for quantum renormalization groups"*, Phys. Rev. Lett. **69**, 2863-2866 (1992).

[79] K. Hallberg, *"New Trends in Density Matrix Renormalization"* Adv. Phys. **55**, 477-526 (2006)

[80] S. Ryu and T. Takayanagi, *"Holographic Derivation of Entanglement Entropy from AdS/CFT"*, arXiv:hep-th/0603001.

[81] S. Ryu and T. Takayanagi, *"Aspects of Holographic Entanglement Entropy"*, arXiv:hep-th/0605073.

[82] V. E. Hubeny, M. Rangamani and T. Takayanagi, *"A Covariant Holographic Entanglement Entropy Proposal"*, arXiv:0705.0016.

[83] V. E. Hubeny, H. Liu and M. Rangamani, *"Bulk-cone singularities and signatures of horizon formation in AdS/CFT"*, JHEP **0701**, 009 (2007) [arXiv:hep-th/0610041].

[84] P. H. Chavanis, *"Relativistic stars with a linear equation of state: analogy with classical isothermal spheres and black holes"*, arXiv:0707.2292

[85] I. R. Klebanov, *"TASI Lectures: Introduction to the AdS/CFT correspondence"*, arXiv:hep-th/0009139

[86] E. D'Hoker and D. Z. Freedman, *"Supersymmetric gauge theories and the AdS/CFT correspondence"*, arXiv:hep-th/0201253.

[87] J. M. Maldacena, *"TASI 2003 lectures on AdS/CFT"*, arXiv:hep-th/0309246

[88] H. Nastase, *"Introduction to AdS/CFT"*, arXiv:hep-th/0712.0689

[89] G. T.Horowitz and J. Polchinski, *"Gauge/gravity duality"*, arXiv:gr-qc/0602037

[90] G. 't Hooft, *"A planar diagram theory for strong interactions"*, Nucl. Phys. B **72** 461-473 (1974)

[91] M. K. Benna, S. Benvenuti, I. R. Klebanov, A. Scardicchio, *"A Test of the AdS/CFT Correspondence Using High-Spin Operators"*, Phys. Rev. Lett. **98** 131603 (2007)

[92] C. Holzhey, F. Larsen and J. Wilczek, *"Geometric and renormalized entropy in conformal field theory"*, Nucl. Phys. B **424**, 443 (1994) [arXiv:hep-th/9403108].

[93] M. Headrick and T. Takayanagi, *"A holographic proof of the strong subadditivity of entanglement entropy"*, Phys. Rev. D **76**, 106013 (2007) [arXiv:hep-th/0704.3719].

[94] T. Hirata and T. Takayanagi, *"AdS/CFT and Strong Subadditivity of Entanglement Entropy"*, JHEP **0702**, 042 (2007) [arXiv:hep-th/0608213].

[95] T. Hirata and T. Takayanagi, *"AdS Bubbles, Entropy and Closed String Tachyons"*, JHEP **0701**, 090 (2007) [arXiv:hep-th/0611035].

[96] D. Fursaev, *"Proof of the Holographic Formula for Entanglement Entropy"*, JHEP **0609**, 018 (2006) [arXiv:hep-th/0606184].

[97] R. Emparan, *"Black hole entropy as entanglement entropy: a holographic derivation"*, JHEP **0606**, 012 (2006) [arXiv:hep-th/0603081].

[98] S. N. Solodukhin, *"Entanglement entropy of black holes and AdS/CFT correspondence"*, Phys. Rev. Lett. **97**, 201601 (2006) [arXiv:hep-th/0606205].

[99] A. Velytsky, *"Entanglement entropy in $d + 1$ $SU(N)$ gauge theory"*, arXiv:0801.4111

[100] A. Schwimmer and S. Theisen, *"Entanglement Entropy, Trace Anomalies and Hologrpahy"*, arXiv:0802.1017

[101] M. S. Berger and R. V. Buniy, *"Entanglement Entropy and Spatial Geometry"*, arXiv:0801.4564

[102] J. I. Latorre, E. Rico and G. Vidal, *"Ground state entanglement in quantum spin chains"*, Quant. Inf. Comput. **4**, 48-92 (2003) [arXiv:quant-ph/0304098].

[103] H. Katsura and Y. Hatsuda, *"Entanglement entropy in the Calogero-Sutherland Model"*, J. Phys. A: Math. Theor. **40**, 13931 (2007) [arXiv:0708.1207].

[104] P. Calabrese and J. Cardy, *"Entanglement and correlation functions following a local quench: a conformal field theory approach"*, J. Stat. Mech. P10004 (2007) [arXiv:0708.3750].

[105] J. D. Brown and M. Henneaux, *"Central Charges in the Canonical Realization of Asymptotic Symmetries: An Example from Three Dimensional Gravity"*, Commun. Math. Phys. **104** 207-226 (1986).

[106] V. Balasubramanian and P. Kraus, *"A Stress Tensor for Anti-de Sitter gravity"*, Commun. Math. Phys. **208**, 413-428 (1999) [arXiv:hep-th/9902121].

[107] S. Gao and R. M. Wald, *"Theorems on gravitational time delay and related issues"*, Class. Quant. Grav. **17** 4999-5008 (2000), [arXiv:gr-qc/0007021].

[108] D. N. Page and K. C. Phillips, *"Selfgravitating radiation in anti-de sitter space"*, GRG (1985).

[109] D. Astefanesi and E. Radu, *"Boson stars with negative cosmological constant"*, Nucl. Phys. **B665** (2003) 594-622 [arXiv:gr-qc/0309131].

[110] D. Astefanesi and E. Radu, *"Rotating boson stars in (2+1) dimensions"*, Phys. Lett. **B587** (2004) 7-15 [arXiv:gr-qc/0310135].

[111] H. J. Matschull, *"Black Hole creation in 2 + 1 dimensions"*, Class. Quantum Grav. **16** (1999) 1069-1095 [arXiv:gr-qc/9809087].

[112] J. G. Loeser and D. R. Herschbach, *"Dimension dependence of correlation energies in two electron atoms"*, J. Chem. Phys. Vol. 86, No. 6, pp. 3512-3521 (1987).

[113] R. Gregory and R. Laflamme, *"Black strings and p-branes are unstable"*, Phys. Rev. Lett. **70**, 2837 (1993) [arXiv:hep-th/9301052].

[114] R. Gregory and R. Laflamme, *"The instability of charged black strings and p-branes"*, Nucl. Phys. B **428**, 399 (1994) [arXiv:hep-th/9404071].

[115] V. A. Belinsky, I. M. Khalatnikov and E. M. Lifshitz, *"Oscillatory approach to a singular point in the relativistic cosmology"*, Adv. Phys. **19**, 525 (1970).

[116] J. Demaret, M. Henneaux and P. Spindel, *"Non-oscillatory behaviour in vacuum Kaluza-Klein cosmologies"*, Phys. Lett. B **164**, 27 (1985).

[117] J. Demaret, J. L. Hanquin, M. Henneaux, P. Spindel and A. Taormina, *"The Fate of the Mixmaster Behaviour in vacuum Inhomogeneous Kaluza-Klein Cosmological Models"*, Phys. Lett. B **175**, 129 (1986).

[118] Y. Elskens and M. Henneaux, *"Chaos in Kaluza-Klein models"*, Class. Quant. Grav. **4**, 161-167 (1987).

[119] J. M. Heinzle, N. Rohr and C. Uggla, *"Spherically Symmetric Relativistic Stellar Structures"*, Class. Quantum Grav. **20** (2003) 4567 [arXiv:gr-qc/0304012].

[120] R. Sorkin, *"A Criterion for the onset of instability at a turning point"*, Astrophys. J. **249**, 254-257 (1981).

[121] R. M. Wald, *"General Relativity"*, Chicago, USA: Univ. Pr. p. 491 (1984).

[122] D. N. Page and K. C. Phillips, *"Self-gravitating radiation in anti-de Sitter space"*, GRG Vol. 17, No. 11 pp. 1029-1041 (1985).

[123] C. Sire and P. H. Chavanis, *"Thermodynamics and collapse of self-gravitating Brownian particles in D dimensions"*, Phys. Rev. **E 66** (2002) 046133 [arXiv:cond-mat/0204303].

[124] P. Hartman, *"Ordinary Differential Equations"*, Birkhäuser, Boston (1982). For an introduction to dynamical systems, see J. D. Crawford, *"Introduction to bifurcation theory"*, Rev. Mod. Phys. **63 4**, 991-1038 (1991).